Karlsruhe Institute of Technology

Multiphase-field simulation of ferroelectric materials

Zur Erlangung des akademischen Grades einer
Doktorin der Ingenieurwissenschaften (Dr.-Ing.)

von der KIT-Fakultät für Maschinenbau des
Karlsruher Instituts für Technologie (KIT)
angenommene

Dissertation
von

M.Sc. Ling Fan

Tag der mündlichen Prüfung:	16.12.2024
Hauptreferentin:	Prof. Dr. rer. nat. Britta Nestler
Korreferent:	Prof. Dr.-Ing. Ralf Müller

Abstract

This dissertation presents two novel models for investigating ferroelectric materials, based on the multiphase-field approach—a powerful tool in materials science and engineering for predicting microstructural and morphological evolution.

The first model integrates the multiphase-field approach with the Landau-Ginzburg-Devonshire Theory (LGDT) for ferroelectric materials. The objective is to investigate the microstructural evolution of coexisting ferroelectric phases, such as the co-existing ferroelectric tetragonal phase (FT) and ferroelectric rhombohedral phase (FR) near the morphotropic phase boundary (MPB) of $\mathrm{Pb(Zr_{1-x}Ti_x)O_3}$ (PZT) material. As both the phase-field ϕ and polarization vector $\boldsymbol{P}$ are order parameters, this model enables the calculation of the transformation between ferroelectric phases, as well as the associated domain structures within each ferroelectric phase. Using this model, this work investigates the PZT-based material PIC 151, in both single-crystal and polycrystalline structures, under external stimuli.

The second model employs the multiphase-field concept to compute ferroelectric materials, with the polarization states of each ferroelectric phase variant predetermined. Unlike the time-dependent Ginzburg-Landau (TDGL) equation, which computes domain structures through the spatial and temporal evolution of the polarization vector, the second model computed them by evolving the multiphase-field order parameter ϕ, representing the predetermined polarization variants. The total energy functional in this model comprises the general interfacial energy in the multiphase-field framework and the phase-dependent bulk energy, accounting for the contributions from the mechanical and electric fields. This model was applied to bulk $\mathrm{BaTiO_3}$ (BTO) ferroelectrics to explore domain structure formation, domain switching, and material properties under external stimuli. It was also extended to investigate (001)-oriented $\mathrm{PbTiO_3}$ (PTO) thin films, examining its epitaxial growth on various conditions. Additionally, this model studies the mechanism of domain structure formation in single-crystal and polycrystalline Methylammonium Lead Iodide ($\mathrm{MAPbI_3}$) thin films, which is the first application of the phase-field approach to compute domain structure formation in Organic metal halide (OMH) perovskite ferroelectrics. The dissertation also discusses potential extensions of the second model for further investigating ferroelectric materials.

Zusammenfassung

Diese Dissertation stellt zwei neuartige Modelle zur Untersuchung von ferroelektrischen Materialien vor, die auf dem Mehrphasenfeldansatz basieren—einem leistungsstarken Werkzeug in der Materialwissenschaft und im Ingenieurwesen zur Vorhersage mikrostruktureller und morphologischer Entwicklungen.

Das erste Modell integriert den Mehrphasen-Feldansatz mit der Landau-Ginzburg-Devonshire-Theorie (LGDT) für ferroelektrische Materialien. Das Ziel ist es, die mikrostrukturelle Entwicklung koexistierender ferroelektrischer Phasen, wie beispielsweise der koexistierenden ferroelektrische tetragonale Phase und ferroelektrische rhombohedrale Phase nahe der morphotropische Phasengrenze des $\mathrm{Pb(Zr_{1-x}Ti_x)O_3}$ (PZT)-Materials, zu untersuchen. Da sowohl das Phasenfeld ϕ als auch der Polarisationsvektor $\boldsymbol{P}$ Ordnungsparameter sind, ermöglicht dieses Modell die Berechnung der Umwandlung zwischen ferroelektrischen Phasen sowie der damit verbundenen Domänenstrukturen innerhalb jeder ferroelektrischen Phase. Mit diesem Modell wird in dieser Arbeit das einkristalline und polykristalline PIC 151 Material, ein auf PZT basierendes Material, unter äußeren Einflüssen umfassend untersucht.

Das zweite Modell verwendet das Multiphasenfeld-Konzept zur Berechnung von Domänenstrukturen, bei denen die Polarisationszustände innerhalb jeder Variante vorgegeben sind. Im Gegensatz zur zeitabhängigen Ginzburg-Landau-Gleichung (TDGL), das Domänenstrukturen durch räumliche und zeitliche Entwicklung des Polarisationsvektors jeder ferroelektrischen Variante berechnet, werden bei diesem Modell die Domänenstrukturen durch Minimierung des Gesamtenergie-Funktionals in Bezug auf den Ordnungsparameter des Multiphasenfelds ϕ berechnet. Das Energie-Funktional beinhaltet die allgemeine Grenzflächenenergie im Rahmen des Multiphasenfeldmodells sowie die phasenabhängige Volumenenergie, wobei die Beiträge der mechanischen und elektrischen Felder berücksichtigt werden. Dieses Modell wurde auf voluminöse $\mathrm{BaTiO_3}$ (BTO)-Ferroelektrika angewendet, um die Domänenbildung/-umschaltung und Materialeigenschaften unter äußeren Einflüssen zu untersuchen. Es wurde zudem erweitert, um (001)-orientierte $\mathrm{PbTiO_3}$ (PTO)-Dünnfilme zu untersuchen und deren epitaktisches Wachstum unter verschiedenen Bedingungen zu analysieren. Zusätzlich untersucht dieses Modell den Mechanismus der Domänenstrukturformation in Methylammoniumbleiiodid ($\mathrm{MAPbI_3}$)-Filmen, was die erste Anwendung des Phasenfeldansatzes zur Berechnung der Domänenstrukturen von $\mathrm{MAPbI_3}$ darstellt. Die Dissertation präsentiert auch mögliche Erweiterungen des Modells zur weiteren Untersuchung von ferroelektrischen Materialien.

Acknowledgments

To end this remarkable journey, I would like to extend my heartfelt gratitude to the people whose support and guidance have made this experience meaningful.

First of all, I would love to thank my supervisor, Prof. Dr. rer. nat. Britta Nestler, for kindly allowing me to join her team, which has been instrumental in my academic and professional development. I am especially thankful for the freedom she gave me to explore the fascinating aspects of ferroelectric material and phase-field modeling.

I extend my sincere thanks to Dr. Daniel Schneider, my group leader, for his invaluable academic discussions and guidance. I would also like to thank him for his patience and assistance in dealing with the paperwork. Special appreciation is reserved for my colleague, Dr. Martin Reder, for his important role in code implementation and insightful discussions. Gratitude also goes to Dr. Manuel Hinterstein, whose experimental support and discussions have significantly contributed to the depth of my work. I also want to thank Swen Subotić, who also provided experimental support in my study. My sincere thanks also extend to Prof. Alexander Colsmann and Dr. Holger Röhm for their crucial roles in the KeraSolar project and all stimulating discussions.

I also thank Prof. Dr. Ralf Müller for serving as the co-referee and Prof. Luise Kärger for chairing the examination committee.

I extend my sincere thanks to my other wonderful colleagues, Walter Werner, Ye Ji, Xiaoying Liu, Paul Hoffrogge, Ahmed Elmoghazy, Simon Daubner, Andreas Prahs, Momin Ahmad, Akash Kumar, Lukas Schöller, Ravi Kumar Jeela, Marcel Weichel, Michael Späth, Nishant Prajapati, Thea Kannenberg, Muhammad Umar, Olena Abramova, as well as others. Thank you for all the helpful as well as funny discussions and warm companionship which made the work environment more enjoyable. Additional thanks are due to all members of the KeraSolar project for their kind and enthusiastic discussions.

I also express my appreciation to Mr. Christof Ratz for his technical support with computers and systems. Special thanks to Mr. Leon Geisen for his assistance in improving English publications. My gratitude also goes to the secretariat—Ms. Inken Heise, Ms. Nadine Saier, and Ms. Birgitt Hardt—for their assistance with paperwork.

I would like to express my gratitude for the financial support received from the China Scholarship Council and the KeraSolar project funded by the Carl Zeiss Foundation.

Last but not least, I would like to thank my family, my boyfriend, and other friends for their love and support.

Contents

Part I
Introduction and Literature review

1. Introduction

1.1. Motivation

Drawing upon the Landau-Ginzburg-Devonshire Theory (LGDT) [1–3], the phase-field method, incorporating the time-dependent Ginzburg-Landau (TDGL) equation, has been employed to study ferroelectric phase coexistence, bidirectional ferroelectric phase transformations, and their associated domain structures in $\mathrm{Pb}(\mathrm{Zr}_{1-x}\mathrm{Ti}_x)\mathrm{O}_3$ (PZT) material at morphotropic phase boundary (MPB), as outlined in Refs. [4–12]. Nonetheless, regarding polycrystalline ferroelectrics exhibiting a composition near the MPB, a model for computing the domain structures, phase coexistence, and grain boundary phenomena is currently absent. To address this gap, the first aim of this dissertation involves enhancing the phase-field model of ferroelectric materials. This is achieved by coupling the multiphase-field method with the TDGL equation, which is based on LGDT, and is referred to as Model I in this dissertation. This combination provides a more comprehensive understanding of microstructural changes and domain morphological evolution under various influencing factors, contributing to the advancement of materials science and engineering.

In using the TDGL equation to study ferroelectric materials, the polarization vector serves as the order parameter [13]. Depending on LGDT, the thermodynamic description of the polarization state is governed by a Landau potential, a high-order polynomial function of the polarization vector. Besides, the analysis of domain walls incorporates the domain wall energy, introduced through the polarization gradient. Consequently, determining the domain walls requires a set of phenomenological Landau and gradient coefficients. However, Landau coefficients are available to only a limited subset of materials [14], and their determination poses significant challenges in materials science. For instance, to investigate domain structures and ferroelectric phase transformations in the PZT-based PIC 151 material using Model I, extensive effort has been dedicated to determining the phase-dependent Landau coefficients in the first work [15]. The lack of coefficients also leaves an unexplored understanding of the domain structure formation and the associated properties of many materials, such as the ferroelectric semiconductor Methylammonium Lead Iodide (MAPbI_3). Consequently, this work proposes a new model based on the multiphase-field approach, termed Model II, to study ferroelectric materials [16, 17].

1.2. Structure of this work

The present work is structured as follows: In Chapter 2, an exploration of the literature review on ferroelectric materials and their thermodynamic theory is undertaken. The phase-field approach is briefly presented in the same chapter, and the phase-field models of the ferroelectrics are summarized. The model description of this dissertation is delineated in Chapters 3 and 4. Chapter 3 thoroughly explains Model I, while the in-depth analysis of Model II is presented in Chapter 4. The research results are primarily covered in Chapters 5 through 8. Employing Model I, Chapter 5 is dedicated to simulating PIC 151 material to explore ferroelectric phase transformations and domain structures. Chapters 6 to 8 provide insights into modeling ferroelectric material using Model II. Chapter 6 studies the domain structure formation and switching in single-crystal and polycrystalline bulk $\mathrm{BaTiO_3}$ (BTO) material, while Chapters 7 and 8 focus on simulating ferroelectric thin films with epitaxial growth and polycrystalline structures, respectively. The contents of Chapters 3 to 7 are adopted from publications in Refs. [15–17]. Lastly, Chapter 9 summarizes the key findings and achievements of the current research. This chapter also suggests potential directions for further exploration.

1.3. Notation

Notation in this work follows Einstein's summation convention [18]. Since a fixed Cartesian coordinate system is assumed throughout, only subscripts are used in the notation. The 0th-order tensors, i.e., scalars, are demonstrated by letters without indices in this dissertation, e.g. α or β. This thesis employs two representations for tensors of high order. One is indicated by bold font, while the other is indicated by tensor notation. For instance, vectors such as polarization are represented by both $\boldsymbol{P}$ and $P_i\,(i = 1, 2, 3)$ while the second-order stress tensor is denoted as $\boldsymbol{\sigma}$ or $\sigma_{ij}\,(i, j = 1, 2, 3)$. Besides, the fourth-order tensor with the bold model is described by calligraphic font to distinguish it from the second-order tensor. The exemplar is the elastic stiffness tensor, which is denoted as $\boldsymbol{\mathcal{C}}$ or $\mathcal{C}_{ijkl}$. The Kronecker's symbol

$$\delta_{ij} = \begin{cases} 1 \text{ for } i = j \\ 0 \text{ for } i \neq j \end{cases} \tag{1.1}$$

is introduced to represent the identity in index notation.

2. Literature review

Ferroelectric materials compose an important class of functional materials that generate spontaneous polarization upon transformation from the paraelectric to ferroelectric phases, with this polarization being switched with an induced electric field. Domain structures, which represent the organized arrangement of electric dipoles and can be easily manipulated by external stimuli, consist of the inherent characteristics of ferroelectric materials. Hence, understanding domain structures and their response to external fields is crucial for the practical using ferroelectric materials. The advancements in computer science and technical capabilities have enabled adopting numerical methodologies such as the phase-field method [13, 19], first-principle calculations [20, 21], Monte Carlo simulations [22–24], Molecular Dynamics [25–27], Machine Learning [28, 29] and so on, for investigating ferroelectric materials. Among them, the phase-field approach enables the probing, prediction, and design of domain structures under various electromechanical boundary conditions, as well as the investigation of the domain switching under electric and mechanical stimuli, accelerating overall analysis and understanding of the behavior and properties of ferroelectric materials. Therefore, this section provides an overview of ferroelectric materials alongside their thermodynamic foundations, supplemented by a brief introduction to the phase-field method and its applications in modeling ferroelectric materials.

2.1. Understanding ferroelectric materials: from polarity origins to domain structures

2.1.1. The origin and description of polarity

The concept of polarity primarily originates from the study of electromagnetism and the behavior of charged particles. With the understanding of the microstructure of matter, the essence of electromagnetic phenomena lies in the existence and movement status of charged particles, recognized in the 19^{th} century. Matter is formed by aggregating positively charged atomic nuclei and negatively charged electrons through Coulomb interactions. Concurrently, those charged particles can be redistributed by external loads. These transfer characteristics of charges have long been known to humanity, for a long time. For instance, one can easily observe static electricity and lightning in nature. Due to the attraction of opposite charges, the system tends to return to an electrically

neutral state after transformation in these phenomena. Therefore, the condition of electrical neutrality of macroscopic matter is widely accepted as an empirical rule at that time. However, although the overall matter is still electrically neutral, its centers of positive and negative charges no longer coincide under an imposed electric field. Therefore, a new physical quantity—polarization— is introduced to describe such a phenomenon.

Mathematically, the concept of electric multipole moments can be introduced to represent polarization, where the electric dipole moment vector ($\boldsymbol{p}$) is the most commonly used, described as:

$$\boldsymbol{p} = q\boldsymbol{d}. \tag{2.1}$$

q represents the magnitude of charges that are equal in magnitude but opposite in sign [30]. $\boldsymbol{d}$ denotes the displacement vector, which points from the negative charge toward the positive charge. The polarization vector $\boldsymbol{P}$ is defined as the average value of dipole moment within the volume V [31], described as:

$$\boldsymbol{P} = \frac{1}{V}\sum \boldsymbol{p}. \tag{2.2}$$

Using the notion of polarization, Maxwell introduced the concept of electric displacement, $\boldsymbol{D}$, refining the fundamental framework of electromagnetic theory. The corresponding constitutive equation is expressed as:

$$\boldsymbol{D} = \kappa_0 \boldsymbol{E} + \boldsymbol{P}, \tag{2.3}$$

within which $\kappa_0 = 8.85 \times 10^{-12}\,\mathrm{F/m}$ denotes the vacuum permittivity, and $\boldsymbol{E}$ is the external electric field vector [31]. Drawing up the definition of polarization in Eq. (2.2), $\boldsymbol{D}$ and $\boldsymbol{P}$ are the statistical averaging results. It should be highlighted that the symbol ε typically represents the permittivity. To avoid confusion with the elastic strain symbol, which is also denoted by ε, this thesis employs κ as the symbol for permittivity.

2.1.2. Polarization in dielectric material

When subjected to an external electric field, dielectric materials that act as insulators or poor conductors due to the absence of mobile charge carriers can exhibit polarization, denoted as:

$$\boldsymbol{P} = \kappa_0 \chi \boldsymbol{E}, \tag{2.4}$$

in which χ represents the dielectric susceptibility [31]. By integrating Eqs. (2.2) (2.3), and (2.4), the electric displacement $\boldsymbol{D}$ in a dielectric material is further formulated as:

$$\boldsymbol{D} = \kappa_0 \boldsymbol{E} + \kappa_0 \chi \boldsymbol{E} = \kappa_0 (1 + \chi)\boldsymbol{E} = \kappa_0 \kappa_r \boldsymbol{E} = \kappa \boldsymbol{E}. \tag{2.5}$$

κ_r denotes the relative dielectric permittivity, and $\kappa = \kappa_0 \kappa_r$, which signifies the dielectric permittivity of the material. It is crucial to recognize that when materials exhibit

anisotropy, both the dielectric susceptibility and dielectric permittivity are described by second-order tensors, denoted as χ_{ij} (or $\boldsymbol{\chi}$) and κ_{ij} (or $\boldsymbol{\kappa}$), respectively. The relationship

$$\kappa_{ij} = \kappa_0(\delta_{ij} + \chi_{ij}) \tag{2.6}$$

remains valid.

The physical process of dielectric polarization is commonly attributed to electronic polarization, ionic polarization, orientation polarization, and space charge polarization [32]. As outlined in Fig. 2.1, the electronic contribution behaves through the displacement of the negatively charged electron shell to a positively charged nucleus, a phenomenon observable across all dielectrics. The ionic contribution denotes the displacement of cations relative to anions, notably observed within ionic crystals. Orientation polarization delineates the alignment of molecules, exemplified by water, possessing a permanent electric dipole moment under an electric field. Space charge polarization results from the non-uniform accumulation of charge carriers at structural interfaces, including grain boundaries, phase boundaries, and domain walls. In perovskite ferroelectrics like $PbTiO_3$ (PTO) and BTO, spontaneous polarization arises from a combination of the four mechanisms, primarily driven by the ionic contribution, especially the off-centered displacement of Ti atoms. The contribution of each mechanism to the overall polarization of a dielectric material is contingent upon its material type, form, and the frequency of the applied electric field.

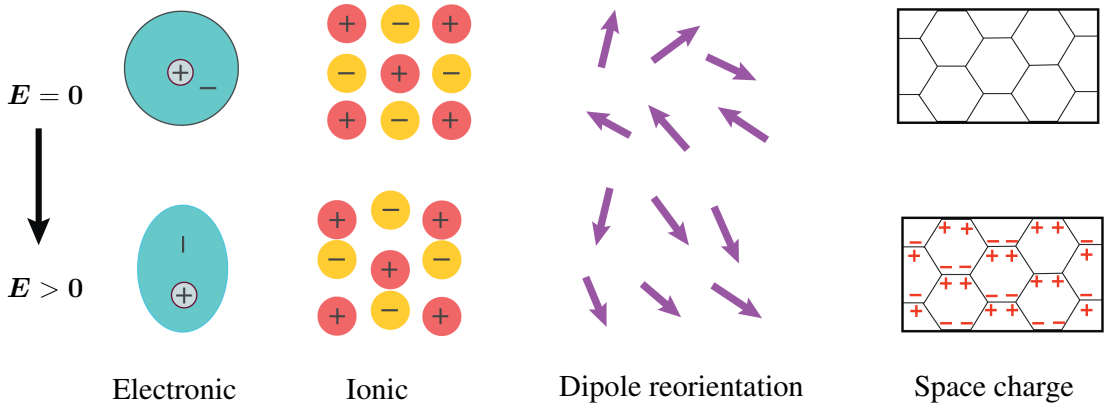

Figure 2.1.: Schematic diagram of the primary physical processes of dielectric polarization.

2.1.3. From dielectrics to ferroelectrics

Depending on the crystal structure, centers of positive and negative charges in special dielectrics may not align without an external electric field. Crystals exhibiting this phenomenon are described as having spontaneous polarization. When an external electric

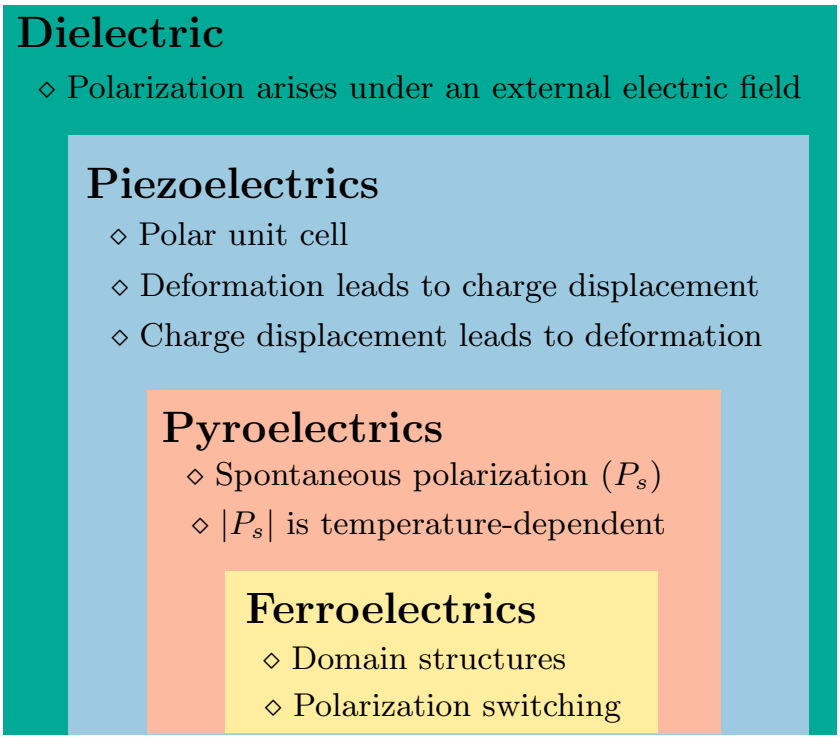

Figure 2.2.: The relationship and character within dielectric, piezoelectrics, pyroelectrics, and ferroelectric. Based on Ref. [33].

field can switch the polarization, such dielectrics are termed ferroelectric. For ferroelectric material characterized by spontaneous polarization, the electric displacement in Eq. (2.5) requires adjustment to:

$$\boldsymbol{D} = \kappa_0(1+\chi)\boldsymbol{E} + \boldsymbol{P}_s, \tag{2.7}$$

where $1 + \chi = \kappa_b$ with κ_b represents the background dielectric constant [34–36]. Similarly, the background dielectric constant also turns into a second tensor when the material has anisotropic characteristics.

There are piezoelectric and pyroelectric materials between dielectric and ferroelectric materials. The foundation of this classification lies in the crystal structures of the materials. According to crystallographic principles, describing three-dimensional crystal structures entails 14 distinct Bravais lattices and 32 unique point groups, resulting in 230 space groups when translational symmetry is considered. Dielectric materials adhere to classification principles, wherein 21 of the 32-point groups lack spatial symmetry, while 11 exhibit spatial symmetry. Within the non-symmetric classification, materials that omit the highly symmetric '432' point group and belong to the remaining 20 point groups capable of generating electric charge under stress are denoted as piezoelectric materials. Of the 20 piezoelectric crystal classes, 10 exhibit a uniquely polar axis.

These classes are characterized by generating spontaneous polarization without an applied electric field and are termed pyroelectric. A pyroelectric material is further defined as ferroelectric when it exhibits domain structures and an external electric field can reorient its spontaneous polarization. For more detail, one could refer to [37]. Fig. 2.2 summarizes the relationship of dielectrics, piezoelectrics, pyroelectrics, and ferroelectric.

2.1.4. Polarization generation in perovskite ferroelectrics

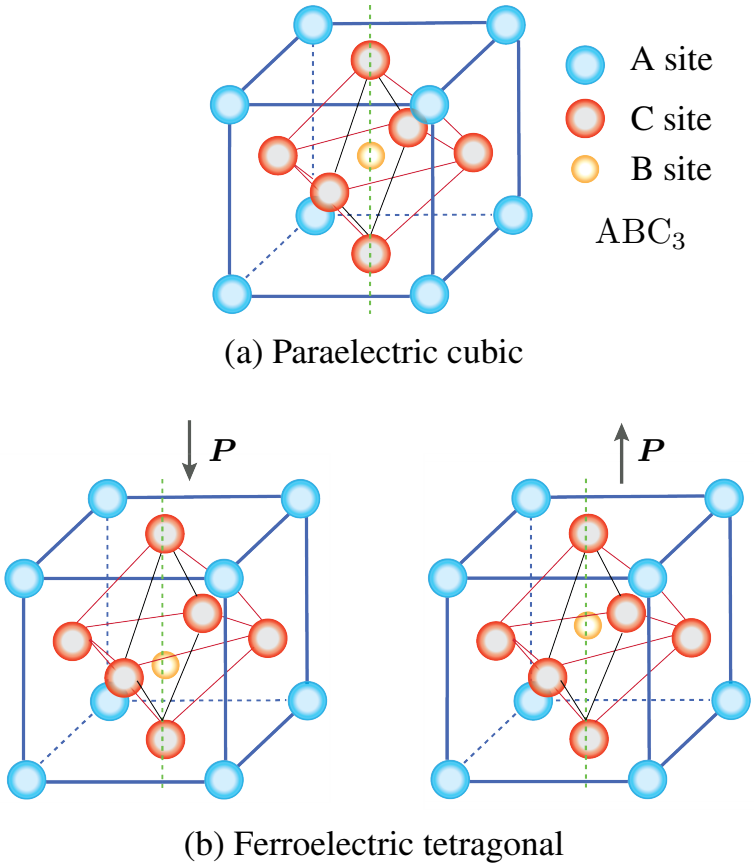

(a) Paraelectric cubic

(b) Ferroelectric tetragonal

Figure 2.3.: Schematic diagram of displacement-type polarization in perovskite ferroelectric materials.

Despite ferroelectric materials exhibiting diverse crystal structures and phase transformation forms, perovskite-structured displacement ferroelectrics, defined by the chemical formula ABC_3, stand as the foremost subjects of study and are widely recognized as essential exemplars in the ferroelectricity field. Fig. 2.3 illustrates the crystal

structure of ABC_3 in both its paraelectric cubic and ferroelectric tetragonal phases. The A-site cation, typically a large ion, is located at the corners of the unit cell, and the B-site cation, usually a smaller ion such as a transition metal ion, occupies the body-centered position. The C-site anion, which could be oxygen or a halide, resides at the face-centered positions of the unit cell. Thus, the compositions of ABC_3 can include $A^{2+}B^{4+}C_3^{-2}$ compounds, examples of which are BTO, PTO, and PZT, and other formulae like $A^{1+}B^{2+}C_3^{-1}$, such as $MAPbI_3$.

The polarization generation in perovskite ferroelectrics primarily stems from the displacement of ions and distortion of the unit cell induced by phase transformations. In the transition from a cubic paraelectric phase to a tetragonal ferroelectric phase, for example, an elongation of the unit cell along the c-axis can occur by comparing Fig. 2.3(b) to (a), leading to a change in the axis ratio where $c/a > 1$. Simultaneously, distortion along the c-axis affects the body-centered B-site, resulting in a displacement of the central positions of positive and negative charges. Specifically, the upward shifting of the positive charge from the central position generates polarization oriented along the positive c-axis. Analogously, polarization along the negative c-axis can be induced when the positive charge is shifted downward.

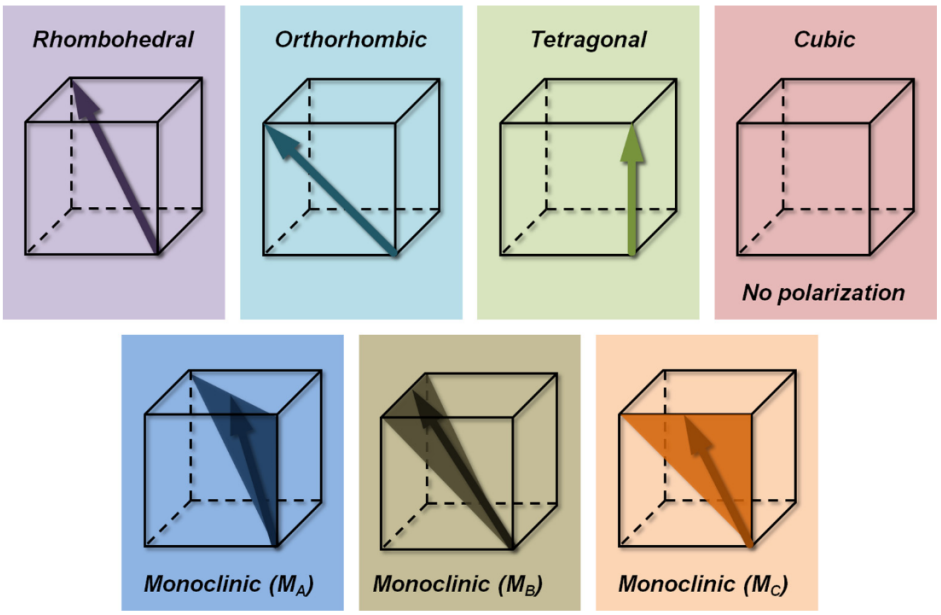

Figure 2.4.: The phase transformation pathway of rhombohedral, orthorhombic, tetragonal, cubic perovskite ferroelectrics (from low to high temperature), and three intermediate monoclinic phases M_A, M_B, and M_C. The arrows denote the polarization direction in the Cartesian coordinate system. The shaded triangle in monoclinic phases indicates the ranges where the polarization orientation can vary. Adapted from Ref. [38].

Polarization in the perovskite ferroelectrics may also be generated along the edge or corner directions, based on the material symmetry. As discussed in Ref. [38], for instance, typical perovskite ferroelectric materials undergo distinct first-order ferroelectric phase transitions upon cooling, sequentially transitioning through tetragonal, orthorhombic, and rhombohedral phases, as illustrated in Fig. 2.4. Monoclinic may also appear as intermediate or secondary phases in materials such as BTO. During the transition from the tetragonal to the monoclinic phase, distinct polarization emerges in each phase, aligning with their energetically equivalent directions.

2.1.5. Domain structures in ferroelectric materials

In order to minimize the energy of the system, different regions within the crystal align the polarization vectors along their energetically equivalent directions. This results in the ferroelectric domain, where the consistent polarization orientation is exhibited in a contiguous region. These domains are demarcated from adjacent ones by domain walls, typically ranging from a few unit cells to the nanometer scale. A domain wall is predicated on the relative orientation between the polarization directions of the neighboring domains. For example, surfaces perpendicular to the ferroelectric polarization exhibit bound charges, generating a depolarizing field, $\boldsymbol{E}_{\mathrm{dep}}$, as shown in Fig. 2.5(a). Strategies to release $\boldsymbol{E}_{\mathrm{dep}}$ include: (i) compensating these charges with surface adsorbates or metallic electrodes (see Fig. 2.5 (b)); or (ii) forming the 180° ferroelectric domain walls to ensure that the net polarization at the surface averages to zero (see Fig. 2.5(c)). When the elastic energy is predominated in the system, non-180° ferroelastic domain walls could even be formed. Examples include the 90° domain wall in the tetragonal ferroelectric (Fig. 2.5 (d)), and 71° or 109° domain walls in the ferroelectric rhombohedral phase. The ferroelectric domain walls only react to the electric field, whereas ferroelastic domain walls are responsible for both the electric and mechanical fields. Those domain walls are also termed neutral domain walls, ideally minimizing the total polarization charge to zero. This occurs when either the polarization projection onto the domain wall plane is zero or the polarization vector maintains continuity across the domain wall.

In contrast to neutral domain walls, charged domain walls with head-to-head or tail-to-tail orientations may arise [40–44], as depicted in Fig. 2.6. Charged domain walls induce a discontinuity in polarization, resulting in the uncompensated domain wall bound charges, i.e., $\nabla \cdot \boldsymbol{P} \neq 0$. As a result, the mobility of carriers is modified, leading to unusually electronic transport characteristics at the domain boundaries [45–47]. For instance, as demonstrated in Ref. [47], the charged domain configurations in $MAPbI_3$ could release the Shockley–Read–Hall recombination losses within grains, enhancing the fill factor and overall power conversion efficiency of associated solar cells. Charged domain walls may also represent intrinsic two-dimensional systems possessing functional properties that can be intentionally introduced, manipulated,

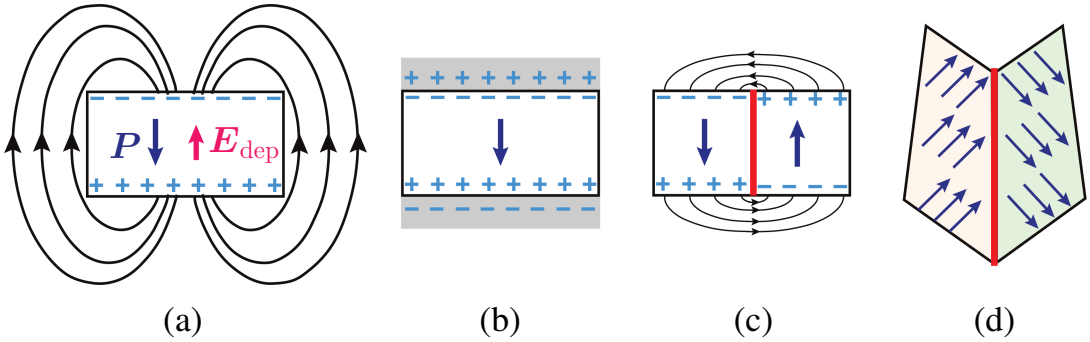

Figure 2.5.: (a)-(c) elucidate the formation of a 180° domain wall in the ferroelectric material (adapted from Ref. [39]), while (d) demonstrates a 90° domain wall. The dark blue arrow indicates the polarization direction, and the black field lines in (a) and (c) depict the electric fields resulting from a ferroelectric monodomain state. The accumulation of the electric fields in (a) induces a depolarizing field ($\boldsymbol{E}_{\mathrm{dep}}$) in the opposing direction, denoted by the dark purple arrow. (b) illustrates the complete polarization screening by surface charges, and (c) represents the 180° domain wall to release the depolarization field. The thick red lines in (c) and (d) show the domain walls.

or eliminated as required [40–44, 48, 49]. The currently theoretical mechanisms for forming charged domain walls include the stabilization of charged impurities [50], the favorable energetic configurations [51], the distribution of screening charges [52], and the interactions with oxygen vacancies [53].

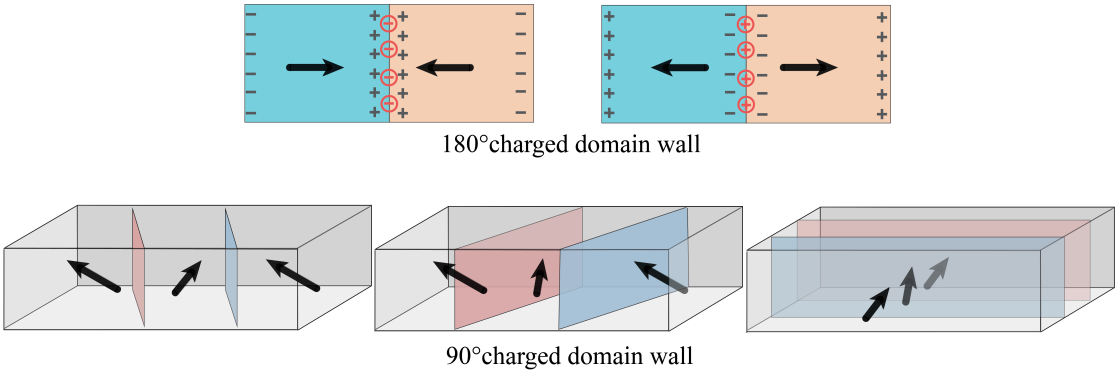

Figure 2.6.: 180° and 90° charged domain wall with head-to-head and tail-to-tail configuration. Adapted from Refs. [39] and [40].

In addition to the neutrally uniform domains, topological domain walls formed by complex polarization patterns have also been reported in recent years. Of particular interest, Fig. 2.7 illustrates typical topological domain walls including vortex [54],

skyrmion [55], hopfion [56], and meron [57]. These structures are likely to be applied in devices such as ferroelectric memories.

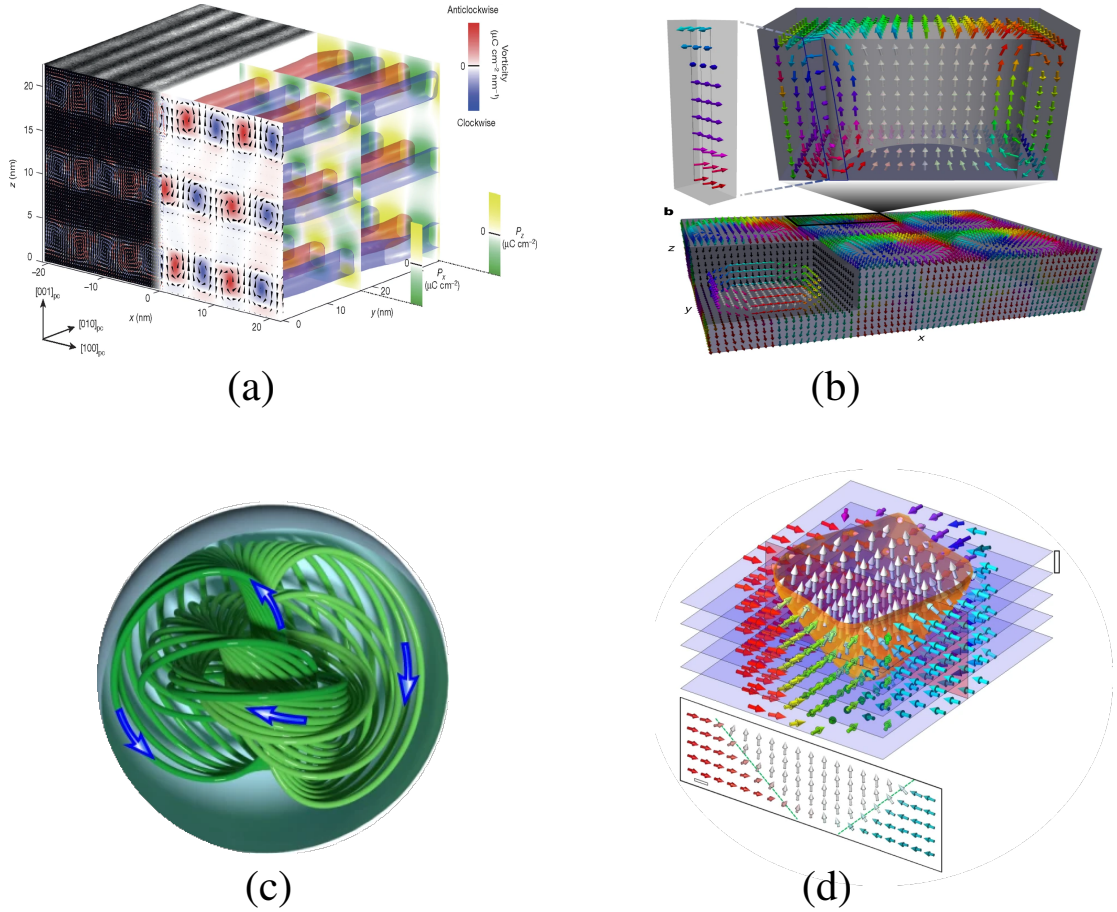

Figure 2.7.: The typical topological domain walls. (a) vortex domain walls in the superlattice [54]; (b)skyrmions [55]; (c) hopfions [56]; (d) merons [57].

2.1.6. Manipulation of domain structures

It is known that the morphology and stability of domain walls can be manipulated, as their formation depends on the details of the energy cost associated with creating domain walls, the local defect structure, and the boundary conditions such as grain size, shape, and orientation. An illustrative example of manipulation is the epitaxial growth of ferroelectric thin films on a substrate. Normally, proper growth requires matching the lattice parameters of the thin film with the substrate in the plane, resulting in misfit strain in thin films, denoted as $\varepsilon^{\mathrm{mis}}$ in 1D. With a_{s} and a_{f} respectively denote the lattice

constants of the substrate and thin film, $\varepsilon^{\mathrm{mis}}$ can be expressed as:

$$\varepsilon^{\mathrm{mis}} = \frac{a_{\mathrm{s}} - a_{\mathrm{f}}}{a_{\mathrm{f}}}. \tag{2.8}$$

When $a_{\mathrm{s}} > a_{\mathrm{f}}$, the film experiences tensile stress, whereas for $a_{\mathrm{s}} < a_{\mathrm{f}}$, it is subjected to compressive stress. Thus, by adjusting the substrate, one can design domain structures, as tensor and compressive misfit strains influence the stability of in-plane and out-of-plane domains, respectively. Additionally, domain configurations can be altered through external stimuli, such as electric fields and mechanical loading. Doping and manipulating boundary effects also offer potential means for controlling domain structures.

2.1.6.1. Domain switching and hysteresis loop

Domain switching by an external electric field (E_{ext}) is an important phenomenon observed in ferroelectric materials. The polarization and strain responses to an electric field are depicted by the polarization versus electric field loop and the butterfly-shaped strain versus electric field loop, respectively. These loops are also commonly referred to as hysteresis loops. Fig. 2.8 illustrates the hysteresis loop for an ideal single-crystal ferroelectric material, for instance. Firstly, the spontaneous polarization directions are

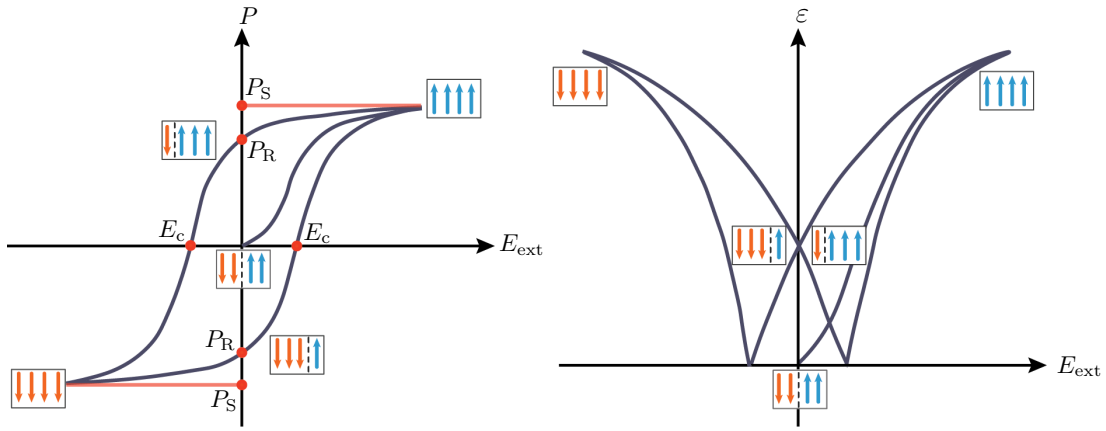

Figure 2.8.: The schematic diagram for polarization hysteresis and strain hysteresis of an ideal single-crystal with the application of an external electric field.

distributed such that the net polarization is zero (the origin point). As the electric field is increased positively, polarization directions switch so that polarization can align along the induced electric field, generating and increasing the average polarization and strain in the same orientation. Until the maximum electric field, all the domains

are aligned along the applied electric field. This point is called saturation polarization (P_{S}) and beyond it, there is no further increase in the value of polarization and strain. Further, if the applied electric field is reduced forward, polarization tends to decrease and reaches a particular value where E_{ext} is zero. At this point, only some domains back-switched, resulting in a net non-zero polarization, known as remnant polarization (P_{R}). Simultaneously, the existence of such polarization leads to non-zero average strain, as shown in the right plot of Fig. 2.8. Remnant polarization is the measure of the permanence of the materials used specifically for memory and storage capacity. In order to attain zero polarization, the applied electric field must be further decreased. The magnitude of the applied electric field where the whole polarization becomes zero is called the coercive field, denoted as E_{c}. Since the average polarization is zero, the average strain also reaches zero at this point. It should be noted that in the practical ferroelectrics, microstructural features, such as grain boundaries and other extended structural defects, may significantly affect the shape of hysteresis loops, resulting in the variation of P_{S}, P_r and E_{c}. In most ferroelectrics, a polarization domain can also be reoriented by an externally applied stress field as the lattice degree of freedom is coupled to the polarization order parameter.

2.2. Phenomenological theory of thermodynamics in ferroelectric material

2.2.1. Thermodynamic theory of ferroelectric phase transitions

The phenomenological theory of thermodynamics in ferroelectric materials seeks to decompose free energy into powers of polarization while establishing correlations between each coefficient in the expansion and experimentally measurable macroscopic quantities. According to thermodynamic theory, a single thermodynamic characteristic function, i.e., a potential function, is deemed sufficient for elucidating the equilibrium state of a homogeneous thermodynamic system depending upon the selection of independent variables. In a homogeneous elastic ferroelectric material, the thermodynamic parameters—temperature (T) and entropy (S), mechanical parameters—stress (denoted as $\boldsymbol{\sigma}$ or σ_{ij}) and strain (denoted as $\boldsymbol{\varepsilon}$ or ε_{ij}), and electric parameters— electric field and electric displacement (or polarization) are employed to describe the state of the system. The construction of the potential function entails the arbitrary selection of a variant from the pairs of these variables, in which one selection corresponds to a potential function, as listed in Table 2.1.

Table 2.1.: The potential function of ferroelectric material, where i, j, m range from 1 to 3.

Potential functions	Equations	Independent variable
Internal energy (U)	-	ε_{ij}, D_m, S
Helmholtz free energy (F)	$F = U - TS$	ε_{ij}, D_m, T
Enthalpy (H)	$H = U - \sigma_{ij}\varepsilon_{ij} - E_m D_m$	σ_{ij}, E_m, S
Elastic enthalpy (H_1)	$H_1 = U - \sigma_{ij}\varepsilon_{ij}$	σ_{ij}, D_m, S
Electric enthalpy (H_2)	$H_2 = U - E_m D_m$	ε_{ij}, E_m, S
Gibbs function (G)	$G = H - TS$	σ_{ij}, E_m, T
Elastic Gibbs function (G_1)	$G_1 = H_1 - TS$	σ_{ij}, D_m, T
Electric Gibbs function (G_2)	$G_2 = H_2 - TS$	ε_{ij}, E_m, T

The first law of thermodynamics states that the variation in the internal energy U of a system is represented as:

$$\mathrm{d}U = \mathrm{d}Q + \mathrm{d}W, \tag{2.9}$$

where $\mathrm{d}Q$ denotes the heat acquired by the system, and $\mathrm{d}W$ signifies the work performed on the system. In the case of an elastic dielectric, $\mathrm{d}W$ encompasses contributions from both mechanical and electrostatic energies, expressed as:

$$\mathrm{d}W = \sigma_{ij}\mathrm{d}\varepsilon_{ij} + E_m \mathrm{d}D_m. \tag{2.10}$$

For a reversible process, the heat transfer $\mathrm{d}Q$ is governed by:

$$\mathrm{d}Q = T\mathrm{d}S. \tag{2.11}$$

Hence, it follows straightforwardly that:

$$\mathrm{d}U = T\mathrm{d}S + \sigma_{ij}\mathrm{d}\varepsilon_{ij} + E_m \mathrm{d}D_m. \tag{2.12}$$

Consequently, the potential functions in Table 2.1 can be derived in differential form, described as:

$$\begin{aligned}
\mathrm{d}F &= -S\mathrm{d}T + \sigma_{ij}\mathrm{d}\varepsilon_{ij} + E_m \mathrm{d}D_m, , \\
\mathrm{d}H &= T\mathrm{d}S - \varepsilon_{ij}\mathrm{d}\sigma_{ij} - D_m \mathrm{d}E_m, \\
\mathrm{d}H_1 &= T\mathrm{d}S - \varepsilon_{ij}\mathrm{d}\sigma_{ij} + E_m \mathrm{d}D_m, \\
\mathrm{d}H_2 &= T\mathrm{d}S + \sigma_{ij}\mathrm{d}\varepsilon_{ij} - D_m \mathrm{d}E_m, \\
\mathrm{d}G &= -S\mathrm{d}T - \varepsilon_{ij}\mathrm{d}\sigma_{ij} - D_m \mathrm{d}E_m, \\
\mathrm{d}G_1 &= -S\mathrm{d}T - \varepsilon_{ij}\mathrm{d}\sigma_{ij} + E_m \mathrm{d}D_m, \\
\mathrm{d}G_2 &= -S\mathrm{d}T + \sigma_{ij}\mathrm{d}\varepsilon_{ij} - D_m \mathrm{d}E_m,
\end{aligned} \tag{2.13}$$

in which i, j, m range from 1 to 3.

According to Table 2.1, the elastic Gibbs function G_1 is a function of temperature, stress, and dielectric displacement. Since temperature and stress can be readily controlled during the experimental determination, it is better to choose them as independent variables. Hence, G_1 emerges as the most convenient potential for analysis. Under isothermal and stress-free conditions, namely $\mathrm{d}T = 0$ and $\mathrm{d}\sigma_{ij} = 0$, G_1 along one axis can be expanded as:

$$G_1 = G_{10} + \frac{1}{2}\alpha P^2 + \frac{1}{4}\beta P^4 + \frac{1}{6}\gamma P^6. \tag{2.14}$$

This formulation is the so-called Landau-Devonshire Theory (LDT) concerning the ferroelectric phase transformation, which is the development of the Landau theory in ferroelectric materials [1, 2]. G_{10} is the elastic Gibbs energy density of the paraelectric phase, and α, β, and γ are the theory coefficients. α is temperature-dependent and can be calculated based on a Curie–Weiss temperature T_0, denoted as:

$$\alpha = \alpha_0(T - T_0), \tag{2.15}$$

within which α_0 is positive. The sign of β determines the nature of the phase transition. $\beta < 0$ indicates a first-order phase transformation, while $\beta > 0$ corresponds to a second-order phase transformation. The sixth-order coefficient γ is required to remain non-negative, otherwise, the minimal energy state of the system may be represented by an infinite polarization.

By examining the expressions for $\mathrm{d}G_1$ in Eq. (2.13), it becomes straightforward to derive the electric field by

$$E = \frac{\partial G_1}{\partial P} \tag{2.16}$$

under isothermal and stress-free conditions. In conjunction with Eq. (2.14), the electric field can be determined as:

$$E = \alpha P + \beta P^3 + \gamma P^5. \tag{2.17}$$

The second derivative of G_1 for polarization is expressed as:

$$\frac{\partial^2 G_1}{\partial P^2} = \frac{\partial E}{\partial P} = \alpha + 3\beta P^2 + 5\gamma P^4. \tag{2.18}$$

Solving Eq. (2.17) leads to the solutions of polarization as:

$$\begin{aligned} P_1 &= 0, \\ P_{2,3} &= \pm\left\{\frac{-\beta + \sqrt{\beta^2 - 4\alpha\gamma}}{2\gamma}\right\}^{\frac{1}{2}}, \\ P_{4,5} &= \pm\left\{\frac{-\beta - \sqrt{\beta^2 - 4\alpha\gamma}}{2\gamma}\right\}^{\frac{1}{2}}. \end{aligned} \tag{2.19}$$

It is evident that there is always an identical zero polarization solution. When $T > T_0$, α is positive (Eq. (2.15)), resulting in a positive second derivative, $\partial^2 G_1/\partial P^2$. This implies that G_1 reaches its minimum at $P = 0$. Conversely, when $T < T_0$, α becomes negative, leading to $\partial^2 G_1/\partial P^2 < 0$. This suggests that the system is unstable at $P = 0$, as G_1 reaches its maximum. These results indicate that as the temperature decreases below T_0, the zero polarization state shifts from stable to unstable, causing the transformation from paraelectric to ferroelectric phase.

By combining Eqs. (2.5) with (2.18), the relationship between the dielectric permittivity of paraelectric phase and parameter α can be derived, expressed as:

$$\left.\frac{\mathrm{d}E}{\mathrm{d}P}\right|_{P=0} = \frac{1}{\kappa} = a. \tag{2.20}$$

Rewriting κ as the reciprocal of a and integrating Eq. (2.15), the so called Curie-Weiss law is obtained:

$$\kappa = \frac{1}{\alpha} = \frac{1}{\alpha_0(T - T_0)}. \tag{2.21}$$

Building on Ref. [58, 59], it follows that:

$$\alpha_0 = \frac{1}{\kappa_0 C} \tag{2.22}$$

with C the Curie constant.

2.2.1.1. Second order phase transformation

As previously mentioned, $\beta > 0$ corresponds to a second-order phase transformation, in which the Curie-Weiss temperature T_0 aligns with the Curie temperature (denoted as T_c). In accordance with the definition, a second-order phase transformation implies that the polarization is continuous at the transition temperatures [60, 61], as depicted in Fig. 2.9 (a). Fig. 2.9 (b) illustrates the relationship between the elastic Gibbs energy G_1 and the polarization P. When $T < T_0$, the system exhibits a ferroelectric state characterized by two distinct minimums, each representing spontaneous polarizations of equal magnitude but opposite directions. These spontaneous polarization solutions correspond to $P_{2,3}$ as delineated in Eq. (2.19). This is because $[-\beta - \sqrt{\beta^2 - 4\alpha\gamma}]$ of $P_{4,5}$ yield negative value when $\beta > 0$, resulting in imaginary solutions that are not physically meaningful in representing polarization states. The spontaneous polarization diminishes at $T = T_0$. For $T > T_0$, stability is only maintained when $P = 0$, signifying the paraelectric state. Regarding the second-order phase transformation, the higher-order terms such as P^6 can be negligible. The temperature-dependent spontaneous polarization $P_{2,3}$ can thus be derived as:

$$P = \sqrt{\frac{\alpha_0(T_c - T)}{\beta}}, \tag{2.23}$$

relaying on Eqs. (2.17) and (2.15). This equation illustrates the continuous decrease in spontaneous polarization with increasing temperature until reaching the Curie point, where no latent heat is detected.

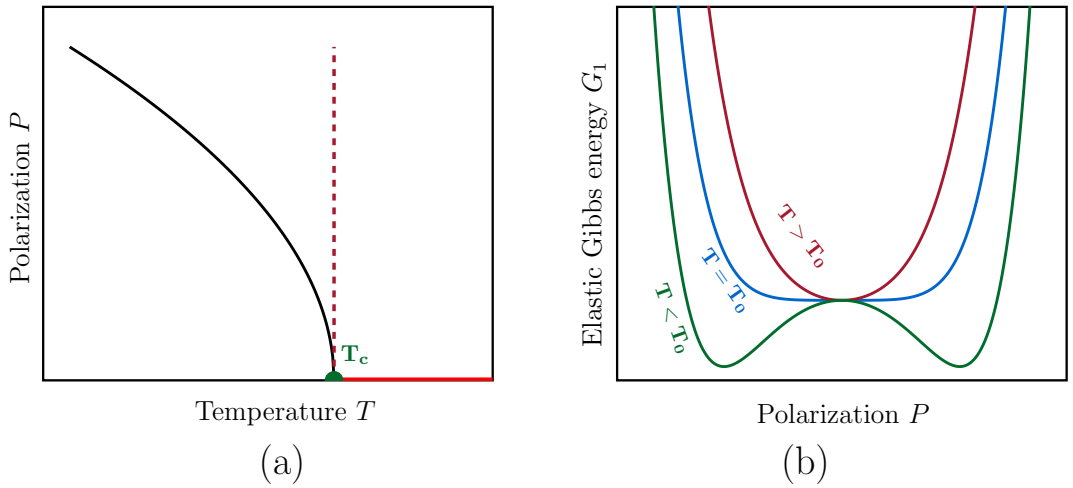

Figure 2.9.: (a) displays the variation of the spontaneous polarization around T_c for the second-order phase transition; (b) illustrates G_1 at $T < T_0$, $T = T_0$, and $T > T_0$ for the second-order phase transition, where $T_0 = T_c$.

2.2.1.2. First order phase transformation

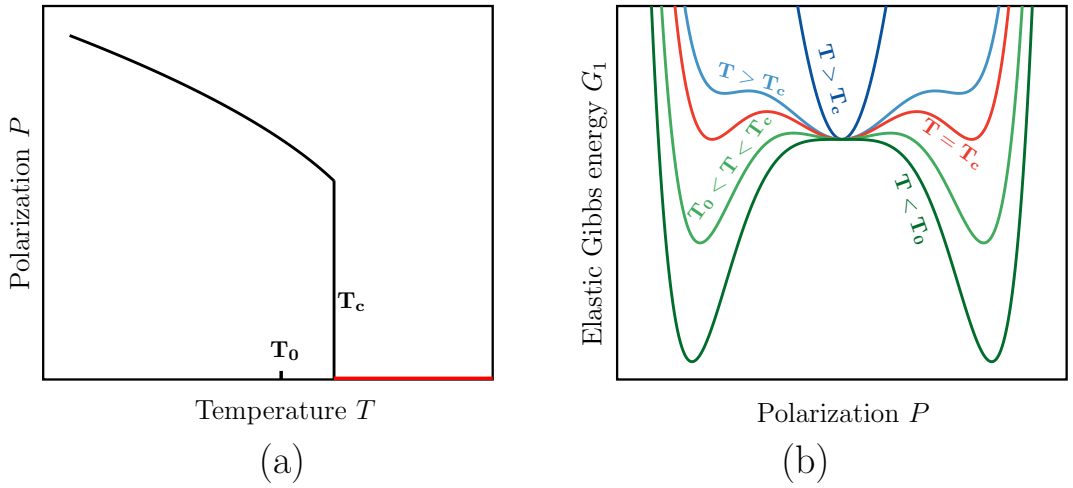

Figure 2.10.: (a) displays the variation of the spontaneous polarization around T_c for the first-order phase transition; (b) illustrates G_1 at $T < T_0$, $T_0 < T < T_c$, $T = T_c$ and $T > T_c$ for the first-order phase transition, where $T_0 < T_c$.

$\beta < 0$ corresponds to a first-order ferroelectric phase transformation, wherein the spontaneous polarization undergoes a discontinuous jump to zero at the transformation temperature T_c, as depicted in Fig. 2.10 (a). In this case, the sixth-order terms of the function G_1 cannot be disregarded, and the solved spontaneous polarizations are $P_{4,5}$ in Eq. (2.19). $T_0 < T_c$ in the first-order phase transformation, and the ferroelectric materials exhibit different behavior near temperatures T_0 and T_c. This distinction is illustrated through the plotted free energy versus spontaneous polarization in Fig. 2.10 (b). The phase transformation behavior above T_c depends on the temperature difference ($\Delta T = T - T_c$) between the investigated temperature T and T_c. The energy minimum appears at $P = 0$ for a significantly large ΔT, suggesting that only the paraelectric phase is stable in the material. Whereas, a small ΔT leads to two minimum values appearing when $P \neq 0$. In this state, the ferroelectric phase is metastable and can be induced by applying an electric field. At $T = T_c$, the system exhibits three energetically degenerate minima points. When $T_0 < T < T_c$, G_1 also exhibits two equal minima values at $P \neq 0$ and a distinct minimum at $P = 0$. G_1 corresponding to $P = 0$ surpasses that of G_1 associated with the other two minima, indicating that the paraelectric phase is in the metastable state in this case. For $T_0 < T_c$, it is observed that the ferroelectric minima are thermodynamically favored. At least two minima of the free energy can be identified, each corresponding to spontaneous polarizations with distinct spatial orientations.

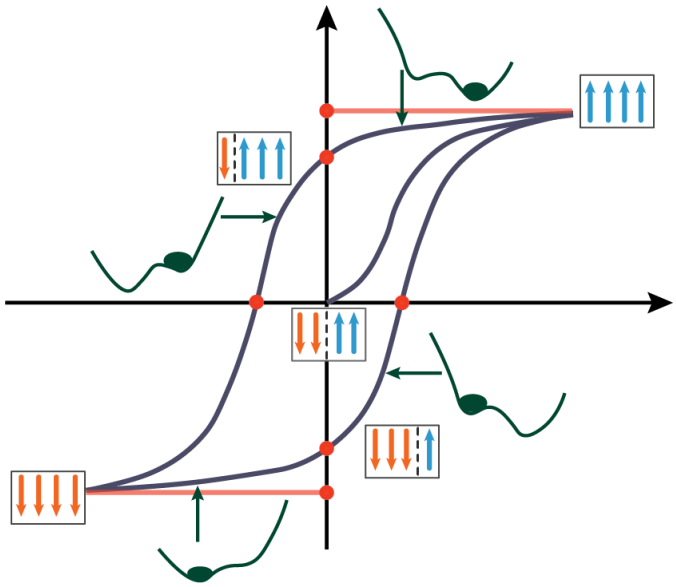

Figure 2.11.: The energy landscape of four typical points in the polarization hysteresis. Based on Ref. [62].

Based on the plotted G_1 in Fig. (2.10)(b), it is evident that the system at T_c depends on whether it is approached by heating or cooling. For example, if the system is heated from an initial low temperature such as $T < T_c$, it settles into one of the two finite polarization ($P \neq 0$) minima. In contrast, it assumes a paraelectric state when cooled from a higher initial temperature of $T > T_c$. This is prevalent in numerous first-order ferroelectrics, including BTO and PTO. The existing energy barrier at temperatures below T_0 also implies that small electric fields are insufficient for switching the polarization, leading to the hysteresis loop illustrated in Fig. 2.8. Fig. 2.11 further outlines the energy distribution of the polarization hysteresis of Fig. 2.8. The LDT suggests that in the ideal scenario, all dipoles must undergo an overall switch to transition from one polarization orientation to another.

2.2.2. Landau-Ginzburg Theory

LDT provides a well-suited framework for elucidating the behavior of a ferroelectric material near its phase transition temperature when the polarization exhibits spatial uniformity below T_0. In response to the challenges posed by spatially inhomogeneous polarization, the Landau-Ginzburg Theory (LGT) was further formulated by integrating spatial polarization variations within the dissertation of LDT. The Landau-Ginzburg free energy for the entire system is accordingly expressed as:

$$\mathcal{F} = \int \left(\frac{1}{2}\alpha\{P(\boldsymbol{x})\}^2 + \frac{1}{4}\beta\{P(\boldsymbol{x})\}^4 + \frac{1}{6}\gamma\{P(\boldsymbol{x})\}^6 + g\{\nabla P(\boldsymbol{x})\}^2\right)\mathrm{d}^3\boldsymbol{x} \tag{2.24}$$

The last term represents the gradient energy and g represents the gradient coefficient. The gradient energy is a short-range interaction energy, also termed domain wall energy, as inhomogeneities only occur in the domain wall region.

2.2.3. Landau-Ginzburg-Devonshire theory

In addition to using the LDT to describe the phase transformation and the gradient term to calculate the spatial distribution, the LGDT further incorporates the elastic and electric energies to explain the mechanics and electrostatic interactions of ferroelectric materials, respectively. When the system is at constant temperature ($\mathrm{d}T = 0$) and stress ($\mathrm{d}\sigma_{ij} = 0$) condition, LGDT using the tensor notation in the case of a central-symmetric paraelectric phase is written as:

$$\begin{aligned} G(\boldsymbol{P}, \boldsymbol{\sigma}) = {} & \frac{1}{2}\alpha_{ij}P_iP_j + \frac{1}{4}\beta_{ijkl}P_iP_jP_kP_l + \frac{1}{6}\gamma_{ijklmn}P_iP_jP_kP_lP_mP_m + \cdots \\ & - \frac{1}{2}\mathcal{S}_{ijkl}\sigma_{ij}\sigma_{kl} - \mathcal{Q}_{ijkl}\sigma_{ij}P_kP_l \\ & - E_iP_i + \frac{1}{2}g_{ijkl}P_{i,j}P_{k,l}, \end{aligned} \tag{2.25}$$

in which α_{ij}, β_{ijkl} and γ_{ijklmn} are the phenomenological Landau expansion coefficients. $\mathcal{S}_{ijkl}$ is the elastic compliance tensors, which are inversely related to the fourth-order elastic stiffness tensors $\mathcal{C}_{ijkl}$. $\mathcal{Q}_{ijkl}$ are the electrostrictive coefficients measured experimental and g_{ijkl} represent the gradient coefficients. i, j, k, l, m, n range from 1 to 3. Whereas, if at constant volume ($\mathrm{d}\varepsilon_{ij} = 0$) and temperature ($\mathrm{d}T = 0$), the appropriate thermodynamic potential expression for the independent variables forms the Helmholtz-free energy. The LGDT in this case is expressed as:

$$\begin{aligned} F(\boldsymbol{P}, \boldsymbol{\varepsilon}) = & \frac{1}{2}a_{ij}P_iP_j + \frac{1}{4}\gamma_{ijkl}P_iP_jP_kP_l + \frac{1}{6}\omega_{ijklmn}P_iP_jP_kP_lP_mP_m \\ & + \frac{1}{2}\mathcal{C}_{ijkl}\varepsilon_{ij}\varepsilon_{kl} - \frac{1}{2}q_{ijkl}\varepsilon_{ij}P_kP_l \\ & - E_iP_i + \frac{1}{2}g_{ijkl}P_{i,j}P_{k,l}. \end{aligned} \tag{2.26}$$

defined in the Helmholtz-free energy represents the electrostrictive constant tensors, which can be obtained from $\mathcal{Q}$ by

$$q_{ijkl} = 2\mathcal{C}_{ijkl}\mathcal{Q}_{ijkl}. \tag{2.27}$$

Accordingly,

$$\mathcal{Q}_{ijkl} = \frac{1}{2}\mathcal{S}_{ijkl}q_{ijkl}. \tag{2.28}$$

There exist four possible solutions for Eqs. (2.25) and (2.26), corresponding to cubic, tetragonal, orthorhombic, and rhombohedral structures. By establishing the relationship between the polarization of each possible solution and the energy profile described in Eq. (2.25) or Eq. (2.26), the phenomenological coefficients in these equations can be determined by experimental determination or theoretical calculations. Examples can be found in Refs. [58, 63–67].

2.3. Phase-field method

Owing to its primary attribute of distinguishing regions with a diffusion interface, the phase-field approach eliminates the requirements of explicitly tracking a distinct interface or making a priori assumptions about its shape. As a result, it has gained popularity in recent years for describing the free-boundary problems in areas such as the microstructure evolution [68–72]. The phase-field method was initially developed to model the two-phase system, in which the microstructural evolution is analyzed employing phase-field variables that are continuous functions of time and spatial coordinates. In this case, the phase-field variable mostly denoted as $\phi(\boldsymbol{x}, t)$, is often referred to as an order parameter or a phase field. While the former naming reflects its original use to distinguish between an ordered and a disordered phase, the latter is applied

to separate a domain into coexisting thermodynamic phases. The order parameter is further classified as either a conserved order parameter if it meets the criteria for local conservation, or a nonconserved order parameter if it does not. Essentially, $\phi = 1$ and $\phi = 0$ respectively designate two distinct bulk regions, whereas $0 < \phi < 1$ denotes the diffusion interface. That is, the interface occurs at the point where ϕ transitions from one phase to another, with the transition range defining the width of the interface. The positions of interfaces are determined implicitly by contours of constant ϕ, in which the temporal evolution of ϕ is described by a set of partial differential equations solved numerically. The driving force for such evolution is the potential reduction in the free energy that comprises the interfacial and bulk energies of the system. Interfacial energy is the combination of potential and gradient energies, while bulk free energy may encompass interactions such as chemical potential, elasticity, magnetic, or electrostatic energies. The two-phase system has also been extended to compute multiple systems, accounting for any number of phases and components. This subsection begins with a discussion of two-phase models, followed by an introduction to the multiphase-field approach.

2.3.1. Two-phase models

2.3.1.1. Energy functional

The construction of a phase-field model usually starts with the formulation of a free-energy functional $\mathcal{F}$ based on the order parameter in the domain Ω of volume V. To start, the simplest two-phase case is considered, with the corresponding phase variables ϕ_1 and ϕ_2. In this case, a single order parameter ϕ is sufficient for distinguishing both phases using $\phi_1 = \phi$ and $\phi_2 = 1 - \phi$. The most basic form of the energy function, which does not take into account the bulk energy [71–73], can be formulated as:

$$\mathcal{F} = \int_V f(\phi) + K|\nabla\phi|^2 \, \mathrm{d}V. \tag{2.29}$$

$f(\phi)$ represents the potential energy, delineating the energetic barrier governing phase transitions. The double-obstacle or the double-well potential are the two common choices for $f(\phi)$ [73], expressed as:

$$\begin{cases} f(\phi) = H_{\mathrm{ob}}\phi(1-\phi) & \text{double-obstacle,} \\ f(\phi) = H_{\mathrm{well}}\phi^2(1-\phi)^2 & \text{double-well,} \end{cases} \tag{2.30}$$

in which H_{ob} and H_{well} (in $\mathrm{J/m^3}$) are constant factors. $K|\nabla\phi|^2$ in Eq.(2.29) represents the gradient energy with a constant factor K (in $\mathrm{J/m}$), which acts to penalize gradients within the order parameter and facilitates interface diffusion result from spatial inhomogeneities. The interplay between the potential and gradient energies is significant for the efficacy of a phase-field model.

2.3.1.2. Allen-Cahn equation

The evolution of the order parameter in a two-phase system is mainly governed by the Allen-Cahn [74] or Cahn-Hilliard [75] models. Following the principles of non-equilibrium thermodynamics, the progression of a non-conserved order parameter correlates directly with the thermodynamic driving force, as represented by:

$$\frac{\partial \phi(\boldsymbol{x},t)}{\partial t} = -\frac{M}{\epsilon}\frac{\delta \mathcal{F}}{\delta \phi} = -\frac{M}{\epsilon}\left[\frac{\partial f(\phi)}{\partial \phi} - 2K\frac{\partial^2 \phi}{\partial \boldsymbol{x}^2}\right]. \tag{2.31}$$

M is the mobility parameter and ϵ scales the interface width. This governing equation is commonly referred to as the Allen-Cahn equation [74], where the essence of the phase variable aims to approach its equilibrium by minimizing the free energy of the system. The Allen-Cahn model is also recognized as the TDGL model.

2.3.1.3. Cahn-Hillard

Composition variables such as molar fractions or concentrations (c) are typically conserved properties. The functional derivative of the energy functional concerning such a conserved order parameter equals a chemical potential μ, expressed as:

$$\mu = \frac{\delta \mathcal{F}}{\delta c}. \tag{2.32}$$

The derivative of μ is defined as the mass current $\boldsymbol{j}$, denoted as:

$$\boldsymbol{j} = -\nabla \mu. \tag{2.33}$$

Since it is a conserved quantity, c conforms to a continuity equation, formulated as:

$$\frac{\partial c}{\partial t} = -m\nabla \cdot \boldsymbol{j}, \tag{2.34}$$

within m represents the atomic mobility. The combination of Eqs. (2.32), (2.33) and (2.34) gives the so called Cahn-Hilliard equation [75], denoted as:

$$\frac{\partial c}{\partial t} = m\nabla^2 \frac{\delta \mathcal{F}}{\delta c}. \tag{2.35}$$

2.3.1.4. Equilibrium profile

In a straightforward 1D scenario depicting a two-phase flat interface, the stable equilibrium requires

$$\frac{\partial \phi}{\partial t} = 0, \tag{2.36}$$

leading to

$$\frac{\mathrm{d}^2\phi}{\mathrm{d}x^2} = \frac{1}{2K}\frac{\mathrm{d}f(\phi)}{\mathrm{d}\phi} \tag{2.37}$$

when taking the Allen-Cahn model Eq. (2.31) into account. Multiplying Eq. (2.37) by $\frac{\mathrm{d}\phi}{\mathrm{d}x}$ on both sides and integrating over the interval $[0, x]$ follows:

$$\begin{aligned} \int_0^x \frac{\mathrm{d}\phi}{\mathrm{d}x}\frac{\mathrm{d}^2\phi}{\mathrm{d}x^2}\mathrm{d}x &= \int_0^x \frac{1}{2K}\frac{\mathrm{d}f(\phi)}{\mathrm{d}\phi}\frac{\mathrm{d}\phi}{\mathrm{d}x}\mathrm{d}x, \\ \int_0^x \frac{1}{2}\frac{\mathrm{d}}{\mathrm{d}x}\Big(\frac{\mathrm{d}\phi}{\mathrm{d}x}\Big)^2\mathrm{d}x &= \frac{1}{2K}\int_0^{\phi(x)} \frac{\mathrm{d}f(\phi)}{\mathrm{d}\phi}\mathrm{d}\phi. \end{aligned} \tag{2.38}$$

If the potential vanishes in $f(0) = 0$ holds for both well and obstacle potential, Eq. (2.38) can be further derived as:

$$\frac{\mathrm{d}\phi}{\mathrm{d}x} = \pm\sqrt{\frac{f(\phi)}{K}}\ . \tag{2.39}$$

Choosing the positive sign for Eq. (2.39), and subsequent division of the right-hand side, followed by integration through substitution, results in:

$$\int_{\frac{1}{2}}^{\phi(x)} \sqrt{\frac{K}{f(\phi(x))}}\ \mathrm{d}\phi = x \tag{2.40}$$

when considering $\phi(x = 0) = 1/2$ as boundary condition. Consequently, one can initially solve for x in terms of ϕ for both obstacle and well potentials, expressed as:

$$x = \begin{cases} -\sqrt{\frac{K}{H_{\mathrm{ob}}}}\arcsin\left(1-2\phi(x)\right) & \text{in } f(\phi) = H_{\mathrm{ob}}\phi(1-\phi), \\ -2\sqrt{\frac{K}{H_{\mathrm{well}}}}\operatorname{arctanh}\left(1-2\phi(x)\right) & \text{in } f(\phi) = H_{\mathrm{well}}\phi^2(1-\phi)^2. \end{cases} \tag{2.41}$$

Subsequently, the relationship between ϕ and x can be obtained as:

$$\phi = \begin{cases} \frac{1}{2} + \frac{1}{2}\sin\left(\sqrt{\frac{H_{\mathrm{ob}}}{K}}x\right) & \text{in } f(\phi) = H_{\mathrm{ob}}\phi(1-\phi), \\ \frac{1}{2} + \frac{1}{2}\tanh\left(\sqrt{\frac{H_{\mathrm{well}}}{4K}}x\right) & \text{in } f(\phi) = H_{\mathrm{well}}\phi^2(1-\phi)^2. \end{cases} \tag{2.42}$$

The equilibrium solutions of Eq. (2.42) are shown in Fig. 2.12, which is plotted against the dimensionless coordinate $\sqrt{H_{\mathrm{ob}}/K}x$ and $\sqrt{H_{\mathrm{well}}/K}x$, respectively. It is obvious that the transition between the two bulk states occurs within a region in both potential formulations respectively proportional to the length $\sqrt{K/H_{\mathrm{ob}}}$ and $\sqrt{K/H_{\mathrm{well}}}$. This suggests the equilibrium interface thickness arising from a balance between the gradient and potential energy terms. Increasing the factor of the potential energy (H_{ob} or H_{well}) enhances the potential term, leading to a thinner interfacial width. In

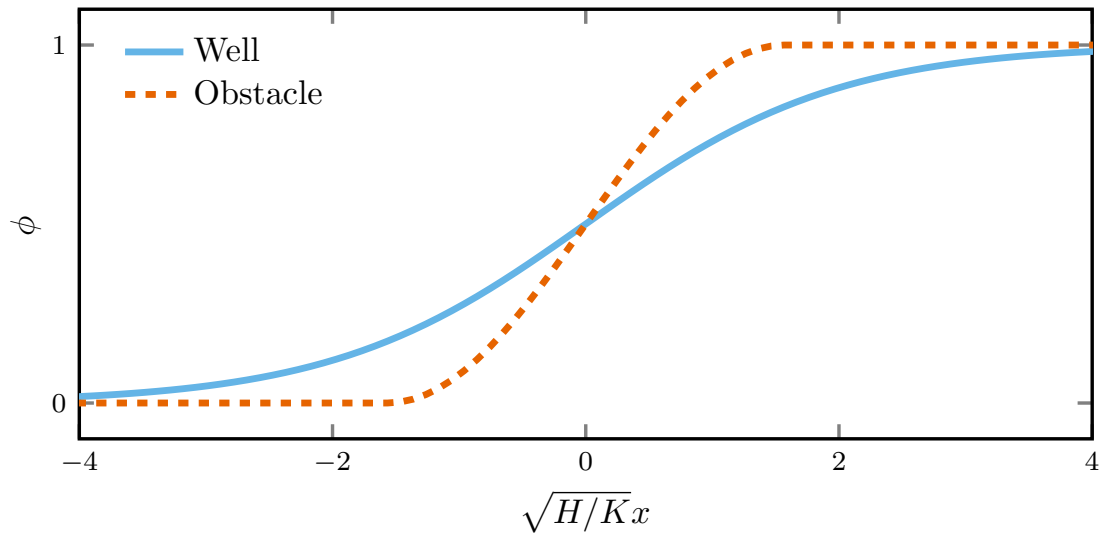

Figure 2.12.: Equilibrium profile of a diffuse interface in a two-phase model for both the obstacle potential as well as the well potential. x represents the signed distance from the location $\phi = 1/2$, while K and H are the parameters that scale the gradient and potential energy density, respectively.

contrast, increasing K strengthens the gradient term, which results in a large diffusion thickness. Defining the interface thickness as $L =: |x_{\phi=1} - x_{\phi=0}|$, it has been found that only the obstacle potential results in a finite interface thickness, which equals $\sqrt{K/H_{\mathrm{ob}}}\pi$, whereas the well potential tends toward values of $\phi = 1$ and $\phi = 0$ at $x = \pm\infty$.

The interfacial energy, σ_{int}, can be calculated for such an equilibrium interface as:

$$\sigma_{\mathrm{int}} = \int_{-\infty}^{+\infty} \left[f(\phi) + K\left(\frac{\mathrm{d}\phi}{\mathrm{d}x}\right)^2 \right] \mathrm{d}x. \tag{2.43}$$

According to the first-order ordinary differential equation in Eq. (2.39), σ_{int} can be further derived as:

$$\sigma_{\mathrm{int}} = \int_{-\infty}^{+\infty} 2f(\phi)\mathrm{d}x. \tag{2.44}$$

By setting $x = \phi$ and using Eq. (2.39) once more, one can derive Eq. (2.44) as:

$$\begin{aligned} \sigma_{\mathrm{int}} &= 2\int_{\phi(-\infty)}^{\phi(+\infty)} \frac{f\big(\phi(x)\big)}{\phi'} \mathrm{d}\phi \\ &= 2\sqrt{K}\int_{\phi(-\infty)}^{\phi(+\infty)} \sqrt{f\big(\phi(x)\big)}\mathrm{d}\phi. \end{aligned} \tag{2.45}$$

Subsequently, by incorporating the expressions for obstacle and well potentials in Eq. (2.30) into Eq. (2.45) and assuming $\phi(+\infty) = 1$ and $\phi(-\infty) = 0$, σ_{int} can finally be

expressed as:

$$\sigma_{\text{int}} = \begin{cases} \dfrac{\pi}{4}\sqrt{KH_{\text{ob}}} & \text{in } f(\phi) = H_{\text{ob}}\phi(1-\phi), \\ \dfrac{1}{3}\sqrt{KH_{\text{well}}} & \text{in } f(\phi) = H_{\text{well}}\phi^2(1-\phi)^2. \end{cases} \tag{2.46}$$

This indicates that the interfacial energy σ_{int} is directly proportional to the square root of the product of the potential energy factor and the gradient energy factor, one could find the same conclusion in Ref. [72]. With this result, one can connect K and $H_{\text{ob}}/H_{\text{well}}$ to σ_{int}, attributing these prefactors with more physical significance.

2.3.2. Multiphase-field models

The two-phase formalism was extended to address multiphase, multigrain, and multicomponent systems as described in Refs. [76–79]. In this framework, a system with N coexisting phases is described through N phase-fields ϕ_N, i.e., $\boldsymbol{\phi} = \{\phi_1, \phi_2, ..., \phi_N\}$. As a result, a sum constraint is enforced to guarantee the summation of the phase variables as one at each point $\boldsymbol{x}$ within the system, denoted by:

$$\sum_{\alpha=1}^{N} \phi_\alpha = 1 \text{ with } \phi_\alpha > 0, \forall\alpha. \tag{2.47}$$

Thus, one can conclude that only $N-1$ phase fields are independent in a system containing N phases. The energy functional including the bulk energy (denoted as $\mathcal{F}_{\text{bulk}}$), can be formulated as:

$$\begin{aligned} \mathcal{F} &= \mathcal{F}_{\text{intf}} + \mathcal{F}_{\text{bulk}} \\ &= \int_V (f_{\text{pot}} + f_{\text{grad}} + \tilde{f}_{\text{bulk}})\, \mathrm{d}V, \end{aligned} \tag{2.48}$$

where $\tilde{f}_{\text{bulk}}$ is the bulk energy density, f_{pot} and f_{grad} represent the potential energy density and gradient energy, respectively.

The construction of the potential energy within the multiphase-field framework begins by substituting ϕ and $1-\phi$ to ϕ_α and ϕ_β, respectively. Using the double-obstacle and double-well formulations as presented in Eq. (2.30), the potential energies can be initially expressed as:

$$f_{\text{pot}}^{\text{ob},1} = \sum_{\alpha=1}\sum_{\beta=\alpha+1} \gamma_{\alpha\beta}\phi_\alpha\phi_\beta, \quad f_{\text{pot}}^{\text{well},1} = \sum_{\alpha=1}\sum_{\beta=\alpha+1} \gamma_{\alpha\beta}\phi_\alpha^2\phi_\beta^2. \tag{2.49}$$

However, the potential energies in the current format result in the so-called spurious phases. Consequently, these energies must be reformulated according to the summation

rule in Eq. (2.47). A thorough review of this topic can be found in Ref. [73]. In general, the formulated multi-obstacle potential can be denoted as:

$$f_{\text{pot}}^{\text{ob}} = \frac{16}{\epsilon\pi^2}\sum_{\alpha=1}^{N}\sum_{\beta=\alpha+1}^{N}\gamma_{\alpha\beta}\phi_\alpha\phi_\beta + \sum_{\alpha=1}^{N}\sum_{\beta=\alpha+1}^{N}\sum_{\tau=\beta+1}^{N}\gamma_{\alpha\beta\tau}\phi_\alpha\phi_\beta\phi_\tau, \tag{2.50}$$

in which $\gamma_{\alpha\beta}$ is the interfacial energy between phases α and β, and $\gamma_{\alpha\beta\tau}$ is the interfacial energy among α, β and τ. The triplet term scaled by $\gamma_{\alpha\beta\tau}$ is used to remove spurious phases that may appear at triple or higher-order junctions. Similarly to the two-phase model, ϵ scales the interface width. Numerically, a Gibbs simplex function, defined as

$$\mathscr{G} = \begin{cases} 1 & \sum_{\alpha=1}^{N}\phi_\alpha = 1 \cap \phi_\alpha \geq 0 \;\forall\; 1 \leqslant \alpha \leqslant N \\ \infty & \text{else}, \end{cases} \tag{2.51}$$

can be incorporated into the multi-obstacle potential to enforce $\phi_\alpha \geq 0$. Several multi-phase extensions of the well-potential have also been widely applied in the phase-field community, and details can be found in Ref. [73].

Similarly, the gradient energy for the multiphase field model can be formulated as a generalization of the two-phase case $K|\nabla\phi|^2$. For example, it can be formulated as:

$$f_{\text{grad}} = \epsilon\sum_{\alpha=1}^{N}\sum_{\beta>\alpha}^{N}\gamma_{\alpha\beta}|\phi_\alpha\nabla\phi_\beta - \phi_\beta\nabla\phi_\alpha|^2, \tag{2.52}$$

as documented in Refs. [76, 78]. Alternatively, in accordance with the formulation provided in Ref. [77], the gradient energy can also be computed by:

$$f_{\text{grad}} = -\epsilon\sum_{\alpha=1}^{N}\sum_{\beta>\alpha}^{N}\gamma_{\alpha\beta}\nabla\phi_\alpha\cdot\nabla\phi_\beta. \tag{2.53}$$

For a more in-depth examination of the distinctions and alternative formulations of gradient energy, and their interactions with various potential energies, it is recommended to consult Ref. [73].

The condition $\phi_\alpha = 1-\phi_\beta$ always holds when reducing multiple phases to two phases, resulting in the simplification of the multi-obstacle potential in Eq. (2.50) as:

$$f_{\text{pot}}^{\text{ob}} = \frac{16\gamma_{\alpha\beta}}{\epsilon\pi^2}\phi_\alpha(1-\phi_\alpha). \tag{2.54}$$

Besides, $\phi_\alpha = 1-\phi_\beta$ leads to $\nabla\phi_\beta = -\nabla\phi_\alpha$, resulting in the gradient energy in Eqs. (2.52) and (2.53) reducing to

$$f_{\text{grad}} = \epsilon\gamma_{\alpha\beta}\nabla\phi_\alpha \tag{2.55}$$

for a two-phase system. Comparing Eqs. (2.54) and (2.55) with Eqs. (2.29) and (2.30), it is straightforward to determine K and H_{ob} in terms of ϵ and $\gamma_{\alpha\beta}$ as:

$$K = \epsilon\gamma_{\alpha\beta}, \quad H_{\mathrm{ob}} = \frac{16\gamma_{\alpha\beta}}{\epsilon\pi^2}. \tag{2.56}$$

Thus, the equilibrium interface thickness L for a binary interface in the application of a multi-obstacle potential can be calculated as:

$$L = \sqrt{\frac{K}{H_{\mathrm{ob}}}}\pi = \sqrt{\frac{\epsilon\gamma_{\alpha\beta}\epsilon\pi^2}{16\gamma_{\alpha\beta}}}\,\pi = \frac{\pi^2\epsilon}{4}. \tag{2.57}$$

Referring to Eq. 2.46, the interfacial energy σ_{int} is expressed as:

$$\sigma_{\mathrm{int}} = \frac{\pi}{4}\sqrt{\frac{\epsilon\gamma_{\alpha\beta}16\gamma_{\alpha\beta}}{\epsilon\pi^2}} = \gamma_{\alpha\beta}, \tag{2.58}$$

which in addition suggests that $\gamma_{\alpha\beta}$ is the parameter governing the interfacial energy at α and β phases interface.

The bulk energy $\tilde{f}_{\mathrm{bulk}}$ can be further express by means of the interpolation function $h^\alpha(\boldsymbol{\phi})$, denoted as:

$$\tilde{f}_{\mathrm{bulk}} = \sum f^\alpha_{\mathrm{bulk}} h^\alpha(\phi_\alpha), \tag{2.59}$$

where $h^\alpha(\boldsymbol{\phi})$ satisfies conditions:

$$\begin{aligned} &h^\alpha(\phi_\alpha = 1, \phi_{\beta\neq\alpha} = 0) = 1, \\ &h^\alpha(\phi_\alpha = 0, \ldots) = 0. \end{aligned} \tag{2.60}$$

For deeper discussions of the interpolation function, one can refer to Ref. [80].

To fulfill the condition $\sum_{\alpha=1}^{N}\phi_\alpha = 1$, the Allen-Cahn model can be extended for the multiphase-field evolution with a Language Multiplier λ [77], denoted as:

$$\frac{\partial\phi_\alpha(\boldsymbol{x},t)}{\partial t} = -\frac{1}{\tau(\phi)\epsilon}\frac{\delta\mathcal{F}}{\delta\phi_\alpha} - \lambda. \tag{2.61}$$

$\tau(\phi)$ is a time relaxation parameter, which represents the reverse of the mobility. With an arithmetic interpolation, $\tau(\phi)$ can be calculated by:

$$\tau(\phi) = \frac{\sum_{\alpha=1}^{N}\sum_{\beta=\alpha+1}^{N}\tau_{\alpha\beta}\phi_\alpha\phi_\beta}{\sum_{\alpha=1}^{N}\sum_{\beta=\alpha+1}^{N}\phi_\alpha\phi_\beta}, \tag{2.62}$$

in which $\tau_{\alpha\beta}$ represents the relaxation parameter between phases α and β. By considering the mobility matrix as the sum of binary interactions, Steinbach and Pezzolla proposed an alternative evolution of $\boldsymbol{\phi}$ in Ref. [77], expressed as:

$$\frac{\partial\phi_\alpha(\boldsymbol{x},t)}{\partial t} = -\frac{1}{\widetilde{N}\epsilon}\sum_{\beta\neq\alpha}^{N}\left[\frac{1}{\tau_{\alpha\beta}}\Big(\frac{\delta\mathcal{F}}{\delta\phi_\alpha} - \frac{\delta\mathcal{F}}{\delta\phi_\beta}\Big)\right]. \tag{2.63}$$

$\tilde{N}$ denotes the number of locally active phases. This model does not involve any averaging or interpolation for time relaxation and eliminates the Lagrange multiplier since the form implicitly ensures the sum constraint if the initial condition complies. When employing the obstacle-type potential, Eq. (2.63) does not yield the correct kinetics, as demonstrated in the analytical discussion in Ref. [70]. Therefore, it can be further refined and implemented as:

$$\frac{\partial \phi_\alpha(\boldsymbol{x},t)}{\partial t} = -\frac{1}{\widetilde{N}\epsilon}\sum_{\beta\neq\alpha}^{N}\left[M^{\alpha\beta}\left(\frac{\delta\mathcal{F}_{\text{intf}}}{\delta\phi_\alpha}-\frac{\delta\mathcal{F}_{\text{intf}}}{\delta\phi_\beta}-\frac{8\sqrt{\phi_\alpha\phi_\beta}}{\pi}\Delta^{\alpha\beta}\right)\right], \tag{2.64}$$

by taking the influence of the interpolation function into account. $\Delta^{\alpha\beta}$ scales the driving force from the bulk energy, which is defined as:

$$\Delta^{\alpha\beta} = \left(\frac{\delta}{\delta\phi_\alpha}-\frac{\delta}{\delta\phi_\beta}\right)\tilde{f}_{\text{bulk}}. \tag{2.65}$$

2.4. Phase-field model of ferroelectric materials

The phase-field simulation is a powerful technique for exploring ferroelectric materials, enabling the elucidation, prediction, and strategic manipulation of ferroelectric domain structures. As of present, two methodologies have been developed to compute domain structures/evolution using the phase-field framework. The first method is the Allen-Cahn type TDGL model, which computes the domain structures using the polarization vector $\boldsymbol{P}$ as the order parameter. The second approach is Model II in this work, which relies on the multiphase-field methodology, and the domain morphologies are determined by minimizing the total energy functional concerning the phase field $\boldsymbol{\phi}$.

2.4.1. TDGL Model

The development of the TDGL equation for investigating domain structures, domain switching dynamics, and their associated material properties in ferroelectrics dates back more than two decades. Since then, it has undergone extensive development to explore a myriad of physical phenomena. In general, the TDGL equation is expressed as:

$$\frac{\partial \boldsymbol{P}(\boldsymbol{x},t)}{\partial t} = -M_i\frac{\delta\mathcal{F}_{\text{LGDT}}}{\delta\boldsymbol{P}(\boldsymbol{x},t)}+\mathcal{G}_i(\boldsymbol{x},t). \tag{2.66}$$

M_i is a kinetic coefficient representing the mobility of domains. $\mathcal{G}_i(\boldsymbol{x},t)$ denotes a negligible Gaussian random fluctuation, detailed in [86]. $\mathcal{F}_{\text{LGDT}}$ demonstrates the total energy functional consisting of the Landau potential, gradient, electric and elastic energies, which is based on the LGDT in Eq. (2.26).

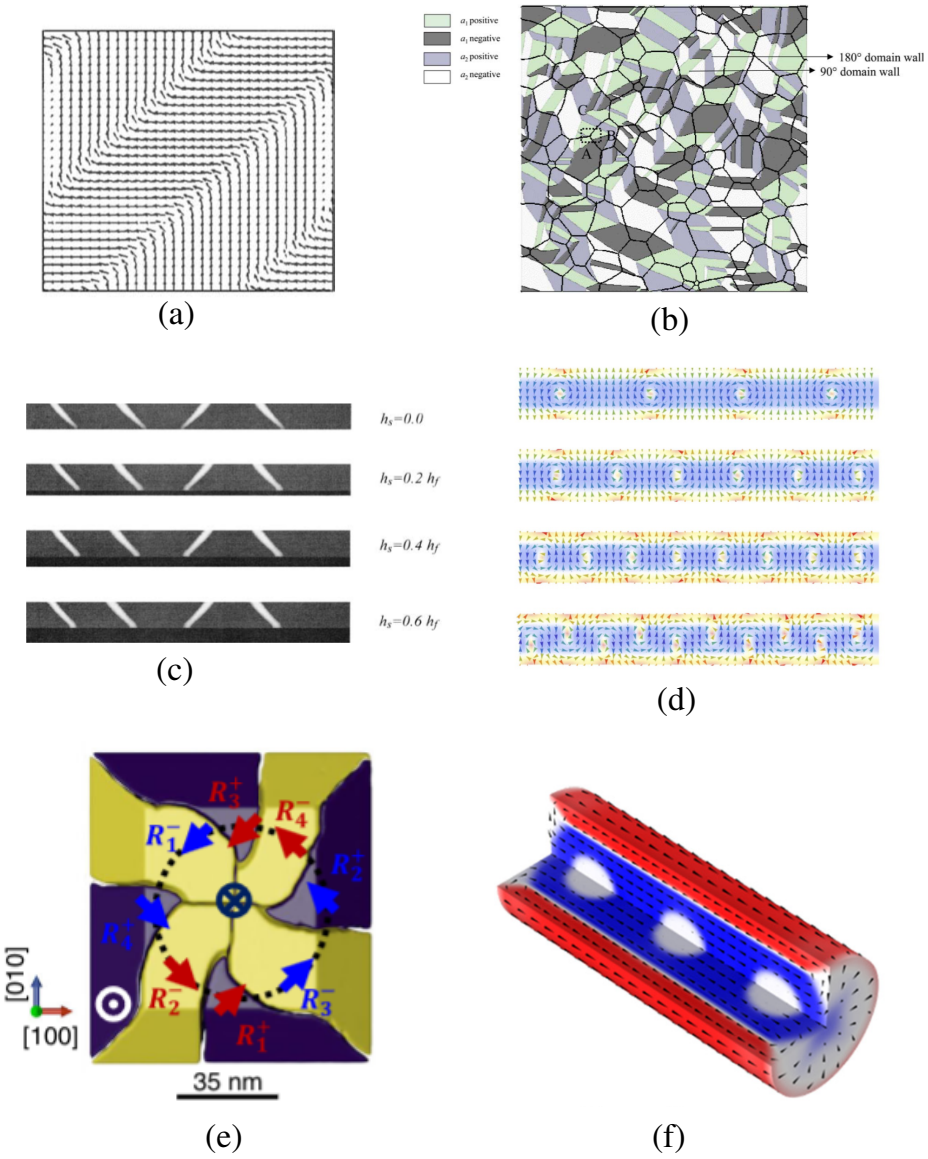

Figure 2.13.: Examples of the computed domain structures using the TDGL model. (a) depicts a simple 90° domain wall in single-crystal bulk PTO [81]; (b) shows the domain morphologies of a polycrystalline bulk PTO [82]; (c) illustrates the 2D domain morphologies of an epitaxial film grown on substrates with different heights; (d) to (f) demonstrate the topological domain walls formed in superlattice (d, [83]), nanoislands (e, [84]), and nanowire (f, [85]).

Fig. 2.13 shows examples of the computed domain structures using the TDGL model. The investigation extends across a wide range of physical systems, including single-

crystal [81] and polycrystalline bulk materials [82, 87, 88], epitaxial thin films [13, 89–91], superlattices [83, 92, 92], and nanostructures such as nanoislands [84, 93], nanowires [85, 94] and nanodots [95]. Furthermore, the computed explorations also include the space charge evolution in semiconductor materials [96–98], the characterization of polarization domain structures and switching mechanisms in improper ferroelectrics [99–101], the high performance in relaxor ferroelectrics [102], the two-dimensional van der Waals ferroelectrics [103]. This model has also been favorable in examining the intricate interplay between ferroelectric domains and structural defects such as dislocations [104–106] and cracks [107]. The strain-related effects such as anisotropic strains [108, 109] and strain gradients [110–113] are also computed. It has also been applied to analyze thermal properties such as thermal conductivity [114] and electrocaloric effects [115, 116]. Moreover, concerted efforts have also been made to integrate TDGL model into multi-scale simulations of ferroelectrics [117, 118].

2.4.2. Multiphase-field model

All the aforementioned studies using the TDGL equation, however, were confined to materials such as PZT, $BiFeO_3$ [119, 120], $CaTiO_3$ [121], $LiTaO_3$ [122] $LiNbO_3$ [123], $SrTiO_3$ [124, 125], $K_{1-x}Na_xNbO_3$ [126, 127], and $SrBi_2Nb_2O_9$ [91], with particular emphasis on PTO and BTO. This limitation arises from the fact that only the phenomenological parameters in those materials were determined [14]. In the work of Ref. [128], the multiphase-field approach was initially proposed for ferroelectric materials to resolve the dynamic motion of domain walls. This work has also developed a novel approach based on the multiphase-field technique demonstrated in Section 2.3.2 for ferroelectric material, details outlined in Section 4 of the Methodology Chapter in this dissertation. At its current stage of development, the primary focus of research is primarily on computing domain structures and material properties in simple physical scenarios, including single and polycrystalline bulk materials [16], as well as the growth of the epitaxial thin films [17].

Part II
Methodology

3. Model I: Coupling of multiphase-field approach with the TDGL model

Model I is adapted from the Methodology Section of Ref. [15].

3.1. Energy functional

To simulate ferroelectric phase coexistence within grains with different orientations in ferroelectric material, the general multiphase-field functional from Ref. [78] is coupled with the LGDT model, resulting in a novel energy functional, expressed as:

$$\begin{aligned}
\mathcal{F} &= \int_V (f_{\text{int}} + f_{\text{bulk}}) \mathrm{d}V, \\
f_{\text{int}} &= f_{\text{grad}}(\nabla \boldsymbol{\phi}) + f_{\text{ob}}(\boldsymbol{\phi}), \\
f_{\text{bulk}} &= \sum_{\alpha=1}^{N} \Big(f^{\alpha}_{\text{Landau}}(\boldsymbol{P}) + f^{\alpha}_{\text{elast}}(\boldsymbol{\varepsilon}^{\alpha}, \boldsymbol{P}) + f^{\alpha}_{\text{G}}(\nabla \boldsymbol{P}) \Big) h^{\alpha}(\boldsymbol{\phi}) + f_{\text{elec}}(\boldsymbol{E}, \boldsymbol{P}).
\end{aligned} \tag{3.1}$$

$\boldsymbol{\phi} = (\phi_{\alpha}, ..., \phi_N)$ is the $N-$tuple phase-field order parameter. ϕ_{α} describes the local fraction of a ferroelectric phase α within a grain or the orientation of a single grain in a polycrystalline system. f_{int} represents the interfacial energy density, consisting of the gradient energy density ($f_{\text{grad}}(\nabla \boldsymbol{\phi})$) and the multi-obstacle-type potential energy density ($f_{\text{ob}}(\boldsymbol{\phi})$). f_{bulk} denotes the bulk energy density, which comprises the phase-dependent Landau potential energy density ($f^{\alpha}_{\text{Landau}}(\boldsymbol{P})$), elastic energy density ($f^{\alpha}_{\text{elast}}(\boldsymbol{\varepsilon}^{\alpha}, \boldsymbol{P})$), domain wall energy density ($f^{\alpha}_{\text{G}}(\nabla \boldsymbol{P})$), and the phase-independent electric energy ($f_{\text{elec}}(\boldsymbol{E}, \boldsymbol{P})$). $h^{\alpha}(\boldsymbol{\phi})$ represents the interpolation function of the phase α, defined as:

$$h^{\alpha}(\boldsymbol{\phi}) = \phi_{\alpha}. \tag{3.2}$$

The polarization vector $\boldsymbol{P}$ is cross-phased in the interface by the interpolation function.

The gradient energy in Model I is formulated based on Eq. (2.52). Considering a Gibbs simplex function ($\mathscr{G}$ in Eq. (2.51)), the multi-obstacle type potential in Eq. (2.50) is employed, expressed as:

$$f_{\text{ob}}(\boldsymbol{\phi}) = \begin{cases} \dfrac{16}{\epsilon \pi^2} \displaystyle\sum_{\alpha<\beta} \gamma^{\alpha\beta} \phi_{\alpha} \phi_{\beta} + \sum_{\alpha=1}^{N} \sum_{\beta=\alpha+1}^{N} \sum_{\tau=\beta+1}^{N} \gamma_{\alpha\beta\tau} \phi_{\alpha} \phi_{\beta} \phi_{\tau}, & \text{if } \boldsymbol{\phi} \in \mathscr{G} \\ \infty, & \text{else.} \end{cases} \tag{3.3}$$

As described in Section 2.3, ϵ is a numerical parameter that scales the interface thickness. $\gamma^{\alpha\beta}$ and $\gamma^{\alpha\beta\gamma}$ represent the isotropic interfacial energy density.

3.2. LGDT for a polycrystalline ferroelectric material

Based on the LGDT, the total energy functional with regard to the polarization vector for a phase α in a single-crystal system can be expressed as:

$$\mathcal{F}^{\alpha}_{\mathrm{LGDT}} = \int_{\mathrm{V}} \left(f^{\alpha}_{\mathrm{Landau}} + f^{\alpha}_{\mathrm{G}} + f^{\alpha}_{\mathrm{elast}} + f^{\alpha}_{\mathrm{elec}} \right) \mathrm{dV}. \tag{3.4}$$

3.2.1. Polarization distribution in polycrystalline ferroelectric materials

To characterize domain structures within grains, it is necessary to describe both the orientation of each grain as well as its associated polarization states. Thus, the global and local coordinates are applied during the simulation. The grain orientations are demonstrated in the global coordinate system, and the domain structures are represented by the polarization distribution in a local coordinate system, denoted by a superscript L. The orientation of an individual grain within a polycrystalline structure is characterized by three Euler angles, φ_1, φ_2, φ_3. These angles represent a sequence of three counterclockwise rotations relative to the global coordinates, x_1, x_2, and x_3. Specifically, φ_1 corresponds to a rotation about the x_3-axis, followed by φ_2, which represents a rotation about the subsequently rotated x_1'-axis, and finally φ_3, corresponding to a rotation about the newly established x_2'-axis.

Accordingly, the second-order transformation matrix from the global to local coordinate system is defined as $\boldsymbol{tr}$, which has the components given as:

$$\begin{aligned}
tr_{11} &= \cos[\varphi_1]\cos[\varphi_3] - \cos[\varphi_2]\sin[\varphi_1]\sin[\varphi_3],\\
tr_{12} &= \sin[\varphi_1]\cos[\varphi_3] + \cos[\varphi_2]\cos[\varphi_1]\sin[\varphi_3],\\
tr_{13} &= \sin[\varphi_2]\sin[\varphi_3],\\
tr_{21} &= -\cos[\varphi_1]\sin[\varphi_3] - \cos[\varphi_2]\sin[\varphi_1]\cos[\varphi_3],\\
tr_{22} &= -\sin[\varphi_1]\sin[\varphi_3] + \cos[\varphi_2]\cos[\varphi_1]\cos[\varphi_3],\\
tr_{23} &= \sin[\varphi_2]\cos[\varphi_3],\\
tr_{31} &= \sin[\varphi_2]\sin[\varphi_1],\\
tr_{32} &= -\sin[\varphi_2]\cos[\varphi_1],\\
tr_{33} &= \cos[\varphi_2].
\end{aligned} \tag{3.5}$$

Thus, the polarization in the local system (P_i^{L}) is related to the global system (P_i) by:

$$P_i^{\mathrm{L}} = tr_{ij} P_j. \tag{3.6}$$

3.2.2. Landau potential energy density

In accordance with the LDT, the phase-dependent Landau potential $f^{\alpha}_{\mathrm{Landau}}(\boldsymbol{P})$ for a phase α in a polycrystalline system can be represented with the local spontaneous polarization components P^{L}_i (i =1, 2, 3) as:

$$\begin{aligned} f^{\alpha}_{\mathrm{Landau}}(\boldsymbol{P}) = \quad & \alpha^{\alpha}_1(T)\Big[(P^{\mathrm{L}}_1)^2 + (P^{\mathrm{L}}_2)^2 + (P^{\mathrm{L}}_3)^2\Big] \\ & + \alpha^{\alpha}_{11}\Big[(P^{\mathrm{L}}_1)^4 + (P^{\mathrm{L}}_2)^4 + (P^{\mathrm{L}}_3)^4\Big] \\ & + \alpha^{\alpha}_{12}\Big[(P^{\mathrm{L}}_1P^{\mathrm{L}}_2)^2 + (P^{\mathrm{L}}_2P^{\mathrm{L}}_3)^2 + (P^{\mathrm{L}}_1P^{\mathrm{L}}_3)^2\Big] \\ & + \alpha^{\alpha}_{111}\Big[(P^{\mathrm{L}}_1)^6 + (P^{\mathrm{L}}_2)^6 + (P^{\mathrm{L}}_3)^6\Big] \\ & + \alpha^{\alpha}_{112}\Big[(P^{\mathrm{L}}_1)^2\Big\{(P^{\mathrm{L}}_2)^4 + (P^{\mathrm{L}}_3)^4\Big\} + (P^{\mathrm{L}}_2)^2\Big\{(P^{\mathrm{L}}_1)^4 + (P^{\mathrm{L}}_3)^4\Big\} \\ & + (P^{\mathrm{L}}_3)^2\Big\{(P^{\mathrm{L}}_1)^4 + (P^{\mathrm{L}}_2)^4\Big\}\Big] \\ & + \alpha^{\alpha}_{123}\Big[P^{\mathrm{L}}_1P^{\mathrm{L}}_2P^{\mathrm{L}}_3\Big]^2. \end{aligned} \tag{3.7}$$

α^{α}_1, α^{α}_{11}, α^{α}_{12}, α^{α}_{111}, α^{α}_{112}, and α^{α}_{123} represent the dielectric stiffness coefficients of phase α, denoted in the Voigt notation under the stress-free conditions. The parameter α^{α}_1 is temperature-dependent, while others are independent of the temperature.

3.2.3. Gradient energy density

The gradient energy is regarded as isotropic in the global coordinate system, which can be calculated as:

$$f^{\alpha}_{\mathrm{G}}(\nabla\boldsymbol{P}) = \frac{1}{2}G^{\alpha}_{11}(P^2_{1,1} + P^2_{1,2} + P^2_{1,3} + P^2_{2,1} + P^2_{2,2} + P^2_{2,3} + P^2_{3,1} + P^2_{3,2} + P^2_{3,3}), \tag{3.8}$$

based on Ref. [129]. G^{α}_{11} is the gradient energy coefficient of phase α, and

$$P_{i,j} = \frac{\partial P_i}{\partial x_j}\,(i,j = 1,2,3) \tag{3.9}$$

is the spatial differentiation of the polarization components.

3.2.4. Elastic energy density

The elastic energy density associated with phase α is expressed within the global coordinate system by:

$$f^{\alpha}_{\mathrm{elast}}(\boldsymbol{\varepsilon}^{\alpha}, \boldsymbol{P}) = \frac{1}{2}\Big[\Big(\boldsymbol{\varepsilon}^{\alpha} - \boldsymbol{\varepsilon}^{\alpha 0}(\boldsymbol{P})\Big)\cdot\boldsymbol{\mathcal{C}}^{\alpha}\cdot\Big(\boldsymbol{\varepsilon}^{\alpha} - \boldsymbol{\varepsilon}^{\alpha 0}(\boldsymbol{P})\Big)\Big]. \tag{3.10}$$

$\boldsymbol{\mathcal{C}}^{\alpha}$ represents the forth-order elastic stiffness tensor specific to phase α. $\boldsymbol{\varepsilon}^{\alpha} - \boldsymbol{\varepsilon}^{\alpha 0}(\boldsymbol{P})$, $\boldsymbol{\varepsilon}^{\alpha}$, and $\boldsymbol{\varepsilon}^{\alpha 0}(\boldsymbol{P})$ denote the elastic strain, the total strain, and the spontaneous strain, respectively.

With $\boldsymbol{u}$ denotes the displacement vector, the total strain $\boldsymbol{\varepsilon}$ is defined as:

$$\boldsymbol{\varepsilon} = \frac{1}{2}\Big(\nabla \boldsymbol{u} + (\nabla \boldsymbol{u})^{\mathrm{T}}\Big), \tag{3.11}$$

which captures the symmetric part of the displacement gradient $\nabla \boldsymbol{u}$. With the application of the jump condition approach described in Refs. [130–133], $\boldsymbol{\varepsilon}$ is further decomposed into its phase components via

$$\boldsymbol{\varepsilon} = \sum_{\alpha} \boldsymbol{\varepsilon}^{\alpha} h^{\alpha}(\boldsymbol{\phi}). \tag{3.12}$$

A corresponding volumetric decomposition of stresses, $\boldsymbol{\sigma}$, can similarly be denoted as:

$$\boldsymbol{\sigma} = \sum_{\alpha} \boldsymbol{\sigma}^{\alpha} h^{\alpha}(\boldsymbol{\phi}). \tag{3.13}$$

The spontaneous strain in the global coordinate system, $\boldsymbol{\varepsilon}^{\alpha 0}(\boldsymbol{P})$, can be derived from the local spontaneous strain $\boldsymbol{\varepsilon}^{\alpha 0\mathrm{L}}(\boldsymbol{P})$ through:

$$\varepsilon_{ij}^{\alpha 0} = tr_{ki} tr_{lj} \varepsilon_{kl}^{\alpha 0\mathrm{L}}. \tag{3.14}$$

$\varepsilon_{ij}^{\alpha 0\mathrm{L}}$ is the local spontaneous strain, written as:

$$\varepsilon_{ij}^{\alpha 0\mathrm{L}} = \mathcal{Q}_{ijkl}^{\alpha}(P_k^{\mathrm{L}})(P_l^{\mathrm{L}}), \tag{3.15}$$

in which $\mathcal{Q}_{ijkl}^{\alpha}$ represents the electrostrictive coefficient tensor of phase α. Using Voigt notation to express the electrostrictive tensor coefficient, the spontaneous strains can be further expanded as:

$$\begin{aligned}
\varepsilon_{11}^{\alpha 0L} &= \mathcal{Q}_{11}^{\alpha}(P_1^{\mathrm{L}})^2 + \mathcal{Q}_{12}^{\alpha}\Big((P_2^{\mathrm{L}})^2 + (P_3^{\mathrm{L}})^2\Big), \\
\varepsilon_{22}^{\alpha 0L} &= \mathcal{Q}_{11}^{\alpha}(P_2^{\mathrm{L}})^2 + \mathcal{Q}_{12}^{\alpha}\Big((P_1^{\mathrm{L}})^2 + (P_3^{\mathrm{L}})^2\Big), \\
\varepsilon_{33}^{\alpha 0L} &= \mathcal{Q}_{11}^{\alpha}(P_3^{\mathrm{L}})^2 + \mathcal{Q}_{12}^{\alpha}\Big((P_1^{\mathrm{L}})^2 + (P_2^{\mathrm{L}})^2\Big), \\
\varepsilon_{12}^{\alpha 0L} &= \mathcal{Q}_{44}^{\alpha}(P_1^{\mathrm{L}} P_2^{\mathrm{L}}), \\
\varepsilon_{13}^{\alpha 0L} &= \mathcal{Q}_{44}^{\alpha}(P_1^{\mathrm{L}} P_3^{\mathrm{L}}), \\
\varepsilon_{23}^{\alpha 0L} &= \mathcal{Q}_{44}^{\alpha}(P_2^{L} P_3^{L}),
\end{aligned} \tag{3.16}$$

in which $\mathcal{Q}_{11} = \mathcal{Q}_{1111}$, $\mathcal{Q}_{12} = \mathcal{Q}_{1122}$ and $\mathcal{Q}_{44} = \mathcal{Q}_{4444}$.

The mechanical jump condition approach is applied to solve the mechanical field. For resolving the local and global mechanical equilibrium, with the segregation of the phase-dependent components for strain and stress using a jump condition framework, it is directed to Refs. [132, 133].

3.2.5. Electric energy density

The electric energy $f_{\mathrm{elec}}(\boldsymbol{E}, \boldsymbol{P})$ arises from the depolarization field $\boldsymbol{E}_{\mathrm{D}}$ and the external electric field $\boldsymbol{E}_{\mathrm{ext}}$, formulated as:

$$f_{\mathrm{elec}}(\boldsymbol{P}, \boldsymbol{E}) = -\frac{1}{2} E_{i,D} P_i - E_{i,\mathrm{ext}} P_i, \tag{3.17}$$

with the total polarization as the order parameter [35]. $E_{i,D}$ is calculated by the gradient of the electric potential ψ, denoted by:

$$E_{i,D} = -\frac{\partial \psi}{\partial x_i} \tag{3.18}$$

where i changes from 1 to 3. By solving the electrostatic equilibrium equation of the electric displacement

$$\frac{\partial D_i}{\partial x_i} = 0, \tag{3.19}$$

ψ can be obtained from the Poisson equation, given by:

$$\frac{\partial D_i}{\partial x_i} = -\kappa_0 \kappa_r \nabla^2 \psi + \nabla \cdot P_i = 0. \tag{3.20}$$

κ_0 denotes the absolute dielectric permittivity and κ_r is the relative dielectric permittivity.

3.3. Governing Equations

3.3.1. Phase-field evolution

The phase transformation between the ferroelectric phases is formulated based on Ref. [77], denoted as:

$$\frac{\partial \phi_\alpha(\boldsymbol{x}, t)}{\partial t} = -\frac{1}{\widetilde{N} \epsilon} \sum_{\alpha<\beta} M^{\alpha\beta} \left(\frac{\delta \mathcal{F}}{\delta \phi_\alpha} - \frac{\delta \mathcal{F}}{\delta \phi_\beta} \right), \tag{3.21}$$

wherein $M^{\alpha\beta}$ is the phase-field mobility matrix for phases α and β, and $\widetilde{N}$ denotes the number of the locally active phases. $\delta \mathcal{F} / \delta \phi_\alpha$ represents the variational derivative of the total energy concerning ϕ_α, given by:

$$\frac{\delta \mathcal{F}}{\delta \phi_\alpha} = \frac{\partial f}{\partial \phi_\alpha} - \nabla \cdot \frac{\partial f}{\partial \nabla \phi_\alpha}. \tag{3.22}$$

3.3.2. Polarization evolution

Considering the total free energy as a function of the global coordinate for the polarization vector, the domain structure in each ferroelectric phase is determined by solving the TDGL equation based on Eq. (2.66), given by:

$$\frac{\partial P_i(\boldsymbol{x},t)}{\partial t} = -M\frac{\delta \mathcal{F}}{\delta P_i(\boldsymbol{x},t)}\,(i=1,2,3), \tag{3.23}$$

where M represents the mobility constant of a domain.

3.3.3. Electrostatic and mechanical equilibrium

Apart from the phase and polarization evolution, the system must also satisfy the electrostatic and mechanical equilibrium. The electrostatic equilibrium is given by the Poisson equation in Eq. (3.20), while the mechanical equilibrium is described by the static momentum balance, expressed as:

$$\nabla \cdot \bar{\boldsymbol{\sigma}} = \mathbf{0}. \tag{3.24}$$

$\bar{\boldsymbol{\sigma}}$ denotes the effective stress tensor in the jump condition framework [132, 133].

4. Model II: Multiphase-field model for ferroelectric material

Model II is adapted from the Methodology Section of Refs. [16, 17].

4.1. Model description

The Schematic diagram of Model II for computing domain structures in ferroelectric material is shown in Fig. 4.1. Based on the multiphase-field approach, the fundamental concept of Model II involves defining the polarization (domain) variants in each ferroelectric material as "phases ($\boldsymbol{\phi}$)", with the formation of domain structures depending on the transformations between these phases. Besides domain variants, the order parameter ϕ_α can also represent other distinct physical regions, such as ferroelectric phases, grains, films, or substrates. These regions are parts of the N-tuple $\boldsymbol{\phi}(\boldsymbol{x},t) = \big(\phi_1(\boldsymbol{x},t),\ldots,\phi_N(\boldsymbol{x},t)\big)$. N quantifies the total number of phases delineated by the diffuse interface, which could manifest as a domain wall, a ferroelectric phase boundary, a grain boundary, or a film-substrate interface. As shown in Fig. 4.1(a), $\phi_\alpha(\boldsymbol{x},t) = 1$ inside phase α, $\phi_\alpha(\boldsymbol{x},t) = 0$ outside phase α, and $\phi_\alpha(\boldsymbol{x},t)$ smoothly changes between 0 and 1 in the diffuse interface region. Since ϕ_α represents the volume fraction of the individual phase, the local condition $\sum_\alpha \phi_\alpha(\boldsymbol{x},t) = 1$ must always be fulfilled.

N for a single crystal with only one ferroelectric phase is determined by the polarization states of the material. When N_v represents the number of polarization variants in such a case, N equals N_v. For instance, there are six polarization variants oriented along the <100>-orientation for the tetragonal ferroelectrics, as shown in Figs. 4.1(a) and (b), resulting in $N = N_\mathrm{v} = 6$. These domain variants could form either $180°$ or $90°$ domain walls, as further detailed in Fig. 4.1(a). By extending N, it is allowed to model polycrystalline systems comprising grains with a single ferroelectric phase (Fig. 4.1(c)), or multiple ferroelectric phases of distinguished polarization states (Fig. 4.1(d)). In the case of Fig. 4.1(c), N is equal to $N_\mathrm{g}N_\mathrm{v}$ and $\boldsymbol{\phi}_\mathrm{grain} = \sum_{\alpha=1}^{N_\mathrm{v}} \phi_\alpha$, where N_g is the grain count and ϕ_grain describes a grain. Regarding the case of Fig. 4.1(d), each grain is defined as $\boldsymbol{\phi}_\mathrm{grain} = \sum_{\mathrm{FP}=1}^{N_\mathrm{fp}} \sum_{\alpha=1}^{N_\mathrm{v}} \phi_{\mathrm{FP},\alpha}(\boldsymbol{x},t)$, in which $\sum_{\alpha=1}^{N_\mathrm{v}} \phi_{\mathrm{FP},\alpha}(\boldsymbol{x},t)$ denotes the domain variants in each ferroelectric phase. FP represents the ferroelectric phase and N_fp signifies the

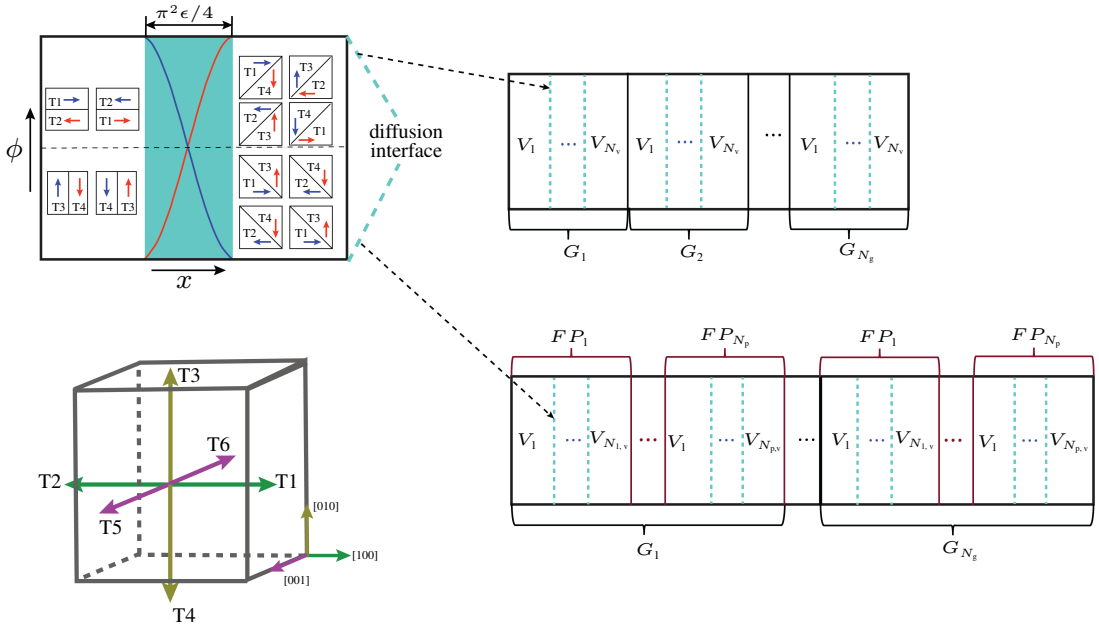

Figure 4.1.: Schematic diagram of Model II. (a) Illustration of the tetragonal variants (T1 and T4) and their associated domain walls across the diffusion region, in which ϵ scales the interfacial thickness; T1 to T4 corresponds to the variants in (b), which shows the six polarization variants in the tetragonal phase; (c) The polycrystalline system with a single ferroelectric phase, where G_{N_g} represents the N_g-th grain (N_g = 1, 2...), and V_{N_v} denotes the N_v-th variant of the ferroelectric phase (N_v = 1, 2...); (d) A polycrystalline structure with multiple ferroelectric phases, where FP_1 to FP_{N_p} represents the ferroelectric phases from 1 to N_p. Based on Ref. [16].

total number of these phases. Hence $N = N_g \sum_{fp=1}^{N_{fp}} N_{v,fp}$, where $N_{v,fp}$ corresponds to the total polarization variants in each ferroelectric phase FP.

Epitaxial film growth on a substrate can also be simulated by constraining the phase transformation between the film and the substrate. For a single-crystal thin film, the substrate can be characterized via the order parameter ϕ_{sub}, coupled with an introduction of ϕ_{film} to represent a film. Thus, ϕ_{film} is algebraically defined as the summation $\sum_{i=1}^{N_v} \phi_i$, where each ϕ_i denotes an order parameter corresponding to individual polarization variants, and N_v signifies the number of polarization variants intrinsic to the ferroelectric film. Consequently, in the scenario of a single-grain thin film containing exclusively one ferroelectric phase, $N = N_v + 1$. Analogous to bulk polycrystalline simulations, polycrystalline ferroelectric films can be modeled by extending ϕ values. When accounting for the substrate, however, the total number of ϕ values in polycrystalline films exceeds that of bulk polycrystalline materials by one.

4.2. Energy formulation

4.2.1. Total energy functional

Elastic and electrostatic energies play a determinative role in the formation and stabilization of domain structures in ferroelectrics. Based on the general multiphase-field approach formulated by Nestler *et al.* [78], the total energy functional of Model II hence can be expressed as:

$$\mathcal{F} = \int_V \Big[f_{\mathrm{grad}}(\nabla\boldsymbol{\phi}) + f_{\mathrm{ob}}(\boldsymbol{\phi}) + \sum_{\alpha=1}^{N} \big(f^{\alpha}_{\mathrm{elast}}(\boldsymbol{\varepsilon}^{\alpha}, \boldsymbol{P}^{\alpha}) + f^{\alpha}_{\mathrm{elec}}(\boldsymbol{P}^{\alpha}, \boldsymbol{E}) \big) h^{\alpha}(\boldsymbol{\phi}) \Big] \, \mathrm{d}V. \tag{4.1}$$

Similar to Model I, the first two terms in Eq. (4.1)—the gradient energy density (f_{grad}) and the multi-obstacle potential (f_{ob})—constitute the interfacial energy density of the system. The summation term represents the phase-dependent bulk energy, including the elastic energy f_{elast} and the electric energy density f_{elec}, where $\boldsymbol{\varepsilon}^{\alpha}$ is the strain tensor and $\boldsymbol{E}_{\mathrm{ext}}$ is the external electric field. $\boldsymbol{P}^{\alpha}$ denotes the polarization of α phase. The orientation of $\boldsymbol{P}^{\alpha}$ is determined by the crystal structure of phase α, while its amplitude is predefined as the absolute value of its spontaneous polarization. $h^{\alpha}(\boldsymbol{\phi})$ represents an interpolation function, also defined as $h^{\alpha}(\boldsymbol{\phi}) = \phi_{\alpha}$ in Model II. The interpolation function allows capturing the transition of polarization states over the interface, helping to compute the bulk driving force across the diffusion region. The gradient energy is calculated using the equation provided in Eq. (2.53), and the multi-obstacle type potential in Eq. (3.3) without the high-order term is applied in Model II. An alternative choice would be considering a multi-well potential, as used in Ref. [128]. The multi-obstacle potential is chosen in this work because it allows ϕ_{α} to take values of 0 and 1 within the interface width, preserving interface information and conserving memory in numerical computations [70]. Additionally, it effectively prevents the expansion of multiple junctions into the interface region [70].

4.2.2. Elastic energy density

In Model II, the multiphase elasticity model is used, which is capable of fulfilling the mechanical jump conditions proposed in Refs. [132–134]. In general, the elastic energy density for phase α is defined as:

$$f^{\alpha}_{\mathrm{elast}}(\boldsymbol{\varepsilon}^{\alpha}, \boldsymbol{P}^{\alpha}) = \frac{1}{2}\big[(\boldsymbol{\varepsilon}^{\alpha} - \tilde{\boldsymbol{\varepsilon}}^{\alpha}) \cdot \boldsymbol{\mathcal{C}}^{\alpha} \cdot (\boldsymbol{\varepsilon}^{\alpha} - \tilde{\boldsymbol{\varepsilon}}^{\alpha}) \big], \tag{4.2}$$

where $\boldsymbol{\mathcal{C}}^{\alpha}$ denotes the elastic stiffness of the material, which is ferroelectric-phase-dependent and independent of the domain variants of a ferroelectric phase. $\boldsymbol{\varepsilon}^{\alpha}$ and $\tilde{\boldsymbol{\varepsilon}}^{\alpha}$ represent the total strain and the inelastic strain, respectively. The definition as well as the calculation of the total strain can refer to Section 3.2.4.

For bulk materials, the inelastic strain corresponds to the spontaneous strain, $\varepsilon^{\alpha,0}$, denoted as:

$$\tilde{\boldsymbol{\varepsilon}}^{\alpha} = \boldsymbol{\varepsilon}^{\alpha,0} \tag{4.3}$$

As polarizations are assigned based on ϕ, it can automatically align with the grain orientation in the polycrystalline system. Therefore, the spontaneous strain for a polycrystalline bulk material is defined as:

$$\varepsilon_{ij}^{\alpha,0} = \boldsymbol{Q}_{ijlk}^{\alpha} P_k^{\alpha} P_l^{\alpha}, \tag{4.4}$$

by using the Einstein summation convention. $\boldsymbol{Q}_{ijkl}^{\alpha}$ are the electrostrictive coefficients that are characteristic of each ferroelectric phase.

The mechanical driving force is important in forming domain structures in ferroelectric materials. This is particularly evident in epitaxial films constrained by substrates. The intrinsic characteristics of the substrate, which encompass aspects such as its crystalline structure and its coefficient of thermal expansion, result in a misfit strain between the thin film and the substrate. Such a strain gives rise to significant alterations in the energy landscape of the domain structures, thereby exerting a profound impact on their behavior, such as switching, dimensions, and orientation. Therefore, it is essential to accurately mimic the misfit strain between the substrate and the film and its associated impact on the driving forces between ferroelectric variants. Therefore, with regards to a thin film system, the nonelastic strain $\tilde{\boldsymbol{\varepsilon}}^{\alpha}$ comprises both the spontaneous strain of Eq. 4.4 and the misfit strain $\boldsymbol{\varepsilon}^{\mathrm{mis}}$, resulting in:

$$\tilde{\boldsymbol{\varepsilon}}^{\alpha} = \boldsymbol{\varepsilon}^{\alpha,0}(\boldsymbol{P}^{\alpha}) + \boldsymbol{\varepsilon}^{\mathrm{mis}}. \tag{4.5}$$

The misfit strain is computed by:

$$\begin{aligned} \varepsilon_{11}^{\mathrm{mis}} &= \varepsilon_{22}^{\mathrm{mis}} = \frac{a_{\mathrm{s}} - a_{\mathrm{f}}}{a_{\mathrm{f}}}, \\ \varepsilon_{12}^{\mathrm{mis}} &= \varepsilon_{i3}^{\mathrm{mis}} = 0, \ (i = 1, 2, 3), \end{aligned} \tag{4.6}$$

where a_{f} and a_{s} denote the lattice parameters of the film and substrate, respectively.

4.2.3. Electric energy density

As the magnitude of the spontaneous polarization is used as the predetermined value for computing the bulk driving force, the electric energy is formulated as:

$$f_{\mathrm{elec}}(\boldsymbol{P}, \boldsymbol{E}) = E_i P_i - \frac{1}{2} \kappa_0 \kappa_{ij,b} E_i E_j. \tag{4.7}$$

This depends on the consideration of the spontaneous polarization as the order parameter [35]. $\kappa_{ij,b}$ represents the background dielectric constants that satisfy the Kronecker

delta condition. The electric field E_i in this case is the summation of the external electric field as well as the depolarization field, i.e.,

$$E_i = E_{i,\mathrm{ext}} + E_{i,\mathrm{D}}. \tag{4.8}$$

Additionally, ψ is determined by the solution of a Poisson equation with background dielectric constant, which reads:

$$\kappa_0 \kappa_{ij,b} \Delta\psi = -\nabla \cdot P_i. \tag{4.9}$$

i and j range from 1 to 3.

4.3. Governing equation

The minimization of the energy functional (Eq. (4.1)) leads to the formation of the domain structure. Relying on Refs. [77, 134], the governing of the order parameter ϕ_α is denoted as:

$$\begin{aligned}\frac{\partial \phi_\alpha(\boldsymbol{x},t)}{\partial t} = &-\frac{1}{\widetilde{N}\epsilon}\sum_{\beta\neq\alpha}^{\widetilde{N}}\left[M^{\alpha\beta}\left(\frac{\delta\mathcal{F}}{\delta\phi_\alpha}+\epsilon\hat{\alpha}(\phi_\alpha,\nabla\phi_\alpha)-\frac{\delta\mathcal{F}}{\delta\phi_\beta}-\epsilon\hat{\alpha}(\phi_\beta,\nabla\phi_\beta)\right)\right]\\ &+\frac{\partial \pounds}{\partial\phi_\alpha},\end{aligned} \tag{4.10}$$

where $M^{\alpha\beta}$ is the mobility coefficients between phases α and β, and $\widetilde{N}$ denotes the number of the locally active phases. Aiming for a more stale interface and describing the right kinetics, as discussed in Ref.[70], Eq. (4.10) can be further improved as:

$$\begin{aligned}\frac{\partial \phi_\alpha(\boldsymbol{x},t)}{\partial t} = &-\frac{1}{\widetilde{N}\epsilon}\sum_{\beta\neq\alpha}^{\widetilde{N}}\left[M^{\alpha\beta}\left(\frac{\delta\mathcal{F}_{\mathrm{int}}}{\delta\phi_\alpha}+\epsilon\hat{\alpha}(\phi_\alpha,\nabla\phi_\alpha)-\frac{\delta\mathcal{F}_{\mathrm{int}}}{\delta\phi_\beta}-\epsilon\hat{\alpha}(\phi_\beta,\nabla\phi_\beta)\right.\right.\\ &\left.\left.-\frac{8\sqrt{\phi_\alpha\phi_\beta}}{\pi}\Delta^{\alpha\beta}\right)\right]+\frac{\partial \pounds}{\partial\phi_\alpha},\end{aligned} \tag{4.11}$$

in which $\Delta^{\alpha\beta}$ is defined as:

$$\Delta^{\alpha\beta} = \left(\frac{\delta}{\delta\phi_\alpha}-\frac{\delta}{\delta\phi_\beta}\right)\mathcal{F}_{\mathrm{bulk}}. \tag{4.12}$$

$\mathcal{F}_{\mathrm{bulk}}$ denotes the bulk contribution, including elastic and electrostatic energy components.

$\delta\mathcal{F}/\delta\phi_\alpha$ is the variational derivative of the total energy with regards to ϕ_α, expressed by:

$$\frac{\delta\mathcal{F}}{\delta\phi_\alpha} = \frac{\partial f}{\partial\phi_\alpha} - \nabla\cdot\frac{\partial f}{\partial\nabla\phi_\alpha}. \tag{4.13}$$

Thus, the driving force stemming from the electric energy can be written as:

$$\boldsymbol{\Delta}^{\alpha\beta}_{\text{elec}}(\boldsymbol{P},\boldsymbol{E}) = f^{\beta}_{\text{elec}}\frac{\partial h^{\beta}(\boldsymbol{\phi})}{\partial\phi_\beta} - f^{\alpha}_{\text{elec}}\frac{\partial h^{\alpha}(\boldsymbol{\phi})}{\partial\phi_\alpha}. \tag{4.14}$$

According to Ref. [16, 133–135], the resulting elastic driving force with the jump condition approach can be characterized as:

$$\boldsymbol{\Delta}^{\alpha\beta}_{\text{elast}}(\boldsymbol{\phi},\boldsymbol{\varepsilon},\boldsymbol{P}) = \frac{\partial W_{\text{elast}}}{\partial\phi_\beta} - \frac{\partial W_{\text{elast}}}{\partial\phi_\alpha}, \tag{4.15}$$

where W_{elast} is the overall elastic potential based on the continuous variables. The detailed expression can be found in Appendix A of [16, 17], and Refs. [133–135].

With the application of the multiple-obstacle-type potential, to describe the nucleation of the polarization variants from the interface, such as domain boundaries, phase boundaries, or grain boundaries, a noise term £ is introduced to account for the thermal fluctuations described as:

$$£ = \sum_{\alpha<\beta<\delta}^{N,N,N}\phi_\alpha\phi_\beta\phi_\delta\cdot D\cdot A. \tag{4.16}$$

D characterizes various forms of noise distribution, including uniform, Gaussian, and others, whereas A determines the magnitude of the fluctuations. The inclusion of £ to model the nucleation is unnecessary if the simulation uses a multiwell potential. This is because the isotropic interface in the multiwell potential naturally induces thermodynamic fluctuations at the interface in external stimuli.

To ensure reasonable interface quality while maintaining highly effective simulation efficiency, an additional $\epsilon\hat{\alpha}(\phi_\alpha,\nabla\phi_\alpha)$ is integrated into the multiphase content and included in the phase-field evolution equations (Eqs. (4.10) and (4.11)). $\epsilon\hat{\alpha}(\phi_\alpha,\nabla\phi_\alpha)$ is defined as:

$$\epsilon\hat{\alpha}(\phi_\alpha,\nabla\phi_\alpha) = \epsilon\gamma^{c}_{\alpha}\left(\Delta\phi_\alpha - |\nabla\phi_\alpha|\nabla\cdot\left(\frac{\nabla\phi_\alpha}{|\nabla\phi_\alpha|}\right)\right), \tag{4.17}$$

where γ^{c}_{α} can be understood as a factor that calibrates the strength of the artificially constructed interface. Eq. (4.17) helps strike a balance between low interfacial energy, high bulk driving forces, and appropriate grid resolution. The second term compensates for the curvature-minimizing property of the Laplace operator, avoiding dynamic curvature minimization to ensure correct interaction between the gradient and the potential energy density. Regarding the nucleation mechanism of Eq. (4.16) and the physical meaning behind Eq. (4.17), the reader is recommended to Ref. [134].

In addition to phase evolution, there are static momentum balance

$$\nabla \cdot \bar{\boldsymbol{\sigma}} = \mathbf{0}, \tag{4.18}$$

and Poisson equations in Eq. (4.9) that control the mechanical and electrostatic equilibrium of the system, respectively.

Part III
Results and Discussion

5. Domain evolution and phase transformation in PZT material using Model I

5.1. Introduction

MPB in the phase-diagram of PZT material separating the stability regions of the ferroelectric rhombohedral phase (FR) and the ferroelectric tetragonal phase (FT) [136], as illustrated in Fig. 5.1(a). The coexistence of these phases in the vicinity of the MPB leads to complex domain structures. For instance, Fig. 5.1(b) presents the Piezoresponse Force Microscopy (PFM) analysis conducted on PZT ceramic with $48\,\%$ Pb, as reported in Ref. [137]. The analysis reveals a complex twinned domain structure within a single grain, exhibiting multiple configurations. Additionally, some large grains exhibit domain structures consistent with FT and FR. Therefore, domain switching and phase transformations within this boundary under the influence of an external stimulus significantly impact the material properties, prompting extensive academic studies.

Thus far, investigations into phase-field simulations at the MPB within the PZT system have primarily been undertaken by Rao and Wang [4–7]. In the first work, they developed a bridging domain mechanism to interpret the coexistence of ferroelectric phases, wherein minority phases are represented as metastable states to connect the majority stable phase [4]. Expanding on this concept, they further observed that the width of the phase coexistence composition range increases as grain sizes decrease in polycrystalline systems [5]. Rao *et al* [6] further integrated the TDGL model with the Cahn-Hilliard equation to explore coherent phase decomposition with local concentration fluctuations. To elucidate the mechanism of inter-ferroelectric phase transformation under an electric field, Rao and Wang also proposed a domain wall broadening theory in Refs. [7, 138]. This theory notes that phase transformation advances through a nucleation-and-growth process within domain boundaries. Building upon this theory, Liu *et al* investigated the synergy between phase transformation and domain switching [9], as well as the reversible phase transformations [10], under imposed electric fields. In general, the TDGL model that describes ferroelectric phase coexistence in Refs. [7, 9, 10, 138] tracks phase transformations through polarization reorientation.

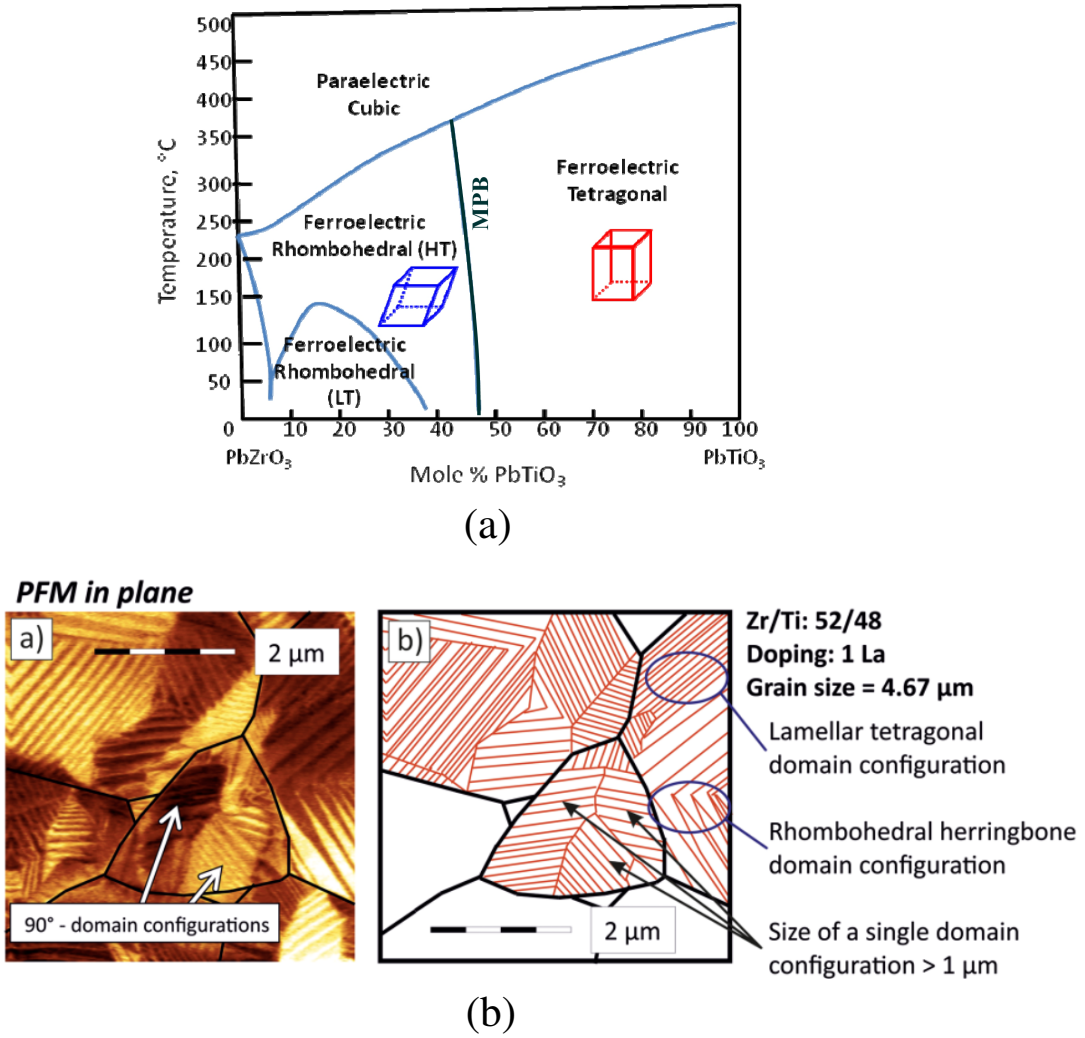

Figure 5.1.: (a) The phase diagram of PZT material (taken from Ref. [136]); (b) Domain configurations of PZT polycrystalline around the MPB region (adapted from Ref. [137]).

In a polycrystalline ferroelectric material positioned at the MPB region, each grain typically consists of two or more ferroelectric phases, delineated by interphase boundaries. Within each ferroelectric phase, distinct domain structures emerge due to domain walls. It is clear that one ferroelectric phase could grow at the expense of another when subjected to external stimuli. Ref. [139] clarifies the mechanism of inter-ferroelectric phase transformation through two distinct approaches. Firstly, a ferroelectric phase may nucleate and grow within others, a concept akin to the domain wall broadening theory outlined in Ref. [88]. Secondly, an existing phase boundary might move towards, inducing the formation of another phase. The second phenomenon remains viable due

to the relatively flat energy landscapes surrounding the MPB, enabling phase transformations at interphase boundaries even under comparatively low electric fields [140]. However, this theory has not been addressed within the scope of the publications.

Therefore, the objective of this chapter is to apply Model I to investigate domain structures and phase transformations in polycrystalline PIC 151 that consists of a composition near the MPB of the PZT solid solution. To drive the phase transformation, ferroelectric phase-dependent material coefficients are required to compute the driving force, as outlined in Eq. (3.1). Therefore, this chapter initially determined the material coefficients for the FT and FR in PIC 151 based on experimental measurements and a proposed numerical approach. Subsequently, phase-field simulations were conducted to investigate domain structures and phase transitions in both single-crystal and polycrystalline PIC 151, under varying external stimuli. This chapter constitutes a primary part of Ref. [15].

5.2. Determination of the coefficients

5.2.1. Determination based on the LDT and experimental measurement

The experimental measurements of cell parameters and atomic positions of PIC 151 are listed in Table 5.1, detailed in Ref. [15]. Based on these data, the phase-dependent spontaneous polarization can be calculated. In the perovskite cell, the approach assumes uniform charge and displacement for all ions (Zr, Ti, Ni, and Sb in the PIC 151) on the B-site, while the Pb ion on the A-site is considered stationary, acting as the origin. Hence the spontaneous polarization of the FT, denoted as $\boldsymbol{P}_{s,\mathrm{FT}}$, can be estimate by:

$$\boldsymbol{P}_{s,\mathrm{FT}} = [4\mathcal{R}(B) - 4\mathcal{R}(O_{2,3}) - 2\mathcal{R}(O_1)]\frac{e}{a^2}\boldsymbol{z}, \tag{5.1}$$

in which e represents the elementary charge, a denotes the unit cell parameter, $\boldsymbol{z}$ is the unit vector along the c axis and $\mathcal{R}$ signifies the displacement of the atomic position away from the pseudocubic position. The rhombohedral cell is configured within a hexagonal setup. The polarization vector [111] in the rhombohedral cell aligns with the [001] orientation in the tetragonal cell. The absolute value of the spontaneous polarization for the FR, $P_{s,\mathrm{FR}}$, can therefore be computed by:

$$\boldsymbol{P}_{s,h} = \frac{12e}{\sqrt{3}a^2}(2t_a + s_a)\boldsymbol{z}, \quad P_{s,\mathrm{FR}} = \frac{P_{s,h}}{\sqrt{3}}, \tag{5.2}$$

within which $\boldsymbol{P}_{s,h}$ represents the spontaneous polarization of the hexagonal cell. t_a and s_a are atomic positions, specified by Megaw *et al.* in Ref. [141].

The spontaneous strain is a measurement of the lattice distortion induced by the spontaneous polarization. In the context of the tetragonal structure, the spontaneous

Table 5.1.: Rietveld refinement results of neutron and X-ray diffraction for the PIC 151 material [15]. a and c: unit cell parameters; V_{PC}: volume of the pseudocubic primitive cell; Θ: unit cell distortion; Φ: unit cell angle; V_ϕ: phase volume fraction. Adapted from Ref. [15].

Coefficients	FT	Hexagonal	FR	Unit
a	4.03669 (3)	5.72881 (5)	4.05740 (8)	Å
c	4.09552 (4)	7.05012 (13)	-	Å
V_{PC}	66.7362 (15)	200.381 (5)	66.794 (6)	Å^3
Θ	1.45	-	0.428 (8)	%
Φ	90.00	-	89.81621(9)	°
V_ϕ	52.71 (0.43)	47.29 (0.44)	-	%

strains $x_{\mathrm{FT},1}$ and $x_{\mathrm{FT},3}$ are characterized by:

$$x_{\mathrm{FT},1} = \frac{a_{\mathrm{FT}} - a_{c,\mathrm{pseudo}}}{a_{c,\mathrm{pseudo}}}, \quad x_{\mathrm{FT},3} = \frac{c_{\mathrm{FT}} - a_{c,\mathrm{pseudo}}}{a_{c,\mathrm{pseudo}}}, \tag{5.3}$$

where a_{FT} and c_{FT} are the unit cell parameters of the FT, and $a_{c,\mathrm{pseudo}}$ corresponds to the unit cell parameter of the pseudo-cubic structure as indicated in Table 5.1. Based on Ref. [142], the spontaneous strains of a rhombohedral cell were determined using a transformation matrix $\boldsymbol{U}$ in a cubic basis, defined by:

$$\boldsymbol{U} = \begin{pmatrix} \Gamma & \Lambda & \Lambda \\ \Lambda & \Gamma & \Lambda \\ \Lambda & \Lambda & \Gamma \end{pmatrix}, \tag{5.4}$$

in which

$$\Gamma = \frac{1}{3}(\sqrt{1 + 2cos(\Phi)} + 2\sqrt{1 - cos(\Phi)}), \tag{5.5}$$

and

$$\Lambda = \frac{1}{3}(\sqrt{1 + 2cos(\Phi)} - \sqrt{1 - cos(\Phi)}). \tag{5.6}$$

Φ is the trigonal angle, as found in Table 5.1. The spontaneous strain $x_{\mathrm{FR},1}$ and $x_{\mathrm{FR},4}$ in the FR thus can be computed using linearised distortion tensors, expressed as:

$$x_{\mathrm{FR},1} = 0.5(\Gamma^2 - 1), \quad x_{\mathrm{FR},4} = 0.5\Lambda^2. \tag{5.7}$$

Since there is a linear dependence between the squared spontaneous polarization and the elastic strain in tetragonal cell [58], the isotopic electrostrictive tensor coefficients in Voigt notation for the FT can be derived by:

$$\mathcal{Q}_{\mathrm{FT},11} = \frac{x_{\mathrm{FT},3}}{P^2_{\mathrm{FT},3}}, \quad \mathcal{Q}_{\mathrm{FT},12} = \frac{x_{\mathrm{FT},1}}{P^2_{\mathrm{FT},3}}, \tag{5.8}$$

in which $P_{\mathrm{FT},3}$ represents the value of the spontaneous polarization along the c-axis. For the rhombohedral phase, electrostrictive stiffness coefficients in the Voigt notation can be calculated by:

$$2\mathcal{Q}_{\mathrm{FR},12} + \mathcal{Q}_{\mathrm{FR},11} = \frac{x_{\mathrm{FR},1}}{P^2_{\mathrm{FR},3}}, \quad \mathcal{Q}_{\mathrm{FR},44} = \frac{x_{\mathrm{FR},4}}{P^2_{\mathrm{FR},3}}. \tag{5.9}$$

To determine $\mathcal{Q}_{\mathrm{FR},12}$, the value of $\mathcal{Q}_{\mathrm{FR},11}$ is sourced from Ref. [143].

The dielectric stiffness coefficients in Eq. (3.7) are calculated under a zero-stress condition. Relying on Ref. [58], the energy function in the LGDT with respect to the polarization for FT and FR can be defined as:

$$\Delta G_{\mathrm{FT}} = \alpha_1 P^2_{\mathrm{FT},3} + \alpha_{11} P^4_{\mathrm{FT},3} + \alpha_{111} P^6_{\mathrm{FT},3}, \tag{5.10}$$

and

$$\Delta G_{\mathrm{FR}} = 3\alpha_1 P^2_{\mathrm{FR},3} + 3(\alpha_{11} + \alpha_{12}) P^4_{\mathrm{FR},3} + (3\alpha_{111} + 6\alpha_{112} + \alpha_{123}) P^6_{\mathrm{FR},3}, \tag{5.11}$$

respectively. As mentioned in the description of Eq. (3.7), all-dielectric stiffness coefficients remain temperature-independent, except for α_1, which was subjected to a linear temperature dependency following the Curie-Weiss law. Based on Eqs. (2.21), (2.22) and (3.7), α_1 can be expressed as:

$$\alpha_1(T) = \frac{T - T_0}{2\kappa_0 C}. \tag{5.12}$$

where T_0 denotes the Curie-Weiss temperature, κ_0 represents the absolute dielectric permittivity and C is the Curie constant. To determine T_0 and C, the Curie-Weiss law was employed to fit the inverse of the relative permittivity in the paraelectric state, as depicted in Fig. 5.2. It is assumed that the dielectric stiffness coefficient α_1 remains phase-independent in this study.

According to Ref. [64], the higher-order dielectric constants α_{11} and α_{111} in Eq. (5.10) can be further calculated by:

$$\alpha_{11} = \frac{-(T_C - T_0)}{\kappa_0 C P^2_{\mathrm{FT},3C}}, \quad \alpha_{111} = \frac{T_C - T_0}{2\kappa_0 C P^4_{\mathrm{FT},3C}}. \tag{5.13}$$

T_C, denoting the Curie temperature, is specified as $250\,^{\circ}\mathrm{C}$ by the manufacturer PI Ceramic GmbH. $P_{\mathrm{FT},3C}$ represents the spontaneous polarization of FT at the Curie temperature, which is proportional to $P_{\mathrm{FT},3}$, represented as:

$$P^2_{\mathrm{FT},3C} = \frac{1}{\Psi} P^2_{\mathrm{FT},3}, \quad \Psi = \left(1 + \left[1 - \frac{3(T - T_0)}{4(T_C - T_0)}\right]^{\frac{1}{2}}\right). \tag{5.14}$$

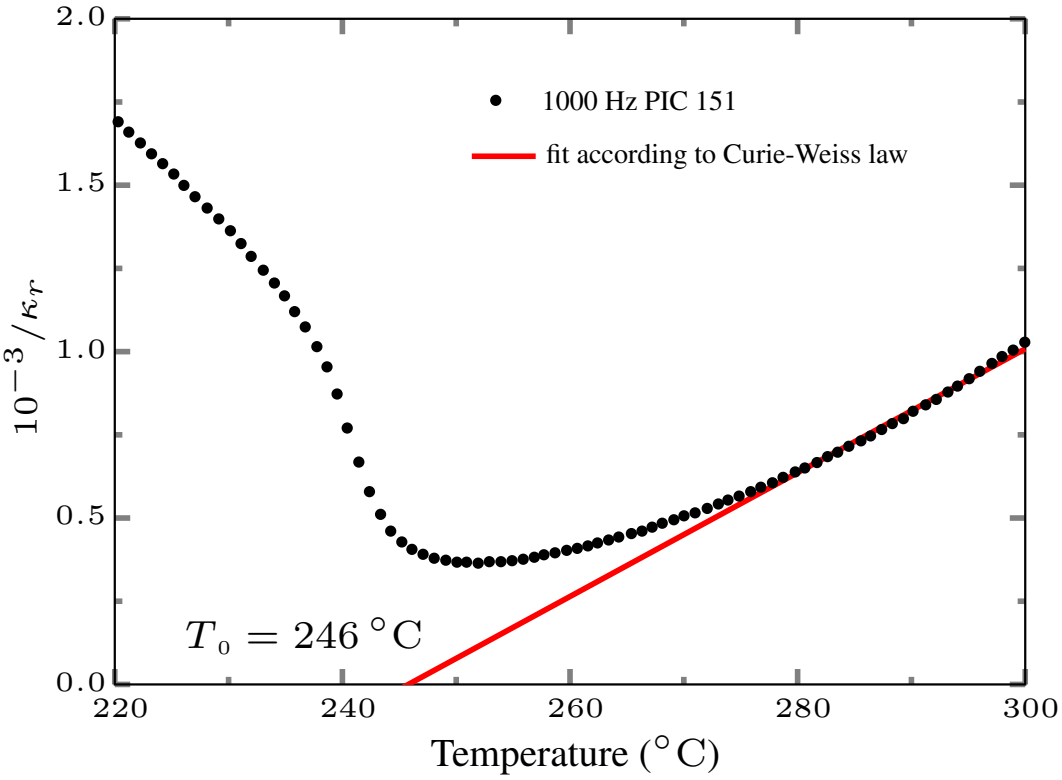

Figure 5.2.: Plot of the inverse susceptibility over temperature for PIC 151. Adapted from Ref. [15].

Furthermore, the forth-order and sixth-order dielectric stiffness coefficients of the FR can be summarized by symbols ζ and ξ, denoted as:

$$\begin{aligned} \zeta &= 3(\alpha_{11} + \alpha_{12}) = \frac{-3(T_C - T_0)}{\kappa_0 C P_{\mathrm{FR},3C}^2} \\ \xi &= 3\alpha_{111} + 6\alpha_{112} + \alpha_{123} = \frac{3(T_C - T_0)}{2\kappa_0 C P_{\mathrm{FR},3C}^4}, \end{aligned} \tag{5.15}$$

where $P_{\mathrm{FR},3C}$ is the spontaneous polarization for FR at the Curie temperature. The measurable and calculated constants are summarized in Table 5.2.

In order to predict α_{12}, α_{112} and α_{123}, the phase-dependent dielectric stiffnesses presented in Table 5.2 were treated as coefficients corresponding to coexisting phases. α_{12} therefore can be determined by substituting α_{11} from the FT phase into Eq. (5.15). To further obtain α_{112} and α_{123}, the experimentally determined, phase-independent piezoelectric modulus coefficient d_{15} in Table 5.2 was derived into phase-related by a

Table 5.2.: The thermophysical properties of the PIC 151 material. Adapted from Ref. [15].

Coefficients	Coexistence	FT	FR	Unit
d_{33}	4.23	-	-	10^{-10}·[C/N]
d_{31}	-2.14	-	-	10^{-10}·[C/N]
d_{15}	6.10	-	-	10^{10}·[C/N]
C	6.70	-	-	10^{5}·[°C]
T_0	246.00	-	-	°C
α_1	-1.89	-	-	10^{7}·[m/F]
$P_{\mathrm{FT},3}$	-	29.47	-	$\mu\mathrm{C/cm^2}$
$x_{\mathrm{FT},1}$	-	-4.81	-	10^{-3}
$x_{\mathrm{FT},3}$	-	9.69	-	10^{-3}
$\mathcal{Q}_{\mathrm{FT},11}$	-	11.16	-	10^{-2}·[$\mathrm{m^4/C^2}$]
$\mathcal{Q}_{\mathrm{FT},12}$	-	-5.54	-	10^{-2}·[$\mathrm{m^4/C^2}$]
α_{11}	-	3.88	-	10^{7}·[$\mathrm{m^5/(C^2F)}$]
α_{111}	-	1.12	-	10^{9}·[$\mathrm{m^9/(C^4F)}$]
$P_{\mathrm{FR},3}$	-	-	23.34	$\mu\mathrm{C/cm^2}$
$x_{\mathrm{FR},1}$	-	-	-2.57	10^{-6}
$x_{\mathrm{FR},4}$	-	-	1.28	10^{-6}
$\mathcal{Q}_{\mathrm{FR},44}$	-	-	7.07	10^{-5}·[$\mathrm{m^4/C^2}$]
$\mathcal{Q}_{\mathrm{sum}}{}^{1}$	-	-	-14.14	10^{-5}·[$\mathrm{m^4/C^2}$]
ζ	-	-	-5.57	10^{8}·[$\mathrm{m^5/(C^2F)}$]
ξ	-	-	7.69	10^{10}·[$\mathrm{m^9/(C^4F)}$]

linear integration of $d_{\mathrm{FT},15}$ and $d_{\mathrm{FR},15}$, expressed as:

$$d_{15} = V_{\phi} * d_{\mathrm{FT},15} + (1 - V_{\phi,\mathrm{FT}}) * d_{\mathrm{FR},15}. \tag{5.16}$$

$V_{\phi,\mathrm{FT}}$ denotes the determined volume fraction of the FT in Table 5.1, and d_{15} is represented by the matrix notation defined in Chapter VII of Ref. [144]. Furthermore, according to Ref. [144], the piezoelectric modulus d_{ij} is the proportionality matrix relating the polarization P_i to the Voigt-nation stress tensor σ_j, expressed as:

$$P_i = d_{ij}\sigma_j \ (i = 1, 2, 3;\ j = 1, 2, \cdots 6). \tag{5.17}$$

As a result, the piezoelectric modulus for each ferroelectric phase can be computed with details provided in Appendix A.1. Overall, the piezoelectric modulus $d_{\mathrm{FT},15}$ and $d_{\mathrm{FR},15}$ can be formulated with respect to α_{112} and α_{123} from Eqs. (A.12) to (A.14), and (A.25) to (A.27), respectively. Since the value of $Q_{\mathrm{FT},44}$ is required according to Eqs. (A.12)-(A.14), an isotropic conditions

$$\mathcal{Q}_{\mathrm{FT},44} = 2(\mathcal{Q}_{\mathrm{FT},11} - \mathcal{Q}_{\mathrm{FT},12}) \tag{5.18}$$

was assumed based upon Ref. [1]. In the end, α_{123} can be computed by substituting Eqs. (5.15), (A.12), (A.13), (A.14), (A.25), (A.26) and (A.27) into Eq. (5.16), resulting in:

$$\frac{6.852 \cdot 10^{-20}\alpha_{123}^2 - 6.693 \cdot 10^{-5}\alpha_{123} + 7.048 \cdot 10^{5}}{1.123 \cdot 10^{-10}\alpha_{123}^2 - 1.097 \cdot 10^{5}\alpha_{123} + 1.156 \cdot 10^{15}} = 0. \tag{5.19}$$

α_{112} was further computed using Eq. (5.15). To be clear, the dielectric stiffness coefficients corresponding to phase coexistence at room temperature are detailed in Table 5.3.

Table 5.3.: Dielectric stiffness coefficients of PIC 151 with phase coexistence at room temperature. Adapted from Ref. [15].

Coefficient	Value	Unit
α_1	-1.861	$10^7 \cdot [\mathrm{m/F}]$
α_{11}	-0.388	$10^8 \cdot [\mathrm{m^5/(C^2F)}]$
α_{12}	-1.473	$10^8 \cdot [\mathrm{m^5/(C^2F)}]$
α_{111}	1.120	$10^9 \cdot [\mathrm{m^9/(C^4F)}]$
α_{112}	10.505	$10^9 \cdot [\mathrm{m^9/(C^4F)}]$
α_{123}	10.532	$10^9 \cdot [\mathrm{m^9/(C^4F)}]$

5.2.2. Separating the thermodynamic coefficients based on phases

To validate the determined dielectric stiffness and electrostrictive coefficients, the 3D energy surface of a single dipole is plotted by minimizing the free energy functional $\mathcal{F}$ in Eq. (3.1). This approach has been previously used to study structural anisotropy, as demonstrated in Refs. [143, 145, 146]. By considering only f_{Landau}, the energy landscape was plotted using the value of dielectric stiffness coefficients from Table 5.3, as illustrated in Fig. 5.3(a). The contour and color represent the free energy, in which blue and red denote the energetic minimum and maximum, respectively. It is evident that the energetic minima are located along the {100} orientations, indicating the stability of the FT. Additionally, the presence of the FR is suggested by an energy saddle point in the {111} direction.

According to Eq. (3.1), each phase should have the driving force to induce the corresponding phase transformation. When mapped onto the energy contour plot, the energy landscape of the FT should lie below the landscape of the FR along the {100} direction, and conversely. While Fig. 5.3(a) suggests a higher occurrence of the FT over the FR, the coefficients in Table 5.3 do not provide the required distinction between their respective driving forces. Accordingly, an independent set of thermodynamic coefficients for each phase should promote the solution of the phase-dependent free

energy. Moreover, as detailed in Section 5.2.1, the thermodynamic coefficients have been recognized as phase-dependent from an experimental perspective. Therefore, a numerical approach was formulated to visually construct phase-dependent coefficients for the energy boundary condition at the MPB, enabling computation of the unknown phenomenological constants.

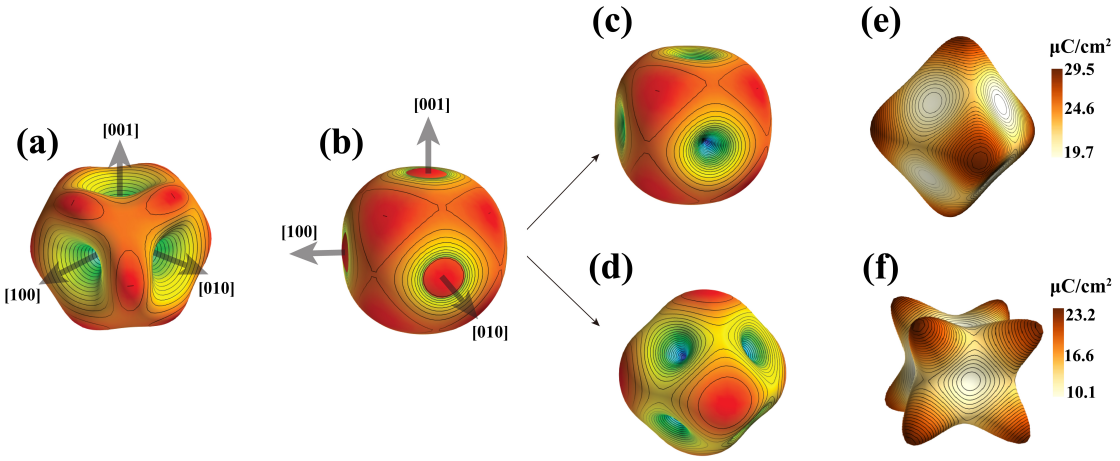

Figure 5.3.: (a) Phase-coexisting Landau potential energy density f_{Landau} based on Table 5.3. (b) The estimated combination of Landau potential energy density and elastic energy density, $f_{\text{Landau}} + f_{\text{elast}}^{\text{strain0}}$, when $\varepsilon_{ij} = 0$. (c) The assumed $f_{\text{Landau}} + f_{\text{elast}}^{\text{strain0}}$ for the FT. (d) The assumed $f_{\text{Landau}} + f_{\text{elast}}^{\text{strain0}}$ for the FR. (e) and (f) respectively depict the polarization overview of the single tetragonal and rhombohedral phases, as determined by the coefficients from Table 5.4. Adapted from Ref. [15].

The essential concept of the approach is to numerically determine the remaining parameters based on phase-dependent structural characteristics and microscopically measured dielectric and electromechanical parameters. To achieve this objective, the assumption is established that the driving force for each phase is equal in the absence of an external field. This establishes the plotted energy boundary condition for phase coexistence in PIC 151. The gradient energy f_{G} in Eq. (3.1) was not taken into account in this approach as the energy contour is drawn for a single dipole. Therefore, the focus was on the combination of the Landau potential energy density f_{Landau} and the elastic energy density f_{elast}. Furthermore, to account for the majority of dipoles being within a domain, the influence of neighboring dipoles was minimized by imposing a total strain condition of $\varepsilon_{ij} = 0$. This condition could be denoted as:

$$f_{\text{elast}} = f_{\text{elast}}^{\text{strain0}} = \frac{1}{2}\varepsilon_{ij}^{0} \cdot C_{ijkl} \cdot \varepsilon_{kl}^{0} \tag{5.20}$$

Expanding upon the aforementioned points, it was further postulated that the coefficients under consideration should adhere to the following principles: (I) the energy

overlap between the phases remains independent of the phase itself, and (II) the energetic minima of each phase should be identical in numerical value while being aligned with their respective polarization directions. These concepts are visually depicted in Figs. 5.3(b)-(d). Besides, the polarization strength within each domain must remain consistent to ensure the stability of the experimental data (Table 5.2). This adherence to Eqs. (5.13) and (5.15) to accurately qualify the parameters involved. The determined parameters thus satisfy the clamped boundary condition. To align with Eq. (3.7), additional conversion is necessary, following the methodology outlined in Ref. [13]. Particularly, Table 5.4 details a solution that corresponds to these assumptions and matches with experimental findings.

Table 5.4.: The coefficients for computing the bulk driving force in Eq. (3.1), including the separated dielectric stiffness coefficients and electrostrictive constants for the FT and FR under stress-free conditions, and the isotropic elastic tensor coefficients obtained from Ref. [147]. All coefficients are denoted in Voigt notation. Adapted from Ref. [15].

Coefficients	FR	FT	Unit
α_1	-1.861	-1.861	$10^7 \cdot [\mathrm{m/F}]$
α_{11}	9.000	-0.388	$10^8 \cdot [\mathrm{m^5/(C^2F)}]$
α_{12}	-10.861	-1.473	$10^8 \cdot [\mathrm{m^5/(C^2F)}]$
α_{111}	1.120	1.120	$10^9 \cdot [\mathrm{m^5/(C^2F)}]$
α_{112}	4.000	1.054	$10^{10} \cdot [\mathrm{m^5/(C^2F)}]$
α_{123}	-16.623	7.447	$10^{10} \cdot [\mathrm{m^5/(C^2F)}]$
$\mathcal{Q}_{11}$	1.720	11.164	$10^{-2} \cdot [\mathrm{m^4/C^2}]$
$\mathcal{Q}_{12}$	-0.867	-5.547	$10^{-2} \cdot [\mathrm{m^4/C^2}]$
$\mathcal{Q}_{44}$	0.007	98.120	$10^{-2} \cdot [\mathrm{m^4/C^2}]$
$\mathcal{C}_{11}$	107.650	107.650	$10^9 \cdot [\mathrm{N/m^2}]$
$\mathcal{C}_{12}$	63.124	63.124	$10^9 \cdot [\mathrm{N/m^2}]$
$\mathcal{C}_{44}$	19.624	19.624	$10^9 \cdot [\mathrm{N/m^2}]$

To validate the calculations, the landscapes of the spontaneous polarization for the tetragonal and rhombohedral phases are represented in Figs. 5.3(e) and (f), with shapes indicating orientation and colors representing magnitude. The polarization for each phase is expected to correspond to its respective crystal structure. Accordingly, the maximum polarization length of the FT appears along the {100} crystallographic directions, whereas the polar axes of the FR align with the {111} orientations. Furthermore, the calculated maximum polarizations, $P_{\mathrm{FR},3} = 23.2\,\mu\mathrm{C/cm^2}$ and $P_{\mathrm{FT},3} = 29.5\,\mu\mathrm{C/cm^2}$, demonstrate significant consistency with the experimental data presented in Table 5.2. These findings underscore the validity of the polarization profiles in representing the individual material characteristics.

5.3. Numerical setup

The simulations were performed using the in-house software package, Parallel Algorithms for Crystal Evolution in 3D (Pace3D) [148]. The quasi-2D simulation was performed to analyze the microstructural evolution of PIC 151 material, given the computational intensity associated with a 3D. The computational domain for the single-crystal system consisted of 200 × 200 × 1 cells. The polycrystalline structure was simulated using a 181 × 209 × 1 voxel grid, generated via Voronoi tessellation. Regardless of the computed size, the domain was discretized into cells with unified dimensions, where $\Delta x_1 = \Delta x_2 = \Delta x_3 = 0.33\,\mathrm{nm}$. The length scale parameter, ϵ, was at $5\Delta x_1$. Although both phases and grains are described by ϕ, it is important to note that they represent different physical phenomena. As a result, the interfacial energies at the phase boundary and the grain boundary are distinct physically, despite having the same diffusion thickness ϵ. A periodic boundary condition was employed to solve all relevant fields, including the phase field, polarization field, mechanical field, and electric field. To optimize computational efficiency, domain decomposition was implemented using the Message-Passing Interface (MPI).

The finite-difference algorithm employing an explicit forward Euler scheme was used to determine the evolution of the polarization vector and phase transformation at room temperature. The solution process is illustrated in Fig. 5.4. The system initialization begins with phases in which the polarization vectors are randomly distributed. This is followed by solving the electrostatic and mechanical equilibrium of the system. Subsequently, the polarization is updated by solving the TDGL equation, as presented in Eq. (3.23). Next, the phase transformation is determined by solving Eq. (3.21) to minimize the energy functional specified in Eq. (3.1). This iterative process of solving for polarization and phases continues until the system achieves both electrical and mechanical equilibrium.

The phase-dependent dielectric coefficients and electrostrictive stiffness for the phase-field simulation are listed in Table 5.4. The elastic stiffness tensor was treated as isotropic and phase-independent, taken from Ref. [147] with values also listed in Table 5.4. Regarding the gradient energy calculation within domain wall regions, the gradient coefficient G_{11} for both the FT and FR was derived from $G_{11}/G_{110} = 0.6$, where $G_{110} = 1.73 \times 10^{-10}\ \mathrm{C^{-2}m^4N}$ [87]. The relative dielectric permittivity $\kappa_r = 1110$ in Ref. [147] was applied to calculate the depolarization energy. The interface width parameter ϵ is set as $5\Delta x_1$, and the interfical energy density parameter $\gamma_{\alpha\beta}$ and $\gamma_{\alpha\beta\tau}$ are set as $0.01\ \mathrm{J/m^2}$. The dimensionless value of the polarization mobility M^* (Eq. (3.23)) and the mobility coefficient $M^{*\alpha\beta}$ (Eq. (3.21)) of the inter-phases were both set as 1 to ensure the stable evolution of domain structures at the domain walls and the steady phases transformation at the phase interfaces while maintaining highly efficient computation. It is also important to emphasize that the simulated results are valid within $0 < M/M^{\alpha\beta} < 1.167$. In PIC 151, grain growth or shrinkage at room temperature

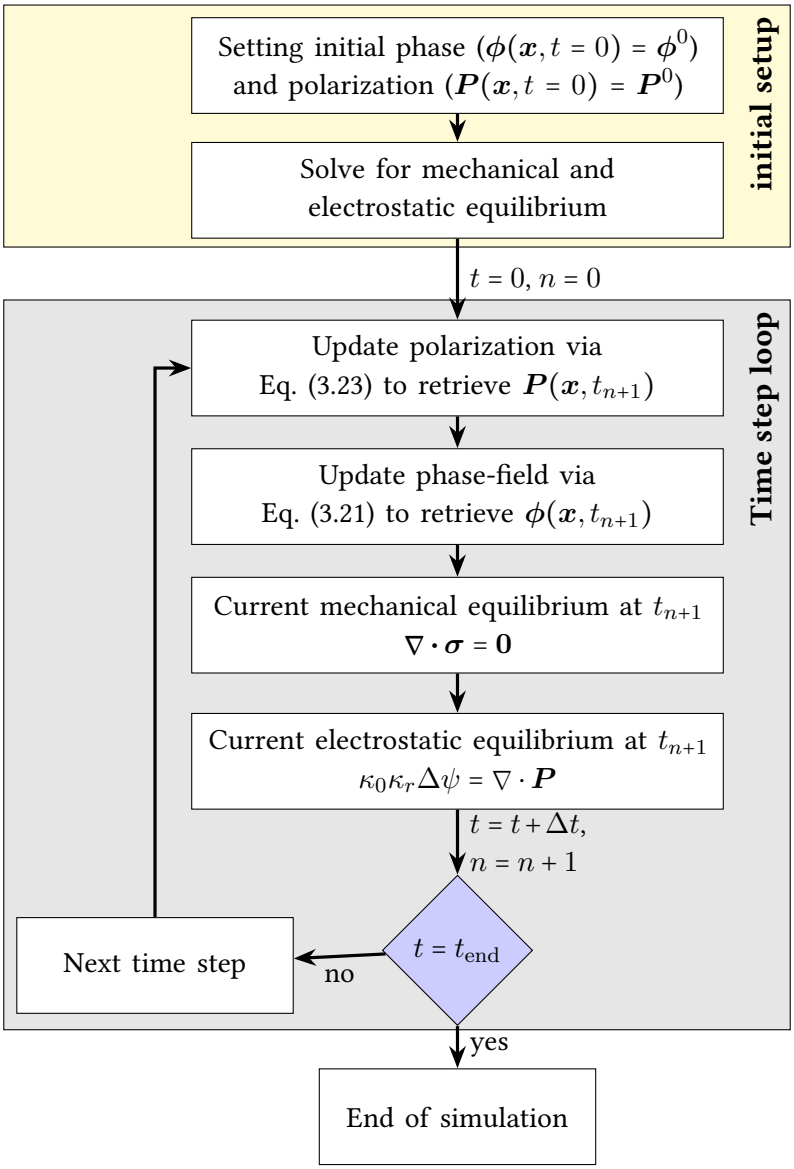

Figure 5.4.: An overview of the solution procedure involves applying Model I to compute domain structures and phase transformations.

is prevented because the activation energy required for grain movement is too high. As a result, the mobility between grains was set to zero.

5.4. Phase-field simulations

5.4.1. Single-crystal simulation

5.4.1.1. Single phase simulation

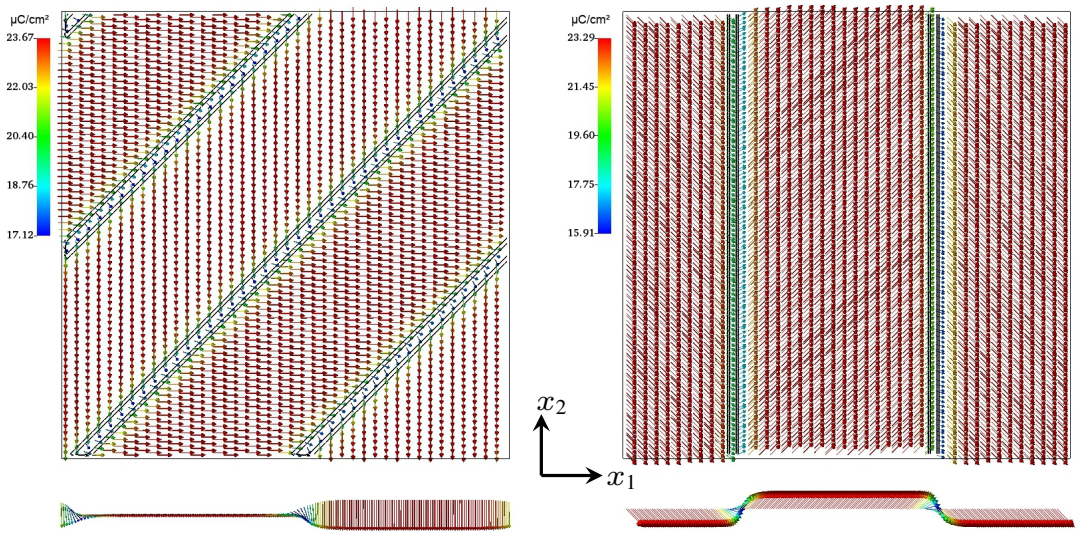

(a) Domain structure in the FT

(b)Domain structure in the FR

Figure 5.5.: The simulated domain structures of the tetragonal and rhombohedral phases within the single crystal are depicted. The black isolines illustrate the distribution of the von Mises stresses. Adapted from Ref. [15].

To validate both the model and the phase-dependent coefficients outlined in Table 5.4, numerical simulations were initiated to compute the domain structure of the pure phase inside a single grain without any stimulus. Figs. 5.5(a) and (b) respectively illustrate the domain structures of pure tetragonal and rhombohedral phases, with the arrow orientation indicating the polarization direction and its color representing the amplitude. The black lines represent the contours of the von Mises stresses, depicting the distribution of elastic energy density. As depicted in Fig. 5.5, the maximum polarization occurs within the domain, with dipoles aligning along various crystallographic directions that are distinct yet equivalent in each phase. The $90°$ domains form in the FT with {110} twin planes in the equilibrium state (Fig. 5.5(a)), signifying the predominance of the strain energy. The simulated domain walls exhibit a head-to-tail arrangement that agrees with findings in Ref. [81]. Furthermore, the computed domain structures for the pure FR in a single crystal are consistent with Ref. [149], where $109°$ domain walls are formed with {100} twin planes to accommodate internal mechanical stress fields, as illustrated

in Fig. 5.5(b). The distribution of the Mises stresses in each phase reveals that elastic strains vary at the domain walls but are equivalent within the domains.

5.4.1.2. Multiphase simulation

Phase-field simulations of a multiphase system within a single crystal were carried out to further verify the coefficients. Fig. 5.6 illustrates the formation of the domain structures as well as associated phase transformations under a zero external electric file condition, where the tetragonal and rhombohedral phases are respectively denoted by the light and dark gray colors. The orientation and color of the arrows within each phase illustrate their respective polarization vectors. At the start of the simulation, polarization vectors were randomly assigned within the computational unit to emulate a paraelectric state. The nucleation and growth of the domain walls can be observed in Fig. 5.6(a), where the polarization in each phase attempted to align with its corresponding crystallographic directions. Fig. 5.6(b) illustrates the domain morphologies after a simulation of $150\Delta t$ time steps, within which 90° domain walls begin to form FT. This phenomenon arises because the polarization in neighboring domains is perpendicular to each other, configured head-to-tail. It is also demonstrated that the single domain in FR stabilizes once the unstable domain walls observed in Fig. 5.6(a) disappear.

An interesting observation from the comparison of microstructures in Figs.5.6(c) and (d) is the continuous transformation of the FR into the FT at the phase interface. This transformation leads to the extension and connection of 90° domain walls in the FT phase, as shown in Figs.5.6(d) and (e). Fig. 5.6(f) illustrates the equilibrium state, highlighting stable polarization directions with white thick arrows. Observations reveal that the entire region adopts an FT with a 90°-domain configuration in its minimum energy state, primarily due to the transformation of almost the entire FR into FT. This finding aligns with polycrystalline samples that predominantly exhibit a tetragonal structure, as observed in Ref. [150]. A high-density isoline of von Mises stresses at the equilibrium state is also depicted with white thin lines in Fig.5.6(f). Given the predominance of the FT phase in the single grain after the phase transformation, the stress distribution resembles that shown in Fig. 5.5(a).

Fig. 5.7 reveals the domain switching, the associated phase transformation, and the von Mises stresses when $|E_{\text{ext}}| = 10\,\text{kV/mm}$ is applied along the [100] direction (the red thick arrow) to the initial state in Fig. 5.7(a), which is a copy of Fig. 5.6(b)). Similarly to Fig. 5.6(f)), the white thick arrows in Fig. 5.7(a) represent the e polarization orientation in the tetragonal phase. Comparing Figs. 5.7(a) and (b) shows that the external electric field switched the dipoles in the tetragonal phase, causing the head-to-tail 90° domain configuration to disappear. This behavior can be explained by the plotted energy landscape of the pure FT in Fig. 5.3(c). Without an external stimulus, there are six equivalent energetic minima in the energy landscape, suggesting six polarization orientations with the same possibility toward six face centers. However,

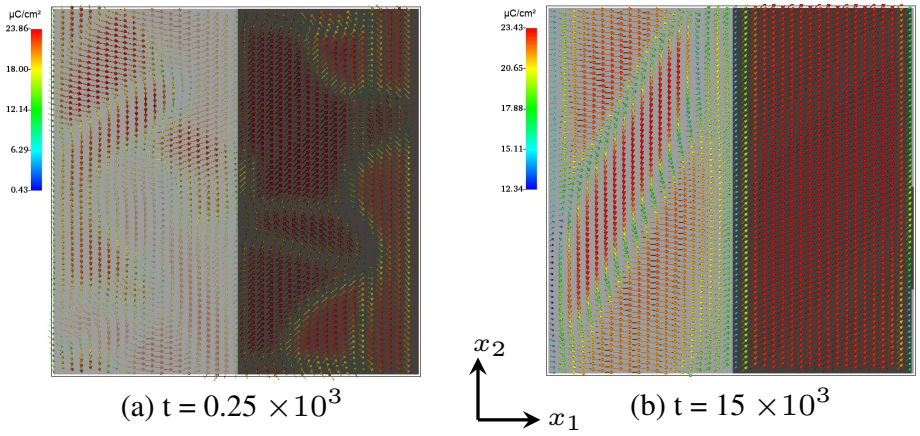

(a) t = 0.25 $\times 10^3$ (b) t = 15 $\times 10^3$

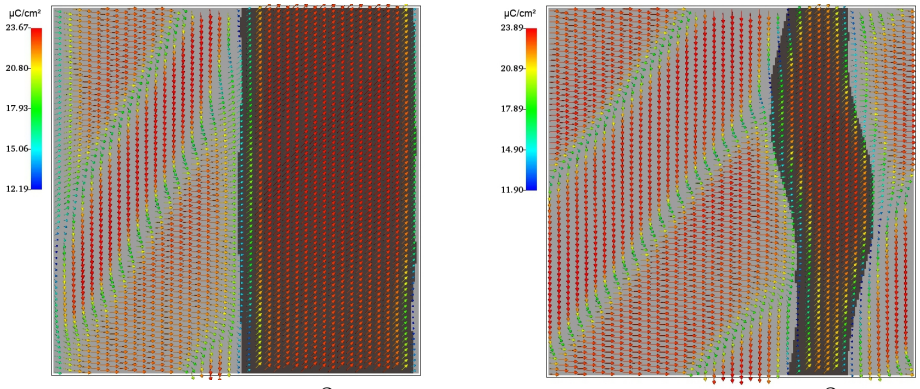

(c) t = 45 $\times 10^3$ (d) t = 400 $\times 10^3$

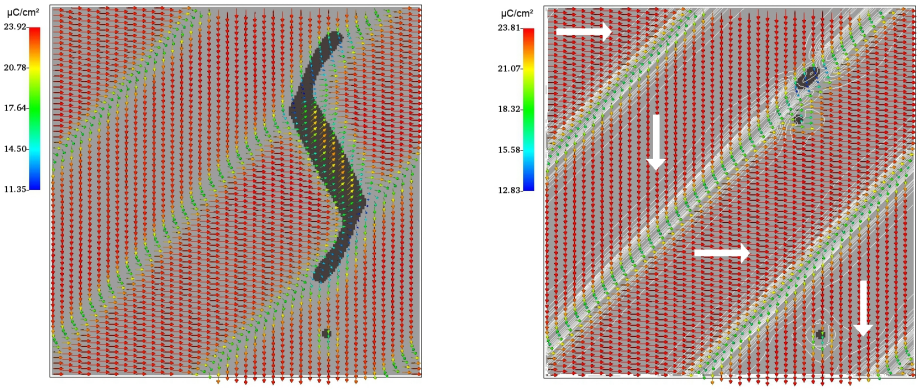

(e) t = 500 $\times 10^3$ (f) t = 600 $\times 10^3$

Figure 5.6.: Temporal evolution of domain structures and the phase transformations in a multiphase single crystal in the absence of an external electric field ($\boldsymbol{E}_{\text{ext}} = 0$). The thick white arrows in (f) indicate the polarization orientation in the stable state, while the thin white lines show the isolines of von Mises stresses. t represents the number of the simulated steps. Adapted from Ref. [15].

the energy landscape deforms with the application of external electric fields, leading to the reorientation of the polarization vector, as described in Ref. [146]. Therefore, dipoles in the FT are switched by $90°$, so as to align themselves with the induced field. Additionally, the polarization orientation in the FR remains unchanged when comparing Figs. 5.7(a) and (b). This is because the applied electric field in Fig. 5.7(a) favors the existing domains in the FR in the special cases of Fig. 5.7.

In addition to the polarization switching, it is noteworthy that the phase transformation from FR to FT occurred precisely at the phase interface, as shown in Fig. 5.7(c). Referring to the energy overlap depicted in Fig. 5.3(c), the induced electric field along its crystallographic direction creates a favorable condition for the driving force toward the FT. Moreover, experimental findings reported in Ref. [140] confirm that the activation energy for this phase transformation is sufficiently low around the phase boundary. Hence, the rhombohedral phase transitions to the tetragonal phase at the phase interface when induced by such an applied electric field. In addition, the observed polarization reorientation in the transferred FT along the induced electric field direction is consistent with the experiment [140]. Figs. 5.7(d) and (e) respectively depict the evolution after $50{\times}10^3$ and $100{\times}10^3$ time steps, suggesting that the microstructure evolution is a synergy between the polarization reorientation as well as the phase transformation, as expected. As can be seen in Fig. 5.7(f), the system reached the equilibrium after a simulation of $250{\times}10^3$ time steps, where almost the entire FR was transformed into FT. The evolution of the von Mises stresses also illustrates that the induced phase transformation helps to release the stresses.

The same external electric field, $|E_{\mathrm{ext}}| = 10\,\mathrm{kV/mm}$, was also applied along the [111] direction to the identical initial state. The temporal evolution of the microstructure is illustrated in Fig. 5.8, where Fig. 5.8(a) replicates Fig. 5.6(b). Similarly, a comparison of Figs. 5.8(a) and (b) demonstrates that polarization switching is initially activated by the applied electric field. As the existing polarization vector in the FR is parallel to the induced electric field, the magnitude of polarization increases without any reorientation in this phase. The $90°$ domain configurations form in the FT, as shown in Fig. 5.8(b). When the induced electric field is insufficient to switch the polarization to align with the external direction, the polarization of the FT is governed by its crystallographic direction and the external field. Consequently, the $90°$ domain structure, with the {110} domain wall plane in the FT, serves to minimize both elastic and electrostatic energies. Based on Figs. 5.8(b) to (f), it can be concluded that the phase transformation from FT to FR can be induced at the phase boundary when the $|E_{\mathrm{ext}}|$ is applied in a direction favorable to the FR. Immediately following the phase transformation, it is observed that the polarization tends to align with the direction of $|E_{\mathrm{ext}}|$. In contrast to the aforementioned simulation, the white isolines indicate that the gradient stresses cannot be released by the electric field applied along the [111] direction.

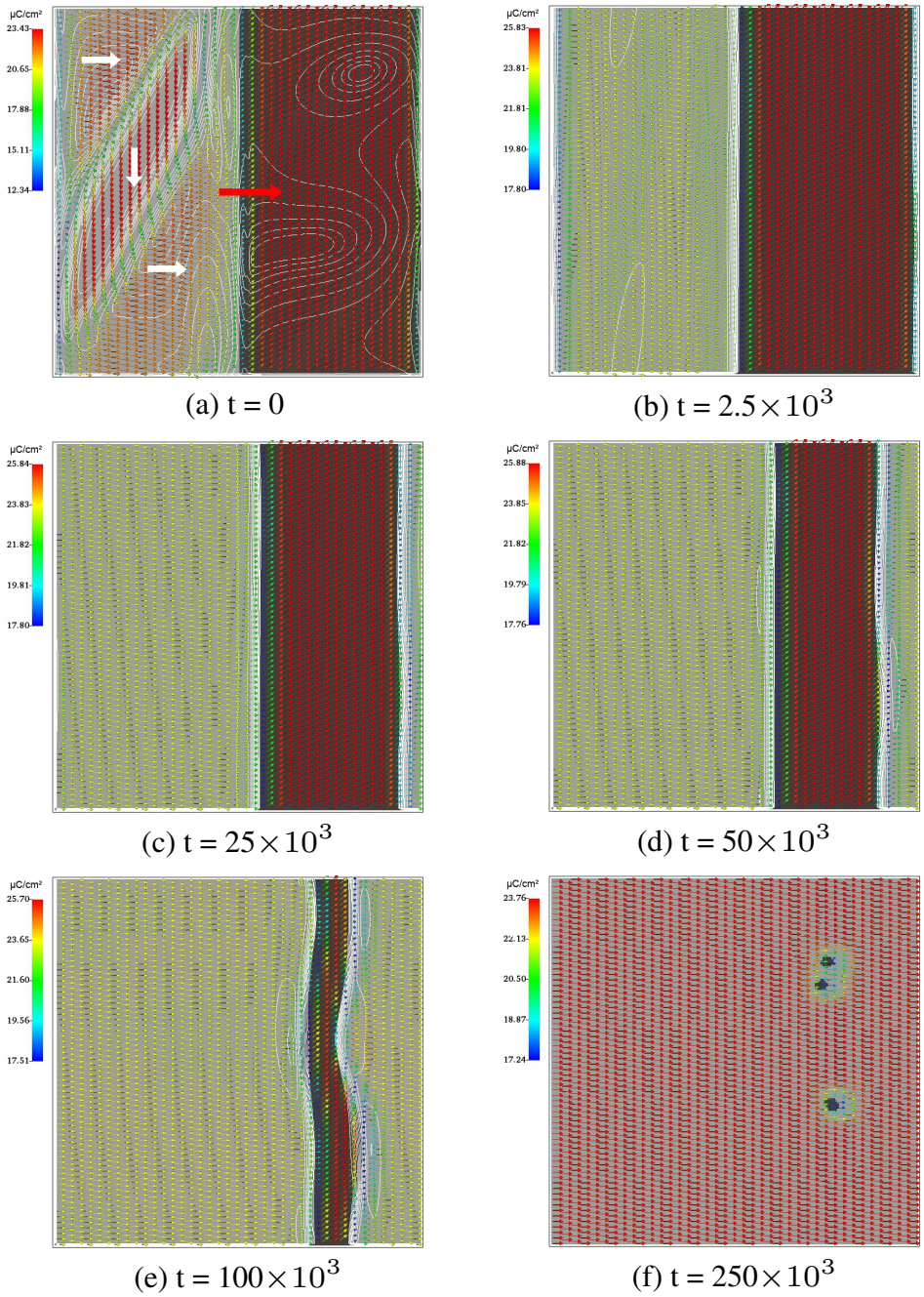

(a) t = 0 (b) t = 2.5×10^3

(c) t = 25×10^3 (d) t = 50×10^3

(e) t = 100×10^3 (f) t = 250×10^3

Figure 5.7.: Domain switching and the associated phase transformation over time in the multiphase single crystal under an external electric field of $|E_{\text{ext}}| = 10\,\text{kV/mm}$ (indicated by the red thick arrow) along the [100] direction. The white thick arrows in the FT demonstrate the polarization direction, while the white thin lines represent the isolines of von Mises stresses. t represents the simulation time step. Adapted from Ref. [15].

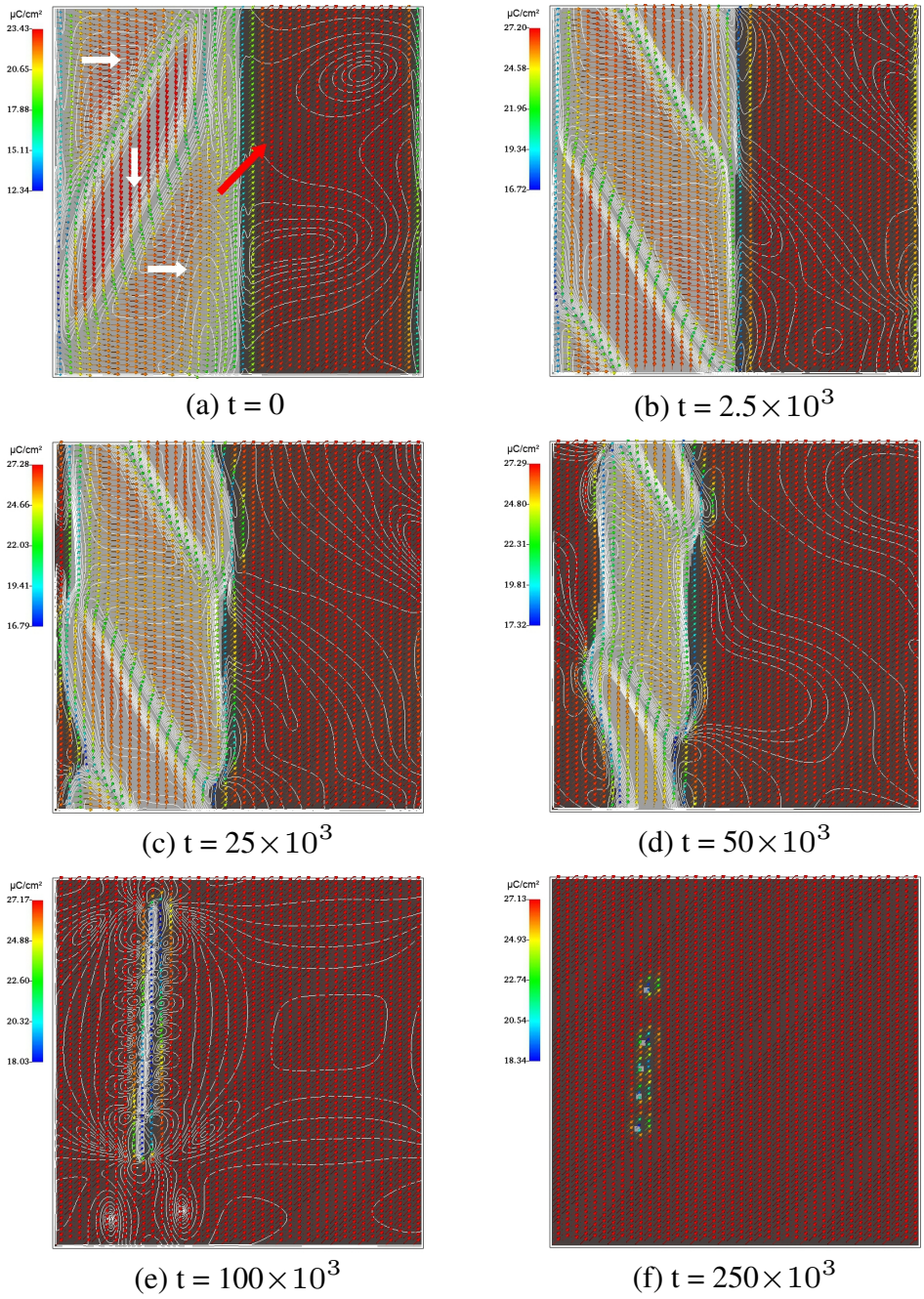

(a) t = 0 (b) t = 2.5×10^3

(c) t = 25×10^3 (d) t = 50×10^3

(e) t = 100×10^3 (f) t = 250×10^3

Figure 5.8.: Domain switching and the associated phase transformation over time in the multiphase single crystal under an external electric field of $|E_{\text{ext}}| = 10\,\text{kV/mm}$ (indicated by the red thick arrow) along the [111] direction. The white thick arrows in the FT demonstrate the polarization direction, while the white thin lines represent the isolines of von Mises stresses. t represents the simulation time step. Adapted from Ref. [15].

The phase transformation between the tetragonal and rhombohedral phases indeed depends on the applied electric field, as expected. In PIC 151, the activation energy for such phase transformations is sufficiently low to be induced by $|E_{\text{ext}}|$ as low as $10\,\text{kV/mm}$. Equilibrium state simulations indicate a strong tendency of the material to adopt tetragonal domain configurations, consistent with findings from experimental studies in Refs. [140, 150]. The simulations further demonstrate that the energy landscape supports stabilization of either tetragonal or rhombohedral phases, depending on the direction of the applied electric field as well. Specifically, applying the electric field along the tetragonal {100} direction stabilizes the FT, whereas applying it along the {111} direction enhances the stability of FR. These results validate Model I, including the distinct coefficients assigned to each phase.

5.4.2. Phase-field simulation of polycrystals

5.4.2.1. Domain structures formation and the associated phase transformation

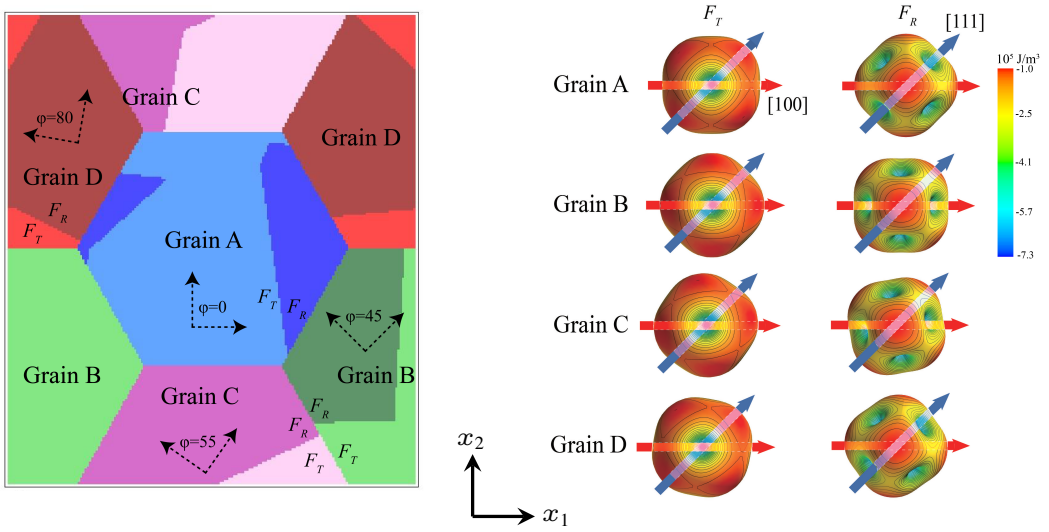

(a) The polycrystalline structure (b) Energy overlap

Figure 5.9.: (a) illustrates the simulated polycrystalline structure, in which A, B, C, and D denote four hexagonal grains. The light and dark colors within each grain represent the FT and FR, respectively. The dotted lines within each grain construct the local coordinates, in which φ represents the grain orientation. (b) shows the energy overlap of the FT and FR within each grain. Arrows indicate the applied electric field along the [100] and [111] directions of grain A, with the transparent region denoting the area pointed by the arrows, which is not visible. Adapted from Ref. [15].

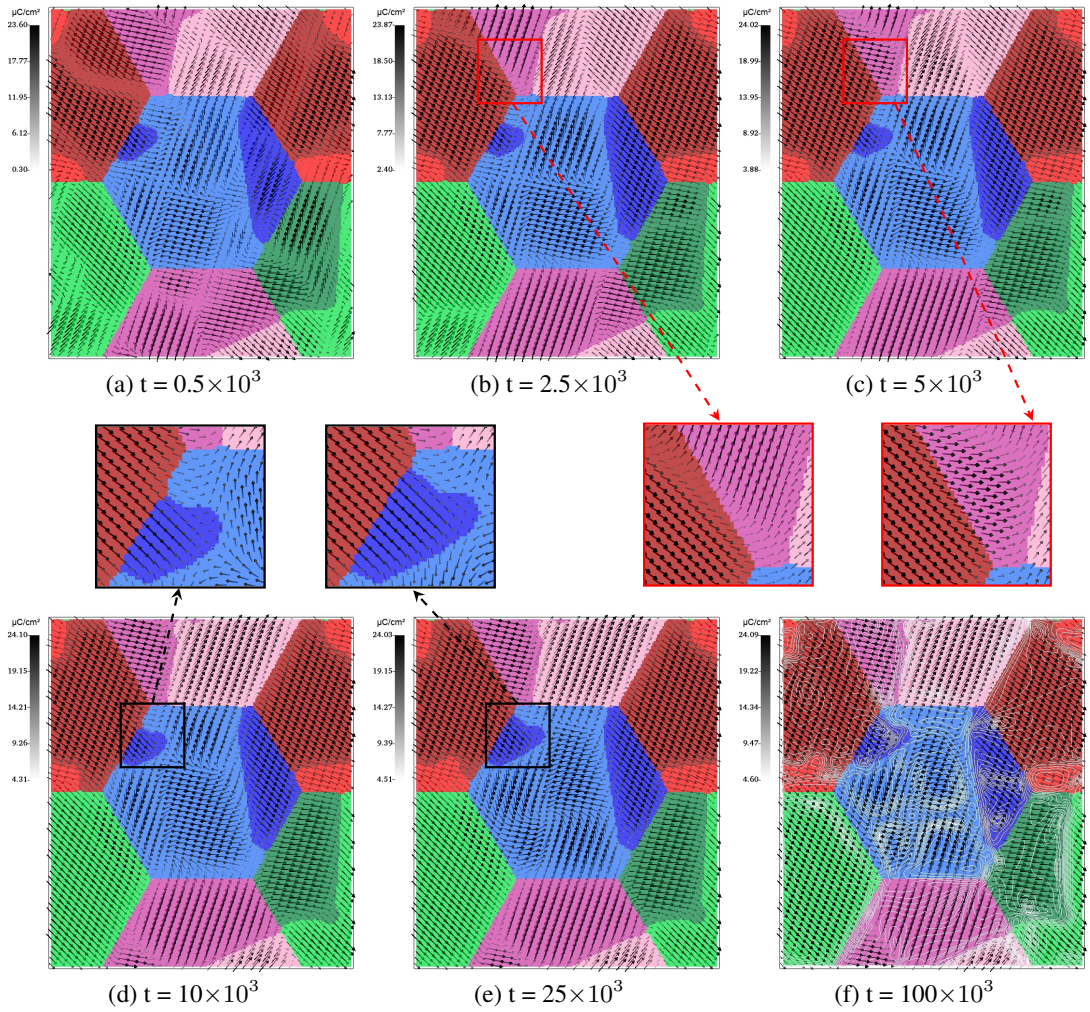

Figure 5.10.: The temporal evolution shows domain structure formation and the corresponding phase transformation in the polycrystalline system, with t representing the simulation time step. The white color in (f) displays the von Mises stress contour. Adapted from Ref. [15].

Fig. 5.9(a) illustrates a schematic diagram of the computed polycrystalline structure, which consists of four hexagonal grains (denoted as A, B, C, and D) with different orientations but equivalent dimensions. The light and dark colors within each grain respectively represent the FT and FR. The computed polycrystalline system consists of a limited range of crystals, taking the limitation of computation time into account. The grain orientations within each grain are denoted by φ, with the dotted line representing the local coordinates, within which the crystalline axes of the grains only rotate in the x_1x_2-plane. In order to establish a reference, the orientation of grain A was fixed at

zero. The rotation angles of the other grains, however, were assigned such that their polarization orientations of FT or FR attempted to align with the [100] or [111] direction of grain A (grain B), or they were set to random orientations (grains C and D).

To offer a theoretical explanation for the later calculated results, the energy landscape inside each grain, including the Landau potential energy density (f_{Landau}) and the elastic energy density under a stress-free condition ($f_{\mathrm{elast}}^{\mathrm{strain0}}$), was plotted, as depicted in Fig. 5.9(b). The coordinate in Fig. 5.9(b) refers to Fig. 5.9(a). In Fig. 5.9(b), the direction of the energetic minimum in each phase corresponds to its polarization orientation. Additionally, the arrows in the energy landscape (Fig. 5.9(b)) denote the external electric field induced along the [111] and [100] directions of grain A. The simulations begin to investigate the domain structure formations and the associated phase transformations with $|E_{\mathrm{ext}}| = 0$. After reaching the equilibrium state where both $\boldsymbol{P}$ and $\boldsymbol{\phi}$ no longer change, electric fields were applied along the [111] and [100] directions to investigate the response of the microstructure, respectively.

Fig. 5.10 illustrates the temporal evolution without an external stimulus, within which the color and orientation of the arrows represent the size and direction of the polarization, respectively. It is evident that domain nucleation inside each phase was observed after a simulation of $0.5{\times}10^3$ time steps, as shown in Fig. 5.10(a). After $2.5{\times}10^3$ and $5{\times}10^3$ time steps, as depicted in Figs. 5.10(b) and (c), one can find that dipoles inside each phase start to orient along their crystallographic direction. In the zoomed-in view of Figs. 5.10(b) and (c), it is also clear that polarizations within the neighboring grains attempt to align with each other, contributing to the release of the electric energy. For instance, the dipole rearrangement can be observed in the FR of grain C (pink), where the polarization vector can align closely with the adjacent FR in grain D (red).

Moreover, one can find that the FR and FT in the neighboring grains influence the polarization evolution of the FT in grain A (blue), suggesting the effect of neighboring grains on domain structures formation, as illustrated in Figs. 5.10(d) and (e). Based on the above description of the domain configurations, one can conclude that the formation of the domain structures in the polycrystalline PIC 151, which has multiple ferroelectric phases, results from the coupling between grain orientations and the crystalline structure of the corresponding ferroelectric phases. In addition to the polarization evolution, the phase transformation induced by a polar reorientation is suggested by a comparison of enlarged regions in Figs. 5.10(d) and (e). For example, complex domain morphologies form in the FT of Grain A as a result of the polarization evolution. During the process of the domain walls formation, the transformation from FT to FR occurs when dipoles reorient closely to the crystallographic direction of the FR. Similarly, one can observe the phase transformation of FR → FT in grain D (red). Finally, the system reaches the equilibrium state after an evolution of $100{\times}10^3$ time steps (Fig. 5.10(f)) with the cooperative motion of the polarization rotation and the phase transformation. At this energy minimum stage, complex domain structures with

different configurations are formed in grain A, while a single-type domain predominates in other grains due to computational limitations. The distribution of the von Mises stress at the stable state has also been shown using white isolines in Fig. 5.10(f). The grain boundary and grain orientation affect the distribution of the elastic strain, resulting in a more complicated distribution of stresses in the polycrystalline system being formed compared to Fig. 5.6(f).

5.4.2.2. Domain switching and the associated phase transformation

Fig. 5.11 shows the temporal evolution of the polarization switching and the related phase transformation when $|E_{\text{ext}}| = 30\,\text{kV/mm}$ is applied along the [111] direction. Fig. 5.11(a) depicts the initial state copied from Fig. 5.10(f), in which the white thick arrow indicates the induced electric field direction. Firstly, the domain morphologies after the computations of 10 and 50-time steps, shown in Figs. 5.11(b) and (c) demonstrate the ongoing polarization switching. This occurs because the imposed $\boldsymbol{E}_{\text{ext}}$ disrupts the energy minimum state of the polycrystalline system in Fig. 5.11(a), leading to the domain reorientation. In addition, the evolution process of the FR in grain B and the FT in grain A suggested that the polarization vector initially switches to the orientation of the applied electric field to release the external electric energy. When $\boldsymbol{E}_{\text{ext}}$ is insufficient to maintain this alignment, the polarization then aligns with its corresponding crystal direction. Based on the domain evolution of grains A (blue), B (green), and D (red) in Figs. 5.11 (b)-(c), it can also be seen that polarization reversal in the polycrystalline material occurs through the movement of the domain wall, which nucleates at the grain boundary. Such an observation is consistent with Refs.[82, 87]. To release both the elastic free energy and the electrostatic energy, the 90° domain walls form in the FT inside grain A under the induced electric field, as illustrated in a simulation of $2.5{\times}10^3$ time steps in Fig. 5.11(d). In general, the polarization in the polycrystalline system tends to align as closely with $\boldsymbol{E}_{\text{ext}}$ as permitted by its associated crystal symmetry to facilitate domain switching.

Apart from the domain switching, another interesting observation of the polycrystalline system shown in Fig. 5.11(d) is the bidirectional phase transformation, starting from the phase interface. For instance, the expected phase transformation from FT to FR due to the induced electric field in grain A is evident, as $\boldsymbol{E}_{\text{ext}}$ is applied exactly along the [111] direction of grain A (Fig. 5.9(b)). According to the energy landscape in Fig. 5.9(b), the orientation of $\boldsymbol{E}_{\text{ext}}$ is also close to the [111] direction of grain D, demonstrating the stability of grain D. Whereas, the phase transformation of FR → FT can be observed in grains B and C, indicating that such an electric field favors the corresponding [100] orientations in those grains. Similarly, this observation aligns with the energy landscape plotted in Fig. 5.9(b).

Figs. 5.11(e)-(f) depict the evolution of this bidirectional phase transformation, which is linked to the polarization reorientation in the polycrystalline material. It is easy

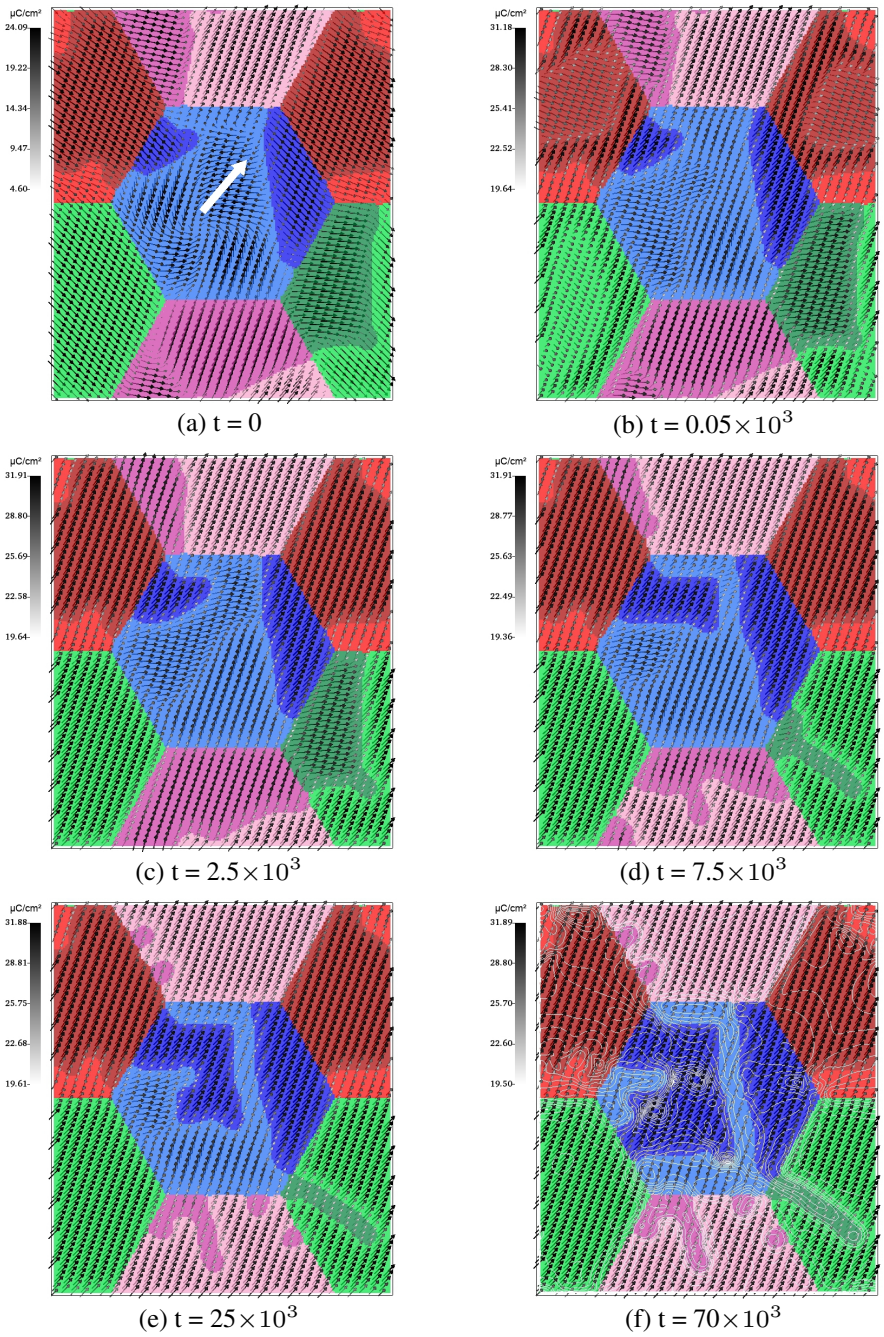

(a) t = 0 (b) t = 0.05×10^3

(c) t = 2.5×10^3 (d) t = 7.5×10^3

(e) t = 25×10^3 (f) t = 70×10^3

Figure 5.11.: Domain switching and the associated phase transformation over time in the polycrystalline PIC 151 material under an external electric field of $|E_{\text{ext}}| = 30\,\text{kV/mm}$ (indicated by the white thick arrow) along the [111] direction. The white thin lines in (f) represent contour plots of the von Mises stresses. t represents the simulation time step. Adapted from Ref. [15].

to find that the phase transformation results in the realignment of the polarization vector in the generated phase towards the orientation of the $\boldsymbol{E}_{\text{ext}}$. Compared to the single crystal simulation mentioned above, it is evident that the phase transformation induced by the external electric field is also dependent on the grain orientation in polycrystalline ferroelectrics with coexisting ferroelectric phases. Again, the white thin color in Fig. 5.11(f) represents the distribution of the von Mises stresses, with the highest stress densities mainly occurring at the phase boundaries inside each grain. This can be attributed to the polarization difference between ferroelectric phases in each grain.

To explore how the amplitude of the external electric field affects both the domain switching and the behavior of phase transformation, a higher electric field strength of $|E_{\text{ext}}| = 100\,\text{kV/mm}$ was applied to the same initial state, oriented along the [111] direction. The simulated results are illustrated in Fig. 5.12, showcasing both the polarization switching and the corresponding phase transformation with the same mechanism as discussed above. A comparison between Fig. 5.11 and Fig. 5.12 reveals that the increased field intensity results in a quicker response and a more thorough phase transformation. This observation is supported by Table 5.5, which details the phase volume fractions within each grain in the equilibrium state of each simulation. Therefore, it can be inferred that the amplitude of the electric field dictates the extent of the phase transformation.

Table 5.5.: Volume fractions of each phase within each grain at the stable state, measured in %. WE represent the simulated result of $E_{\text{ext}} = 0$; E1 and E2 represent the computed results with $|E_{\text{ext}}| = 30\,\text{kV/mm}$ and $|E_{\text{ext}}| = 100\,\text{kV/mm}$ applied along the [111] direction, respectively. E3 and E4 represent the computed results with $|E_{\text{ext}}| = 30\,\text{kV/mm}$ and $|E_{\text{ext}}| = 100\,\text{kV/mm}$ applied along the [100] direction, respectively. Adapted from Ref. [15].

Grain	Phase	WE	E1	E2	E3	E4
Grain A	FT	73.47	35.26	11.28	94.58	97.33
	FR	26.53	64.74	88.72	5.42	2.67
Grain B	FT	68.14	93.42	94.77	92.38	94.46
	FR	31.86	6.58	5.23	7.62	5.54
Grain C	FT	41.11	86.54	100.00	81.32	94.17
	FR	58.89	13.46	0.00	18.68	5.83
Grain D	FT	16.56	15.23	5.04	78.97	85.86
	FR	83.44	84.77	94.96	21.03	14.14

In order to investigate how the orientation of the induced electric fields influences both domain switching and phase transformation in the polycrystalline material, an electric field was applied to the same initial state along the [100] direction, with magni-

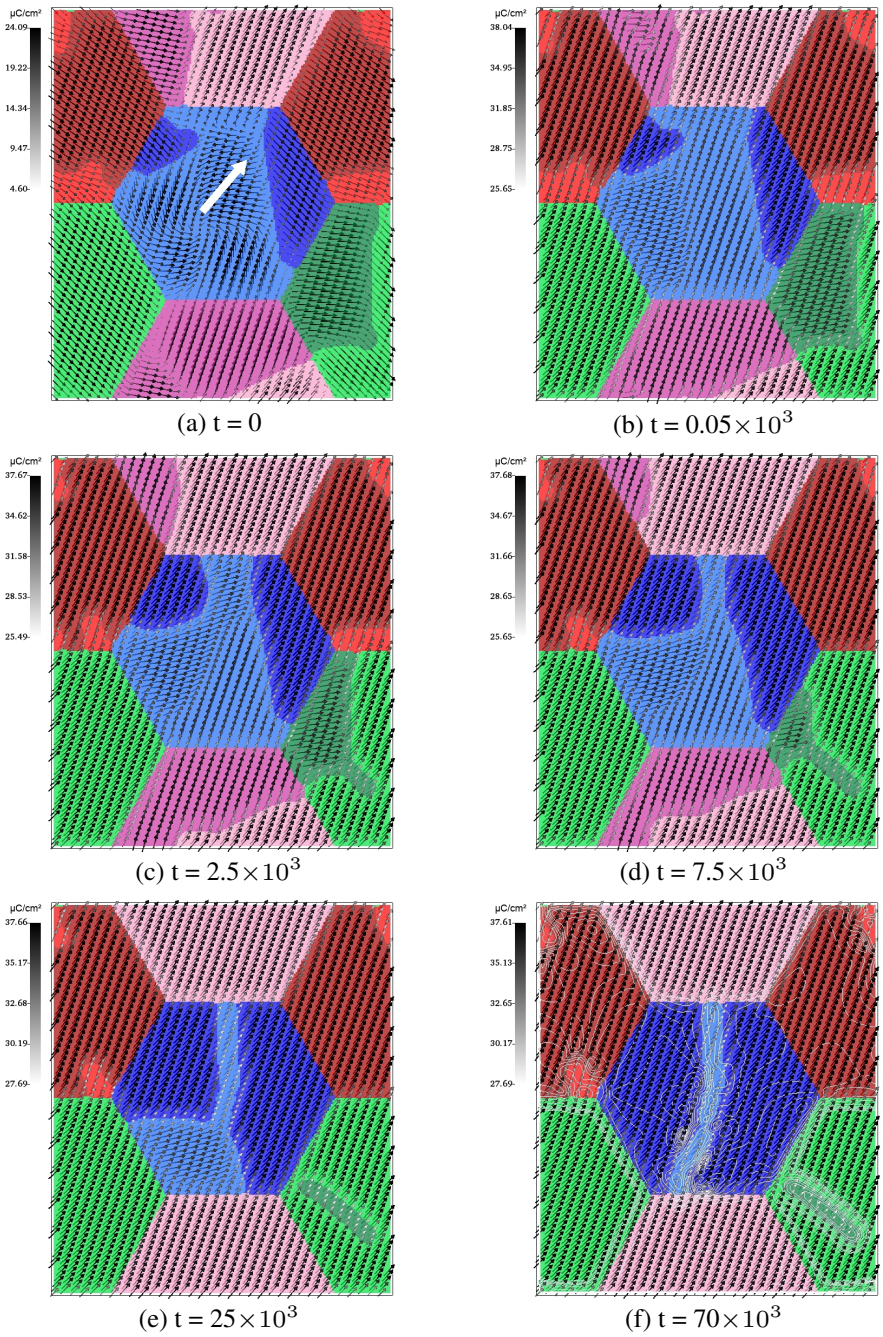

(a) t = 0 (b) t = 0.05×10^3

(c) t = 2.5×10^3 (d) t = 7.5×10^3

(e) t = 25×10^3 (f) t = 70×10^3

Figure 5.12.: Domain switching and the associated phase transformation over time in the polycrystalline PIC 151 material under an external electric field of $|E_{\text{ext}}| = 100\,\text{kV/mm}$ (indicated by the white thick arrow) along the [111] direction. The white thin lines in (f) represent contour plots of the von Mises stresses. t represents the simulation time step. Adapted from Ref. [15].

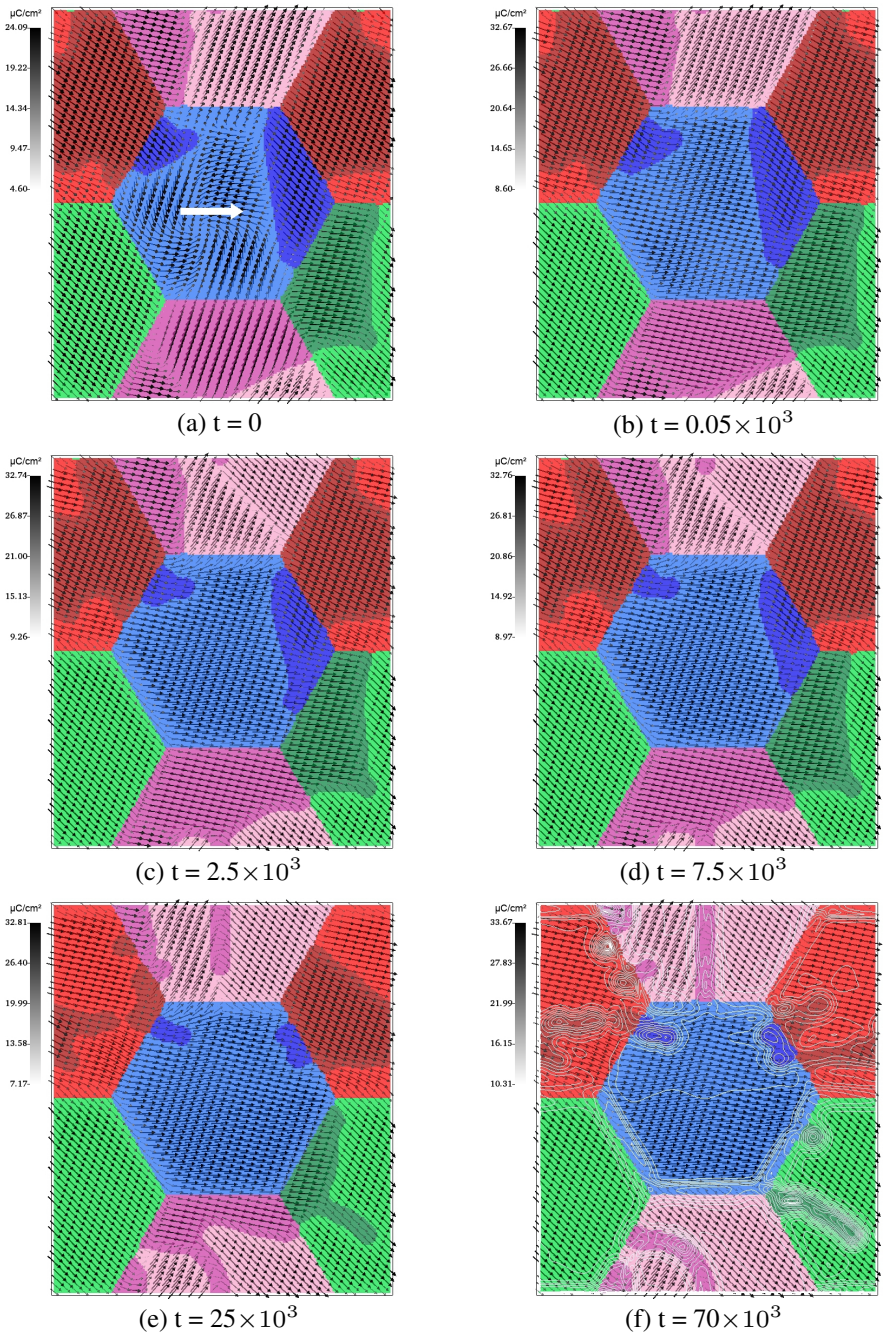

(a) t = 0 (b) t = 0.05×10^3

(c) t = 2.5×10^3 (d) t = 7.5×10^3

(e) t = 25×10^3 (f) t = 70×10^3

Figure 5.13.: Domain switching and the associated phase transformation over time in the polycrystalline PIC 151 material under an external electric field of $|E_{\text{ext}}| = 30\,\text{kV/mm}$ (indicated by the white thick arrow) along the [100] direction. The thin white lines in (f) represent contour plots of the von Mises stresses. t represents the simulation time step. Adapted from Ref. [15].

tudes of 30 and 100 $\mathrm{kV/mm}$, respectively. The corresponding temporal evolution of the domain structure and the phase transition can be observed in Fig. 5.13 and Fig. 5.14, respectively. Fig. 5.13(a) and Fig. 5.14(a) are the initial states. First of all, the polarization vectors of the tetragonal phase in grain A can be easily and completely switched to the [100] direction when the induced electric field is applied along the [100] direction, as depicted in Fig. 5.13(b) and Fig. 5.14(b). A comparison of Figs. 5.13(b) and 5.14(b) suggests that a large $|E_{\mathrm{ext}}|$ can manipulate the polarization vector to align more closely with the direction of the external electric field. Therefore, the polarization switching of FR in grain A propagates to the neighboring grain D, resulting in a corresponding polar change in FR.

As shown in Fig. 5.13(c) and Fig. 5.14(c), after a simulation of $2.5{\times}10^3$ time steps, the induced electric field generates a phase transformation of FR → FT, indicating that the applied electric field in the [100] direction favors FT for the entire polycrystalline system. Once again, this can be explained by the drawing energy surface in Fig. 5.9(b), where the external electric field along [100] direction directly aligns with or is close to the favorable direction of the tetragonal phase within each grain. The phase transformations with $|E_{\mathrm{ext}}|$ = 30 and 100 $\mathrm{kV/mm}$ are primarily illustrated in Figs. 5.13(d)-(f) and Figs. 5.14(d)-(f), respectively. Comparing these figures reveals a significant difference in the evolution of grain C (pink). Under a smaller induced electric field, the domains of FT in grain C were unable to switch completely, as FR nucleates and grows to separate FT into two regions. Thus, the 90° domain structure forms, which promotes the growth of FR along the domain wall, as shown in Figs. 5.13(d)-(f).

Furthermore, the volume fraction of FR and FT in Table 5.5 again shows that the microstructure can be manipulated with different imposed electric fields. In particular, the phase transformation is more gradual and less complete at lower field strengths (Figs. 5.13), while it is faster and more extensive at higher field strengths (Figs. 5.14). Moreover, PIC 151 material exhibits a predominantly tetragonal symmetry, which increases the tendency for FR to transform into FT. For instance, when the external electric field is applied along the [100] orientation of grain A, neighboring grains, such as B and C, which have crystallographic directions deviating from the tetragonal polar orientation, still predominately exhibit FT. This also suggests that when the direction of the induced electric field is ideal for one grain (grain A in this case), the domain switching from complex domain structures to a single domain state may affect the neighboring grains with less ideal grain orientations.

To sum up, the simulated results discussed above describe the mechanisms of domain formation, domain switching, and their associated phase transformation in polycrystalline ferroelectrics with multiple ferroelectric phases under different electric fields. The formation of domain structures results from the interaction between the crystallographic orientations of the ferroelectric phases, the orientations of the grains, and the accompanying phase transformation processes. With the application of external

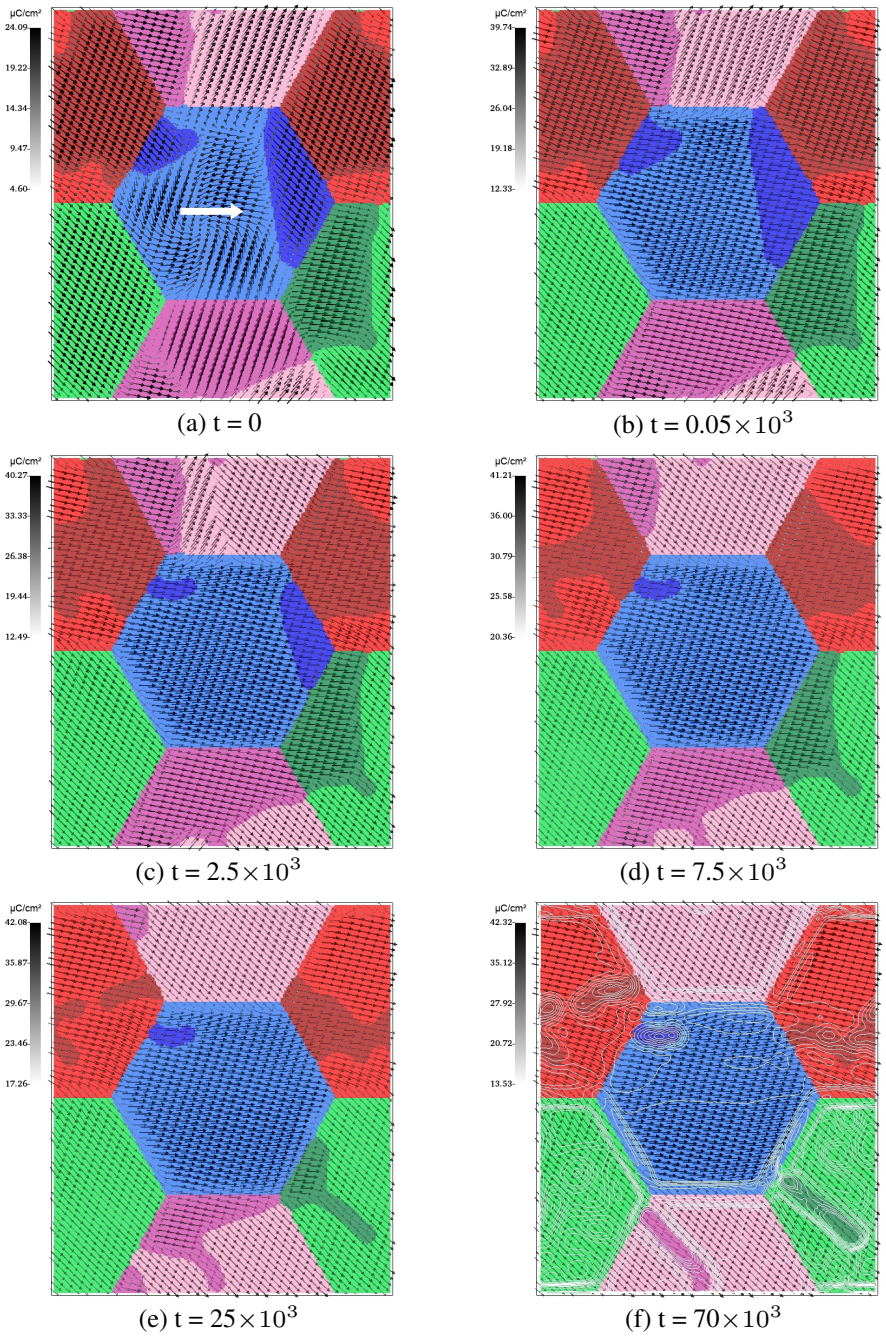

(a) t = 0 (b) t = 0.05×10^3

(c) t = 2.5×10^3 (d) t = 7.5×10^3

(e) t = 25×10^3 (f) t = 70×10^3

Figure 5.14.: Domain switching and the associated phase transformation over time in the polycrystalline PIC 151 material under an external electric field of $|E_{\text{ext}}| = 100\,\text{kV/mm}$ (indicated by the white thick arrow) along the [100] direction. The white thin lines in (f) represent contour plots of the von Mises stresses. t represents the simulation time step. Adapted from Ref. [15].

electric fields, domain switching is always the first response, significantly dependent upon the size and direction of the imposed electric field. For example, the polarization vector can be aligned with the orientation of the applied electric field when it reaches a suitable magnitude. Following domain switching, the induced phase transformation occurs at the phase or grain boundary. In particular, the observed bidirectional phase transformation suggests that the phase transition between ferroelectric phases is determined by both induced electric fields and grain orientations. This has already been predicted by experimental results from Refs. [140, 150, 151]. On a local scale, however, direct observation of these processes is still lacking. The phase-field simulation results in the current work provide insight into the local processes and mechanisms involved in the response of materials to different imposed electric fields. It is also evident that the magnitude of the external electric field plays a significant role in controlling the degree of phase transformation, specifically in manipulating the residual volume fraction of each phase. While the minor phase of PIC 151 (FR) can only be stabilized with a high electric field, the major phase (FT) stabilizes early to a large fraction at a lower applied electric field. This also indicates a preferential phase fraction under the influence of an induced electric field. The simulated results have implications for the fundamental understanding of the role of the applied field on the domain structure and phase transformation, providing valuable understanding for the development of polycrystalline ferroelectric materials with phase coexistence.

5.5. Conclusions

Model I, which integrates the TDGL with the general multiphase phase-field functional, has been employed in this chapter to investigate the domain structure and associated phase transformations in ferroelectric materials exhibiting ferroelectric phase coexistence. To determine the phase-dependent coefficients, i.e., the dielectric stiffness and electrostrictive stiffness coefficients, a numerical energy-overlap approach was designed based on the coefficients identified for phase coexistence. The reliability of the phase-dependent parameters and the practicality of Model I was validated by conducting single crystal simulations with both single and multiple phases. The domain structures and associated phase transformations under different external electric fields have been investigated in the polycrystalline material. It was observed that the equilibrium of a polycrystalline system depends on the cooperative interplay between polarization evolution and phase transformation when without any induced external fields. Simulations conducted under different external-electric-field values demonstrate externally induced polarization switching as well as phase transformation. In general, the polarization switching firstly occurs under an external electric field, followed by the corresponding phase transformation at the phase interface or grain boundary. It has been shown that the phase transformation varies depending on the grain orientations

when an electric field is applied. It was also observed that the magnitude of the induced electric field significantly influences both the domain structure and the proportion of the phase volume fraction.

6. Computing domain structures in bulk ferroelectrics using Model II

6.1. Introduction

Research employing the multiphase-field approach to analyze ferroelectric materials has increased in recent years [15, 152–159]. For instance, Torres *et al.* has developed a multiphase-field model that couples four Allen-Cahn-type formulas to study the transformation kinetics as well as domain structures for ferroelectric materials [152–155]. This model has been used to study the mechanisms responsible for the coexisting ferroelectric phases and the correspondingly enhanced electromechanical properties found in experiments performed near the polymorphic phase boundary in barium zirconate titanate-barium calcium titanate. It enables a thermodynamically correct and more accurate analysis near the inter-ferroelectric phase transitions, as it incorporates the homogeneous free energy density of the individual ferroelectric phases with phase-dependent Landau coefficients. However, the model proposed by Torres *et al.* ignored the mechanical field, which influences the formation of non-$180°$ ferroelastic domain walls. Besides, the straightforward coupling of the Allen-Cahn equations confines the calculations to a single crystal in one or two spatial dimensions [153].

As outlined in Chapter 5, Model I was further developed through integrating the TDGL equation with the multiphase-field approach in the work [15]. Compared with the work of Torres *et al.*, this model extends the numerical calculations to polycrystalline ferroelectric materials with multiple ferroelectric phases in arbitrary dimensions, in which it can also accurately describe and quantitatively compute the contribution of the mechanical field on domain structures. By using this new model, the phase transformation between FT and FR along with the corresponding domain structures have been studied for both the single- and polycrystalline PIC 151 material. Apart from these, the multiphase-field method has also demonstrated broader applicability beyond perovskite ferroelectric materials. For example, Sugathan *et al.* coupled the multiphase-field approach proposed by Steinbach *et al.* in Ref. [77] with TDGL model to compute the switching behavior of polycrystalline $Hf_{1-x}Zr_xO_2$ thin films, while Zhu *et al.* [156], Li *et al.* [157], Chen *et al.* [158], and others [159] employed it to investigate domain structures in different Hf-based ferroelectric materials.

However, despite the primary focus of these works being on distinguishing paraelectric/ferroelectric phases or coexisting ferroelectric phases, the domain formation and switching are still controlled by the TDGL model. That is, domain structures are computed by evolving the polarization vector. Interestingly, in order to capture the nonlinear dynamic motions of domain walls, Guin *et al.* [128] have also proposed a novel model based on the multiphase-field approach. In contrast to the conventional approach of using polarization as the order parameter, their model employs the possible polarization states within the ferroelectric phase as phase-field variables. As a result, the domain structure is determined by the transformation and evolution of the phase-field variables. Nevertheless, contributions from the mechanical field have been overlooked in their work. Possessing the same concept, Model II was created to ferroelectric materials. In contrast to Ref. [128], Model II employs a multi-obstacle potential in conjunction with a distinct gradient energy formulation to quantify the interfacial energy, so as to capture the interphase profile. In addition, the mechanical field is evolved and solved using the jump condition technique described in Refs. [132, 133, 160]. This chapter presents an application of Model II to study the BTO material, with reference to the published results presented in Ref. [16].

6.2. Numerical simulation setup

Simulations were conducted in Pace3D. An overview of the computing process is shown in Fig. 6.1. A finite difference algorithm with an explicit forward Euler scheme is used to solve the phase-field evolution equation (Eq. (4.10)), so as to determine the domain structure at room temperature (T = $300\,\mathrm{K}$). The mechanical equilibrium condition (Eq. (3.24)) is subsequently solved implicitly in every time step after solving Eq. (4.10). The reader is recommended to [132, 161, 162] for detailed insights into this procedure. In parallel, the electrostatic equilibrium condition of Eq. 4.9 is solved using the conjugate gradient approach. The Voronoi tessellation was used to create the calculated structures for both single-crystal and polycrystalline systems. Regardless of the system size, the computed region was discretized into cells with uniform dimensions of $\Delta x_1 = \Delta x_2 = \Delta x_3 = 0.5\,\mathrm{nm}$. Using the MPI standard, the computational cells were decomposed in both the x_1- and x_2-directions to reduce simulation time and achieve high computational efficiency.

The ferroelectric phase in BTO of this work was limited to the tetragonal structure. One can also investigate other ferroelectric structures, such as rhombohedral, monoclinic, orthorhombic, and others, by defining their corresponding polarization variants. To ensure numerical stability, the diffuse interface width parameter ϵ was set as $4\Delta x_1$ with the application of a multi-obstacle-type potential. This parameter yields the interface width as $L \approx 4.9\,\mathrm{nm}$ based on Eq. (2.57). Given that L aligns with the observed $90°$ domain wall widths in BTO, which ranges from $2\,\mathrm{nm}$ to $25\,\mathrm{nm}$, it can

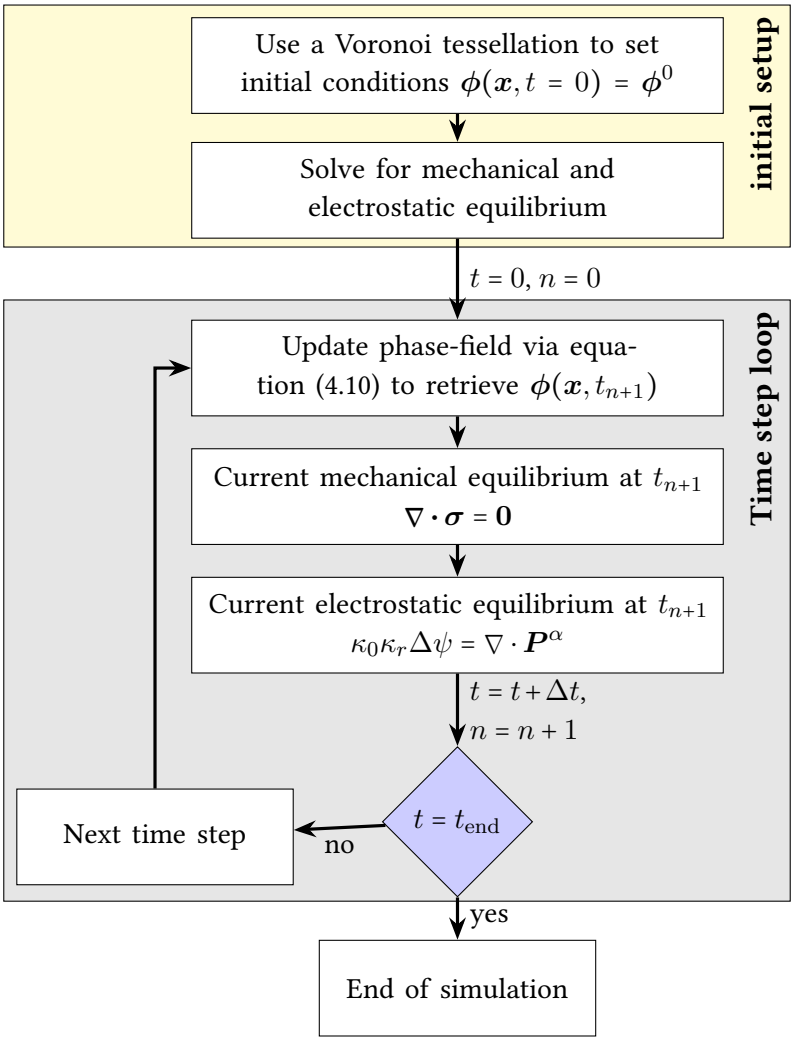

Figure 6.1.: Overview of the solution procedure for the numerical simulations.

be concluded that such an interfacial width is physically meaningful. Furthermore, to convey a physical implication rather than a computational input coefficient, the interfacial energy $\gamma^{\alpha\beta}$ was set as the $180°$ domain wall energy in $1\,\mathrm{nm}$, denoted by:

$$\gamma^{\alpha\beta} = 1.26|\alpha_1|l_0 P_0^2, \tag{6.1}$$

relying on Ref. [82]. α_1 in Eq. (6.1) represents the first-order dielectric stiffness at room temperature. l_0 is calculated as:

$$l_0 = \sqrt{G_{11}/(0.6|\alpha_1|)} \tag{6.2}$$

with G_{11} the gradient coefficient. P_0 is the spontaneous polarization with a value of $26\,\mu\mathrm{C/cm^2}$, obtained from Ref. [163]. In order to solve the Poisson formula, the

Table 6.1.: The phase-field parameters and material coefficients used in the current simulation. Adapted from Ref. [16].

Material Coefficients	Symbol	Value	Unit
Dielectric stiffness	α_1	(T-381)*3.34	$10^5 \cdot [\mathrm{m/F}]$
Interfacial length parameter	$\epsilon/\Delta x$	4	-
Interfacial energy	$\gamma_{\alpha\beta}$	0.01	$\mathrm{J/m^2}$
-	γ_α^c	0.01	$\mathrm{J/m^2}$
Elastic tensor	$\mathcal{C}_{11}$	27.50	$10^{10}\cdot[\mathrm{N/m^2}]$
	$\mathcal{C}_{12}$	17.90	$10^{10}\cdot[\mathrm{N/m^2}]$
	$\mathcal{C}_{44}$	4.80	$10^{10}\cdot[\mathrm{N/m^2}]$
Electrostrictive tensor	$\mathcal{Q}_{11}$	11.00	$10^{-2}\cdot[\mathrm{m^4/C^2}]$
	$\mathcal{Q}_{12}$	4.50	$10^{-2}\cdot[\mathrm{m^4/C^2}]$
	$\mathcal{Q}_{44}$	7.75	$10^{-2}\cdot[\mathrm{m^4/C^2}]$
Gradient coefficient	G_{11}	51	$10^{-11} \cdot [\mathrm{N\,m^4/C^2}]$

Values of dielectric stiffness, elastic tensor, and Electrostrictive tensor coefficients are taken from Ref. [97]

background dielectric constant was set to a value of 50. γ_α^c, which scales the compensate of the curvature effect in Eq. (4.17), was set to the same value as $\gamma^{\alpha\beta}$. As there is no reliable data for capturing the kinetics of the tetragonal domain walls in BTO, the discrete-time step width was set as Δt^*=1 and the mobility $M^{\alpha\beta}$ was determined to ensure numerical stability. In general, the dimensionless value of mobility coefficient $M^{\alpha\beta}$ between ferroelectric variants was set to one. In the case where $M^{\alpha\beta}$ represents the mobility between grains, it was set as zero because grains are immobilized in BTO at room temperature. For clarity, the simulated parameters are listed in Table 6.1. To achieve high computational efficiency and increase accuracy, the input data is transformed into a dimensionless form, with the main dimensionless formulas given by:

$$\begin{aligned} \mathcal{Q}^*_{ijkl} &= \mathcal{Q}_{ijkl} P_0^2, \\ \mathcal{C}^*_{ijkl} &= \frac{\mathcal{C}_{ijkl}}{|\alpha_1 P_0^2|}, \\ \kappa_0^* &= \kappa_0 \cdot |\alpha_1|. \end{aligned} \tag{6.3}$$

6.3. Phase-field simulation in a single-crystal system

6.3.1. Domain structures formation

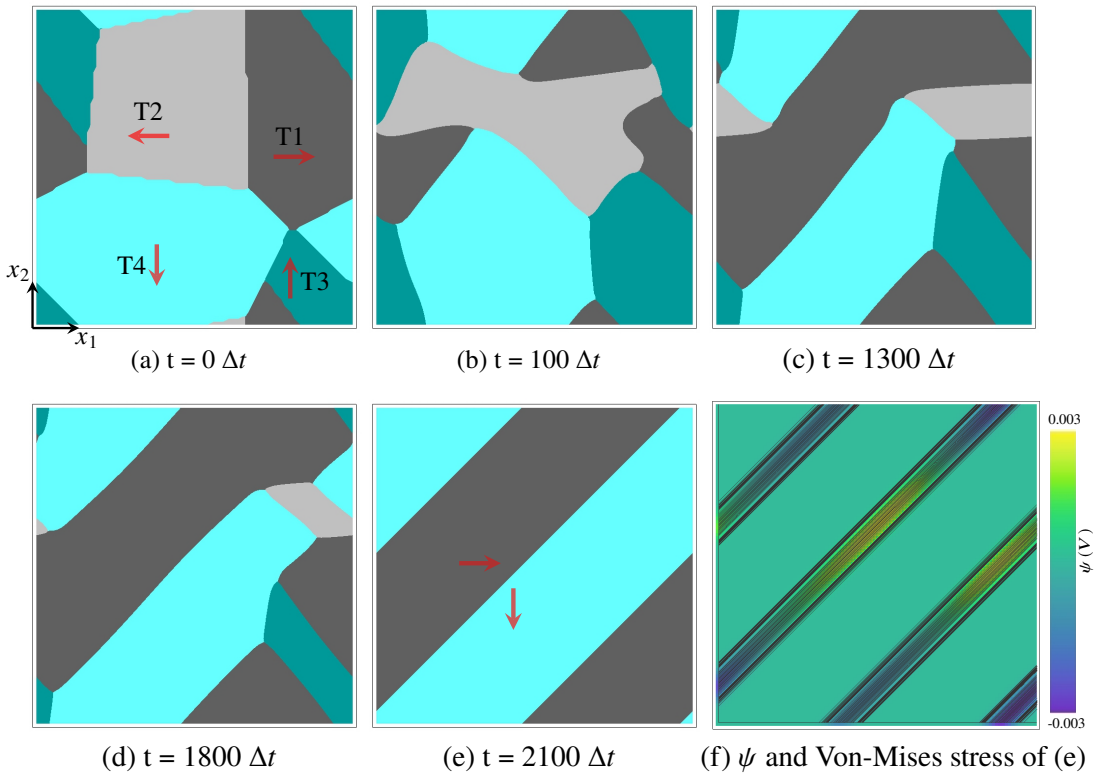

(a) t = 0 Δt (b) t = 100 Δt (c) t = 1300 Δt

(d) t = 1800 Δt (e) t = 2100 Δt (f) ψ and Von-Mises stress of (e)

Figure 6.2.: (a)represents the initial configuration of the quasi-2D single crystal, while (b-e) illustrates the temporal evolution of domain structure formation. (f) illustrates the distribution of the von Mises stress (black lines) and the electric potential ψ at the equilibrium state ($t = 2100\Delta t$). Red arrows represent the polarization orientation of each variant. Adapted from Ref. [16].

To achieve computational convenience, the current work mainly focuses on quasi-2D simulations using 100×100×1 cells to illustrate the domain structures formation and the response of domain walls to an external field. Additionally, to validate the dimensional extension of the model, a 3D calculation of a single crystal with 100×100×100 voxels was further performed, as shown in Fig. 6.4. At the start of the simulations, the domain structure within a single grain was calculated without applying any external field, as shown in Fig. 6.2, with periodic boundary conditions employed to solve all fields. Fig. 6.2(a) demonstrates the initialization of the quasi-2D single crystal, in which four tetragonal polarization variants randomly occupy the computational area. The red

arrows inside each variant represent their corresponding orientation, with each variant represented by a dark color if its polarization vector is aligned with the positive direction of the axis, and vice versa. Since all variants in the quasi-2D case can be presented in the initial state, the phase-field governing equation (Eq.(4.10)) is solved without activating the nucleation function, so as to reduce the computational time.

The main process for the domain formation is shown in Figs. 6.2(b)-(e). Firstly, the system naturally forms head-to-tail domain walls by consuming T3 and T2 variants to remove the initially assigned charged domain configurations (head-to-head or tail-to-tail domain structures), thereby releasing the depolarization field (Figs. 6.2(b)-(d)). Fig. 6.2(e) illustrates the equilibrium profile after 2100 time steps, where 90° domain walls form with {100} twin planes. This suggests the contribution of the strain energy to the formation of the domain structures. The simulated 90° domain walls with head-to-tail configurations are in agreement with Refs. [81] and [15], where the simulation was conducted using a TDGL framework. This provides the first reliable validation of Model II. Fig. 6.2(f) additionally shows the distribution of ψ (color map) as well as the contours of the von Mises stresses (black lines) at the equilibrium state, reflecting the effect of the electrostatic energy and elastic energy, respectively. It is clear that both energies are uniform throughout the domain, with variations at the domain walls.

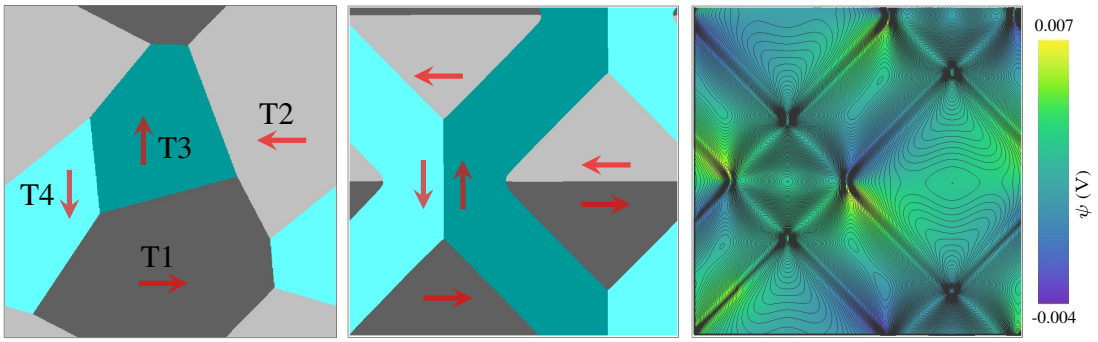

(a) Initial setup (b) Equilibrium state (c) ψ and Von Mises stress of (b)

Figure 6.3.: (a) is the initial setup of a 2D single crystal with 500×500×1 cells. (b) represents the domain configurations of (a) at the equilibrium state. Red arrows in (a) and (b) represent the direction of the polarization. (c) illustrates the electric potential ψ and the distribution of the von Mises stress (shown as black thin lines) of (b). Adapted from Ref. [16].

It should be addressed that in addition to the simple 90° lamellar domain structures, complex domain configurations can also be obtained where both 90°and180° domain walls are stable. These complex structures depend on the interaction between elastic and electric energies, as well as on the original setup or computed geometry. For instance, Fig. 6.3 depicts the simulated results of a single quasi-2D tetragonal crystal

with $500 \times 500 \times 1$ cells. With different sizes and initial setup compared to Fig. 6.2(a), both the $90°$ ferroelastic domain walls and the $180°$ ferroelectric domains coexist at the equilibrium state (Fig. 6.3(b)), starting from the initial state shown in Fig. 6.3(a). This leads to more intricate distributions of von Mises stress and a complex variation in electric potential (Fig. 6.3(c)).

The first column of Fig. 6.4 illustrates the initial setup, the computed domain structures at the equilibrium state as well as the associated ε_{11} and ε_{33} for a 3D single crystal. The polarization direction for each variant corresponds to Fig. 4.1(d). Similarly, the dark colors indicate tetragonal variants with the polarization direction aligned along the positive x_1, x_2, or x_3-axis, while the light colors correspond to variants with the polar vector in the opposite direction. The computed domain structure is configured by head-to-tail $90°$ domain walls, constructed by T2 and T6 variants. In the 3D tetragonal single crystal, the domain structure and distribution of total strain suggest that strain energy predominantly influences the formation of the domain structure. To provide insight into the formation mechanism of the domain configuration in a 3D system, the temporal evolution of the morphologies across three sectional planes (x_1x_2, x_1x_3, and x_2x_3) is also illustrated from the second column to the fourth column in Fig. 6.4. In order to ensure a consistent point of comparison, the sections in the x_1x_2, x_1x_3, and x_2x_3 planes are centered at the midpoint of the axis that is perpendicular to each plane. Evolution from 0 to 100 steps in each section indicates the influence of the depolarization field to dismiss the tail-to-tail and head-to-head charged domain walls. The notable observation of the unfilled T6 variant appearing at the boundary in the x_1x_3 plane suggests that the domain structure formation in one plane is influenced by interactions with other domains. With time, the $90°$ domain structure stabilizes in each plane, leading to the formation of $90°$ ferroelastic domain walls within the whole 3D single crystal.

During the simulation at $t = 100\Delta t$, one may observe the emergence of a curved interface, characterized by a curvature domain wall connecting the T4 and T6 variants in the x_1x_2-plane, located between the highlighted red circles. The presence of such a curved interface could be attributed to the reduced resolution in 3D simulations, particularly around the triple junction where the phase interfaces could intersect at a $120°$ angle and advance accordingly because of the associated driving force. As a result, the phase interface that bridges two triple junctions could be affected by two different directions, leading to the manifestation of curvature in the domain wall during the simulation.

6.3.2. Domain switching induced by an electric field

The domain switching under an external electric field was conducted, so as to further validate the practical applicability of the current model in depicting the behavior of ferroelectric materials. Switching domain in ferroelectrics under induced electric field

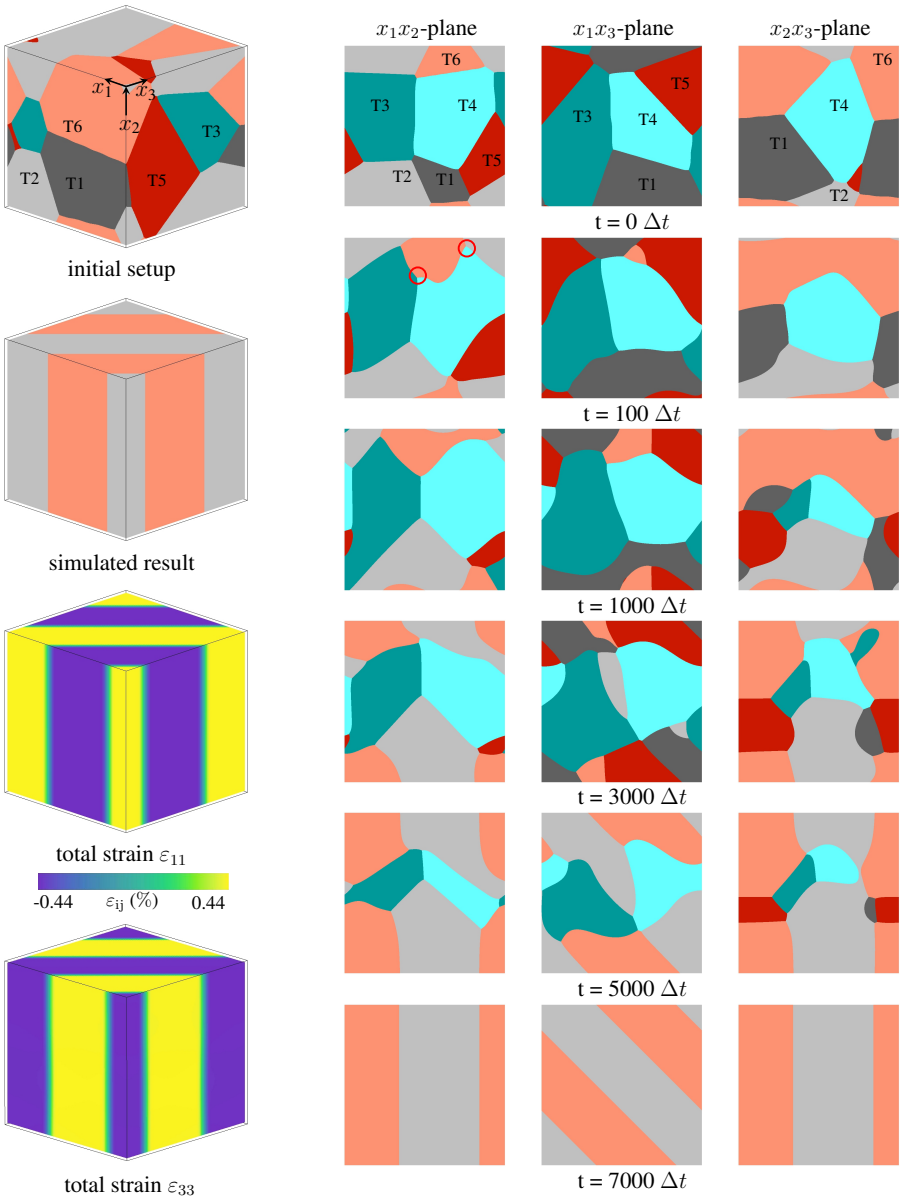

Figure 6.4.: The simulation of the 3D single crystal with $100 \times 100 \times 100$ cells. The initial setup, the computed domain structure and strain ε_{11} and ε_{33} are illustrated in the first column. The temporal evolution of the x_1x_2-plane at $x_3 = 50$, the x_1x_3-plane at $x_2 = 50$, and the x_2x_3-plane at $x_1 = 50$ are shown in the second, third, and fourth columns, respectively. The polarization orientation for each variant is consistent with Fig. 4.1(d). Adapted from Ref. [16].

can be categorized into three primary stages [164]: (1) domain nucleation aligns its

polarization direction with an imposed electric field, typically at interfaces or defects where local free energy is elevated; (2) the high energy at the leading edge of the newly formed and unstable charged domain results in rapid propagation in the induced electric field to release the depolarization field; meanwhile, (3) lateral domain growth perpendicular to the imposed electric field is facilitated by lateral movement of the neutral domain wall. That is, domain switching comprises nucleation, growth, and the movement of the corresponding domain walls. In order to simulate these processes using Model II, the noise term £ in Eq. (4.10) is applied at every fiftieth-time step, following a uniform distribution for the initial 1000 iteration steps. Likewise, periodic boundary conditions are implemented on all sides to solve the phase field, electric field, and mechanical field.

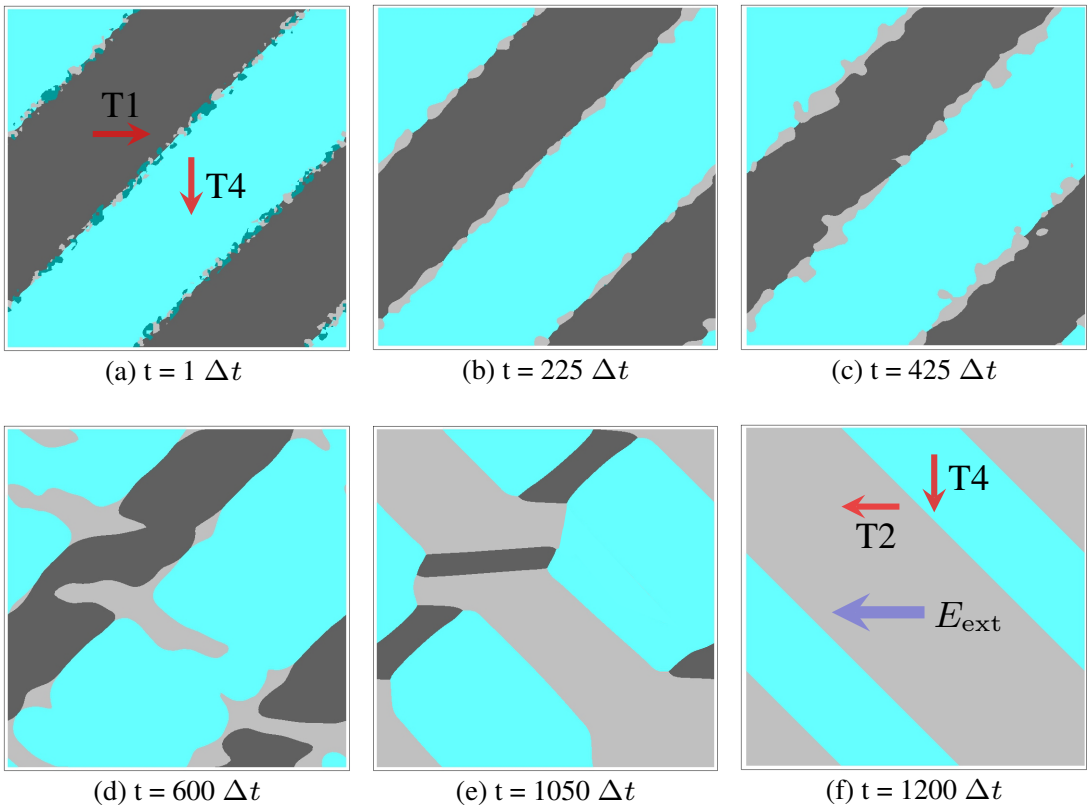

(a) t = 1 Δt (b) t = 225 Δt (c) t = 425 Δt

(d) t = 600 Δt (e) t = 1050 Δt (f) t = 1200 Δt

Figure 6.5.: Domain switching when E^*_{ext} was induced along the direction of T2 variant ($[\bar{1}00]$ direction), in which (a)-(f) shows the temporal evolution. Red arrows represent the associated polarization orientation within each variant and the blue arrow in (f) depicts the direction of E^*_{ext}. Adapted from Ref. [16].

Fig. 6.5 illustrates the simulated results when inducing the dimensionless electric field $E^*_{\text{ext}} = 1$ ($|E_{\text{ext}}| = E^*_{\text{ext}}|\alpha_1|P_0 \times 10^6\,\text{kV/mm}$) to the equilibrium profile shown in

Fig. 6.2(e), along the direction of T2 variant ($[\bar{1}00]$-orientation). Due to the inclusion of the noise term £, T2 and T3 appear initially and temporarily in small quantities at the binary T1-T4 interface, as depicted in Fig. 6.5(a). The growth of the new phase depends on the energy dynamics of the system. If the new phase is energetically favorable, it may overcome the energy barrier to growth. Otherwise, the introduced disturbances typically dissipate within a few time steps. As a result, T2 grows while T3 disappears in Figs. 6.5(b) and (c). This approach improves simulation efficiency and enables precise computation of all interpolated quantities. The choice of the interval between two noise steps plays a significant role during the simulation. It should be small enough to avoid significant effects on the resulting microstructure, while large enough to allow the system to suppress undesired variations at energetically unfavorable nucleation sites. Meanwhile, T4 is energetically more favorable compared to T1, as E^*_{ext} was applied along the $[\bar{1}00]$ direction. As shown in Fig. 6.5(d), thus T4 grow while consuming T1 phase (Fig. 6.5(d)). Simultaneously, the most favorable T2 nucleate successfully and grow from the domain wall by consuming both T1 and T4 variants, as illustrated in Figs. 6.5(d) and (e). Eventually, the system reaches a stable state in Fig. 6.5(f), where a $90°$ domain wall is formed composed of T2 and T4. The domain wall has been switched from the [110] plane to the $[\bar{1}10]$ plane.

In contrast, Figs. 6.6(a)-(d) illustrate the process of the domain switching when the same E^*_{ext} is applied to the [100] direction. It can be observed that T2 and T3 variants do not nucleate, despite repeated thermodynamic perturbations caused by the noise £. This is due to such an external electric field favoring the T1 variant, allowing it to remain stable in the system. Domain switching in this case occurred by either widening or narrowing the corresponding variants. In general, domain switching in Model II is achieved through the nucleation and growth of ferroelectric variants, consistent with the previous discussion.

E^*_{ext} with the same amplitude was applied to the positive and negative x_2 axes as well, as shown in Figs. 6.6(e) and (f). Comparing Figs. 6.5(f) and Figs. 6.6 (d)-(f) reveals that after switching from the initial domain structure (Fig .6.2(e)) under varying E^*_{ext}, not only can the orientation of the domain change, but its size and configuration can also be altered. These simulations demonstrate that domain switching of both $180°$ and $90°$ occurs when E^*_{ext} aligns with the direction of the absent variants. Conversely, when the induced field aligns parallel to the existing variants, domain switching of $90°$ is exclusively observed. The computed results with the current model align with the previous simulations described in Ref. [81], confirming the suitability of Model II for investigating domain switching.

6.3.3. Polarization and strain hysteresis

Besides the qualitative analysis of domain structures, a phase-field model for ferroelectrics should also allow for quantitative calculations when an external stimulus is

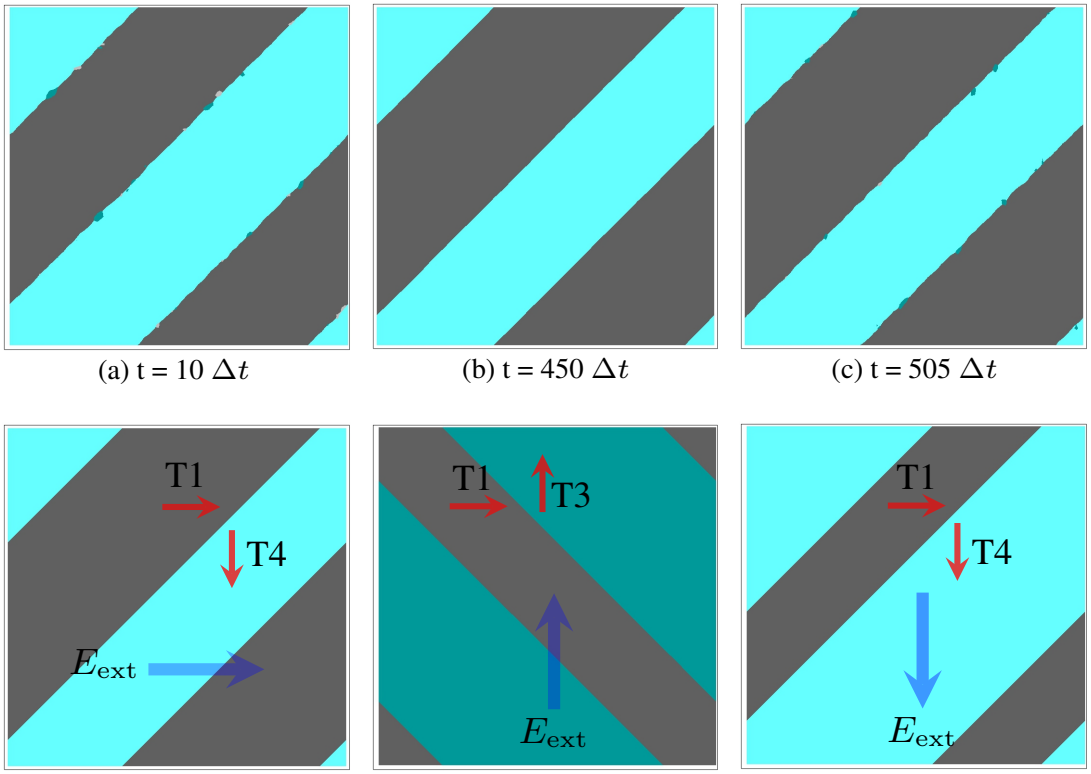

(a) t = 10 Δt (b) t = 450 Δt (c) t = 505 Δt

(d) t = 1200 Δt (e) t = 1200 Δt (f) t = 1200 Δt

Figure 6.6.: Domain switching of E^*_{ext} was applied along the direction of T1, T3, and T4 variants, respectively. (a)-(d) show the temporal evolution of E^*_{ext} applied along the [100] orientation, while (e) and (f) display the simulated results of applying E_{ext} along [010] and $[0\bar{1}0]$ direction, respectively. The blue arrows in (d)-(f) represent the direction of the induced electric field, and the red arrows illustrate the polarization direction of each variant. Adapted from Ref. [16].

applied. As discussed in Section 2.1.6.1, ferroelectrics exhibit nonlinear polarization and mechanical variations under cyclic external electric fields. Thus, the polarization and strain hysteresis of the BTO material under external electric fields are calculated in this subsection. Firstly, Fig. 6.2(e) was established as the original state. The E^*_{ext} was applied to parallel to the positive x_1-axis if it had a positive magnitude. In contrast, for a negative magnitude of E^*_{ext}, the field aligned antiparallel to the positive x_1-axis. The applying E^*_{ext} detail proceeded as follows: starting from 0 to 1.2, it increased initially by in by increments of 0.24 in strength. Subsequently, maintaining the same strength, it decreased from 1.2 to -1.2, followed by another increase from -1.2 to 1.2. At each loading point, iterations consisting of 4000 steps were performed to ensure that the computed domain structures reached an equilibrium profile. Meanwhile, the same

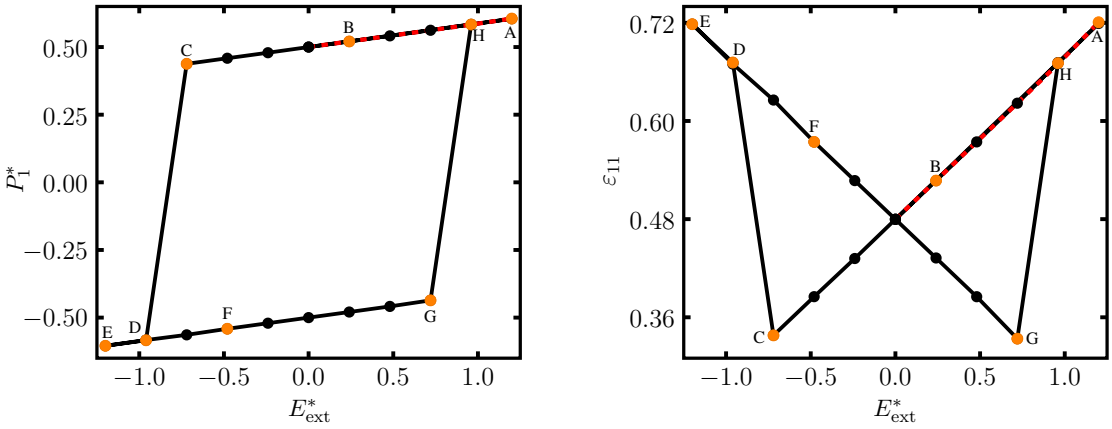

(a) polarization hysteresis

(b) strain hysteresis

Figure 6.7.: (a) and (b) respectively illustrate the computed polarization and strain hysteresis under circularly applied electric fields. Adapted from Ref. [16].

nucleation mechanism discussed in Section 6.3.2 was applied during the first 1000 steps at each point. The average polarization $\bar{P}_1^*$ ($P_1^* = P_1/|P_0|$) and the average strain $\bar{\varepsilon}_{11}$ along the [100] direction were evaluated as the microscopical response of the BTO to external electric fields. Figs. 6.7(a) and (b) respectively depict the computed polarization hysteresis and strain hysteresis, while the domain structures of the correspondingly marked points A-H are illustrated in Figs. 6.8(a)-(h).

Starting from Fig. 6.2(e), applying E_{ext}^* along [100] direction leads to an increment in both the average polarization and the average strain along the positive x_1-direction, as illustrated in Figs. 6.7(a) and (b). A comparison of the domain configurations in Figs. 6.8(a) and Fig. 6.2(e) suggests that the T1 is more energetically favorable, which explains the absence of nucleation and growth of T2 and T3. Thus, domain switching from the original state to point A is caused by the movement of the domain walls, resulting in the growth of the T1 at the expense of T4. The multiple domains in point A also indicate that under $E_{\text{ext}}^* = 1.2$, the system has not yet reached the saturation state with only one domain existing. As shown in Figs. 6.7(a)-(c), the domain structures indicate that both the average polarization $\bar{P}_1^*$ and the average strain $\bar{\varepsilon}_{11}$ decrease linearly, consistent with the plots in Figs. 6.7(a) and (b). With an increase in the magnitude of E_{ext}^* applied along the $[1\bar{0}0]$ direction, domain walls initially in the [110] plane were switched into the $[\bar{1}10]$ plane, causing a jump from point C to point D in both the polarization hysteresis plot (Fig. 6.7(a)) and strain hysteresis plot (Fig. 6.7(b)). The coercive field in such a single crystal system can then be evaluated based on this jump. According to domain structures in Fig. 6.8(e), T2 grows when the size of E_{ext}^* increases to point E, which accordingly increases $\bar{P}_1^*$ and $\bar{\varepsilon}_{11}$, as demonstrated in Fig. 6.7.

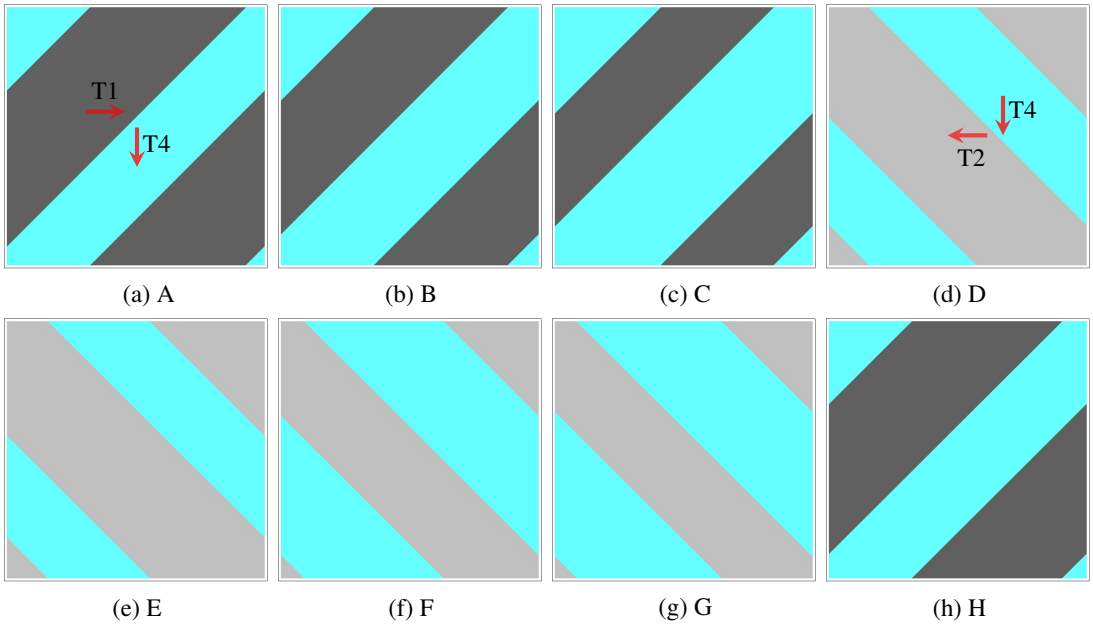

Figure 6.8.: Domain configurations for the marked points of Fig. 6.7. Red arrows demonstrate the polarization orientations of variants. Adapted from Ref. [16].

As E^*_{ext} gradually varies from -1.2 to 1.2, both the absolute value of the average polarization and the average strain decreases steadily. This can be explained by the growth of T4 in the domain structures, as shown in Figs. 6.8(e)-(g). Similarly, P^*_1 jumps from negative to positive when the electric field reaches the coercive field, as indicated by points G and H in Fig. 6.7 (a). Meanwhile, there is also a jump in the strain hysteresis (Fig. 6.7(b)). Comparing Figs. 6.8(g) and (h), this is consistent with the associated change in the domain structures. Even though the jumps and their associated domain switching have been observed in Figs. 6.15 and 6.8 using Model II, the computed hysteresis loop generally exhibits linearly variations in the average polarization and average strain. This is because polarization does not evolve during the simulation and the spontaneous polarization with a constant magnitude of $|P| = 26\,\mu\text{C}/\text{cm}^2$ was kept constant even under different electric fields.

6.3.4. Domain switching induced by a mechanical field

Domain switching under mechanical loading, either through external stress or strain, is another important property of ferroelectric materials. Therefore, this subsection computes the domain evolution induced by an applied strain along the [100] direction using Model II. Typically, Fig. 6.9 demonstrates the temporal evolution of the domain switching as well as its associated elastic strain evolution when a compressive strain

$\varepsilon_{11}^{\text{ext}} = 0.01$ is applied to the domain configuration shown in Fig. 6.2(e). To mimic the variant nucleation, the same nucleation mechanism was employed in this calculation. However, observations from Fig. 6.9 suggest that variants T2 and T3 do not successfully nucleate and grow, revealing that the energetically favorable variant already present in the initial state is T4 in this case. The domain switching induced by mechanical loading is therefore achieved through the movement of the already-present variants. Thus, one can find the growth of the T4 variant by shrinking T1, as shown in Fig. 6.9(a). This transformation continues until multiple domains are completely replaced by a single domain where the T4 variant occupies the entire region after 1200 simulation steps. Comparing the equilibrium structure at 300 steps with the initial structure (0 steps) in Figs. 6.9(a) also indicates that only a 90-degree domain wall switching occurs under such an external strain.

Figs. 6.9(b) and (c) additionally demonstrate the temporal evolution of ε_{11} and ε_{22}, respectively. It is clear that the 90° domain wall switching leads to a change in the strain distribution. This, in turn, reduces the induced strain energy to minimize the free energy of the system. Since the 180° domain switching is mainly driven by electric energy penalties instead of strain energy penalties, the nucleation of T2 and T3 variants—essential for such domain switching—does not take place in the simulation. This result is in agreement with the work of Wang *et al.* in Ref.[81], where it was found that only 90° domain switching can occur under external mechanical loading. Meanwhile, such a conclusion is also consistent with the predictions of the continuum theory, which suggests that the external mechanical loading can only lead to 90° domain switching in ferroelectrics.

To sum up, this section employs Model II to investigate domain formation and switching under various external stimuli in a single-crystal bulk BTO material. The computed results align with existing literature [81], confirming the efficacy of Model II with the multiphase-field framework for accurately characterizing domain structures in ferroelectric materials.

6.4. Phase-field simulation in polycrystalline systems

6.4.1. Simulations in bicrystalline system

6.4.1.1. Domain formation

To explore mechanisms of domain formation and switching in polycrystalline ferroelectrics with varying orientations, simulations were initially conducted for four bicrystalline systems labeled B0, B1, B2, and B3. Fig. 6.10(a) illustrates the initial configuration of these bicrystalline structures, employing a quasi-2D grid consisting of 300×300 ×1 voxels. The grain orientation in each bicrystalline system is confined to rotations within the x_1x_2-plane. For comparison, Grain 2 in each bicrystalline system

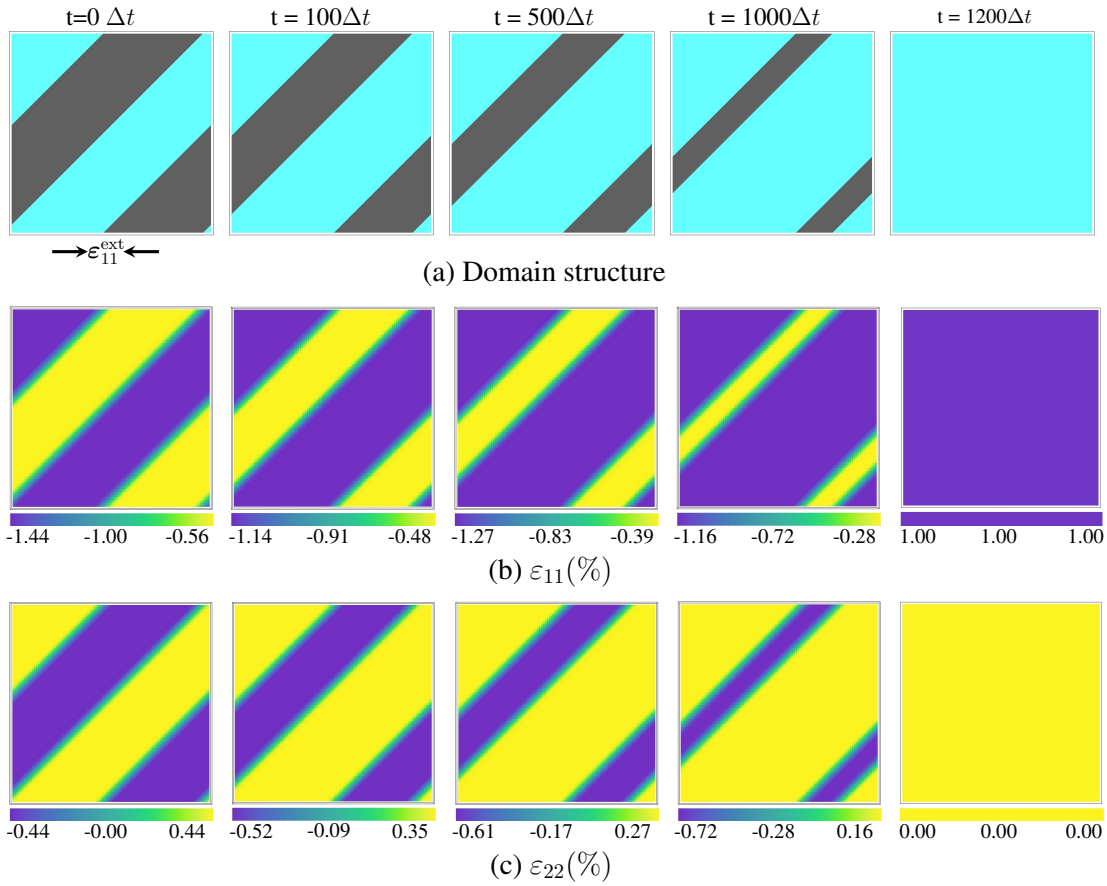

Figure 6.9.: The temporal evolution is illustrated when a compressive strain is introduced along the [100] direction to Fig. 6.2(e). (a) shows the domain switching, while (b) and (c) depict ε_{11} (%) and ε_{22} (%), respectively. Adapted from Ref. [16].

maintains an orientation with $\varphi_2 = 0$, while Grain 1 is rotated to different angles in each system. Additionally, each grain consists of four randomly assigned tetragonal variants. The grains are distinguished by the different color series, specifically blue colors denote Grain 1 while Grain 2 is represented with purple. Colors in each grain range from dark to light, depicting variants from T1 to T4. For these bicrystalline systems, periodic boundary conditions are applied for the phase, electric as well as mechanical fields along the top and bottom surfaces. To solve the phase-field ϕ on the left and right surface, a homogeneous Neumann boundary condition is used, denoted as:

$$\frac{\partial \phi}{\partial x_i}\Big|_{x_i \epsilon \partial \Omega_i} = 0, \tag{6.4}$$

where i represents the x_1- or x_2-direction, and $\partial\Omega_i$ stands for the corresponding field edge. Regarding the solving of the depolarization field, a short circuit condition, i.e.,

$\psi_i = 0$, was applied to the left and right surfaces. In addition, the clamped boundary condition was employed for solving the mechanical field on the left and right surfaces, ensuring zero displacements in the orthogonal directions. In particular, the mechanical field of all polycrystalline systems of BTO in this work using Model II is effectively resolved through the application of a mechanical jump condition approach at a diffuse interface. Such an interface can also represent a grain boundary, rather than a domain wall. This approach aligns with a no-slip mechanical boundary condition that has also been used in Ref. [165] to characterize domain structures for ferroelectric polycrystalline systems.

The simulation was first performed in the absence of an external stimulus, so as to investigate the process of domain structure formation. The temporal evolution for B0 to B3 is shown in Figs. 6.10(b)-(e), where the white arrows represent the polarization orientation of each variant. The electric potential ψ as well as an isoline of the von Mises stress (thin black line) are also illustrated in Figs. 6.10(b)-(e) to compare the influence of the bulk energy to the domain structure formation. For reference, the simulation of a particular grain named B0, which has the same initial configuration but without any grain orientation ($\varphi_1 = \varphi_2 = 0$), was performed. It should be addressed that B0 differs from the single crystal as it has a dielectric grain boundary formed by setting the mobility of the grain boundary to zero. The computed results for 200 and 1200 time steps in Fig. 6.10(b) indicate that the absence of a grain orientation difference results in the formation of a continuous $90°$ domain structure. Similarly to Section 6.3.1, B0 initially releases electric energy to avoid the charged domain walls ($t = 200\Delta t$), while minimizing the elastic energy ($t = 1200\Delta t$) to from the ferroelastic domain walls. However, despite forming a $90°$ domain wall, B0 exhibits significant differences in both the electric potential and the von Mises stress when comparing Fig. 6.10(b) and Fig. 6.2(f). This can be attributed to the influence of a grain boundary.

Simulations of B1 to B3 over 200 iterations also reveal that these systems attempt to release the depolarization field to prevent the formation of tail-to-tail or head-to-head domain walls, despite differences in grain orientations. For example, one can observe that T3 tends to align parallel to T4 to form a natural $180°$ domain wall in B1. Furthermore, a comparison of Figs. 6.10(b) and 6.10(c) suggests the influence of the grain orientation on the primary simulation process of variant transformations, causing different domain structures at equilibrium in B1. For instance, the $5°$ rotation of Grain 1 in B1 stabilized a metastable ferroelectric domain wall formed by variants T1 and T2, leading to a distinct transformation pathway for domains in Grain 2 (500 and 1200 iterations in B1). At equilibrium, the domain morphology of B1 also reveals that both $180°$ and $90°$ domain walls could be stable in the polycrystalline system, highlighting the effect of the $5°$ rotation in Grain 1 on the domain structure formation. Figs. 6.10(d) and (e) depict the temporal evolution of domain profiles in B2 and B3, respectively. It is additionally observed that the grain orientations impact not only just the domain

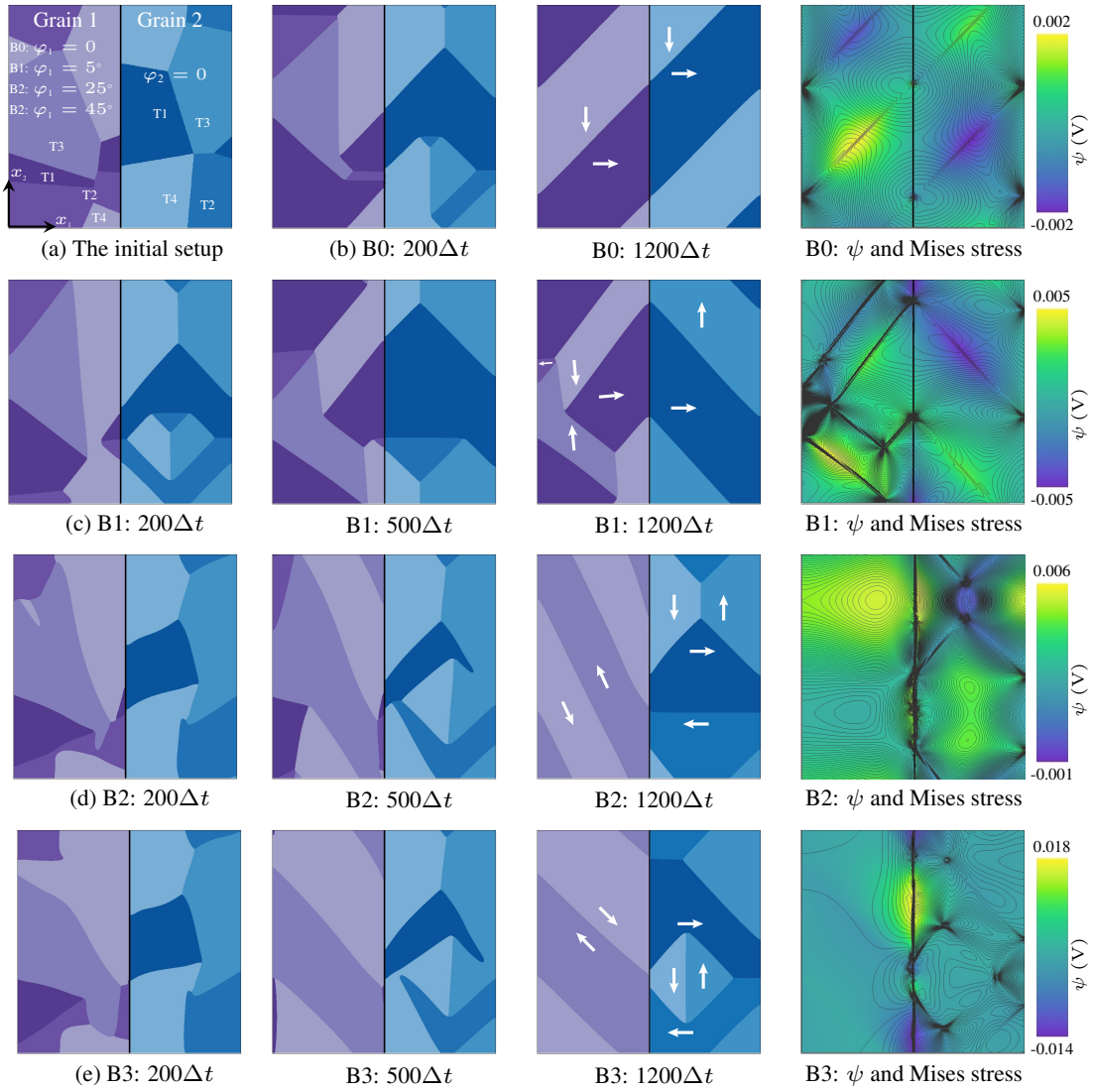

(a) The initial setup (b) B0: $200\Delta t$ B0: $1200\Delta t$ B0: ψ and Mises stress

(c) B1: $200\Delta t$ B1: $500\Delta t$ B1: $1200\Delta t$ B1: ψ and Mises stress

(d) B2: $200\Delta t$ B2: $500\Delta t$ B2: $1200\Delta t$ B2: ψ and Mises stress

(e) B3: $200\Delta t$ B3: $500\Delta t$ B3: $1200\Delta t$ B3: ψ and Mises stress

Figure 6.10.: Domain formation in the bicrystalline systems. (a) represents the initial state and schematic diagram of the bi-crystals. φ_1 and φ_2 respectively represent the orientations of grains in each bicrystalline system, in which φ_2 is maintained as zero, while φ_1 varies across the systems: $\varphi_1 = 0$ in B0, $\varphi_1 = 5°$ in B1, $\varphi_1 = 25°$ in B2, and $\varphi_1 = 45°$ in B3. (b)-(e) shows the process of the domain structures formation, and the electric potential ψ as well as the distribution of von Mises stress (represented as contour plots with thin black lines) at the equilibrium state for bicrystalline systems B0 to B3. White arrows demonstrate the polarization orientation of each variant. Adapted from Ref. [16].

morphology but also the domain size, leading to varied domain structures in Grain 2. Furthermore, comparing the von Mises stress and electrical potential at equilibrium in the bicrystalline system reveals that an increasing orientation difference between Grain 1 and Grain 2 promotes the formation of a $180°$ domain structure in Grain 1. Therefore, B1 demonstrates a dense stress distribution around the domain wall and the domain junctions, while systems B2 and B3 primarily concentrate stresses at the junctions, influenced by the inherent $180°$ domains crucial for releasing the electrostatic energy.

6.4.1.2. Domain switching under an external field

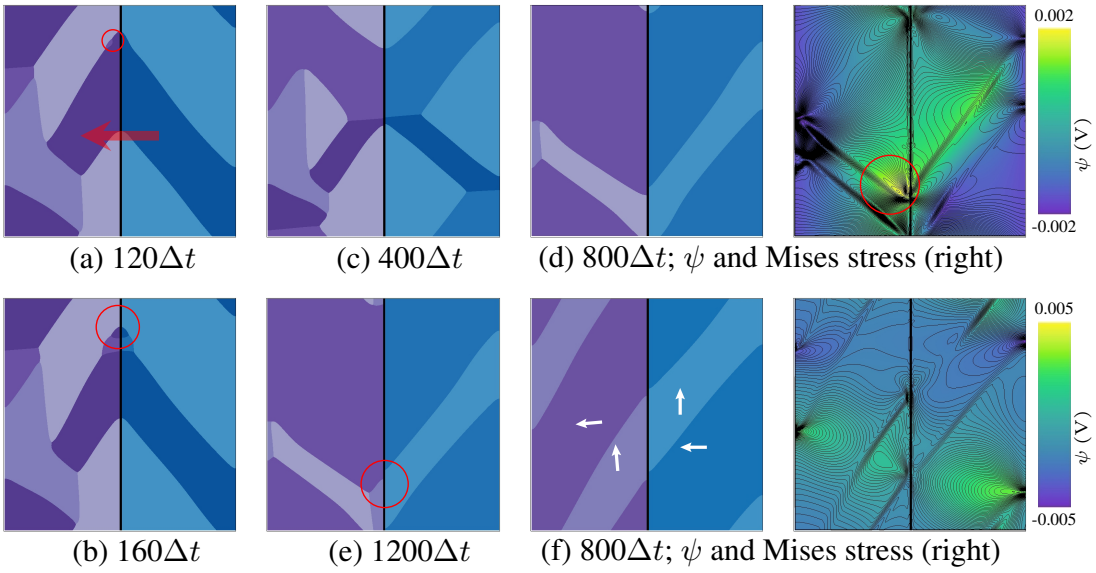

Figure 6.11.: The domain switching process of B1 when $E^*_{\text{ext}} = 1$ was applied along $[\bar{1}10]$ direction to its equilibrium state shown in Fig. 6.10(c). The transparent red arrow in (a) shows the orientation of E^*_{ext}, while the white arrows in (f) denote polarization directions. The right images of (d) and (f) show their associated von Mises stress (represented as contour plots with thin black lines) and electric potential (ψ). Adapted from Ref. [16].

To investigate the influence of grain orientation on domain switching, an external electric field $E^*_{\text{ext}} = 1$ was applied along the $[\bar{1}10]$ direction to the equilibrium profile of B0 to B3 (Fig. 6.10). Typically, the temporal evolution of domain switching in the B1 system is shown in Fig. 6.11, where the boundary conditions described in Section 6.4.1.1 were used. Additionally, Fig. A.1 in Appendix A.2 provides the temporal evolution of B2 and B3 systems under the same E^*_{ext}. A perturbation with a frequency of 50 intervals was introduced during the first 1000 steps to mimic the nucleation of absent variants.

The nucleation of the T2 variant in Grain 1, starting from the boundary between T1 and T4 variants after 120 iterations, can be observed by the marked red circle in Fig. 6.11(a). Afterward, the nucleated T2 in Grain 1 grows and extends to the grain boundary, leading to another T2 nucleation in Grain 2, depicted by an additional red circle in Fig. 6.11(b). In Fig. 6.11(c), it is evident that the T2 variant within each grain subsequently grew over time, predominantly consuming T1. However, as illustrated in the depicted electric potential and distribution of von Misses stress in Fig. 6.11(d), the growth of T2 after 800 time steps cased in a high concentration of both electric and elastic energy at the junction of different variants at the grain boundary, indicated by the highlighted red circle. This phenomenon is attributed to the orientation difference between grains 1 and 2. As marked by the red circle in Fig. 6.11(e), to overcome this energy concentration, T3 nucleated and grew around the grain boundary region. Eventually, the domain structures of B1 shown in Fig. 6.10(c) are switched into two $90°$ domain walls composed of T2 and T3 in both grains, as depicted in Fig. 6.11(f), where the red arrows represent the polarization directions for the associated variants.

Similar to the single crystal simulation, the present study also investigates domain switching under an external mechanical field. In particular, Fig. 6.12 represents the temporal evolution of the B2 system in the equilibrium (Fig. 6.10(d)) under an external strain $\varepsilon_{22}^{\text{ext}} = -0.005$ along the [010] direction. The temporal evolution of the switching process under the same condition for B1 and B3 bicrystalline systems can be further found in Fig. A.2 of Appendix A.2. With the same nucleation parameters, a simulation of 150 iterations shows the nucleation of T1 and T2 in Grain 1 from the grain boundary, as indicated by the red circle in Fig. 6.12(a). As the driving force is the same when subjected to a compressive strain in the x_2-direction, T1 and T2 grow equally by consuming the T4 variant, as observed in Fig. 6.12(b). Domain switching under the external strain is still driven by the growth of energetically favorable variants at the expense of unfavorable variants in the domain wall region, even in the bicrystalline system. Moreover, it is easy to observe that there is no domain switching in Grain 1, within which has a $180°$ domain wall. This suggests that mechanical loading is unable to induce domain switching in the natural domain structures. This finding is also in agreement with the calculation of B3 in Fig. A.2 of Appendix A.2.

6.4.2. Phase-field simulation in a 10-grain polycrystalline BTO material

The simulations for both single-crystal and bicrystalline systems discussed above have validated the reliability of Model II for analyzing domain structures under different conditions. Here, Model II is further employed to compute domain formation, domain switching, and the associated material properties such as polarization and strain hysteresis in a 10-grain polycrystalline system. The schematic diagram of such a system is shown in Fig. 6.14(a), which consists of $400 \times 400 \times 1$ voxels and each grain randomly rotates on the x_1x_2-plane. Each grain is uniquely identified by a distinct set of colors.

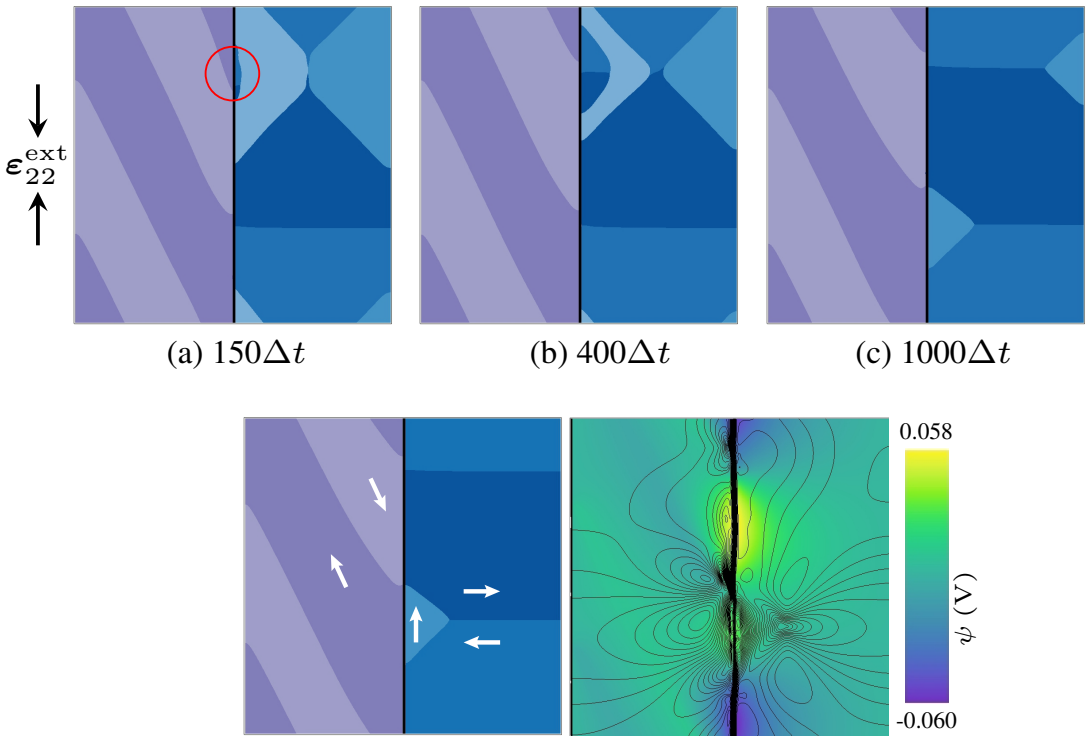

(a) $150\Delta t$ (b) $400\Delta t$ (c) $1000\Delta t$

(d) $1500\Delta t$; ψ and Mises stress (right)

Figure 6.12.: The domain switching process of B2 under a compressive strain $\varepsilon_{22}^{\mathrm{ext}} = 0.005$ applied along the x_2-edges to its equilibrium (Fig. 6.10(c)). The white arrows in (d) represent the associated polarization orientations, while the right image in (d) shows von Mises stress (contour plots with thin black lines) and the electric potential (ψ). Adapted from Ref. [16].

Similar to the bi-crystal simulations in Fig. 6.10(a), those colors range from light to dark to distinguish variants T4 to T1 within each grain. Periodic boundary conditions are applied to solve all fields during the simulations.

The process of forming the domain structures without any external stimulus is illustrated in Fig. 6.14, in which the white arrows represent the polarization directions of the corresponding variants. Differing from the initialization of bicrystalline systems in Fig. 6.10(a) and the single-crystal system in Fig .6.2(a), variants within each grain could be missing because of the size limitation when using the Voronoi approach to generate the computational structures. Therefore, the noise function £ (Eq. (4.10)) was activated to promote the nucleation of the unassigned variants in order to obtain self-consistent domain structures in equilibrium. Additionally, the allowed nucleation time step was set to 10000 with a frequency of 200 time steps, ensuring a stable simulation.

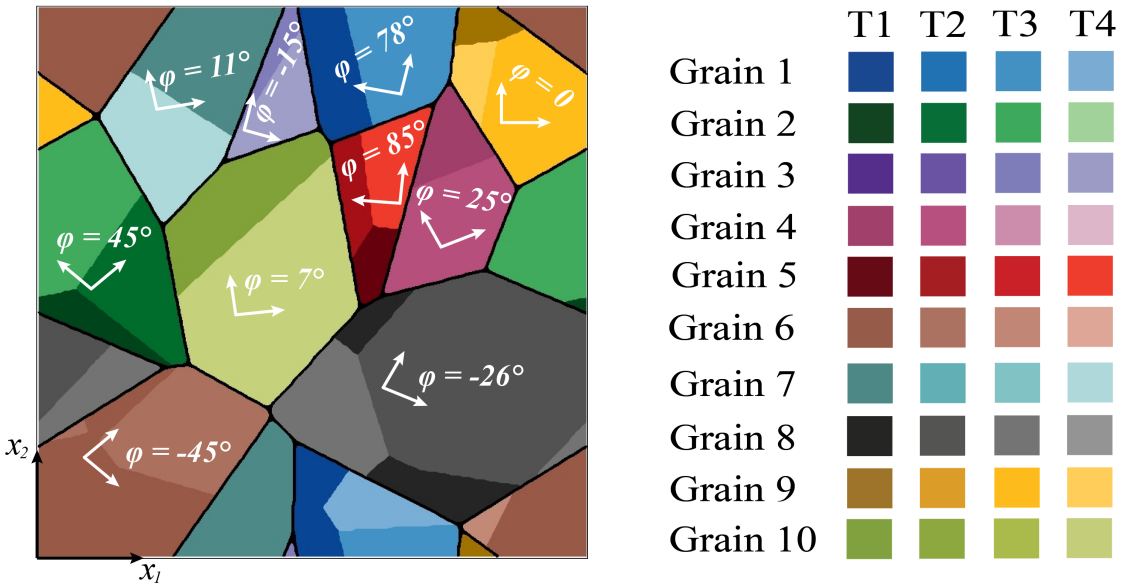

Figure 6.13.: Schematic diagram of the simulated 10-grain polycrystalline system, in which grains are distinguished by different color series, and colors from dark to light in each grain represent variants from T1 to T4. Adapted from Ref. [16].

An observation of Grains 4 and 5 in Fig. 6.14(a) suggests the formation of ferroelectric domain walls to release the high energy density generated by the depolarization field. Apart from that, the marked circles in Figs. 6.14(a) and (b) show the nucleation and growth of variants near the grain boundary. This phenomenon occurs as variants in neighboring grains attempt to align their polarization directions, which leads to the release of the built-in depolarization field generated at the grain boundary. As depicted in Figs. 6.14(c) and (d), domain structures are subsequently formed by the continuous nucleation, growth, and disappearance of variants in each grain, aiming to minimize the elastic and electric energy. After reaching the equilibrium state shown in Fig. 6.14(f), a complex domain structure is formed, characterized by the coexistence of $90°$ and $180°$ domain walls. The corresponding von Mises stress and electric potential ψ, which respectively represent the contributions from the mechanical and depolarization fields, are also demonstrated in the right image of Fig. 6.14(f). In addition to domain wall regions within each grain, stress concentration is also observed at the grain boundary, especially in areas with multiple junctions, suggesting that elastic energy plays an important role in forming domain structures in these regions.

Following the calculation procedure described in Section 6.3.3, Figs. 6.15(a) and (b) depict the computed polarization and strain hysteresis for the polycrystalline system, with the equilibrium state shown in Fig. 6.14(f) as the original state. To ensure stability at each E_{ext}, simulations were performed with 50000 iterations at each induced point,

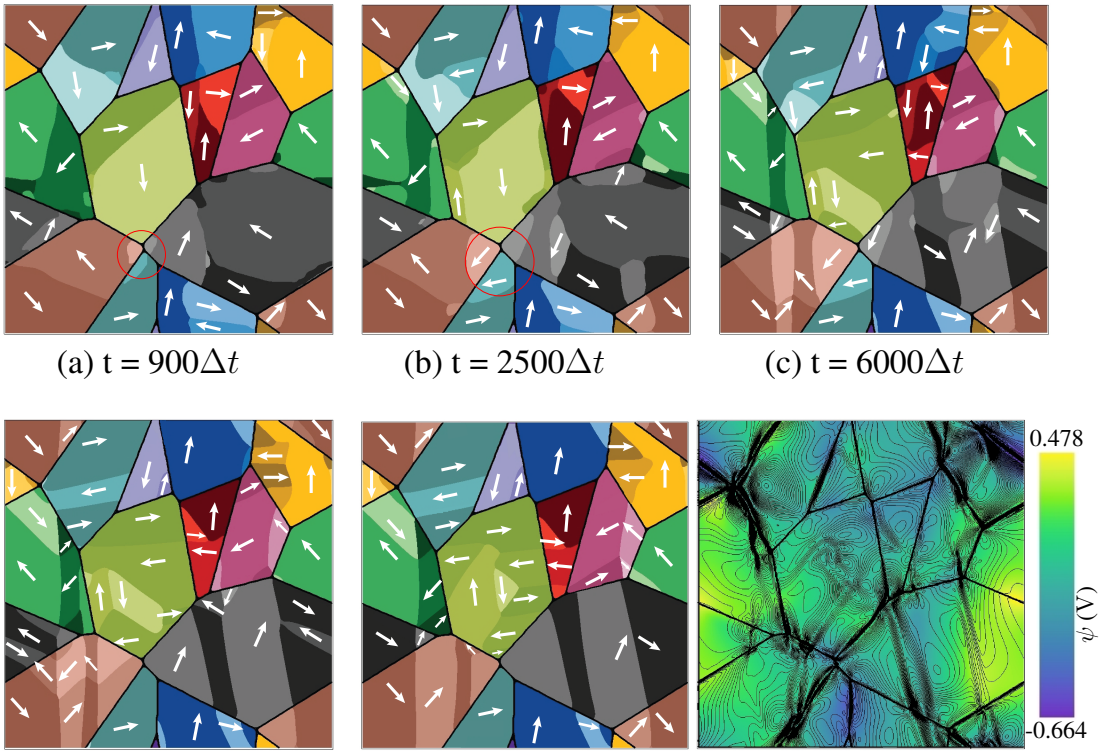

(a) t = 900Δt (b) t = 2500Δt (c) t = 6000Δt

(d) t = 10000Δt (e) t = 50000Δt; ψ and von Mises stress (right)

Figure 6.14.: Domain formation of the 10-grain polycrystalline system is represented in Fig. 6.13. The right image of (f) additionally shows von Mises stress (black thin line) and electric potential ψ at equilibrium. Adapted from Ref. [16].

which differs from the simulations in the single-grain case. Besides, a noise disturbance with a frequency of 200 time steps was introduced during the first 10000 time steps. Similarly, the polarization calculated in Fig. 6.15(a) and strain computed in Fig. 6.15(b) represents the average values in the x_1-direction. In general, the average polarization increases or decreases with increasing or decreasing the external electric field strength ($|E^*_{\text{ext}}|$).

Interestingly, when comparing the profile of the simulated polarization and strain hysteresis of the single-crystal structure (depicted in Fig. 6.7) with that of the 10-grain structure (illustrated in Figs. 6.15(a)-(b)), a notable finding is that the change in polarization in response to variations in E^*_{ext} exhibits nonlinear behavior. Even when the magnitude of the polarization remains constant under different induced electric fields, nonlinear behavior is observed, indicating the influence of grain orientations on domain switching. The domain structures of marked points A to F at equilibrium are shown in Figs. 6.15(c) to (h), with white arrows indicating the polarization direction.

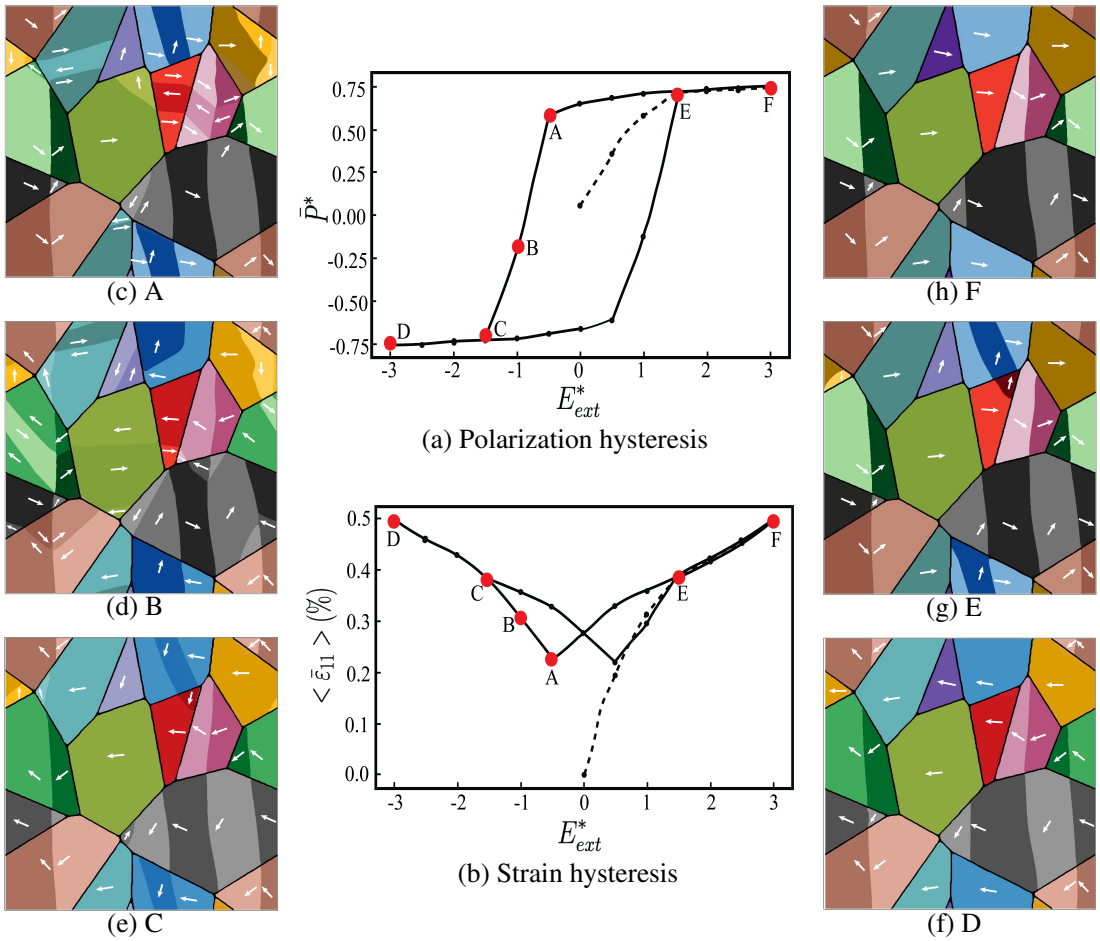

Figure 6.15.: (a) and (b) respectively demonstrate the simulated polarization and strain hysteresis of the polycrystalline system with the application of external electric fields. The associated domain structures of points A to F are shown in (c)-(h). Adapted from Ref. [16].

Imposing the electric field in the reverse direction, the domain morphology of point A (refer to Fig. 6.15(c)) tends the domain in certain grains to align with the applied field, particularly near the grain boundaries. As the external electric field varies from A to C, there is a notable increase in the formation and growth of domains aligned with the external electric field, as depicted in Figs. 6.15(d) and (e). This domain switching causes a significant jump in polarization and strain (Figs. 6.15(a) and (b)). One can observe another contrasting jump when the magnitude of E^*_{ext} along [100] direction is increased (point E), where the polarization direction in each grain is once again switched to align with [100] direction. The domain morphology at the endpoint of the external electric field (point F) is illustrated in Fig. 6.15(h). It can be seen that the polarization

direction in the grains aligns with the imposed electric field and the respective crystal orientations. Whereas, the presence of multiple domains within certain grains suggests that the saturation polarization state has not been reached in the current calculation, analogous to point C.

As a summary, this section illustrates the mechanisms of domain formation and switching under an external field in polycrystalline ferroelectric materials, using Model II based on the multiphase-field approach. In general, to achieve a self-consistent domain structure for complex polycrystalline systems, it is recommended to activate variant nucleation at the beginning of the simulations, regardless of whether there is an external stimulus. Akin to the single-crystal simulations, incorporating variants nucleation also enables domain switching under external fields in polycrystalline systems. Therefore, Model II can also compute polarization and strain hysteresis in polycrystalline systems. However, differing from single crystal simulations, grain boundaries, and orientations affect the domain formation and domain switching, leading to the nonlinear behavior in the calculated hysteresis loop.

6.5. Conclusion

This chapter shows the application of Model II to calculate domain structures and domain switching in the single-crystal, bi-crystal, and polycrystalline BTO material. In general, noise perturbations are unnecessary for domain formation in a single crystal or a simple multigrain system like a bi-crystal system where all variants can be assigned initially, and if there are no external fields. However, for more complex polycrystalline structures where all energetically equivalent polarization states of ferroelectric phases could not be assigned due to dimension limitations, the noise function £ in Eq. (4.10) is required to form self-consistent domain structures. Apart from that, the thermal fluctuation should also be included to account for the nucleation of all lacking variants near the interface such as domain walls or grain boundaries, so as to accurately simulate domain switching under external fields. Based on the computed domain switching process, the polarization and strain hysteresis loops under external electric fields are computed for the single crystal and 10-grain polycrystalline system. A comparison of the simulated results suggests the influence of grain boundary and orientations on the properties of the ferroelectric material. In the present study, the noise term is integrated to represent the nucleation process because of the use of the multi-obstacle type potential. In contrast, it is unnecessary to activate the noise term when using a multiwell potential. The computed results in this chapter are in agreement with the literature, verifying the reliability and feasibility of Model II.

Model II is based on the multiphase and multicomponent concept in Ref. [78], within which the mechanical solution is performed using a jump condition technique described in Refs. [132, 133, 160]. This enables the calculation of both single-crystal and polycrys-

talline systems, in addition to the analysis of the influence of the mechanical field on the domain structures. By replacing the domain wall energy density with a phase-field gradient energy density and substituting the Landau potential with a multi-obstacle potential, Model II facilitates numerical simulations of BTO materials without using gradient and Landau coefficients. Moreover, Model II can allow the interfacial energy to be independently adjusted to capture specific interfacial properties, including interfaces for varying variants, grains with different orientations, or interfaces separating distinct ferroelectric phases. In summary, the simulations in this chapter serve as a significant reference for the further development of the multiphase concept in ferroelectrics.

7. Computing domain structures in PTO thin film using Model II

7.1. Introduction

Due to their intrinsic electrical polarization at nanometer thicknesses, ferroelectric thin films exhibit remarkable properties. Their ability to switch domains in response to an electric field, coupled with their extraordinary piezoelectric, nonlinear optical properties, and pyroelectric, positions them at the forefront of research and development in diverse fields such as sensors, memory devices, photovoltaic, and other applications [166–169]. Domain structure is an inherent property of ferroelectric thin films, playing a crucial role in determining their performance. A deep understanding of the domain structures, together with the ability to manipulate their configurations, is therefore of importance for developing ferroelectric thin films.

Since Li *et al.* introduced their methodology for solving the mechanical field of an epitaxial ferroelectric film constrained by a substrate in Ref. [89], the TDGL approach has been extensively adopted for in-depth studies of ferroelectric thin films. For instance, over the past two decades, this approach has played a significant role in understanding the complexities of ferroelectric phase transformations in various ferroelectric thin films and the corresponding domain structures [13, 19, 90, 170–172]. The effect of a wide range of scenarios on the domain structures has been covered in these investigations, such as the effects of mechanical strain, thin film thickness, electrical control, paraelectric-ferroelectric transformation temperature, and other relevant variables. Besides, taking the strain gradient effect into account, investigations of the flexoelectric properties in ferroelectric films have also been extended in literature such as [110, 173, 174].

However, the lack of Landau coefficients limits the examination of domain formations and the mechanisms underlying the exceptional performance of some recently developed ferroelectric thin films. Therefore, Model II has been extended to investigate the ferroelectric thin films in this chapter, based on the publication in Ref. [17]. The analysis includes investigating domain wall stability influenced by substrate deformation, substrate constraints, film thicknesses, and paraelectric-ferroelectric transformation temperature.

7.2. Simulation setup

The schematic diagram for the simulated film system is visually illustrated in Fig. 7.1(a). The investigation centers on the domain structures of an epitaxial single-crystal PTO thin film with (001)-oriented growth on a cubic substrate. The PTO film, with a thickness h_f characterized by a vertical dimension along the growth axis, is subjected to confinement from a substrate that has an allowed deformation height h_s. As shown in Fig. 7.1(b), the order parameters in the film area have the values $\phi_{\text{film}}(\boldsymbol{x}, t) = 1$ and $\phi_{\text{sub}}(\boldsymbol{x}, t) = 0$, while $\phi_{\text{film}}(\boldsymbol{x}, t) = 0$ and $\phi_{\text{sub}}(\boldsymbol{x}, t) = 1$ are maintained within the spatial extent of the substrate region. The diffuse interface represents the region of transformation between the film and the substrate, where the mobility of the phase transformation is set to zero. This allows for representing time invariance between the two phases. Moreover, the thin film consists of different regions representing different polarization variants. In the PTO material with a tetragonal ferroelectric phase, there are also six polarization variants oriented along the <100>-directions, as depicted in Fig. 7.1(c). In this work, domains with the polarization direction aligned with the in-plane directions are termed a-domains, while those perpendicular to the substrate are classified as c-domains (see Fig. 7.1(c)).

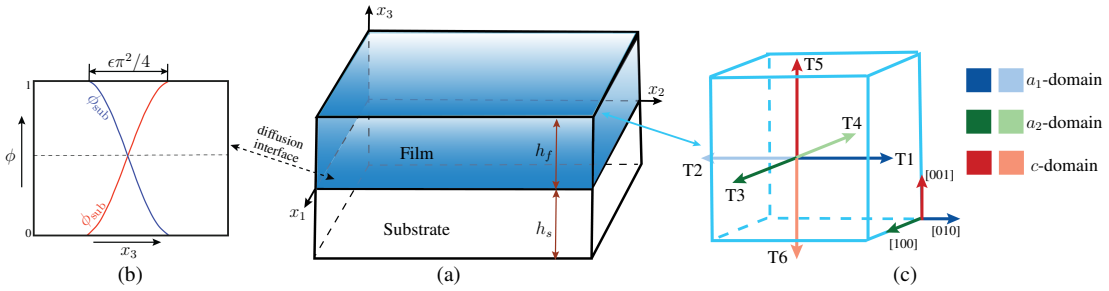

Figure 7.1.: Application of Model II in an epitaxial ferroelectric thin film. (a) describes the simulated system; (b) exhibit the thin film and the substrate across the diffusion region, in which $\epsilon\pi^2/4$ describes the interfacial thickness; (c) presents the variants and their associated polarization state in the tetragonal phase. Adapted from Ref. [17].

Once again, all simulations are conducted in Pace3D [148] from our group. The flow chart illustrating the overview of the solution process is referred to Fig. 6.1 in Chapter 6. Similarly, a finite difference algorithm using an explicit forward Euler scheme was employed to rigorously solve the phase-field evolution equation given by Eq. (4.11). The equidistant Cartesian grid is used for the spatial discretization of all governing equations. Following this, the stationary momentum balance formulae (Eq. (3.24)) is solved implicitly to evolve the displacement field $\boldsymbol{u}$. Concurrently, the electrostatic equilibrium condition in Eq. (4.9) is addressed using conjugate gradient methodology. Voronoi tessellation was used to create the initial configuration for the computed film.

In order to enhance the computational efficiency, the domain was partitioned in both x_1- and x_2-directions using the MPI standard during the simulation.

The domain structure formation within a ferroelectric thin film depends on the use of well-defined boundary conditions to solve for variables including the phase-field tuple $\boldsymbol{\phi}$, the mechanical fields, as well as the electric field. Firstly, all fields are subjected to periodic boundary conditions along the x_1 and x_2 axes. For solving the phase-field field on the top ($x_3 = h_f$) and bottom ($x_3 = 0$) surfaces of the thin film, Neumann boundary conditions were used, denoted as:

$$\nabla \boldsymbol{\phi} \cdot \boldsymbol{e}_3 = 0, \tag{7.1}$$

in which $\boldsymbol{e}_3$ denote the unit vector in x_3-direction. This boundary condition enforces all interfaces to be perpendicular to the film boundary. Since the polarization is predetermined for each variant and its value across the interface is obtained by the interpolation of $\boldsymbol{\phi}$, this boundary condition for $\boldsymbol{\phi}$ thus corresponds to a Neumann boundary condition for polarization, expressed as:

$$\nabla \boldsymbol{P} \cdot \boldsymbol{e}_3 = 0. \tag{7.2}$$

Based on the Poisson equation in Eq.(4.9), this suggests that the electric potential ψ equals zero at the boundary, indicating no electric charge flux across the boundary. Therefore, short-circuited boundary conditions are applied on the top and bottom surfaces for solving the electric field, denoted as:

$$\psi \cdot \boldsymbol{e}_3 = 0. \tag{7.3}$$

With regard to the mechanic fields, a condition of

$$\sigma_{i3}\big|_{x_3=h_f} = 0 \tag{7.4}$$

is enforced at $x_3 = h_f$ (top surface) to simulate a stress-free interface, whereas the lowermost layer of the substrate (bottom surface of the film-substrate system) is held in a fixed position via prescribing a vanishing displacement, denoted as:

$$\boldsymbol{u}\big|_{x_3=-h_s} = \boldsymbol{0}. \tag{7.5}$$

Table 7.1.: The material coefficients and phase-field parameters used in the current simulation. Adapted from Ref. [17].

Material Coefficients	Symbol	Value	Unit
Dielectric stiffness	α_1	(T-497)*3.8[a]	$10^5 \cdot [\mathrm{m/F}]$
Interfacial energy	$\gamma_{\alpha\beta}$	0.01	$\mathrm{J/m^2}$
-	γ_α^c	0.01	$\mathrm{J/m^2}$
Elastic tensor	$\mathcal{C}_{11}$	17.46	$10^{10}\cdot[\mathrm{N/m^2}]$
PTO[a]	$\mathcal{C}_{12}$	7.94	$10^{10}\cdot[\mathrm{N/m^2}]$
	C_{44}	11.11	$10^{10}\cdot[\mathrm{N/m^2}]$
Electrostrictive tensor	$\mathcal{Q}_{11}$	8.90	$10^{-2}\cdot[\mathrm{m^4/C^2}]$
PTO[a]	$\mathcal{Q}_{12}$	-2.60	$10^{-2}\cdot[\mathrm{m^4/C^2}]$
	$\mathcal{Q}_{44}$	6.75	$10^{-2}\cdot[\mathrm{m^4/C^2}]$
Elastic tensor	$\mathcal{C}_{11}$	43.10	$10^{10}\cdot[\mathrm{N/m^2}]$
KTO[b]	$\mathcal{C}_{12}$	10.30	$10^{10}\cdot[\mathrm{N/m^2}]$
	$\mathcal{C}_{44}$	10.90	$10^{10}\cdot[\mathrm{N/m^2}]$
Gradient coefficient	G_{11}	10.56	$10^{-11}\cdot[\mathrm{N\,m^4/C^2}]$
Thermal expansion[c]	α_f	12.60	$10^{-6}\cdot[\mathrm{1/K}]$
	α_s	6.67	$10^{-6}\cdot[\mathrm{1/K}]$

[a] The dielectric stiffness, elastic tensor coefficients, and electrostrictive tensor coefficients of PTO are from Ref. [89].
[b] Elastic tensor coefficients of KTO are found in Ref. [175].
[c] Ref. [176] describe the thermal expansion of α_f and α_s.

The computed region was partitioned into cells with dimensions of $\Delta x_1 = \Delta x_2 = 1\,\mathrm{nm}$ and $\Delta x_3 = 0.5\,\mathrm{nm}$. ϵ was established at a value of $2\Delta x_3$ by talking the interface stability into account. The input interfacial energy $\gamma^{\alpha\beta}$ is assigned physical meaning by setting it equal to the domain wall energy density. PTO exhibits a ferroelectric tetragonal phase, capable of formatting either $90°$ or $180°$ domain structures in this work. The case of the $180°$ domain wall energy is employed for $\gamma^{\alpha\beta}$, which is computed based on Eq. (6.1). The parameter γ_α^c in Eq. (4.17) is assigned the same value as $\gamma^{\alpha\beta}$. The $M^{\alpha\beta}$ in Eq. (4.11) governs the mobility of variants within the film set to be one while setting as zero between film and substrate. Similarly, the background dielectric constant was set to 50.

The simulation starts with exploring the impact of substrate heights and constraints on domain morphologies. This is followed by examining the epitaxial growth of PTO on a (001)-oriented KTO substrate, in which the formation of domain structures was explored with varying film thickness and different paraelectric-ferroelectric transformation temperatures. The required phase-field parameters and material coefficients of PTO in the current simulation are listed in Table 7.1. In order to increase accuracy,

the input coefficients were transformed into dimensionless values with further details available in Eq. (6.3).

7.3. Results and discussion

7.3.1. Influence of substrate deformation on the domain structures

The simulations begin with investigating how substrate deformation influences domain structures. This is achieved through implementing simulations of the thin film with a thickness of $20\,\mathrm{nm}$ growth on varying substrate heights (h_s) at room temperature. Simultaneously, the film is subjected to a specified tensile misfit strain with a value of 0.006. Here, h_s also represents the deformation region of the substrate, while $x_3 = -h_s$ indicates the surface of zero displacements enforced by appropriate boundary conditions. The scenario where $h_s = 0$ corresponds to a rigid substrate. Following this, the volume fraction and morphology of the c-domains are compared and analyzed across different h_s. These simulations were conducted in a quasi-2D thin film system, in which the initial configuration is shown in Fig. 7.2(a). The system was discretized into $128 \times 1 \times (40 + n_s)$ cells, where $n_s = h_s/\Delta x_3$ denotes the number of cells discretizing the substrate, depending on the considered h_s. Topically, n_s was allowed to vary in a range from 0 to 36, with an internal step size of 3. The film region was divided into six randomly distributed polarization states. The polarization directions for T1, T2, T5, and T6 variants are illustrated by the black arrows. In the T3 and T4 variants, the dots and cross indicate their polarization direction towards or away from the observer, respectively.

Figs. 7.2(b)-(h) depict the domain structures for typical substrate thickness h_s. Each figure corresponds to a point marked on graphical Fig. 7.2(i), which represents the computed volume fraction of the c-domain (V_c) within the film at the equilibrium stage for different substrate heights h_s. From Figs. 7.2(b)-(h), it is apparent that the morphology of the domain changes with varying substrate height. However, it eventually stabilizes into a consistent configuration once the substrate height reaches a convergent value that cases only slightly changes in V_c. This observation aligns with the data plotted in Fig. 7.2(i), where V_c exhibits a decrease and finally converges to a constant value as h_s increases sufficiently. These findings indicate that the influence of the displacement boundary condition at $x_3 = -h_s$ on the domain evolution becomes negligible. To explain the simulated results, the average bulk driving force $f^*_{\mathrm{bulk}} = f^*_{\mathrm{elast}} + f^*_{\mathrm{elec}}$ and its elastic contribution f^*_{elast} of the thin film as a function of the substrate height have also been plotted in Fig. 7.2(i). Notably, both the elastic energy and the total bulk energy (the sum of the elastic and electrostatic energy) demonstrate a consistent decreasing trend, mirroring the behavior observed in V_c. This suggests that the driving force stemming from the elastic energy promotes and contributes to the stability of the a-domain across

various substrate deformation thicknesses. The substrate deformation results from the non-uniform deformations within the thin film, leading to the displacements in the substrate to approach zero at a sufficient distance from the substrate-film interface. This contributes to reduced elastic energy density, thus resulting in a decrease of c-domains.

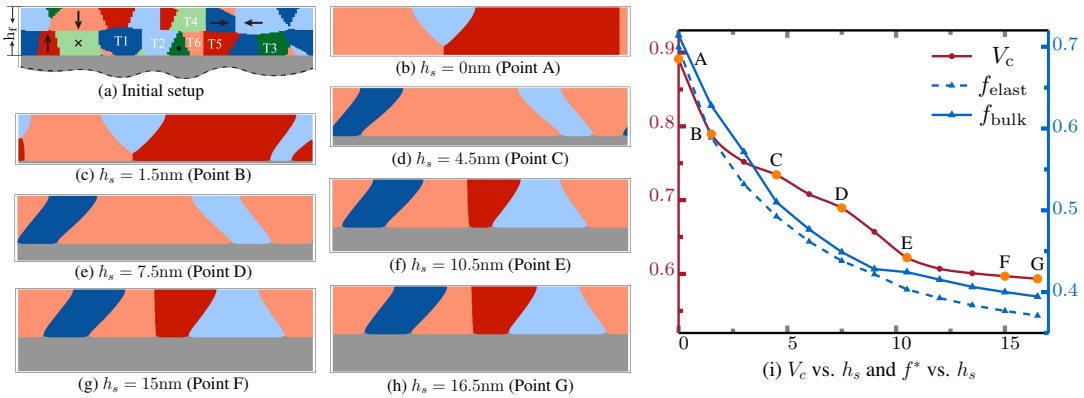

Figure 7.2.: (a) is the initial setup of the simulated 2D-film system. (b)-(h) are the computed domain structures for varying substrate height h_s in the equilibrium state. (i) illustrates the computed volume fraction of the c-domain (V_c), the dimensionless elastic energy (f^*_{elast}), and the summation of elastic energy and electrostatic energy (f^*_{bulk}). Domain morphologies from (b)-(h) correspond to the marked points A to G in (i). Adapted from Ref. [17].

Furthermore, the substrate thickness has a recognizable influence on the domain morphology, as shown in Figs. 7.2(b)-(h). At Point A, where the substrate height h_s = 0, a-domains are unable to exist near the film-substrate interface. Even for substrate heights h_s ranging from $1.5\,\text{nm}$ to $7.5\,\text{nm}$ (points B to D), the width of the a-domains near the surface appears slightly narrower. Interestingly, at h_s =$4.5\,\text{nm}$, the emergence of T2 is observed. As depicted in Figs. 7.2(f) to (h), as the substrate height changes from $10.5\,\text{nm}$ to $16.5\,\text{nm}$, both the $90°$ and $180°$ domain walls stabilize. Concurrently, the orientation of the domain walls between a-domains and c-domains shows a slight deviation from the ideal $45°$ angle relative to the film-substrate interface.

It is worth mentioning that the motivation for conducting these simulations was to determine the critical height of the substrate deformation, identified in the simulation as $h_s = 0.6h_f$. Beyond this threshold, the influence of substrate deformation on the domain structures of the film converges to a specific value. For large-scale simulations, knowing this critical value is important because it indicates that substrate thickness beyond this threshold has a negligible influence on the domain structures of films. Thus, by identifying this critical height as a key parameter to determine the substrate thickness corresponding to its film, efficient preservation of computing resources can

be achieved. Depending on the simulation results, the substrate height h_s was chosen as $0.75h_f$ in subsequent simulations.

7.3.2. Effects of substrate constraints on volume fractions and the morphology of domains

To study the influence of substrate constraints on the domain configuration and volume fraction of c-domains at room temperature, a 3D simulation was conducted in this subsection. The simulated system is fixed as $128\,\mathrm{nm} \times 128\,\mathrm{nm} \times 35\mathrm{nm}$, with a film thickness $h_f = 20\,\mathrm{nm}$ and substrate height $h_s = 15\,\mathrm{nm}$. The initial 3D setup is shown in Fig. 7.3, where each color in the thin film corresponds to a tetragonal variant, similar to the representation in Fig. 7.2. Additionally, the polarization direction for each variant can be cross-referenced in Fig. 7.1, in which the red color series represents the c-domains. The computed V_c, average $\bar{\varepsilon}_{33}$, and the domain morphologies under varying misfit strain are also shown in Fig. 7.3.

From the observations presented in Fig. 7.3, it is clear that the misfit strains significantly influence both the domain structures and the stability of polarization states across different orientations. For example, under significant tensile strain with a value of 0.012, the c-domain does not remain stable. Consequently, all domain walls between a_1- and a_2-domains align perpendicular to the film surface as well as follow the [110] or [$1\bar{1}0$] crystallographic directions. However, as the magnitude of misfit strain decreases (indicating a reduction in tensile strain), the c-domain starts to emerge, resulting in an increment in the volume fraction of the c-domains in its plotted profile. As a result, the equilibrium domain structures consist of both $a-$ and c-domains. Additionally, the domain walls between the a- and c-domains exhibit orientations that deviate slightly from the 45° angle relative to the film-substrate interface. Based on the simulated results in Fig. 7.3, it is additionally clear that a-domains can be absent when the film is subjected to a compressive misfit strain with an amplitude of 0.003 or more.

For misfits of $\varepsilon^{\mathrm{mis}} \geq 0.01$, the domain morphologies exhibit the typical 90° configurations characteristic of tetragonal compositions. In these cases, the polarization vectors are aligned parallel to the plane of the film, producing the characteristic stripe patterns. In contrast, for misfits of $\varepsilon^{\mathrm{mis}} \leq -0.001$, the domain morphologies display the typical watermark patterns associated with 180° domain configurations. In these instances with different domain variants, the polarization vectors are oriented perpendicular to the plane of the film, leading to the observed meandering domain walls. It is worth noting that the critical thresholds for the absolute magnitudes of compressive and tensile misfit strains, which are necessary to sustain either only c-domains or a-domains, are not the same. The difference can be attributed to the short-circuited boundary conditions imposed at both the top and bottom surfaces of the thin film. Such an observation aligns with earlier findings from TDGL-based phase-field simulations in Ref. [90], which sug-

gest that applying the short-circuited boundary conditions is a benefit for the stability of c-domains.

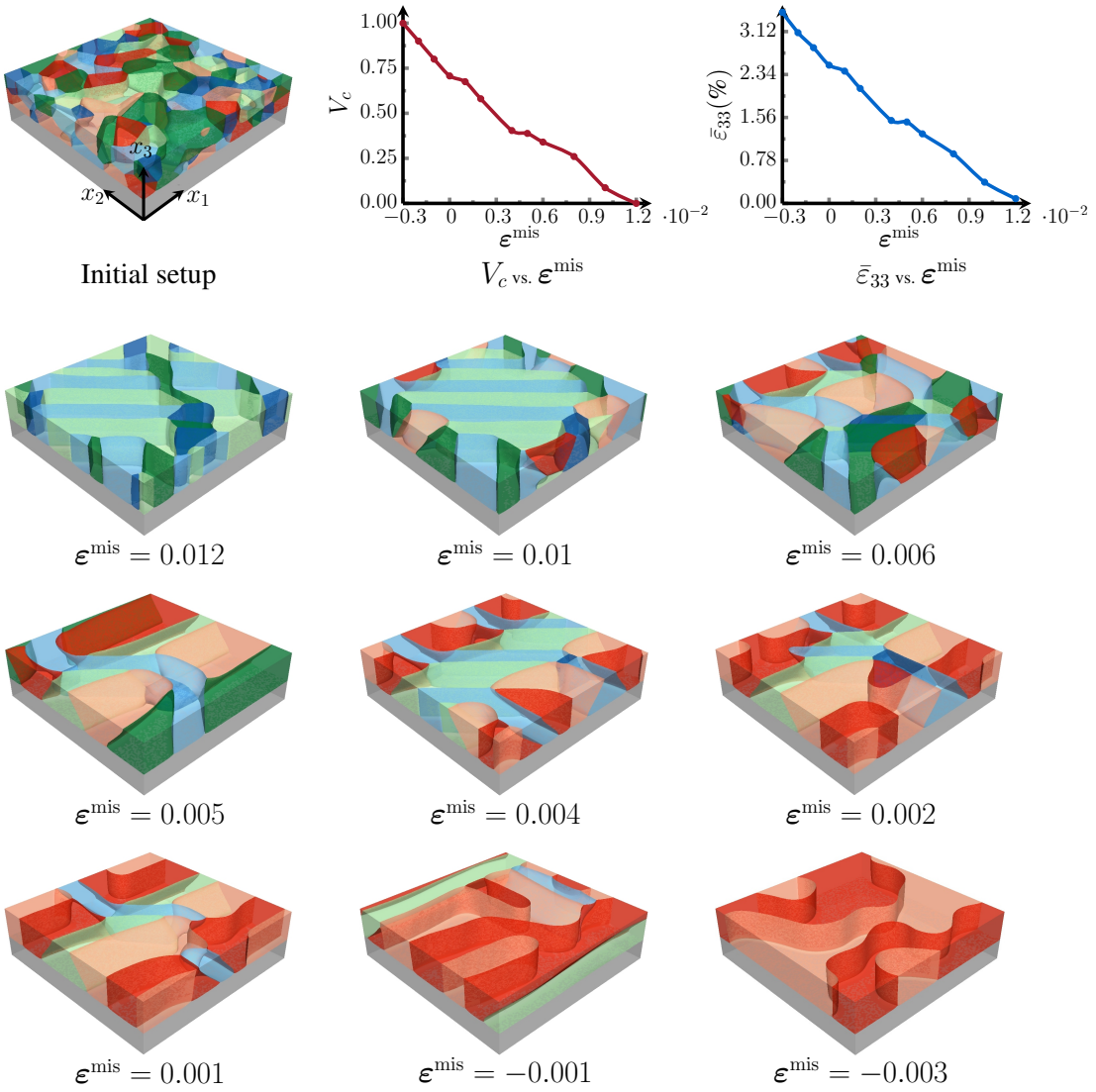

Figure 7.3.: The initial setup of the 3D structure for the current simulation, and the computed domain structures, the volume fraction of the c-domain, and $\bar{\varepsilon}_{33}$, under different misfit strains. Adapted from Ref. [17].

The average value of $\bar{\varepsilon}_{33}$ in the $\bar{\varepsilon}_{33}$ vs. $\varepsilon^{\mathrm{mis}}$ plot of Fig. 7.3 illustrates a significant decrease as the misfit strain shifts from the compressive to tensile value, which enhances the stability of the a-domains. Therefore, a similar varied shape can be observed in the plot of V_c versus $\varepsilon^{\mathrm{mis}}$. It should be mentioned that because of the use of the periodic boundary conditions along the x_1- and x_2-axes, both the average value of ε_{11} and

ε_{22} equal to zero. Therefore, these components are not considered in this paper. In order to investigate the formation mechanisms of domain structures under varying substrate constraints, the temporal evolution of domain structures formation at misfit strain of $\varepsilon^{\mathrm{mis}} \in \{0.012, 0.006, -0.003\}$ is further illustrated from Figs. 7.4 to 7.6. For a comparative analysis of how different constraints affect the final domain morphology, the associated evolution of the principal strains, ε_{11}, ε_{22}, and $\varepsilon_{33}$for each respective case, has also been included in Figs. 7.4 to 7.6.

As illustrated in Fig. 7.4, with a significant tensile strain $\varepsilon^{\mathrm{mis}} = 0.012$, the gradual disappearance of c-domains over time suggests that substrate confinement promotes the preferential formation of a-domains with the application of the short-circuited electric boundary conditions, in line with the above discussion. Upon examining the evolution of the principal strains, a significant decrease in ε_{33} becomes apparent, stemming from the unstable of c-domains. At the equilibrium state, it is evident that only the two principal strains which are aligned with the orientations of the a-domains remain. This observation underscores the notion that elastic energy has a strong influence in favoring the formation of the a-domains under large tensile constraints.

As the value of the misfit strain decreases from 0.012 to 0.006, the evolution of domain structures shown in Fig. 7.5 over time suggests the stability of both a- and c-domains, leading to the formation of a complex domain morphology at equilibrium. In this scenario, all principal strains are present evidently. Differing from the tensile constraint, the compressive constraint from the substrate with $\varepsilon^{\mathrm{mis}} = -0.003$ causes an absence of the a-domains, as depicted in Fig. 7.6. In comparison to Fig. 7.4, this alteration results in a complete change in the stability of a- and c-domains during the domain structures formation, finally characterizing the domain morphology with only c-domains. ε_{11} and ε_{22} disappear in this case, indicating that the compressive constraint strengthens the elastic driving force favoring c-domains while weakening it for a-domains.

The computed influence of substrate deformations and constraints on domain morphologies are in agreement with publications that employ the TDGL approach in Refs. [89, 90]. Thus, the following subsections will explore the domain structures associated with PTO growth on the real substrate KTO.

7.3.3. Impact of film thickness on domain structures

In this simulation, the (001)-oriented PTO films with varying thickness grown on KTO substrates were analyzed. The in-plane dimensions of the film were represented using a computational grid consisting of 128 cells along the x_1- and x_2-axes. In the above simulations, the ferroelectric film was assumed to be completely constrained by the underlying substrate. Except for the spontaneous stresses stemming from the ferroelectric phase transition, such an assumption leads to the emergence of internal stresses from the epitaxy. If the internal stresses caused by lattice misfit exceed a

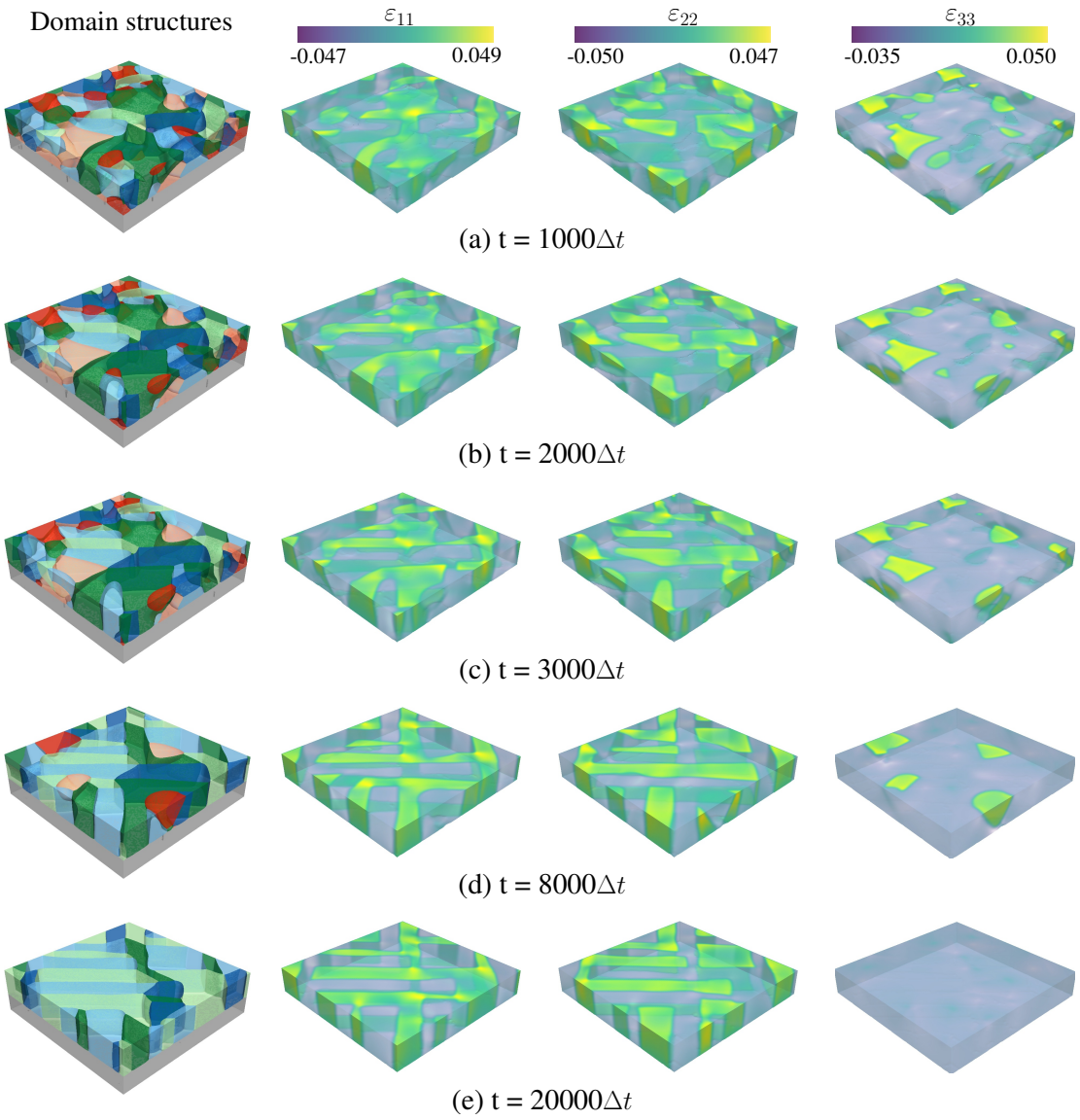

Figure 7.4.: The temporal evolution of domain structures, along with the associated ε_{11}, ε_{22}, and ε_{33}, at a misfit strain with a value of 0.012. Adapted from Ref. [17].

critical value, the internal stresses could be immediately relaxed. As a result, the above assumption becomes inappropriate in situations where internal stresses are excessively high, which may lead to an overestimation of the misfit strain. To address this issue, the misfit strain at room temperature was considered as thickness-dependent, denoted

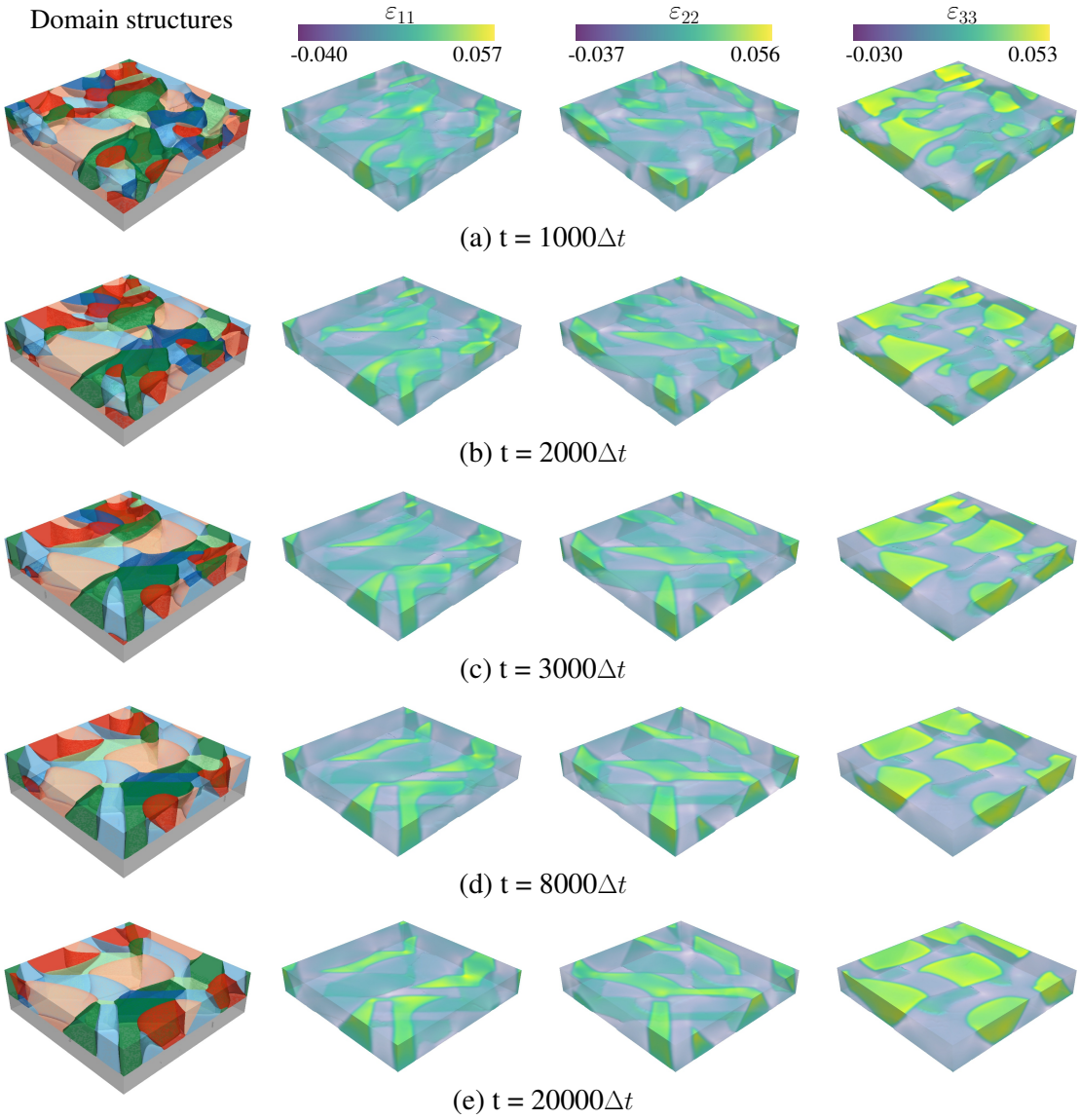

Figure 7.5.: The temporal evolution of domain structures, along with the associated ε_{11}, ε_{22}, and ε_{33}, at a misfit strain with a value of 0.006. Adapted from Ref. [17].

as $\varepsilon_{ij}^{\mathrm{mis}}(h)$ and expressed as:

$$\varepsilon_{ij}^{\mathrm{mis}}(h) = 1 - \frac{1 - \tilde{\varepsilon}_{ij}^{0}}{1 - \tilde{\varepsilon}_{ij}^{0}(1 - h_c/h)} \, (i, j = 1, 2, \text{ and } i = j). \tag{7.6}$$

$\tilde{\varepsilon}_{ij}^{0}$ illustrates the ideal misfit strain at room temperature, which is determined by Eq. (4.6). Based on the lattice parameters of cubic unstrained PTO (3.956 Å) and KTO

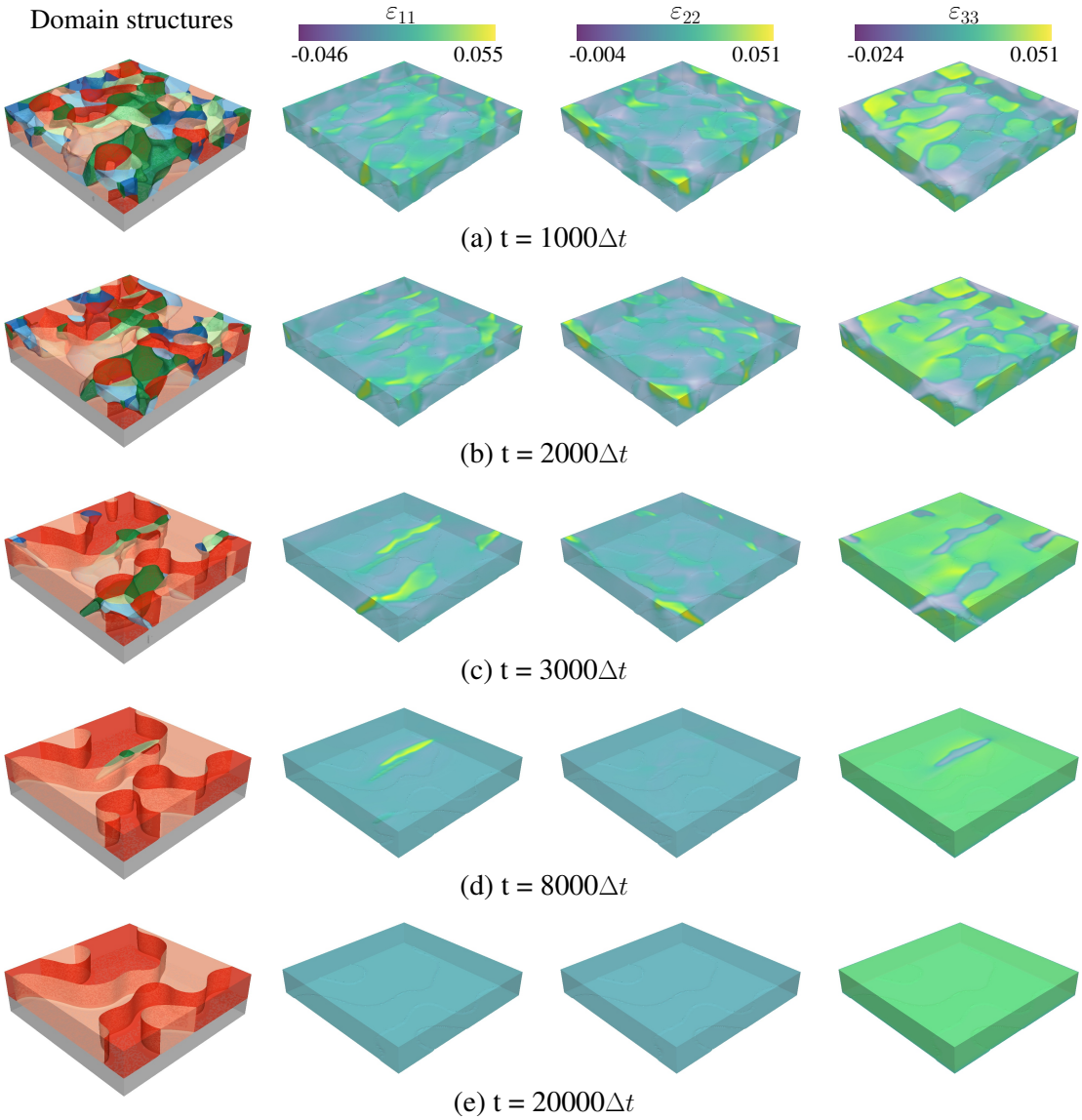

Figure 7.6.: The temporal evolution of domain structures, along with the associated ε_{11}, ε_{22}, and ε_{33}, at a misfit strain with a value of -0.003. Adapted from Ref. [17].

(3.989 Å) at room temperature [172], $\tilde{\varepsilon}^0_{ij}$ for PTO growing on KTO is calculated to be $0.83\,\%$. h_c in Eq. (7.6) is the critical thickness for the dislocation formation, which is derived by a People–Bean model [177, 178] in this work. The application for using the People–Bean model to calculate h_c can be found in Ref. [172], wherein the computed results in Figs. 1 and 3 are employed as a reference for this simulation.

Fig. 7.7 illustrates the computed domain morphologies, the dimensional elastic energy (f^*_{elast}), and the volume fraction of the c-domains (V_c), with varying film thickness. The

temporal evolution of domain structure formation and the associated ε_{11}, ε_{22} and ε_{33} for three film thicknesses, h_f = 10, 30, 50 nm, are additionally illustrated in Figs. 7.8 to 7.10. It is evident to observe that the domain morphologies depend on the film thickness. Besides, the reduction of the in-plane domains, a_1 and a_2 domains, was found to increase with the thickness of the film. This finding is consistent with the plotted V_c vs. h_f profile, which suggests that there is an increase in the volume of c-domains corresponding to larger film thicknesses. This phenomenon can be explained by reference to plotted f^*_{elast}, which demonstrates that f^*_{elast} is elevated with increasing film thickness.

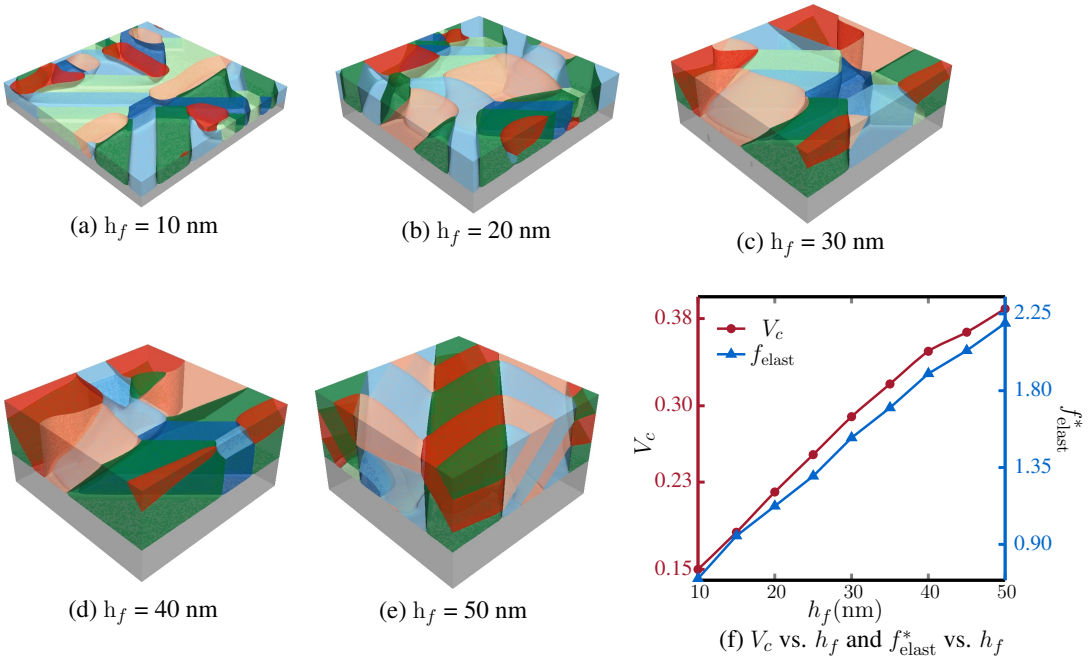

(a) h_f = 10 nm (b) h_f = 20 nm (c) h_f = 30 nm

(d) h_f = 40 nm (e) h_f = 50 nm (f) V_c vs. h_f and f^*_{elast} vs. h_f

Figure 7.7.: Computed result of (001)-oriented PTO epitaxial thin films with different thicknesses grown on KTO. (a)-(e) shows the domain structures with different thicknesses at the equilibrium state. (f) demonstrates the variations of f^*_{elast} as well as V_c with varying film thickness. Adapted from Ref. [17].

Depending on Fig. 7.8-7.10, it is easy to observe that the temporal evolution of films at different thicknesses (h_f = 10, 30, 50 nm) has an increasing tendency in the distribution of ε_{33} and a decreasing trend in ε_{11} and ε_{22}. This behavior explains the increment of c-domains with increasing film thickness. Specifically, the significant increase in the c-domains results from the strain relaxation in the system, with thicker films experiencing comparatively less strain than thinner films. It is worth noting that while the observed phenomenon of increasing c-domains with greater film thickness aligns with findings in Ref. [172], a quantitative inconsistency in the assessment of c-domains between this

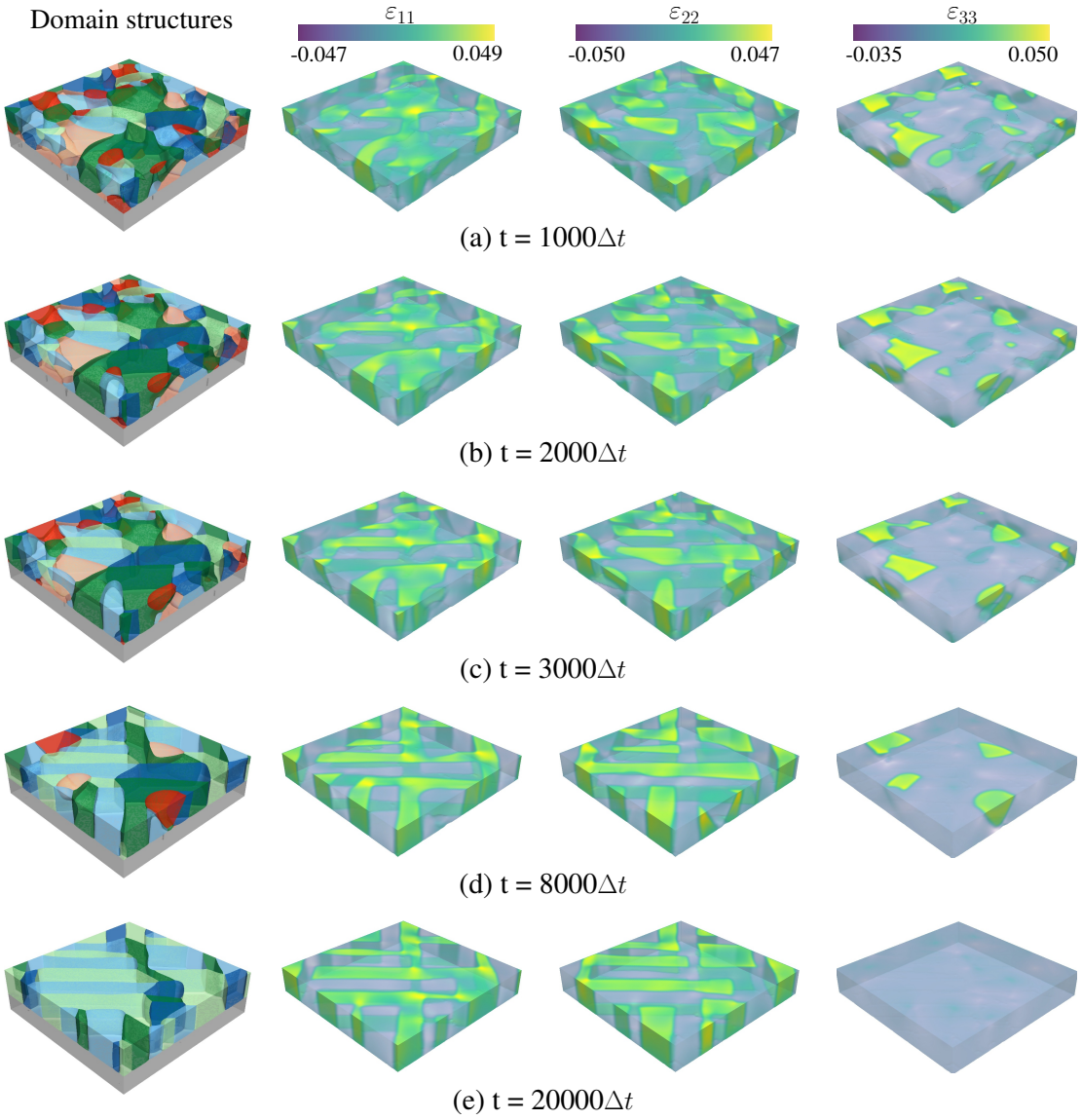

Figure 7.8.: The temporal evolution of the domain structure formation and the associated ε_{11}, ε_{22} and ε_{33} for a film thickness of $h_f = 10\,\mathrm{nm}$. Adapted from Ref. [17].

work and Ref. [172]. This could stem from applying short-circuited boundary conditions for solving electric fields, as it promotes the formation of c-domains, aligning with the outcome mentioned above. Thus, this condition determines a significant volume fraction of the c-domain, even when h_f is only 10 nm. Furthermore, the elastic tensor stiffness of KTO was used to replicate a real system during the simulation, while the details in Ref. [172] are not specified.

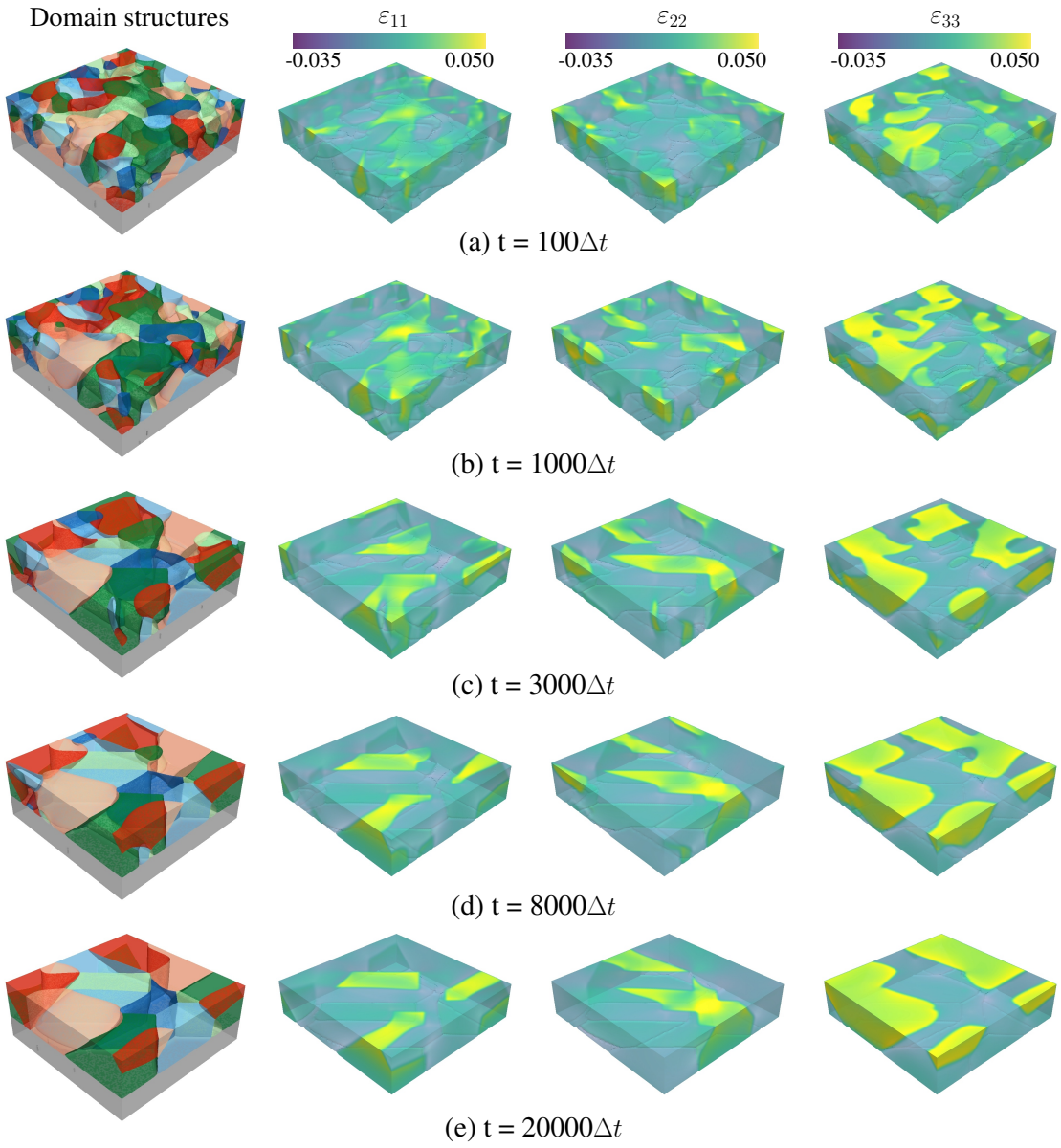

Figure 7.9.: The temporal evolution of the domain structure formation and the associated ε_{11}, ε_{22} and ε_{33} for a film thickness of $h_f = 30\,\mathrm{nm}$. Adapted from Ref. [17].

7.3.4. Temperature-dependent domain fraction and configuration

In this study, domain structures were investigated during the growth of (001)-oriented PTO films with 128×128×40 cells (20 cells for the PTO film) on KTO substrates under varying temperatures. Given that temperature influences thermal expansion, thermal vibrations, and phase transitions, it is expected that the magnitude of both the sponta-

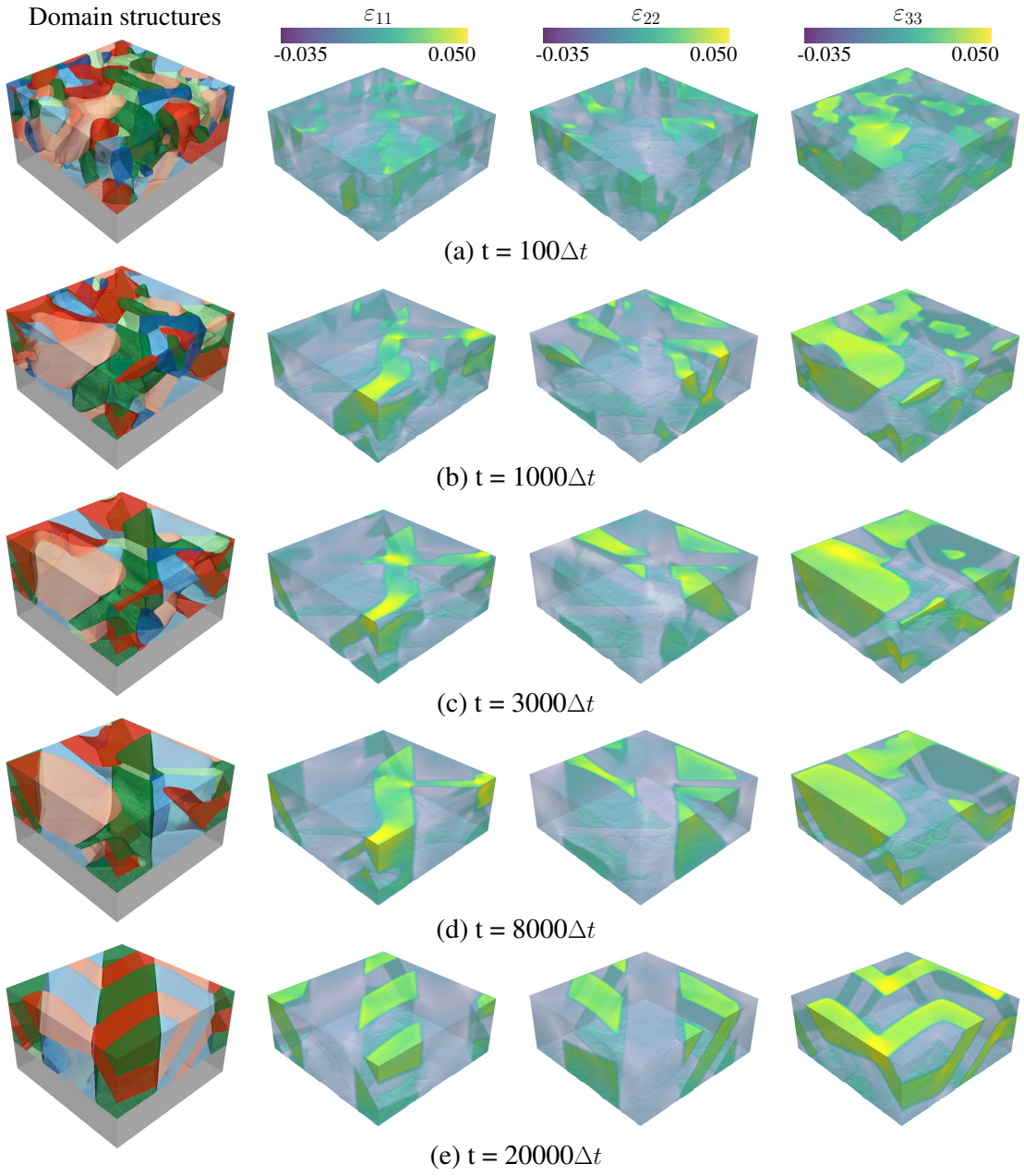

Figure 7.10.: The temporal evolution of the domain structure formation and the associated ε_{11}, ε_{22} and ε_{33} for a film thickness of $h_f = 50\,\mathrm{nm}$. Adapted from Ref. [17].

neous polarization and inelastic strain depend on the temperature. The effect of high temperatures on the spontaneous polarization of PTO has been previously investigated in Ref. [63], which provides a reference for the present simulation. As the thermal

expansion properties of PTO and KTO are different, the corresponding misfit strain between them at different temperatures is respectively defined as:

$$\begin{aligned} \tilde{\varepsilon}_{ij}^{\mathrm{mis},f} &= \tilde{\varepsilon}_{ij}^{0} + \alpha_f \Delta T, \\ \tilde{\varepsilon}_{ij}^{\mathrm{mis},s} &= \tilde{\varepsilon}_{ij}^{0} + \alpha_s \Delta T, \end{aligned} \tag{7.7}$$

where $i,\ j\ = 1,\ 2$ and $i = j$. In Eq. (7.7), α_f and α_s are the thermal expansion coefficients for PTO and KTO, respectively, as provided in Table 7.1. $\tilde{\varepsilon}_{ij}^{0} \approx 0.83\,\%$ is the mismatch between PTO and KTO at room temperature, as discussed in the above subsection. ΔT represents the temperature difference between the calculated temperature and the room temperature. By Eq. (7.7), the graphical representation of the temperature-dependent misfit strains of the PTO and KTO systems is plotted in Fig.7.11(a). Furthermore, the lattice distortion used to evaluate the electrostatic coefficients has the same temperature-dependent profile as the spontaneous polarization, which leads to subtle changes in the electrostatic coefficients [63]. Therefore, the electrostatic coefficients are considered to be temperature-independent, and the variations in spontaneous strain are primarily attributed to changes in spontaneous polarization induced by temperature.

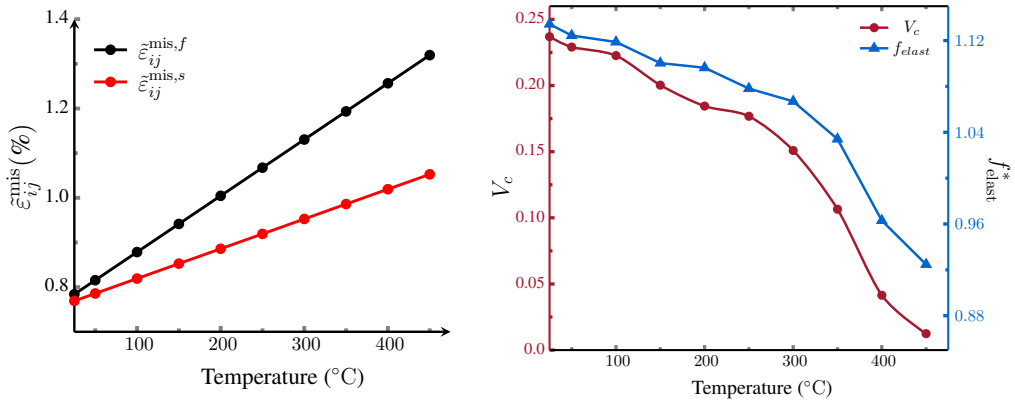

(a) ε_{ij}^{mis} vs. Temperature

(b) V_{c} & f_{elast} vs. Temperature

Figure 7.11.: (a) illustrates the temperature-dependent elastic strain of the PTO and KTO systems without considering the spontaneous strain. (b) demonstrates the variation of the average elastic energy density (f^*_{elast}) and the volume fraction of the c-domain (V_c) with temperature. Adapted from Ref. [17].

The initial configuration was taken from Fig. 7.3 and a homogeneous temperature distribution is assumed for each simulation. The computed volume fraction of the c-domain and average elastic energy was illustrated in Fig. 7.11(b), while the domain configurations at the equilibrium of different temperatures were shown in Fig. 7.12.

Fig. 7.12(a) demonstrates the temperature-dependent variations in the domain morphologies, showing a significant decrease in the c-domain as temperature increases. Referring to Fig. 7.11, it is evident that the magnitude of misfit strain increases with temperature for both PTO and KTO materials. Building upon the above subsection, it has been deduced that the tensile misfit promotes the formation of a-domains, therefore leading to a decrease in c-domains at higher temperatures. It can also be observed from Fig. 7.11(a) that the different thermal expansion of PTO and KTO result in different amplitudes of the increase in eigenstrain. This helps to maintain the stability of c-domains. Therefore, c-domains can still be observed even at the elevated temperature of $400\,^{\circ}\mathrm{C}$, in which the PTO film has a tensile misfit strain of 0.0125. This contrasts with the findings in Fig. 7.3, where it was found that the stability of the c-domain could not be maintained when $\varepsilon^{\mathrm{mis}} = 0.012$.

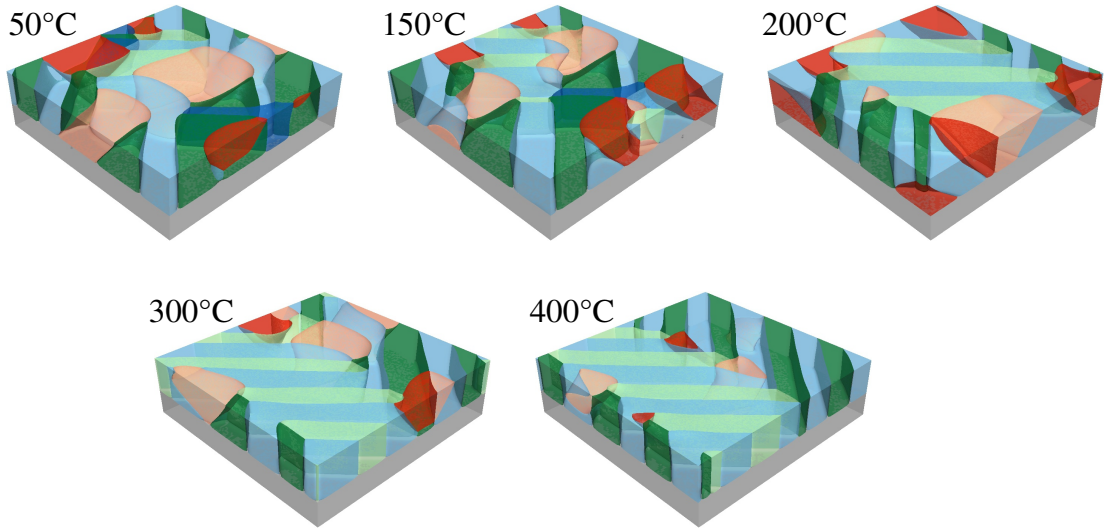

Figure 7.12.: Domain structures of (001)-oriented PTO epitaxial thin films growing on the KTO substrate, at different temperatures. Adapted from Ref. [17].

As shown in Fig.7.11(b), the dark red line demonstrates that the computed V_c shows a decrease with increasing temperature, which is in agreement with the expected variation in domain configurations. The observed phenomenon is also consistent with the findings in Ref. [179]. In Fig. 7.11(b), the dark blue line depicts the variation of the average elastic energy density of the thin film with temperature. It is evident that f^{*}_{elast} decreases with increasing temperature, showing a similar trend as V_c vs. temperature. The computed results in Fig. 7.2 clearly suggest that a higher average elastic energy f^{*}_{elast} within the thin film system contributes to the formation and stability of c-domains. The increasing magnitude of inelastic strain results in a reduction of elastic energy within the thin film, as temperature increases. This decrease in elastic

energy subsequently diminishes the driving force responsible for the transformation from the a-domains to the c-domains. As a result, c-domains decrease, and the system reaches an equilibrium with different domain configurations at higher temperatures, driven by the minimization of the total energy. It is worth mentioning that the electric energy also decreases with increasing temperature. Nonetheless, due to its relatively minor influence on the overall analysis, it was not included in the context. The temporal evolution of domain structure formations and the corresponding ε_{11}, ε_{22}, and ε_{33} are represented in Appendix. A.3. There is a clear trend where the distribution of ε_{33} shows a decreasing pattern as temperatures increase. This indicates a decrease in elastic energy correlated with increasing temperature. Therefore, the observed decrease in the occurrence of c-domains is linked to higher temperatures.

7.4. Advantages and limitations of Model II for investigating domain structures in ferroelectric thin film

The advantages of Model II have been previously discussed in Section 6.5. This section will present an extension of those advantages and limitations for modeling ferroelectric thin films, which is achieved by comparison with the TDGL model.

As it solves for the polarization vector, the TDGL model could be employed to predict the equilibrium polarization state at varying temperatures or under different constraints, enabling the computation of misfit strain–temperature phase diagrams like Ref. [89]. However, given that the domain structures are computed by minimizing the energy functional with regard to polarization, the polarization vector undergoes a temporal evolution, which results in an inhomogeneous distribution of polarization within a single domain. The polarization state is predefined for each ferroelectric variant in Model II, leading to the polarization within each variant remaining homogeneous. This is more realistic compared with the TDGL model. Whereas, the orientation and magnitude of polarization for the ferroelectric variants are predefined in Model II with the current format, preventing the calculation of the misfit strain-temperature phase diagram as demonstrated in Ref. [89]. Instead, to explore domain morphologies of films at specific temperatures alongside corresponding misfit strains, such a phase diagram can be used as a reference for predetermining the polarization state for ferroelectric variants. The predetermination data can also be obtained through experimental determinations or other theoretical simulations such as first-principle calculations. The absence of polarization evolution within a single domain could enhance computational efficiency by allowing a large time-scale factor to be selected while maintaining system stability. Model II is based on the multiphase-field concepts, which enable the simulation of large-scale phenomena such as martensite transformations, as demonstrated in Ref. [134].

7.5. Conclusion

In summary, this chapter has advanced the application of Model II to study PTO thin films. In contrast with the periodic boundary conditions employed in Chapter 6 for bulk materials, the specific boundary conditions were implemented at the top and bottom of the system in order to simulate a constraint film. Using the jump condition approach provides an accurate scheme for calculating the mechanical field across the film and substrate, allowing the easy capture of the misfit strain between the film and substrate. The simulation starts with analyzing substrate deformation, where its influence on domain morphologies converges to a critical substrate height. As expected, the domain structures vary when subjected to different misfit strains. In the case of tensile misfit strain, the a-domains are favored, while compressive misfit strain enhances the stability of c-domains. Furthermore, the research was expanded to study the growth of PTO on KTO, incorporating a range of film thickness and temperatures. The simulations reveal an increasing distribution of c-domains in conjunction with either a higher film thickness or a lower growth temperature.

8. Domain structures in $MAPbI_3$ material

8.1. Introduction

Properties such as efficient charge separation and transport discovered in Organic metal halide (OMH) perovskites have made this class of material ideal for use in solar cells [180–183]. Up to now, several computational studies have investigated the crystal properties of $MAPbI_3$, to understand the fundamental mechanisms behind the exceptional charge carrier dynamics of OMH materials [184–186]. These studies suggest that $MAPbI_3$ may exhibit ferroelectric properties. Upon cooling, $MAPbI_3$ exhibit centrosymmetric cubic (Pm3m, paraelectric phase), non-centrosymmetric tetragonal (I4cm, ferroelectric phase) and orthorhombic (Pna21, ferroelectric phase) crystal structures [187, 188]. For solar cell applications, the relevant phases are the room-temperature-stable tetragonal and the high-temperature cubic that is stable above $327\,\mathrm{K}$. Fig. 8.1(a) depicts the tetragonal crystal structure of $MAPbI_3$ at room temperature, taken from Ref. [47]. The unit cell of $MAPbI_3$ consists of two perovskite cubes with slightly twisted PbI_6 octahedrons (shown in purple). Due to the $0.5\,\%$ strained along the c-axis, the quasi-cubic perovskite lattice adopts a tetragonal crystal structure.

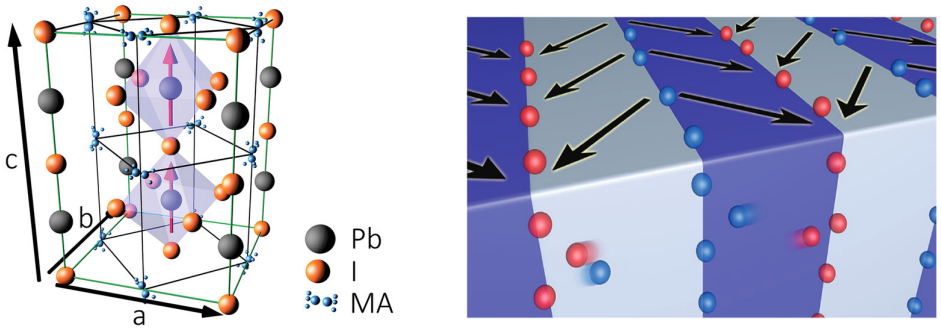

(a) (b)

Figure 8.1.: (a) is the schematic diagram of the $MAPbI_3$ tetragonal unit cell at room temperature (green frame), in which the red arrows indicate the polarization direction along the c-axis and the black frames indicate the pseudocubic perovskite lattice. (b) represents the charged domain walls and the associated separation of electrons and holes. Both (a) and (b) are adapted from Ref. [47].

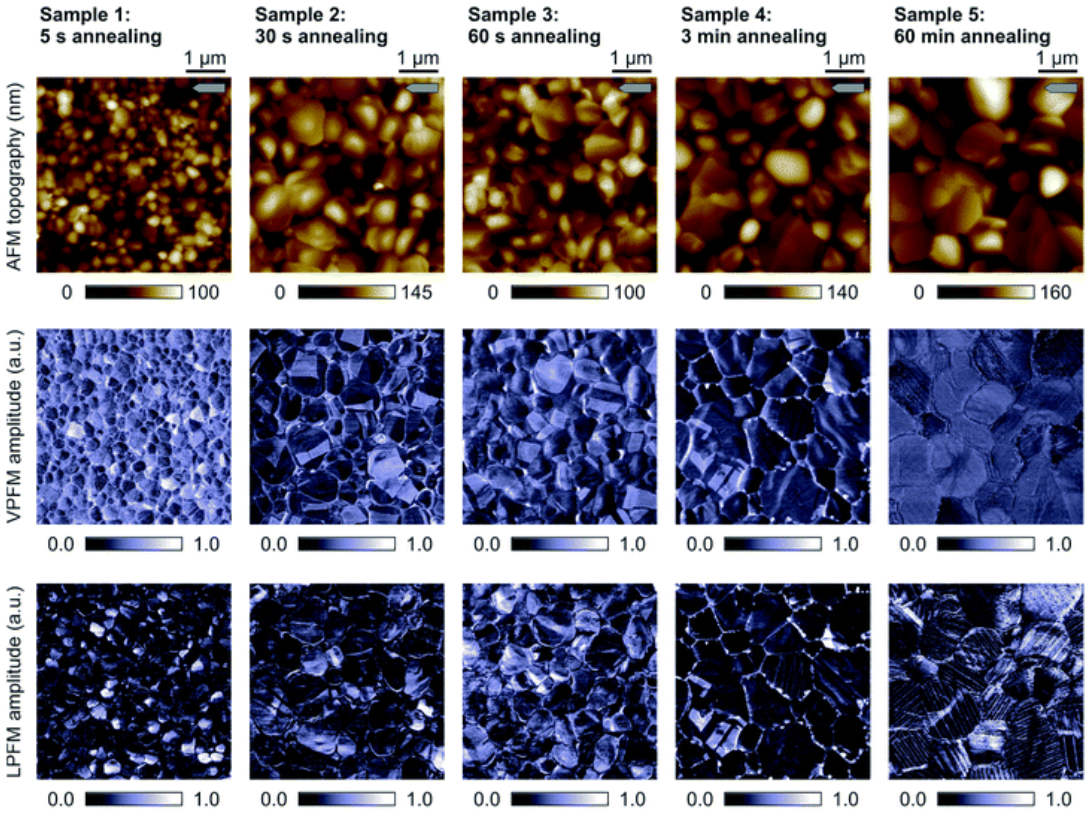

Figure 8.2.: Effects of thermal annealing on polycrystalline $MAPbI_3$ thin films. Samples 1–5 (left to right) annealed for 5 s to 60 min showed changes in grain sizes and domain structures. Atomic force microscopy (AFM) topography, Vertical PFM (VPFM) and Lateral PFM (LPFM) amplitude are shown in rows, with cantilever orientation indicated by a small grey arrow. Grain growth was most pronounced within the first 30 s (samples 1 and 2). Sample 1 initially had uniform vertical and lateral ferroelectric polarization due to small grain size and varied surface facets. With longer annealing and increased grain size, polarization evolved to a predominant lateral orientation with alternating domains in sample 5. Adapted from Ref. [189].

On the one hand, 90° ferroelastic and 180° ferroelectric domain walls are known to form for minimizing energy within the tetragonal phase. Early investigations predicted that these domain walls have a positive influence on solar cell properties by creating separate charge carrier pathways. Such pathways are energetically favorable for electrons or holes, thus reducing charge carrier recombination losses. Specifically, forming head-to-head and tail-to-tail charged domain walls can create a built-in electric field that drives electrons and holes apart toward different domain walls, reducing the

overall charge carrier recombination rate. A schematic diagram of such domain walls and their associated electron-hole separation is illustrated in Fig. 8.1(b) [190].

On the other hand, the correlation between ferroelectric polarization and device performance discussed in Ref. [189] suggests that the configuration and evolution of ferroelectric domains should be considered a critical mechanism affecting solar cell characteristics. Leonhard *et al.* in Ref. [189] investigated the grain growth and formation of domain structures under different annealing processes and their associated effects on solar cell properties. As shown in Fig. 8.2 (adapted from Ref. [189]), it has been found that vertical domains (c-domains) become unstable with increasing annealing time due to grain growth. This instability influences the current density-voltage characteristics of the materials. Solar cells with alternating lateral domains (a-domains) exhibit the best fill factors and efficiencies. In contrast, solar cells with shortly-annealed $MAPbI_3$ thin films and c-domains show only moderate performance.

Given the above reasons, it is evident that understanding the mechanism of domain structure formation and manipulating domain walls are crucial for the application of $MAPbI_3$ materials. The intricate crystal structure in $MAPbI_3$ obscures the determination of its Landau coefficients, which has impeded the investigation of domain structures using the TDGL equation. Model II has successfully investigated ferroelectric bulk and thin film materials without relying on Landau coefficients, as discussed in Chapters 6 and 7. Consequently, this chapter aims to further employ it to explore the domain structure formation in $MAPbI_3$ film.

8.2. Simulation setup

It was confirmed that the constraint from the substrate does not influence the domain structures in polycrystalline $MAPbI_3$ thin film. Therefore, simulations in this chapter consider a rigid-body film by setting substrate height (h_s) to zero, so as to streamline the simulated system and reduce the computational time. All simulations are conducted in Pace3D as well. The calculating process is referred to in Fig. 6.1, and the approach for solving each governing equation is detailed in Section 7.2. Again, the initial setups of the film structures were created by Voronoi tessellation, and the computed region was discrete with a MPI standard during the simulation.

Similarly to PTO simulations, all fields are solved by employing periodic boundary conditions along the x_1 and x_2 axes and Neumann type boundary condition is imposed for solving ϕ at the top and bottom surfaces of the film. The open-circuited electric boundary conditions are applied at both the top and bottom surfaces when solving for the electric field, denoted as:

$$\begin{aligned} &D_3|_{x_3=0,\, x_3=h_f} = 0, \\ &\nabla\psi \cdot \boldsymbol{e}_3 = 0. \end{aligned} \tag{8.1}$$

To reduce the depolarization field, the polarization is set as zero at the upper and lower surfaces of the film, denoted as:

$$\boldsymbol{P}|_{x_3=0,\, x_3=h_f} = \mathbf{0}. \tag{8.2}$$

In addressing the mechanical field solution, the stresses on the top surface were set freely based on Eq. (7.4). Conversely, the bottom of the film was constrained by:

$$\boldsymbol{u}|_{x_3=-h_s} = \mathbf{0} \tag{8.3}$$

Table 8.1.: Material parameters of $\mathrm{MAPbI_3}$ material for the phase-field simulation (TW: This work).

Material Coefficients	Symbol	Value	Unit	Ref
Spontaneous polarization	P_s	0.12 ($\pm$0.27/$\pm$0.04)	$\mu\mathrm{C/cm^2}$	[191]
Elastic tensor	$\mathcal{C}_{11}$	21.8	$10^9\cdot[\mathrm{N/m^2}]$	[192]
	$\mathcal{C}_{12}$	11.3	$10^9\cdot[\mathrm{N/m^2}]$	[192]
	$\mathcal{C}_{44}$	7.8	$10^9\cdot[\mathrm{N/m^2}]$	[192]
Spontaneous strain	$x_{\mathrm{FT},1}$	-0.00303	-	[191]
	$x_{\mathrm{FT},3}$	0.00609	-	[191]
Electrostrictive stiffness	$\mathcal{Q}_{11}$	0.423	$\mathrm{m^4/C^2}$	TW
	$\mathcal{Q}_{12}$	-0.210	$\mathrm{m^4/C^2}$	TW
	$\mathcal{Q}_{44}$	1.267	$\mathrm{m^4/C^2}$	TW
Interfacial energy	$\gamma_{\alpha\beta}$	0.01	$\mathrm{J/m^2}$	TW
-	γ^c_α	0.01	$\mathrm{J/m^2}$	TW

The computational geometry was divided into cells with different dimensions in the in-plane and out-of-plane. Specifically, Δx_3 was set to $2\,\mathrm{nm}$, while Δx_1 and Δx_2 were set to $4\,\mathrm{nm}$. ϵ was set to a value of $3.75\Delta x_1$. Due to the lack of the dielectric constant α_0 in $\mathrm{MAPbI_3}$ for competing for the domain wall energy density, the interfacial energy density parameter $\gamma^{\alpha\beta}$ was selected to ensure numerical stability during the simulation. Similarly, γ^c_α was assigned the same value as $\gamma^{\alpha\beta}$. The dimensionless value of the mobility coefficient $M^{\alpha\beta}$ in Eq. (4.11) was set to one to govern the dynamic of domain formation within the film. The required material coefficients of $\mathrm{MAPbI_3}$ in the current simulation are listed in Table 8.1.

Based on Section 4, the absolute value of the spontaneous polarization (P_s), the elastic and electrostrictive stiffness coefficients are also required to determine the bulk energy density, except for the above-mentioned parameters. The material was deemed isotropic, and the value of the elastic stiffness coefficients was derived from Ref. [192]. The value of $|P_s|$ as determined by Ref. [191] is listed in Table 8.1. It has been found that P_0 was determined to be $0.12\,\mu\mathrm{C/cm^2}$ with an associated error of $0.27\,\mu\mathrm{C/cm^2}$,

approximately twice the magnitude of P_0. Such a considerable error can be attributed to the large positional uncertainty of the $\mathrm{CH_3}$-$\mathrm{NH_3}$ groups, whose positional error is about an order of magnitude greater than that of the other atoms. Excluding these groups, the error would be around $0.04\,\mu\mathrm{C/cm^2}$. P_0 was chosen to be $0.12\,\mu\mathrm{C/cm^2}$ for this simulation. Additionally, with the determined spontaneous strain from Table 8.1, the electrostrictive stiffness coefficients $\mathcal{Q}_{11}$ and $\mathcal{Q}_{12}$ (Voigt notation) were calculated on the basis of Eq. (5.8). $\mathcal{Q}_{\mathrm{FT},44}$ was derived under the isotropic condition in Eq. (5.18). Relying on Eq. (6.3), all input coefficients for the phase-field modeling were transformed into dimensionless values during the simulation.

8.3. Results

8.3.1. Phase-field simulation of a single-crystal thin film

Simulations were conducted on a single-crystal thin film with dimensions of $512\,\mathrm{nm} \times 512\,\mathrm{nm} \times h_f$, in which film thickness h_f ranges from $80\,\mathrm{nm}$ to $140\,\mathrm{nm}$ with an interval of $10\,\mathrm{nm}$. The resulting domain structures and the computed average f^*_{elast} and ψ^* are demonstrated in Fig. 8.3, where the variant of each color and its corresponding polarization orientation are referenced in Fig. 7.1 (c). Firstly, the absence of c-domains is evident, which can be attributed to the assumption of a complete compensation of the free charge on the top and bottom surfaces of the film. Without polarization flux, the driving force from the electric energy favors the formation of a-domains. This observation aligns with the findings in Ref. [189], within which the vertical domains can not remain stable as annealing time increases. In addition, it is easily found that the domain morphologies vary with different film thicknesses. The domain structures become more complex with narrower domain widths at smaller film thicknesses, while simpler structures with wider domains can be seen at larger film thicknesses.

The plotted f^*_{elast} vs. h_f and ψ^* vs. h_f provide an interpretation of these observations. In the absence of polarization flux at the top and bottom surfaces of the film, and in accordance with the periodic boundary conditions applied along x_1 and x_2, the average f^*_{elec} is consistently zero. Consequently, to compare the contributions from electric energy, the average electric potential ψ, which quantifies the contribution of electric energy to domain structure formation, is considered in this work. It has been demonstrated that electric energy plays a critical role in the formation of ferroelectric domain walls, specifically $180°$ domain walls. Conversely, the ferroelastic domain walls (non$180°$ domain walls) are predominantly governed by elastic energy. The increase in f^*_{elast} and the decrease in ψ with increasing film thickness thus leads to the reduction and disappearance of $180°$ domain walls, resulting in the formation of only $90°$ domain walls at high film thicknesses. It should be noted that simulations were also performed for film thicknesses greater than $140\,\mathrm{nm}$, such as $200\,\mathrm{nm}$, but the domain configurations

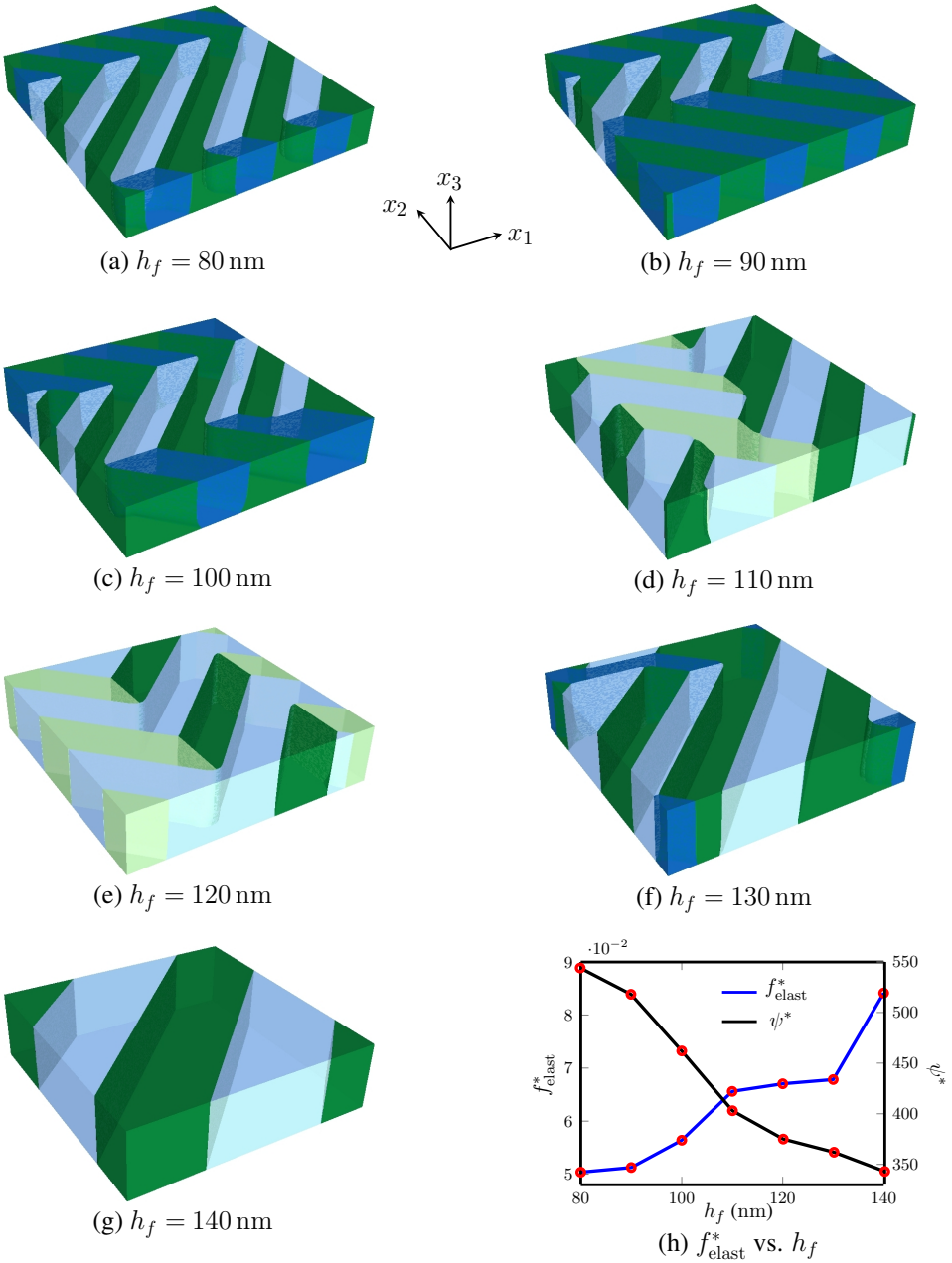

(a) $h_f = 80\,\text{nm}$ (b) $h_f = 90\,\text{nm}$ (c) $h_f = 100\,\text{nm}$ (d) $h_f = 110\,\text{nm}$ (e) $h_f = 120\,\text{nm}$ (f) $h_f = 130\,\text{nm}$ (g) $h_f = 140\,\text{nm}$ (h) f^*_{elast} vs. h_f

Figure 8.3.: Simulations of single-crystal $MAPbI_3$ thin films with varying film thickness. (a)-(g) shows the domain morphologies, while (h) represents the computed average f^*_{elast} and ψ^* across film thicknesses.

were identical to those observed at $140\,\text{nm}$. Therefore, the results for these thicker films are not shown.

8.3.2. Phase-field simulations of polycrystalline thin film

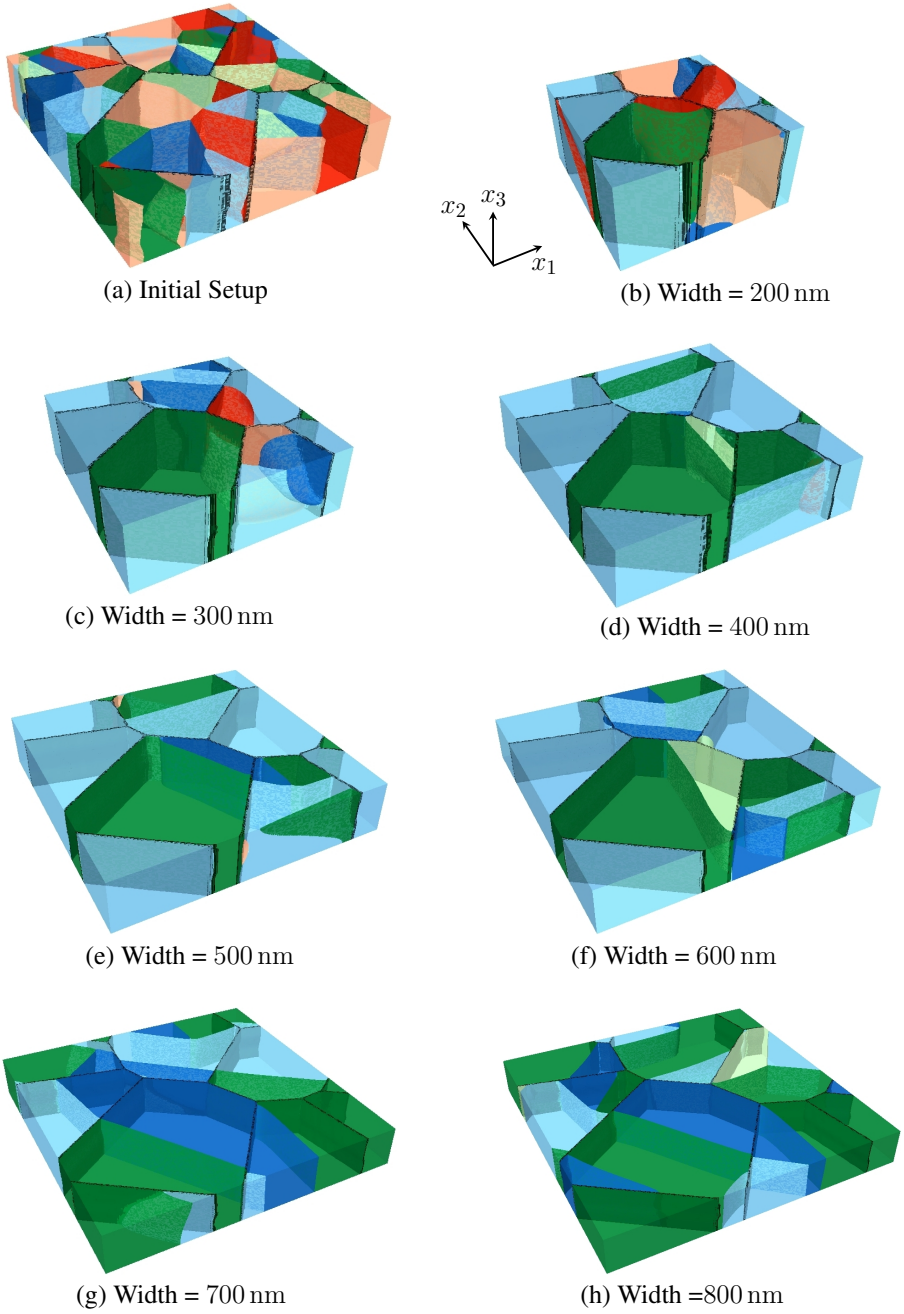

(a) Initial Setup (b) Width = 200 nm

(c) Width = 300 nm (d) Width = 400 nm

(e) Width = 500 nm (f) Width = 600 nm

(g) Width = 700 nm (h) Width =800 nm

Figure 8.4.: (a) is the initial setup of a polycrystalline $MAPbI_3$ thin film composing four grains, where grains are rotated only along the x_3-axis; (b)-(h) are equilibrium domain structures with varying in-plane width, with h_f set to 40 nm in each simulation.

Fig. 8.4 shows simulations of the polycrystalline $\mathrm{MAPbI_3}$ thin film, which includes four grains separated by grain boundaries illustrated as black. The initial setup is demonstrated in Fig. 8.4(a), in which six tetragonal variants are randomly assigned in each domain. The grain orientation in the x_3-direction barely exists, as described in Ref. [193], grains are thus only rotated along the x_1x_2-plane in the current simulation. Red regions in Fig. 8.4(a) still represent the c-domains. To simulate domain structure formation with different grain sizes, the film thickness was kept as $40\,\mathrm{nm}$, while the in-plane width varied from $200\,\mathrm{nm}$ to $800\,\mathrm{nm}$. As a result, each grain has an average size with a diameter ranging from $50\,\mathrm{nm}$ to $200\,\mathrm{nm}$. The noise function in Eq. (4.16) is activated to obtain a self-consistent domain configuration in each grain, with the nucleation time step set to 2000 and a frequency of 200 time steps.

Fig. 8.4 (b)-(h) represent the computed domain structures. It is evident that c-domains become unstable with grain growth. For instance, a substantial number of c-domains can be observed when the grain diameter is approximately $50\,\mathrm{nm}$. However, they gradually decrease from $75\,\mathrm{nm}$ to $125\,\mathrm{nm}$ and ultimately vanishes as the grain diameter reaches $150\,\mathrm{nm}$. Furthermore, it can be observed that a complex domain configuration consisting of both $90°$ and $180°$ domain walls, rather than a single domain, can be formed and stable with grain growth. These findings are consistent with the experimental observations presented in Ref. [189], which concluded that due to the small grain diameters and diverse surface facets, each grain exhibits uniform $a-$ and $c-$ domains. Concurrently, the polarization changes and evolves towards a predominant in-plane orientation with alternating domains upon grain growth.

8.4. Conclusion

This chapter presents single-crystal and polycrystalline simulations to investigate $\mathrm{MAPbI_3}$ thin films. For the single-crystal simulations, films of varying thickness were considered. The results indicate that c-domains are unstable when polarization is fully compensated at the top and bottom surfaces of the film. Moreover, the domain width increases with film thickness, with domain configurations transitioning from complex to simpler forms as thickness increases. In the polycrystalline simulations, variations in in-plane width were implemented to model grain growth. It was observed that the out-of-plane domains are present in films with small grain sizes but gradually decrease and eventually disappear as the grains grow. Furthermore, in films with large grain sizes, domain structures are characterized by the presence of both $90°$ and $180°$ domain walls. All simulations are consistent with experimental observations, thus providing a fundamental framework for investigating domain structures in $\mathrm{MAPbI_3}$ thin films.

Part IV
Conclusion and Outlook

9. Conclusion and outlook

9.1. Conclusions and remark

In this dissertation, two models, Model I and Model II, were created to investigate ferroelectric materials.

Model I couples the multiphase-field approach with the LGDT. Both polarization vectors and phase-field ϕ are the order parameters in Model I, and the domain structures are formed by evolving polarization. Using this model, the evolution of domain structures and the corresponding phase transformation between FT and FR in PIC 151 material under the influence of external stimuli has been investigated, as detailed in Chapter 5. To calculate the phase transformation driving force, the phenomenological coefficients for FT and FR are determined separately based on the experimental examination and the designed numerical energy overlap. The simulated results reveal that polarization switching is the first response with the application of an external electric field, followed by the corresponding phase transformation. This suggests the synergistic effect between the polarization switching and phase transformation. Besides, the single crystal simulation suggests the predominate of the tetragonal phase in the PIC 151 material, which is in agreement with the experimental observation. Moreover, the simulations of the polycrystalline system show that the phase transformation is bi-directional between FT and FR, decided by the grain orientations. In general, Model I has provided a foundational framework for investigating domain structures in coexisting ferroelectric phases by considering polarization evolution.

Model II was designed to compute domain structures of ferroelectric materials based on the multiphase-field concept, where the polarization state of each variant was predetermined during the simulation and the domain structures are calculated by evolving the phase-field ϕ. Using Model II, Chapter 6 investigates the formation of domain structure in both single-crystal and polycrystalline BTO materials. The mechanism of domain switching was also studied under the influence of external electric fields and mechanical loading in these systems. Based on these investigations, the hysteresis loops in BTO material are further computed. Chapter 6 has also offered examples for adding thermal fluctuations to mimic the variant nucleation under different scenarios. Model II was also extended to investigate ferroelectric thin films, as demonstrated in Chapters 7 and 8. In Chapters 7, the (001)-orientated PTO film has been investigated when considering it grows on a cubic substrate. The influence of substrate deformation,

substrate constraints, film thicknesses, and growth temperature on domain structure formation has been studied systematically. By analyzing the driving force, Model II enables the exploration of the mechanism behind domain structure formation under these conditions. Chapter 8 illustrates the simulation of single-crystal $MAPbI_3$ films under varying film thickness and polycrystalline $MAPbI_3$ films with varying in-plane width. This highlighted the application of Model II because it showcases its significant advantage—the ability to calculate domain walls of ferroelectrics without relying on Landau coefficients. Chapter 8 also marks the first instance of using the phase-field approach to investigate domain structure formation in the OMH material. Generally speaking, the simulations using Model II demonstrate the success of applying the multiphase-field approach to study ferroelectric materials, which can also serve as a fundamental reference.

In Model I, the phenomenological representation of thermodynamics for each ferroelectric phase is treated separately, providing greater freedom of phase transformations. However, computing polarization and ϕ simultaneously results in a low computational efficiency. Besides, the lack of the phenomenological coefficients for ferroelectric phases causes an obstacle to investigating other ferroelectric systems. Since the polarization state is predetermined for each variant, Model II does not require computing polarization states over time. Except for the non-requirement of Landau coefficients, this achieves a high computational efficiency. However, a disadvantage can also serve as an advantage. With the polarization magnitude fixed, except for the jump caused by the $180°$ domain switching when external electric fields are applied, the computed hysteresis loops for a single-crystal BTO display a linear change. Since polarization information is predefined, Model II is unable to calculate the temperature-misfit strain phase diagram in the current format.

9.2. Outlook

While the work detailed in this dissertation stands well on its own, there are several interesting extensions for further development. Since it is the first application of the multiphase-field approach to study domain structures without involving the evolution of polarization states in variants, this subsection specifically explores potential extensions related to Model II.

The present studies constitute the initial phase in the development of Model II, and there are numerous potential research directions for its further extension. For instance, the predetermined polarization state for each variant should be determined based on external stimuli, such as external electric fields and mechanical loading. With regard to the film material, the predefined polarization states should also depend on the misfit strain when accounting for the substrate constraints. These could be improved by incorporating findings from experimental research or theoretical studies. Moreover,

by including the flexoelectric energy, simulations can be further conducted to study the influence of strain gradient on the formation and stability of domain walls. By applying specific boundary conditions and controlling computed geometry, Model II can be further extended to study topological domain walls in nanostructures like nano-dots, nano-wires, and nano-islands. Understanding the Relaxor ferroelectrics and the mechanism of their domain switching using Model II may be enhanced to explore their structure-property relationships.

Furthermore, the computational results presented in Chapter 8 offer a reference foundation for investigating the solar properties of the $MAPbI_3$ materials. However, only simulation studies of ferroelectric domain formation in single-grain $MAPbI_3$ films have been conducted. For future studies, simulations of microstructure formation during the annealing process and large-scale 2D and 3D simulation studies of domain structure and grain formation in polycrystalline $MAPbI_3$ films can be performed. Based on these studies, one can also conduct simulations targeting the growth of OMH perovskite thin films related to experimental investigations of grain growth with a large number of grains in 3D. The simulation results could be analyzed to quantify the ferroelectric and solar cell properties of these films at different growth stages and under varying growth conditions. This analysis would provide valuable information for designing target-oriented, novel light-harvesting perovskites. Besides, theoretical studies have indicated that charged domain walls are more effective in reducing the recombination between holes and electrons in $MAPbI_3$ material. However, the mechanisms underlying the formation and stability of these unnaturally charged domain structures in $MAPbI_3$ films remain unexplored. As a result, another potential research direction could involve investigating the formations and stability of charged domain walls under special physical conditions, such as unique electric or mechanical boundary conditions, doping, charge screening, or other applicable approaches. Additionally, given the strong correlation between solar cell properties and the dynamics of electrons and holes, incorporating the transport equation of the space charge into Model II could provide a valuable reference for investigating ferroelectric domain structures and space charge evolution. Based on this, Model II can be further employed to guide the engineering of ferroelectric domain walls and the design of solar cell devices.

In summary, this dissertation presents a workflow, results, and analysis approach that can guide the proposal, development, and execution of research projects integrating both experimental and numerical approaches. These guidelines are especially useful for projects that bridge different scientific disciplines. By using precise experimental data, researchers can refine, correct, and validate phase-field models, resulting in the achievement of more accurate and detailed modeling of the processes under study.

Part V
Appendix

A. Appendixes

A.1. The dielectric susceptibility and piezoelectric charge coefficients

Based on Ref. [58], the relative dielectric stiffness η_{ij} in tensor notation can be denoted as:

$$\eta_{ij} = \frac{\partial^2 G}{\partial P_i \partial P_j} \, (i, j = 1, 2, 3) \tag{A.1}$$

With regards to FT, η_{ij} can be written as:

$$\eta_{\mathrm{FT},ij} = \begin{bmatrix} \eta_{\mathrm{FT},11} & 0 & 0 \\ 0 & \eta_{\mathrm{FT},22} & 0 \\ 0 & 0 & \eta_{\mathrm{FT},33} \end{bmatrix}, \tag{A.2}$$

in which

$$\eta_{\mathrm{FT},11} = \eta_{\mathrm{FT},22} = P_{\mathrm{FT}}^4 \alpha_{112} + P_{\mathrm{FT}}^2 \alpha_{12} + \alpha_1, \tag{A.3}$$

and

$$\eta_{\mathrm{FT},33} = 15 P_{\mathrm{FT}}^4 \alpha_{111} + 6 P_{\mathrm{FT}}^2 \alpha_{11} + \alpha_1. \tag{A.4}$$

Regarding FR, η_{ij} becomes:

$$\eta_{\mathrm{FR},ij} = \begin{bmatrix} \eta_{\mathrm{FR},11} & \eta_{\mathrm{FR},12} & \eta_{\mathrm{FR},13} \\ \eta_{\mathrm{FR},21} & \eta_{\mathrm{FR},22} & \eta_{\mathrm{FR},23} \\ \eta_{\mathrm{FR},31} & \eta_{\mathrm{FR},32} & \eta_{\mathrm{FR},33} \end{bmatrix}, \tag{A.5}$$

where

$$\begin{aligned} \eta_{\mathrm{FR},11} &= \eta_{\mathrm{FR},22} = \eta_{\mathrm{FR},33} \\ &= 2\alpha_1 + 4\alpha_{11} P_{\mathrm{FR}}^2 + \frac{4}{3}\alpha_{12} P_{\mathrm{FR}}^2 + \frac{10}{3}\alpha_{111} P_{\mathrm{FR}}^4 + \frac{28}{9}\alpha_{112} P_{\mathrm{FR}}^4 + \frac{2}{9}\alpha_{123} P_{\mathrm{FR}}^4, \end{aligned} \tag{A.6}$$

and

$$\begin{aligned} \eta_{\mathrm{FR},12} = \eta_{\mathrm{FR},13} = \eta_{\mathrm{FR},21} = \eta_{\mathrm{FR},23} = \eta_{\mathrm{FR},31} = \eta_{\mathrm{FR},32} \\ = \frac{4}{3}\alpha_{12} P_{\mathrm{FR}}^2 + \frac{16}{9}\alpha_{112} P_{\mathrm{FR}}^2 + \frac{4}{9}\alpha_{123} P_{\mathrm{FR}}^2. \end{aligned} \tag{A.7}$$

The dielectric susceptibility stiffness χ_{ij} is the reciprocal of η_{ij}, i.e.,

$$\chi_{ij} = \frac{A_{ij}}{\Delta} \, (i, j = 1, 2, 3) \tag{A.8}$$

where Δ is the determinant of η_{ij} and A_{ij} is the cofactor.

The piezoelectric coefficients, denoted by b_{ij} in matrix notation (Chapter VII of Ref. [144]), is calculated by:

$$b_{ij} = -\frac{\partial^2 G}{\partial P_i \partial \sigma_j} \, (i = 1, 2, 3; \; j = 1, 2, \cdots 6). \tag{A.9}$$

Based on Ref. [3], the piezoelectric moduli coefficients (d_{ij}) can be computed according to b_{ij}, denoted as:

$$d_{ij} = b_{kj} \chi_{ik} \, (i, k = 1, 2, 3; \; j = 1, 2, \cdots 6). \tag{A.10}$$

Thus, for the FT around MPB of PZT system, the coefficients of d_{ij} can be further extended as:

$$d_{\mathrm{FT},ij} = \begin{bmatrix} 0 & 0 & 0 & 0 & d_{\mathrm{FT},15} & 0 \\ 0 & 0 & 0 & d_{\mathrm{FT},24} & 0 & 0 \\ d_{\mathrm{FT},31} & d_{\mathrm{FT},32} & d_{\mathrm{FT},33} & 0 & 0 & 0 \end{bmatrix}, \tag{A.11}$$

where

$$d_{\mathrm{FT},31} = d_{\mathrm{FT},32} = \frac{Q_{12} P_{\mathrm{FT}}}{\alpha_1 + 6\alpha_{11} P_{\mathrm{FT}}^2 + 15\alpha_{111} P_{\mathrm{FT}}^4}, \tag{A.12}$$

$$d_{\mathrm{FT},33} = \frac{Q_{11} P_{\mathrm{FT}}}{\alpha_1 + 6\alpha_{11} P_{\mathrm{FT}}^2 + 15\alpha_{111} P_{\mathrm{FT}}^4}, \tag{A.13}$$

and

$$d_{\mathrm{FT},15} = d_{\mathrm{FT},24} = \frac{Q_{44} P_{\mathrm{FT}}}{2\left(\alpha_1 + \alpha_{12} P_{\mathrm{FT}}^2 + 2\alpha_{112} P_{\mathrm{FT}}^4\right)}. \tag{A.14}$$

Similarly, coefficients within d_{ij} for the FR phase results in:

$$d_{\mathrm{FR},ij} = \begin{bmatrix} d_{\mathrm{FR},11} & d_{\mathrm{FR},12} & d_{\mathrm{FR},13} & d_{\mathrm{FR},14} & d_{\mathrm{FR},15} & d_{\mathrm{FR},16} \\ d_{\mathrm{FR},21} & d_{\mathrm{FR},22} & d_{\mathrm{FR},23} & d_{\mathrm{FR},24} & d_{\mathrm{FR},25} & d_{\mathrm{FR},26} \\ d_{\mathrm{FR},31} & d_{\mathrm{FR},32} & d_{\mathrm{FR},33} & d_{\mathrm{FR},34} & d_{\mathrm{FR},35} & d_{\mathrm{FR},36} \end{bmatrix}. \tag{A.15}$$

For ease of reading, defining

$$d_{\mathrm{FR},11} = d_{\mathrm{FR},22} = d_{\mathrm{FR},33} = \frac{\mathrm{num}_1}{\mathrm{den}_1} \tag{A.16}$$

where num_1 is defined by:

$$\begin{aligned}\mathrm{num}_1 = &-3\sqrt{3}P_{\mathrm{FR}}\Big[4P_{\mathrm{FR}}^2Q_{12}\big(4P_{\mathrm{FR}}^2\alpha_{112}+P_{\mathrm{FR}}^2\alpha_{123}+3\alpha_{12}\big)\\ &-Q_{11}\big(15P_{\mathrm{FR}}^4\alpha_{111}+22P_{\mathrm{FR}}^4\alpha_{112}+3P_{\mathrm{FR}}^4\alpha_{123}\\ &+18P_{\mathrm{FR}}^2\alpha_{11}+12P_{\mathrm{FR}}^2\alpha_{12}+9\alpha_1\big)\Big],\end{aligned} \tag{A.17}$$

and den_1 is denoted as:

$$\begin{aligned}\mathrm{den}_1 = &225P_{\mathrm{FR}}^8\alpha_{111}^2+540P_{\mathrm{FR}}^8\alpha_{111}\alpha_{112}+60P_{\mathrm{FR}}^8\alpha_{111}\alpha_{123}+180P_{\mathrm{FR}}^8\alpha_{112}^2\\ &-5P_{\mathrm{FR}}^8\alpha_{123}^2+540P_{\mathrm{FR}}^6\alpha_{111}\alpha_{11}+270P_{\mathrm{FR}}^6\alpha_{111}\alpha_{12}+648P_{\mathrm{FR}}^6\alpha_{112}\alpha_{11}\\ &+108P_{\mathrm{FR}}^6\alpha_{112}\alpha_{12}+72P_{\mathrm{FR}}^6\alpha_{11}\alpha_{123}-18P_{\mathrm{FR}}^6\alpha_{123}\alpha_{12}+270P_{\mathrm{FR}}^4\alpha_{111}\alpha_1\\ &+324P_{\mathrm{FR}}^4\alpha_{112}\alpha_1+324P_{\mathrm{FR}}^4\alpha_{11}^2+324P_{\mathrm{FR}}^4\alpha_{11}\alpha_{12}+36P_{\mathrm{FR}}^4\alpha_{123}\alpha_1\\ &+324P_{\mathrm{FR}}^2\alpha_{11}\alpha_1+162P_{\mathrm{FR}}^2\alpha_{12}\alpha_1+81\alpha_1^2.\end{aligned} \tag{A.18}$$

Similarly,

$$d_{\mathrm{FR},12}=d_{\mathrm{FR},21}=d_{\mathrm{FR},13}=d_{\mathrm{FR},31}=d_{\mathrm{FR},23}=d_{\mathrm{FR},32}=\frac{\mathrm{num}_2}{\mathrm{den}_2} \tag{A.19}$$

with num_2 calculated from:

$$\begin{aligned}\mathrm{num}_2 =&3\sqrt{3}P_{\mathrm{FR}}\big(-8P_{\mathrm{FR}}^4Q_{11}\alpha_{112}-2P_{\mathrm{FR}}^4Q_{11}\alpha_{123}+15P_{\mathrm{FR}}^4Q_{12}\alpha_{111}\\ &+14P_{\mathrm{FR}}^4Q_{12}\alpha_{112}+P_{\mathrm{FR}}^4Q_{12}\alpha_{123}-6P_{\mathrm{FR}}^2Q_{11}\alpha_{12}\\ &+18P_{\mathrm{FR}}^2Q_{12}\alpha_{11}+6P_{\mathrm{FR}}^2Q_{12}\alpha_{12}+9Q_{12}\alpha_1\big),\end{aligned} \tag{A.20}$$

and den_2 based on:

$$\begin{aligned}\mathrm{den}_2 =&225P_{\mathrm{FR}}^8\alpha_{111}^2+540P_{\mathrm{FR}}^8\alpha_{111}\alpha_{112}+60P_{\mathrm{FR}}^8\alpha_{111}\alpha_{123}+180P_{\mathrm{FR}}^8\alpha_{112}^2\\ &-5P_{\mathrm{FR}}^8\alpha_{123}^2+540P_{\mathrm{FR}}^6\alpha_{111}\alpha_{11}+270P_{\mathrm{FR}}^6\alpha_{111}\alpha_{12}+648P_{\mathrm{FR}}^6\alpha_{112}\alpha_{11}\\ &+108P_{\mathrm{FR}}^6\alpha_{112}\alpha_{12}+72P_{\mathrm{FR}}^6\alpha_{11}\alpha_{123}-18P_{\mathrm{FR}}^6\alpha_{123}\alpha_{12}+270P_{\mathrm{FR}}^4\alpha_{111}\alpha_1\\ &+324P_{\mathrm{FR}}^4\alpha_{112}\alpha_1+324P_{\mathrm{FR}}^4\alpha_{11}^2+324P_{\mathrm{FR}}^4\alpha_{11}\alpha_{12}+36P_{\mathrm{FR}}^4\alpha_{123}\alpha_1\\ &+324P_{\mathrm{FR}}^2\alpha_{11}\alpha_1+162P_{\mathrm{FR}}^2\alpha_{12}\alpha_1+81\alpha_1^2.\end{aligned} \tag{A.21}$$

In addition,

$$d_{\mathrm{FR},14}=d_{\mathrm{FR},25}=d_{\mathrm{FR},36}=\frac{\mathrm{num}_3}{\mathrm{den}_3}, \tag{A.22}$$

where num_3 is defined as:

$$\mathrm{num}_3=-6\sqrt{3}P_{\mathrm{FR}}^3Q_{44}(4P_{\mathrm{FR}}^2\alpha_{112}+P_{\mathrm{FR}}^2\alpha_{123}+3\alpha_{12}), \tag{A.23}$$

and den_3 is:

$$\begin{aligned}\mathrm{den}_3 =& 225P_{\mathrm{FR}}^8\alpha_{111}^2 + 540P_{\mathrm{FR}}^8\alpha_{111}\alpha_{112} + 60P_{\mathrm{FR}}^8\alpha_{111}\alpha_{123} + 180P_{\mathrm{FR}}^8\alpha_{112}^2 \\ &- 5P_{\mathrm{FR}}^8\alpha_{123}^2 + 540P_{\mathrm{FR}}^6\alpha_{111}\alpha_{11} + 270P_{\mathrm{FR}}^6\alpha_{111}\alpha_{12} + 648P_{\mathrm{FR}}^6\alpha_{112}\alpha_{11} \\ &+ 108P_{\mathrm{FR}}^6\alpha_{112}\alpha_{12} + 72P_{\mathrm{FR}}^6\alpha_{11}\alpha_{123} - 18P_{\mathrm{FR}}^6\alpha_{123}\alpha_{12} + 270P_{\mathrm{FR}}^4\alpha_{111}\alpha_1 \\ &+ 324P_{\mathrm{FR}}^4\alpha_{112}\alpha_1 + 324P_{\mathrm{FR}}^4\alpha_{11}^2 + 324P_{\mathrm{FR}}^4\alpha_{11}\alpha_{12} + 36P_{\mathrm{FR}}^4\alpha_{123}\alpha_1 \\ &+ 324P_{\mathrm{FR}}^2\alpha_{11}\alpha_1 + 162P_{\mathrm{FR}}^2\alpha_{12}\alpha_1 + 81\alpha_1^2.\end{aligned} \tag{A.24}$$

Additionally,

$$d_{FR,15} = d_{\mathrm{FR},16} = d_{\mathrm{FR},24} = d_{\mathrm{FR},26} = d_{\mathrm{FR},34} = d_{\mathrm{FR},35} = \frac{\mathrm{num}_4}{\mathrm{den}_4}, \tag{A.25}$$

in which num_4 can be calculated by:

$$\begin{aligned}\mathrm{num}_4 =& 3\sqrt{3}P_{\mathrm{FR}}Q_{44}\big(15P_{\mathrm{FR}}^4\alpha_{111} + 14P_{\mathrm{FR}}^4\alpha_{112} + P_{\mathrm{FR}}^4\alpha_{123} \\ &+ 18P_{\mathrm{FR}}^2\alpha_{11} + 6P_{\mathrm{FR}}^2\alpha_{12} + 9\alpha_1,\end{aligned} \tag{A.26}$$

and den_4 is expressed as:

$$\begin{aligned}\mathrm{den}_4 =& 2\big(225P_{\mathrm{FR}}^8\alpha_{111}^2 + 540P_{\mathrm{FR}}^8\alpha_{111}\alpha_{112} + 60P_{\mathrm{FR}}^8\alpha_{111}\alpha_{123} + 180P_{\mathrm{FR}}^8\alpha_{112}^2 \\ &- 5P_{\mathrm{FR}}^8\alpha_{123}^2 + 540P_{\mathrm{FR}}^6\alpha_{111}\alpha_{11} + 270P_{\mathrm{FR}}^6\alpha_{111}\alpha_{12} + 648P_{\mathrm{FR}}^6\alpha_{112}\alpha_{11} \\ &+ 108P_{\mathrm{FR}}^6\alpha_{112}\alpha_{12} + 72P_{\mathrm{FR}}^6\alpha_{11}\alpha_{123} - 18P_{\mathrm{FR}}^6\alpha_{123}\alpha_{12} + 270P_{\mathrm{FR}}^4\alpha_{111}\alpha_1 \\ &+ 324P_{\mathrm{FR}}^4\alpha_{112}\alpha_1 + 324P_{\mathrm{FR}}^4\alpha_{11}^2 + 324P_{\mathrm{FR}}^4\alpha_{11}\alpha_{12} + 36P_{\mathrm{FR}}^4\alpha_{123}\alpha_1 \\ &+ 324P_{\mathrm{FR}}^2\alpha_{11}\alpha_1 + 162P_{\mathrm{FR}}^2\alpha_{12}\alpha_1 + 81\alpha_1^2\big).\end{aligned} \tag{A.27}$$

A.2. Simulated domain structures of BTO using Model II

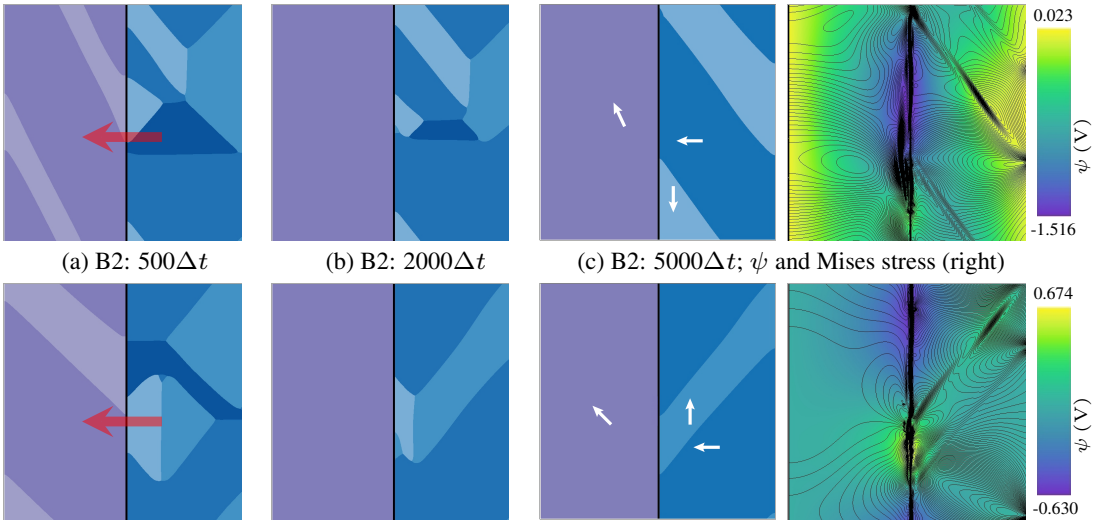

(a) B2: $500\Delta t$ (b) B2: $2000\Delta t$ (c) B2: $5000\Delta t$; ψ and Mises stress (right)

(d) B3: $500\Delta t$ (e) B3: $2000\Delta t$ (f) B3: $5000\Delta t$; ψ and Mises stress(right)

Figure A.1.: Temporal evolution of the domain switching in the B2 and B3 system when applying an external electric field of $E^*_{\text{ext}} = 1$ to their equilibrium state in Figs. 6.10(d) and (e). Red arrows in (a) and (d) indicate the orientation of the applied electric field, while the white arrows in (c) and (f) indicate the polarization direction of each variant at equilibrium. In addition, the right images in (c) and (f) show the corresponding distribution of von Mises stress (contour plots with thin black lines) and electric potential (ψ). Adapted from Ref. [16].

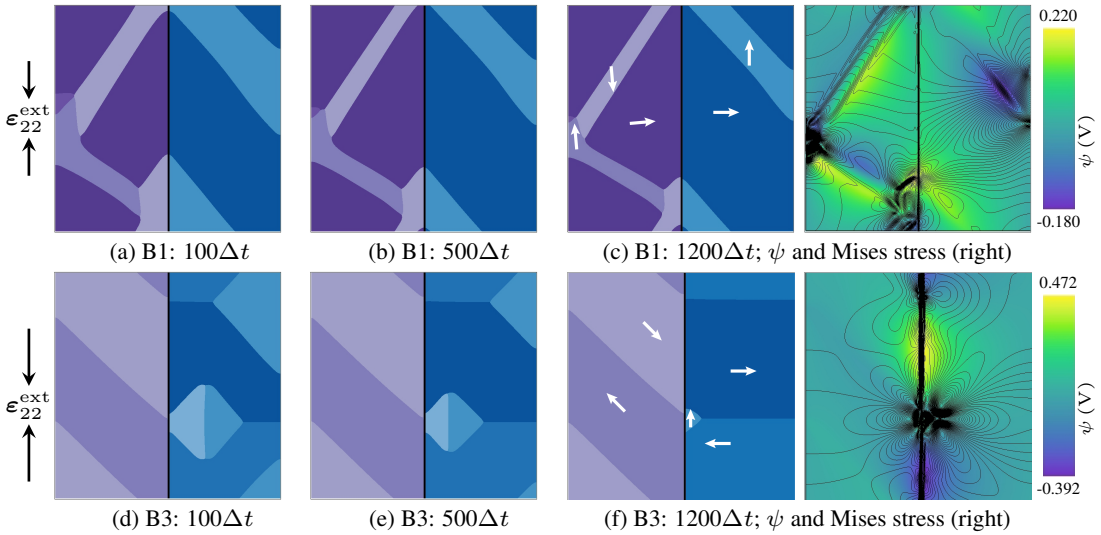

(a) B1: $100\Delta t$ (b) B1: $500\Delta t$ (c) B1: $1200\Delta t$; ψ and Mises stress (right)

(d) B3: $100\Delta t$ (e) B3: $500\Delta t$ (f) B3: $1200\Delta t$; ψ and Mises stress (right)

Figure A.2.: Temporal evolution of the domain switching in the B2 and B3 system when a compressive strain $\varepsilon_{22}^{\mathrm{ext}} = 0.005$ was induced to the y-edges. The initial configurations can be found in their equilibrium state of Figs. 6.10(d) and (e). The white arrows in (c) and (f) indicate the polarization direction of each variant after switching domains. In addition, the right images in (c) and (f) show the corresponding distribution of von Mises stress (contour plots with thin black lines) and electric potential (ψ). Adapted from Ref. [16].

A.3. Temporal evolution of (001)-oriented PTO grows on KTO at various temperatures

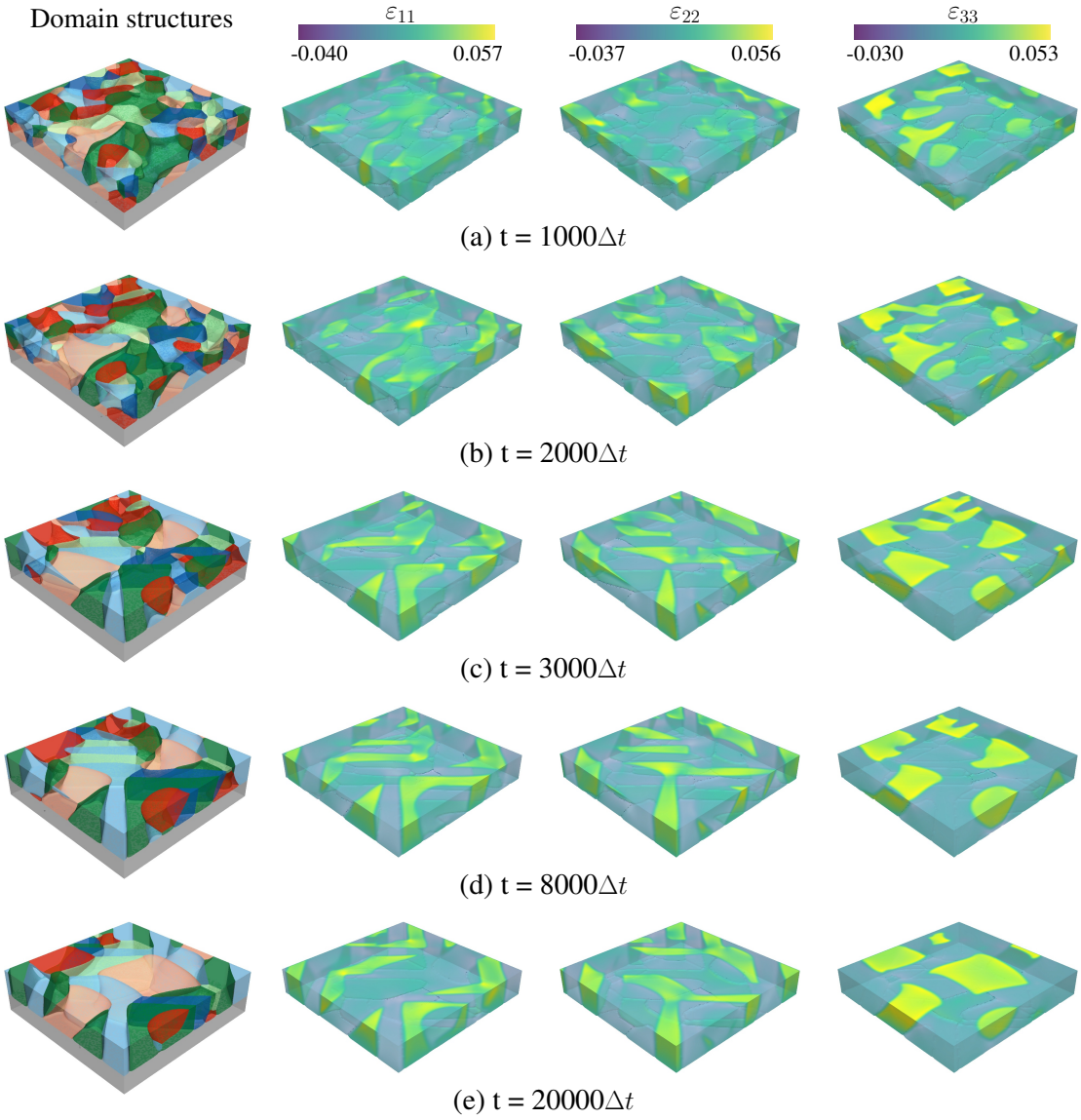

Figure A.3.: The temporal evolution of domain structures, along with the corresponding ε_{11}, ε_{22}, and ε_{33}, in the context of PTO growth on KTO at 25 °C. Adapted from Ref. [17].

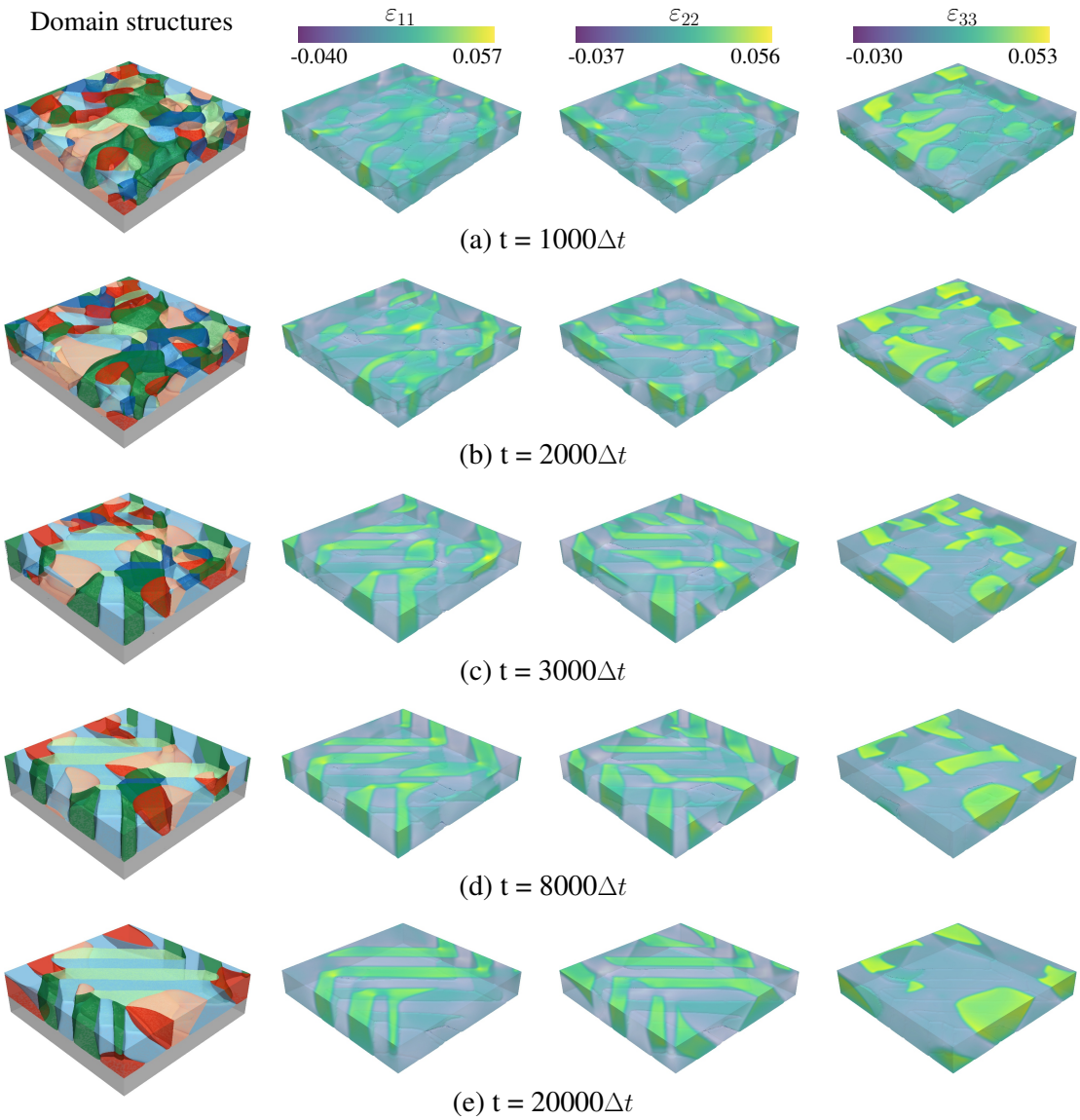

Figure A.4.: The temporal evolution of domain structures, along with the corresponding ε_{11}, ε_{22}, and ε_{33}, in the context of PTO growth on KTO at $200\,^{\circ}\mathrm{C}$. Adapted from Ref. [17].

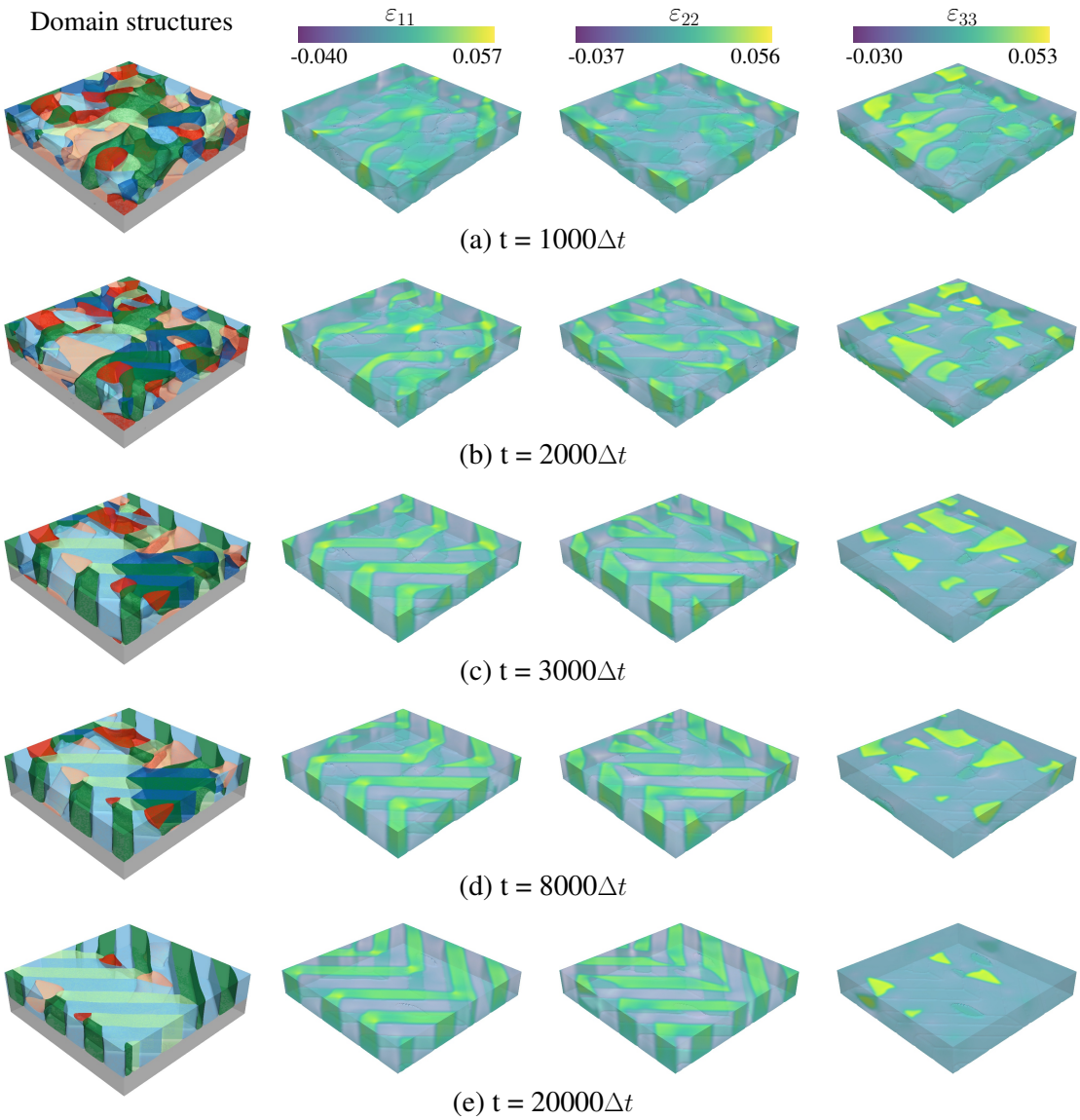

Figure A.5.: The temporal evolution of domain structures, along with the corresponding ε_{11}, ε_{22}, and ε_{33}, in the context of PTO growth on KTO at $400\,^{\circ}\mathrm{C}$. Adapted from Ref. [17].

List of Symbols

Phase-field modeling

α	Indicating phase α
β	Indicating phase β
$\boldsymbol{\phi}$	Phase field vector
$\boldsymbol{j}$	Mass current vector
$\boldsymbol{x}$	Position vector
Δt	Numerical time step width
Δx	Numerical grid size
ϵ	Interface thickness scale parameter
γ_α^c	Normal component of the surface energy density
$\gamma_{\alpha\beta\tau}$	Surface energy density of the α-β-τ interface
$\gamma_{\alpha\beta}$	Surface energy density of the α-β interface
λ	Language Multiplier
$\mathcal{F}$	Free energy functional
$\mathscr{G}$	Gibbs function
μ	Chemical potential
$\widetilde{N}$	Number of locally active phases
$\mathfrak{L}$	Noise function
σ_{int}	Interfacial energy
τ	Indicating phase τ

τ Relaxation constant (inverse of interface mobility)

c Concentration

f Free energy density

H Potential energy coefficient in two-phase field model

$h^{\alpha}(\boldsymbol{\phi})$ Interpolation function

h_f Film thickness

h_s Substrate height

K Gradient energy coefficient in two-phase field model

L Interface thickness

M Mobility coefficient in Allen-Cahn equation

m Atomic mobility in Cahn-Hilliard equation,

$M^{\alpha\beta}$ Phase-field mobility matrix

N Number of phases

N_{fp} Number of ferroelectric phases

N_{g} Number of grains

N_{v} Number of ferroelectric variants

n_s Number of cells discretizing the substrate

t Time

V_c Volume fraction of c-domains

W_{elast} Overall elastic potential based on continuous variables.

Polarization and Electric

$\boldsymbol{D}$ Electric displacement vector

$\boldsymbol{E}$ Electric field vector

$\boldsymbol{E}_{\mathrm{D}}$ Depolarization field vector

$\boldsymbol{d}$	Displacement vector between charges
$\boldsymbol{E}_{\mathrm{ext}}$	External electric field vector
$\boldsymbol{P}$	Polarization vector
$\boldsymbol{p}$	Dipole moment vector
$\boldsymbol{P}_s$	Spontaneous polarization vector
ψ	Electric potential
e	Elementary charge
q	Electric charge
E_c	Coercive field
P_{R}	Remnant polarization
P_{S}	Saturation polarization
P_C	Polarization at Curie temperature

Dielectric properties

$\boldsymbol{\chi}$	Dielectric susceptibility tensor
$\boldsymbol{\eta}$	Relative dielectric tensor
$\boldsymbol{\kappa}$	Dielectric tensor
$\boldsymbol{\kappa}_b$	Dielectric tensor
$\boldsymbol{d}$	Piezoelectric charge matrix
κ	Dielectric permittivity
κ_0	Vacuum permittivity
κ_b	Background dielectric permittivity
κ_r	Relative dielectric permittivity

Coefficients in LDT and LGT

α	Landau potential coefficient

g	Gradient coefficient
β	Landau potential coefficient
γ	Landau potential coefficient

Coefficients in LGDT

α_1	Landau potential coefficient in Voigt notation
α_{111}	Landau potential coefficient in Voigt notation
α_{112}	Landau potential coefficient in Voigt notation
α_{11}	Landau potential coefficient in Voigt notation
α_{123}	Landau potential coefficient in Voigt notation
α_{12}	Landau potential coefficient in Voigt notation
α_{ij}	Landau potential coefficient in tensor notation
G_{11}	Gradient coefficients in in Voigt notation
g_{ijkl}	Gradient coefficients in tensor notation
β_{ijkl}	Landau potential coefficient in tensor notation
γ_{ijklmn}	Landau potential coefficient in tensor notation

Thermodynamic Properties

C	Curie Constant
F	Helmholtz free energy of ferroelectrics
G	Gibbs function
G_1	Elastic Gibbs function
G_2	Electric Gibbs function
H	Enthalpy
H_1	Elastic enthalpy
H_2	Electric enthalpy

Q	Heat
S	Entropy
T	Temperature
T_0	Curie-Weiss temperature
T_c	Curie point
U	Internal energy
W	Work

Lattice parameters

$\boldsymbol{z}$	Unit vector
$\mathcal{R}$	Atomic position deviation
Φ	Unit cell angle
Θ	Unit cell distortion
a	Lattice constants
c	Lattice constants
s_a	Atomic position
t_a	Atomic position
V_ϕ	Phase volume fraction
V_{PC}	Volume of the pseudocubic primitive cell
x_{FR}	Spontaneous strain of rhombohedral phase
x_{FT}	Spontaneous strain of tetragonal phase

Mechanics

$\bar{\boldsymbol{\sigma}}$	Effective stress tensor
$\boldsymbol{\mathcal{C}}$	Elastic stiffness tensor
$\boldsymbol{\mathcal{Q}}$	Electrostrictive tensor

$\boldsymbol{\mathcal{S}}$	Elastic compliance tensor
$\boldsymbol{\varepsilon}$	Strain tensor
$\boldsymbol{\varepsilon}^0$	Spontaneous strain tensor
$\boldsymbol{\varepsilon}^{\mathrm{mis}}$	Misfit strain tensor
$\boldsymbol{u}$	Displacement field
$\boldsymbol{\sigma}$	Stress tensor
$\tilde{\boldsymbol{\varepsilon}}$	Inelastic strain

Mathematics and Operators

$\nabla\cdot$	Divergence
∇	Gradient
∇^2	Laplacian
$\boldsymbol{e}_3$	Unit vector in x_3-direction
$\boldsymbol{tr}$	Euler transformation matrices
$\boldsymbol{U}$	Niggli matrix
δ_{ij}	Kronecker's symbol
$\frac{\delta^n}{\delta x^n}$	Functional derivative of order n w.r.t. x
$\frac{\mathrm{d}^n}{\mathrm{d}x^n}$	Ordinary derivative of order n w.r.t. x
$\frac{\partial^n}{\partial x^n}$	Partial derivative of order n w.r.t. x
Ω	Spatial domain
$\partial\Omega_i$	Spatial domain edge
φ	Grain orientation
V	Volume

List of Abbreviations

BTO $BaTiO_3$. i, ii, 3, 6, 9, 10, 20, 31, 78, 80, 87, 88, 90, 92, 100, 101, 131, 132

FR ferroelectric rhombohedral phase. i, 47, 49–57, 59, 60, 62, 65–68, 70, 73, 75, 77, 131, 135, 136, 152, 153, 160

FT ferroelectric tetragonal phase. i, 47, 49–57, 59, 60, 62–68, 70, 73, 75, 77, 131, 135, 136, 152, 153, 160

KTO $KTaO_3$. 105, 110, 112–116, 118, 119, 121, 157

LDT Landau-Devonshire Theory. 16, 20, 35, 146

LGDT Landau-Ginzburg-Devonshire Theory. i, 2, 20, 21, 29, 33, 34, 51, 131, 147

LGT Landau-Ginzburg Theory. 20, 146

MAPbI$_3$ Methylammonium Lead Iodide. i, ii, 2, 9, 10, 122–125, 127–129, 132, 133, 157, 158, 160

MPB morphotropic phase boundary. i, 2, 47–49, 55, 152

MPI Message-Passing Interface. 57, 78, 104, 124

OMH Organic metal halide. i, 122, 132, 133

Pace3D Parallel Algorithms for Crystal Evolution in 3D. 57, 78, 103, 124

PFM Piezoresponse Force Microscopy. 47, 123, 158

PTO $PbTiO_3$. i, ii, 6, 9, 20, 30, 31, 103, 105, 110, 112–114, 116–119, 121, 124, 131, 152, 157

PZT $Pb(Zr_{1-x}Ti_x)O_3$. i, ii, 2, 9, 31, 47–49, 152

TDGL time-dependent Ginzburg-Landau. i, ii, 2, 23, 29–31, 38, 47, 57, 75, 77, 78, 82, 102, 108, 110, 120, 124, 152

List of Figures

List of Tables

Bibliography

[1] A.F. Devonshire. XCVI. Theory of barium titanate: Part I. Philos. Mag, 40(309):1040–1063, 1949.

[2] A.F. Devonshire. CIX. Theory of barium titanate–Part II. Philos. Mag., 42(333):1065–1079, 1951.

[3] A.F. Devonshire. Theory of ferroelectrics. Adv. Phys., 3(10):85–130, 1954.

[4] W.F. Rao and Y.U. Wang. Bridging domain mechanism for phase coexistence in morphotropic phase boundary ferroelectrics. Appl. Phys. Lett., 90(18):182906, 2007.

[5] W.F. Rao and Y.U. Wang. Grain size effect of phase coexistence around morphotropic phase boundary in ferroelectric polycrystalline ceramics. Appl. Phys. Lett., 92(10):102905, 2008.

[6] W.F. Rao and Y.U. Wang. Microstructures of coherent phase decomposition near morphotropic phase boundary in lead zirconate titanate. Appl. Phys. Lett., 91(5):052901, 2007.

[7] W.F. Rao and Y.U. Wang. Domain wall broadening mechanism for domain size effect of enhanced piezoelectricity in crystallographically engineered ferroelectric single crystals. Appl. Phys. Lett., 90(4):041915, 2007.

[8] X.Q. Ke, D. Wang, X.B. Ren, and Y.Z. Wang. Polarization spinodal at ferroelectric morphotropic phase boundary. Phys. Rev. Lett., 125(12):127602, 2020.

[9] H. Liu, H. Huang, L. Fan, Y. Ren, H. Zhou, L.Q. Chen, J. Chen, and X. Xing. Synergy between phase transformation and domain switching in two morphotropic phase boundary ferroelectrics. Phys. Rev. Mater., 2(11):111403, 2018.

[10] H. Liu, J. Chen, H.B. Huang, L.L. Fan, Y. Ren, Z. Pan, J.X. Deng, L.Q. Chen, and X.R. Xing. Role of reversible phase transformation for strong piezoelectric performance at the morphotropic phase boundary. Phys. Rev. Lett., 120(5):055501, 2018.

[11] Y. Zhang, F. Xue, Z. Chen, J.M. Liu, and L.Q. Chen. Presence of a purely tetragonal phase in ultrathin $BiFeO_3$ films: Thermodynamics and phase-field simulations. Acta Mater., 183:110–117, 2020.

[12] F. Xue, Y. Li, Y. Gu, J. Zhang, and L.Q. Chen. Strain phase separation: Formation of ferroelastic domain structures. Phys. Rev. B, 94(22):220101, 2016.

[13] L.Q. Chen. Phase-field method of phase transitions/domain structures in ferroelectric thin films: a review. J. Am. Ceram. Soc., 91(6):1835–1844, 2008.

[14] J.J. Wang and L.Q. Chen. Strain control of domain structures in ferroelectric thin films: Applications of phase-field method. Handb. Mater. Model. Appl., pages 1213–1230, 2020.

[15] L. Fan, W. Werner, S. Subotić, D. Schneider, M. Hinterstein, and B. Nestler. Multigrain phase-field simulation in ferroelectrics with phase coexistences: An improved phase-field model. Comput. Mater. Sci., 203:111056, 2022.

[16] L. Fan, M. Reder, D. Schneider, M. Hinterstein, and B. Nestler. A phase-field model for ferroelectric materials—based on the multiphase-field method. Comput. Mater. Sci., 230:112510, 2023.

[17] L. Fan, M. Reder, D. Schneider, M. Hinterstein, and B. Nestler. Multiphase-field modeling of domain structure evolution in ferroelectric thin film. J. Eur. Ceram. Soc., 45(1):116875, 2025.

[18] Albert Einstein. Die grundlagen der allgemeinen. Relativitats- teorie, Annale der Physic, 49:769, 1916.

[19] J.J. Wang, B Wang, and L.Q. Chen. Understanding, predicting, and designing ferroelectric domain structures and switching guided by the phase-field method. Annu. Rev. Mater. Res., 49:127–152, 2019.

[20] R. Resta. Ab initio simulation of the properties of ferroelectric materials. Model. Simul. Mater. Sci. Eng., 11(4):R69, 2003.

[21] K.M. Rabe. Theoretical investigations of epitaxial strain effects in ferroelectric oxide thin films and superlattices. Curr. Opin. Solid State Mater. Sci., 9(3):122–127, 2005.

[22] D. Bolten, U. Böttger, and R. Waser. Influence of defects on the properties of a 2d ferroelectric: A monte-carlo simulation study. Jpn. J. Appl. Phys., 41(11S):7202, 2002.

[23] Y.B. Ma, K. Albe, and B.X. Xu. Lattice-based monte carlo simulations of the electrocaloric effect in ferroelectrics and relaxor ferroelectrics. Phys. Rev. B., 91(18):184108, 2015.

[24] B.G. Potter Jr, V. Tikare, and B.A. Tuttle. Monte carlo simulation of ferroelectric domain structure and applied field response in two dimensions. J. Appl. Phys., 87(9):4415–4424, 2000.

[25] V. Boddu, F. Endres, and P. Steinmann. Molecular dynamics study of ferroelectric domain nucleation and domain switching dynamics. Sci. Rep., 7(1):806, 2017.

[26] I. Grinberg, Y.H. Shin, and A.M Rappe. Molecular dynamics study of dielectric response in a relaxor ferroelectric. Phys. Rev. Lett., 103(19):197601, 2009.

[27] J. Očenášek, J. Minár, and J. Alcalá. Dynamics of lattice disorder in perovskite materials, polarization nanoclusters and ferroelectric domain wall structures. npj Comput. Mater., 9(1):118, 2023.

[28] L. Li, Y. Yang, D. Zhang, Z.G. Ye, S. Jesse, S.V Kalinin, and R.K Vasudevan. Machine learning–enabled identification of material phase transitions based on experimental data: Exploring collective dynamics in ferroelectric relaxors. Sci. Adv., 4(3):eaap8672, 2018.

[29] S. Lu, Q. Zhou, L. Ma, Y. Guo, and J. Wang. Rapid discovery of ferroelectric photovoltaic perovskites and material descriptors via machine learning. Small Methods, 3(11):1900360, 2019.

[30] I.E. Irodov. Basic Laws Of Electromegnitism. Arihant Publication India Limited, 2018.

[31] D.J. Griffiths. Introduction to electrodynamics. Cambridge University Press, 2023.

[32] K.C. Kao. Dielectric phenomena in solids. Elsevier, 2004.

[33] M.H. Zhang. Field-induced phase transition of lead-free antiferroelectric niobates. TU Darmstadt, 2022.

[34] A.P. Levanyuk, B.A. Strukov, and A. Cano. Background dielectric permittivity: Material constant or fitting parameter? Ferroelectrics, 503(1):94–103, 2016.

[35] Y. Zheng and C.H. Woo. Thermodynamic modeling of critical properties of ferroelectric superlattices in nano-scale. Appl. Phys. A, 97:617–626, 2009.

[36] A.K. Tagantsev. Landau expansion for ferroelectrics: Which variable to use? Ferroelectrics, 375(1):19–27, 2008.

[37] Y. Xu. Ferroelectric materials and their applications. Elsevier, 2013.

[38] Y. Gu, F. Xue, S. Lei, T.TA. Lummen, J. Wang, V. Gopalan, and L.Q. Chen. Monoclinic phases arising across thermal inter-ferroelectric phase transitions. Phys. Rev. B, 90(2):024104, 2014.

[39] D.M. Evans, V. Garcia, D. Meier, and M. Bibes. Domains and domain walls in multiferroics. Phys. Sci. Rev., 5(9), 2020.

[40] P.S. Bednyakov, T. Sluka, A.K. Tagantsev, D. Damjanovic, and N. Setter. Formation of charged ferroelectric domain walls with controlled periodicity. Sci. Rep., 5(1):15819, 2015.

[41] P.S. Bednyakov, B.I. Sturman, T. Sluka, A.K. Tagantsev, and P.V. Yudin. Physics and applications of charged domain walls. npj Comput. Mater., 4(1):65, 2018.

[42] D. Meier. Functional domain walls in multiferroics. J. Phys. Condens. Matter, 27(46):463003, 2015.

[43] G. Catalan, J. Seidel, R. Ramesh, and J.F. Scott. Domain wall nanoelectronics. Rev. Mod. Phys., 84(1):119, 2012.

[44] J.R. Whyte and J.M. Gregg. A diode for ferroelectric domain-wall motion. Nat. Commun., 6(1):7361, 2015.

[45] Y. Zuo, Y.A. Genenko, and B.X. Xu. Charge compensation of head-to-head and tail-to-tail domain walls in barium titanate and its influence on conductivity. J. Appl. Phys., 116(4):044109, 2014.

[46] D. Rossi, A. Pecchia, M.A. der Maur, T. Leonhard, H. Röhm, M.J. Hoffmann, A. Colsmann, and A. Di Carlo. On the importance of ferroelectric domains for the performance of perovskite solarf cells. Nano Energy, 48:20–26, 2018.

[47] H. Röhm, T. Leonhard, A.D. Schulz, S. Wagner, M.J. Hoffmann, and A. Colsmann. Ferroelectric properties of perovskite thin films and their implications for solar energy conversion. Adv. Mater., 31(26):1806661, 2019.

[48] J.A. Mundy, J. Schaab, Y. Kumagai, A. Cano, M. Stengel, I.P. Krug, D.M. Gottlob, H. Doğanay, M.E. Holtz, R. Held, et al. Functional electronic inversion layers at ferroelectric domain walls. Nat. Mater., 16(6):622–627, 2017.

[49] J.R. Whyte, R.G.P. McQuaid, P. Sharma, C. Canalias, J.F. Scott, A. Gruverman, and J. M. Gregg. Ferroelectric domain wall injection. Adv. Mater., 26(2):293–298, 2014.

[50] X. Wu and D. Vanderbilt. Theory of hypothetical ferroelectric superlattices incorporating head-to-head and tail-to-tail 180° domain walls. Phys. Rev. B: Condens. Matter Mater. Phys., 73(2):020103, 2006.

[51] M.Y. Gureev, A.K. Tagantsev, and N. Setter. Head-to-head and tail-to-tail 180° domain walls in an isolated ferroelectric. Phys. Rev. B, 83(18):184104, 2011.

[52] E.A. Eliseev, A.N. Morozovska, G.S. Svechnikov, V. Gopalan, and V.Ya Shur. Static conductivity of charged domain walls in uniaxial ferroelectric semiconductors. Phys. Rev. B: Condens. Matter Mater. Phys., 83(23):235313, 2011.

[53] M.H. Zhang, Y. Tan, T. Yang, and L.Q. Chen. Influence of oxygen vacancies on the domain wall stability in bifeo3. J. Am. Ceram. Soc., 2024.

[54] A.K. Yadav, C.T. Nelson, S.L. Hsu, Z. Hong, J.D. Clarkson, C.M. Schlepütz, A.R. Damodaran, P. Shafer, E. Arenholz, L.R. Dedon, et al. Observation of polar vortices in oxide superlattices. Nature, 530(7589):198–201, 2016.

[55] S. Das, Y.L. Tang, Z. Hong, M.A.P. Gonçalves, M.R. McCarter, C. Klewe, K.X. Nguyen, F. Gómez-Ortiz, P. Shafer, E. Arenholz, et al. Observation of room-temperature polar skyrmions. Nature, 568(7752):368–372, 2019.

[56] I. Luk'Yanchuk, Y. Tikhonov, A. Razumnaya, and V.M. Vinokur. Hopfions emerge in ferroelectrics. Nat. Commun., 11(1):2433, 2020.

[57] Y.J. Wang, Y.P. Feng, Y.L. Zhu, Y.L. Tang, L.X. Yang, M.J. Zou, W.R. Geng, M.J. Han, X.W. Guo, B. Wu, et al. Polar meron lattice in strained oxide ferroelectrics. Nat. Mater., 19(8):881–886, 2020.

[58] M.J. Haun, E. Furman, S.J. Jang, and L.E. Cross. Thermodynamic theory of the lead zirconate-titanate solid solution system, part I: phenomenology. Ferroelectrics, 99(1):13–25, 1989.

[59] N.A. Pertsev, A.G. Zembilgotov, S. Hoffmann, R. Waser, and A.K. Tagantsev. Ferroelectric thin films grown on tensile substrates: Renormalization of the Curie–Weiss law and apparent absence of ferroelectricity. J. Appl. Phys., 85(3):1698–1701, 1999.

[60] K. Binder. Theory of first-order phase transitions. Rep. Prog. Phys, 50(7):783, 1987.

[61] D. Damjanovic. Ferroelectric, dielectric and piezoelectric properties of ferroelectric thin films and ceramics. Rep. Prog. Phys, 61(9):1267, 1998.

[62] K. Rabe, Ch.H. Ahn, and J.M. Triscone. Physics of ferroelectrics: a modern perspective, volume 105. Springer Science & Business Media, 2007.

[63] M.J. Haun, E. Furman, S.J. Jang, H.A. McKinstry, and L.E. Cross. Thermodynamic theory of $PbTiO_3$. J. Appl. Phys., 62(8):3331–3338, 1987.

[64] M.J. Haun, E. Furman, H.A. McKinstry, and L.E. Cross. Thermodynamic theory of the lead zirconate-titanate solid solution system, part II: Tricritical behavior. Ferroelectrics, 99(1):27–44, 1989.

[65] M.J. Haun, Z.Q. Zhuang, E. Furman, S.J. Jang, and L.E. Cross. Thermodynamic theory of the lead zirconate-titanate solid solution system, part III: Curie constant and sixth-order polarization interaction dielectric stiffness coefficients. Ferroelectrics, 99(1):45–54, 1989.

[66] M.J. Haun, E. Furman, T.R. Halemane, and L.E. Cross. Thermodynamic theory of the lead zirconate-titanate solid solution system, part IV: Tilting of the oxygen octahedra. Ferroelectrics, 99(1):55–62, 1989.

[67] M.J. Haun, E. Furman, S.J. Jang, and L.E. Cross. Thermodynamic theory of the lead zirconate-titanate solid solution system, part V: Theoretical calculations. Ferroelectrics, 99(1):63–86, 1989.

[68] L.Q. Chen. Phase-field models for microstructure evolution. Annu. Rev. Mater. Res.chen, 32(1):113–140, 2002.

[69] W.J. Boettinger, J.A. Warren, C. Beckermann, and A. Karma. Phase-field simulation of solidification. Annu. Rev. Mater. Res., 32(1):163–194, 2002.

[70] I. Steinbach. Phase-field models in materials science. Model. Simul. Mater. Sci. Eng., 17(7):073001, 2009.

[71] N. Moelans, B. Blanpain, and P. Wollants. An introduction to phase-field modeling of microstructure evolution. Calphad, 32(2):268–294, 2008.

[72] M. Plapp. Phase-field models. In Handbook of Crystal Growth, pages 631–668. Elsevier, 2015.

[73] S. Daubner, P.W. Hoffrogge, M. Minar, and B. Nestler. Triple junction benchmark for multiphase-field and multi-order parameter models. Comput. Mater. Sci., 219:111995, 2023.

[74] S.M Allen and J.W Cahn. A microscopic theory for antiphase boundary motion and its application to antiphase domain coarsening. Acta metall., 27(6):1085–1095, 1979.

[75] J.W Cahn and J.E Hilliard. Free energy of a nonuniform system. i. interfacial free energy. J. Chem. Phys., 28(2):258–267, 1958.

[76] I. Steinbach, F. Pezzolla, B. Nestler, M. Seeßelberg, R. Prieler, G.J. Schmitz, and J.LL Rezende. A phase field concept for multiphase systems. Physica D, 94(3):135–147, 1996.

[77] I. Steinbach and F. Pezzolla. A generalized field method for multiphase transformations using interface fields. Physica D, 134(4):385–393, 1999.

[78] B. Nestler, H. Garcke, and B. Stinner. Multicomponent alloy solidification: phase-field modeling and simulations. Phys. Rev. E, 71(4):041609, 2005.

[79] B. Nestler and A. Choudhury. Phase-field modeling of multi-component systems. Curr. Opin. Solid State Mater. Sci., 15(3):93–105, 2011.

[80] P. Hoffrogge, A. Mukherjee, E.S. Nani, PG.K. Amos, F. Wang, D. Schneider, and B. Nestler. Multiphase-field model for surface diffusion and attachment kinetics in the grand-potential framework. Phys. Rev. E, 103(3):033307, 2021.

[81] J. Wang, S.Q. Shi, L.Q. Chen, Y. Li, and T.Y. Zhang. Phase-field simulations of ferroelectric/ferroelastic polarization switching. Acta Mater., 52(3):749–764, 2004.

[82] S. Choudhury, Y.L. Li, C.E. Krill Iii, and L.Q. Chen. Phase-field simulation of polarization switching and domain evolution in ferroelectric polycrystals. Acta Mater., 53(20):5313–5321, 2005.

[83] Y. Ji, W.J. Chen, and Y. Zheng. The emergence of tunable negative electrocaloric effect in ferroelectric/paraelectric superlattices. J. Phys. D Appl. Phys., 53(50):505302, 2020.

[84] J. Wang, D. Liang, J. Ma, Y. Fan, J. Ma, H.M.i Jafri, H. Yang, Q. Zhang, Y. Wang, C. Guo, et al. Polar solomon rings in ferroelectric nanocrystals. Nat. Commun., 14(1):3941, 2023.

[85] M.J. Zhou, K. Peng, T. Yang, L.Q. Chen, and C.W. Nan. Effect of electrical boundary conditions on the domain stability of porous ferroelectric nanowires. J. Appl. Phys., 134(8), 2023.

[86] H.L. Hu and L.Q. Chen. Three-dimensional computer simulation of ferroelectric domain formation. J. Am. Ceram. Soc., 81(3):492–500, 1998.

[87] S. Choudhury, Y.L. Li, C. Krill Iii, and L.Q. Chen. Effect of grain orientation and grain size on ferroelectric domain switching and evolution: Phase field simulations. Acta Mater., 55(4):1415–1426, 2007.

[88] J. Wang, W.L. Shu, T. Shimada, T. Kitamura, and T.Y. Zhang. Role of grain orientation distribution in the ferroelectric and ferroelastic domain switching of ferroelectric polycrystals. Acta Mater., 61(16):6037–6049, 2013.

[89] Y.L. Li, S.Y. Hu, Z.K. Liu, and L.Q. Chen. Effect of substrate constraint on the stability and evolution of ferroelectric domain structures in thin films. Acta mater., 50(2):395–411, 2002.

[90] Y.L. Li, S.Y. Hu, Z.K. Liu, and L.Q. Chen. Effect of electrical boundary conditions on ferroelectric domain structures in thin films. Appl. Phys. Lett., 81(3):427–429, 2002.

[91] Y.L. Li, L.Q. Chen, G. Asayama, D.G. Schlom, M.A. Zurbuchen, and S.K. Streiffer. Ferroelectric domain structures in $SrBi_2Nb_2O_9$ epitaxial thin films: Electron microscopy and phase-field simulations. J. Appl. Phys., 95(11):6332–6340, 2004.

[92] Z. Hong, A.R. Damodaran, F. Xue, S.L. Hsu, J. Britson, A.K. Yadav, C.T. Nelson, J.J. Wang, J.F. Scott, L.W. Martin, R. Ramesh, and L.Q. Chen. Stability of polar vortex lattice in ferroelectric superlattices. Nano Lett., 17(4):2246–2252, 2017.

[93] J.J. Wang, T.N. Yang, J.A. Zorn, E. Wang, J. Irwin, S. Lindemann, M.S. Rzchowski, J.M. Hu, C.B. Eom, and L.Q. Chen. Strain anisotropy and magnetic domain structures in multiferroic heterostructures: High-throughput finite-element and phase-field studies. Acta Mater., 176:73–83, 2019.

[94] J. Liu, Y. Ji, S. Yuan, L. Ding, W. Chen, and Y. Zheng. Controlling polar-toroidal multi-order states in twisted ferroelectric nanowires. Npj Comput. Mater., 4(1):78, 2018.

[95] Y. Ji, W.J. Chen, and Y. Zheng. Crossover of polar and toroidal orders in ferroelectric nanodots with a morphotropic phase boundary and nonvolatile polar-vortex transformations. Phys. Rev. B, 100(1):014101, 2019.

[96] Y. Xiao, V.B. Shenoy, and K. Bhattacharya. Depletion layers and domain walls in semiconducting ferroelectric thin films. Phys. Rev. Lett., 95(24):247603, 2005.

[97] T. Sluka, A.K. Tagantsev, D. Damjanovic, M. Gureev, and N. Setter. Enhanced electromechanical response of ferroelectrics due to charged domain walls. Nat. Commun., 3(1):1–7, 2012.

[98] Y.S. Teh and K. Bhattacharya. Photovoltaic effect in multi-domain ferroelectric perovskite oxides. J. Appl. Phys., 125(6):064103, 2019.

[99] K.L. Yang, Y. Zhang, S.H. Zheng, L. Lin, Z.B. Yan, J.M. Liu, and S.W. Cheong. Spatial anisotropy of topological domain structure in hexagonal manganites. Phy. Rev. B, 95(2):024114, 2017.

[100] A.N. Morozovska, E.A. Eliseev, J.J. Wang, G.S. Svechnikov, Y.M. Vysochanskii, V. Gopalan, and L.Q. Chen. Phase diagram and domain splitting in thin ferroelectric films with incommensurate phase. Phy. Rev. B, 81(19):195437, 2010.

[101] F. Xue, X. Wang, I. Socolenco, Y. Gu, L.Q. Chen, and S.W. Cheong. Evolution of the statistical distribution in a topological defect network. Sci. Rep., 5(1):17057, 2015.

[102] F. Li, S. Zhang, T. Yang, Z. Xu, N. Zhang, G. Liu, J. Wang, J. Wang, Z. Cheng, Z.G. Ye, et al. The origin of ultrahigh piezoelectricity in relaxor-ferroelectric solid solution crystals. Nat. Commun., 7(1):13807, 2016.

[103] C. Shi, N. Mao, K. Zhang, T. Zhang, M.H. Chiu, K. Ashen, B. Wang, X. Tang, G. Guo, S. Lei, et al. Domain-dependent strain and stacking in two-dimensional van der waals ferroelectrics. Nat. Commun., 14(1):7168, 2023.

[104] A. Kontsos and C.M. Landis. Computational modeling of domain wall interactions with dislocations in ferroelectric crystals. Int. J. Solids and Struct, 46(6):1491–1498, 2009.

[105] H.H. Wu, J. Wang, S.G. Cao, L.Q. Chen, and T.Y. Zhang. Micro-/macro-responses of a ferroelectric single crystal with domain pinning and depinning by dislocations. J. Appl. Phys., 114(16), 2013.

[106] J. Britson, C. Neflson, X. Pan, and L.Q. Chen. First-order morphological transition of ferroelastic domains in ferroelectric thin films. Acta mater., 75:188–197, 2014.

[107] S. Pan, Q. Li, and Q. Liu. Ferroelectric creep associated with domain switching emission in the cracked ferroelectrics. Comput. Mater. Sci., 140:244–252, 2017.

[108] G. Sheng, J.X. Zhang, Y.L. Li, S. Choudhury, Q.X. Jia, Z.K. Liu, and L.Q. Chen. Domain stability of $PbTiO_3$ thin films under anisotropic misfit strains: Phase-field simulations. J. Appl. Phys., 104(5), 2008.

[109] G. Sheng, J.X. Zhang, Y.L. Li, S. Choudhury, Q.X. Jia, Z.K. Liu, and L.Q. Chen. Misfit strain–misfit strain diagram of epitaxial $BaTiO_3$ thin films: Thermodynamic calculations and phase-field simulations. Appl. Phys. Lett., 93(23), 2008.

[110] H.T. Chen, A.K. Soh, and Y. Ni. Phase field modeling of flexoelectric effects in ferroelectric epitaxial thin films. Acta Mech., 225(4-5):1323–1333, 2014.

[111] R. Ahluwalia, A.K. Tagantsev, P. Yudin, N. Setter, N. Ng, and D.J. Srolovitz. Influence of flexoelectric coupling on domain patterns in ferroelectrics. Phy. Rev. B, 89(17):174105, 2014.

[112] Y.J. Wang, J. Li, Y.L. Zhu, and X.L. Ma. Phase-field modeling and electronic structural analysis of flexoelectric effect at 180° domain walls in ferroelectric $PbTiO_3$. J. Appl. Phys., 122(22):224101, 2017.

[113] Z. Liu, X. Zhou, B. Feng, and B.X. Xu. Engineered periodic quadrupole superstructure in ferroelectric thin films via flexoelectricity. Acta Mater., 216:117126, 2021.

[114] J.J. Wang, Y. Wang, J.F. Ihlefeld, P.E. Hopkins, and L.Q. Chen. Tunable thermal conductivity via domain structure engineering in ferroelectric thin films: A phase-field simulation. Acta Mater., 111:220–231, 2016.

[115] H.H. Wu, J. Zhu, and T.Y. Zhang. Pseudo-first-order phase transition for ultrahigh positive/negative electrocaloric effects in perovskite ferroelectrics. Nano Energy, 16:419–427, 2015.

[116] Y.H. Huang, J.J. Wang, T.N. Yang, Y.J. Wu, X.M. Chen, and L.Q. Chen. A thermodynamic potential, energy storage performances, and electrocaloric effects of $Ba_{1-x}Sr_xTiO_3$ single crystals. Appl. Phys. Lett., 112(10), 2018.

[117] B. Völker, P. Marton, C. Elsässer, and M. Kamlah. Multiscale modeling for ferroelectric materials: a transition from the atomic level to phase-field modeling. Contin. Mech. Thermodyn., 23:435–451, 2011.

[118] B. Völker, C.M. Landis, and M. Kamlah. Multiscale modeling for ferroelectric materials: identification of the phase-field model's free energy for PZT from atomistic simulations. Smart Mater. Struct., 21(3):035025, 2012.

[119] R.C. Peng, X. Cheng, B. Peng, Z. Zhou, L.Q. Chen, and M. Liu. Domain patterns and super-elasticity of freestanding $BiFeO_3$ membranes via phase-field simulations. Acta Mater., 208:116689, 2021.

[120] J.X. Zhang, Y.L. Li, S. Choudhury, L.Q. Chen, Y.H. Chu, F. Zavaliche, M.P. Cruz, R. Ramesh, and Q.X. Jia. Computer simulation of ferroelectric domain structures in epitaxial $BiFeO_3$ thin films. J. Appl. Phys., 103(9), 2008.

[121] M.D. Biegalski, L. Qiao, Y. Gu, A. Mehta, Q. He, Y. Takamura, A. Borisevich, and L.Q. Chen. Impact of symmetry on the ferroelectric properties of $CaTiO_3$ thin films. Appl. Phys. Lett, 106(16), 2015.

[122] G.L. Brennecka and B.M. Winchester. Simulation studies of nucleation of ferroelectric polarization reversal. Technical report, Sandia National Lab.(SNL-NM), Albuquerque, NM (United States), 2014.

[123] H. Lu, Y. Tan, J.PV McConville, Z. Ahmadi, B. Wang, M. Conroy, K. Moore, U. Bangert, J.E Shield, L.Q. Chen, et al. Electrical tunability of domain wall conductivity in $LiNbO_3$ thin films. Adv. Mater., 31(48):1902890, 2019.

[124] Q. Li, C.T. Nelson, S.L. Hsu, A.R. Damodaran, L.L. Li, A.K. Yadav, M. McCarter, L.W. Martin, R. Ramesh, and S.V. Kalinin. Quantification of flexoelectricity in $PbTi_O3/SrTi_O3$ superlattice polar vortices using machine learning and phase-field modeling. Nat. Commun., 8(1):1468, 2017.

[125] E. Enriquez, Q. Li, P. Bowlan, B. Lu, P.and Zhang, L. Li, H. Wang, A.J Taylor, D. Yarotski, R.P Prasankumar, et al. Induced ferroelectric phases in $SrTiO_3$ by a nanocomposite approach. Nanoscale, 12(35):18193–18199, 2020.

[126] B. Wang, H.N. Chen, J.J. Wang, and L.Q. Chen. Ferroelectric domain structures and temperature-misfit strain phase diagrams of $K_{1-x}Na_xNbO_3$ thin films: A phase-field study. Appl. Phys. Lett, 115(9), 2019.

[127] M.J. Zhou, B. Wang, K. Peng, H.X. Liu, L.Q. Chen, and C.W. Nan. Phase-field simulation of domain size effect on dielectric and piezoelectric responses in $K_{0.5}Na_{0.5}NbO_3$ epitaxial thin films with superdomain structures. Acta Mater., 248:118777, 2023.

[128] L. Guin and D. Kochmann. A phase-field model for ferroelectrics with general kinetics. Part I: Model formulation. arXiv:2203.16479, 2022.

[129] J. Hlinka and P. Márton. Phenomenological model of a 90° domain wall in $BaTiO_3$-type ferroelectrics. Phys. Rev. B, 74(10):104104, 2006.

[130] C. Mennerich, F. Wendler, M. Jainta, and B. Nestler. A phase-field model for the magnetic shape memory effect. Arch. Mech., 63(5-6):549–571, 2011.

[131] C. Mennerich, F. Wendler, M. Jainta, and B. Nestler. Rearrangement of martensitic variants in Ni_2MnGa studied with the phase-field method. Eur. Phys. J. B., 86(4):1–9, 2013.

[132] D. Schneider, O. Tschukin, A. Choudhury, M. Selzer, T. Böhlke, and B. Nestler. Phase-field elasticity model based on mechanical jump conditions. Comput. Mech., 55(5):887–901, 2015.

[133] D. Schneider, E. Schoof, O. Tschukin, A. Reiter, C. Herrmann, F. Schwab, M. Selzer, and B. Nestler. Small strain multiphase-field model accounting for configurational forces and mechanical jump conditions. Comput. Mech., 61(3):277–295, 2018.

[134] E. Schoof, D. Schneider, N. Streichhan, T. Mittnacht, M. Selzer, and B. Nestler. Multiphase-field modeling of martensitic phase transformation in a dual-phase microstructure. Int J Solids Struct., 134:181–194, 2018.

[135] D. Schneider, S. Schmid, M. Selzer, T. Böhlke, and B. Nestler. Small strain elasto-plastic multiphase-field model. Comput. Mech., 55(1):27–35, 2015.

[136] B. Noheda, D.E. Cox, G. Shirane, J.A. Gonzalo, L.E. Cross, and S.E. Park. A monoclinic ferroelectric phase in the $\mathrm{Pb(Zr_{1-x}Ti_x)O_3}$ solid solution. Appl. Phys. Lett., 74(14):2059–2061, 1999.

[137] G. Picht, N.H. Khansur, K.G. Webber, H. Kungl, M.J. Hoffmann, and M. Hinterstein. Grain size effects in donor doped lead zirconate titanate ceramics. J. Appl. Phys., 128(21):214105, 2020.

[138] Y.U. Wang. Field-induced inter-ferroelectric phase transformations and domain mechanisms in high-strain piezoelectric materials: insights from phase field modeling and simulation. J. Mater. Sci., 44(19):5225–5234, 2009.

[139] D.K. Khatua, C.M. Fancher, J.L. Jones, and R. Ranjan. Anomalous reduction in domain wall displacement at the morphotropic phase boundary of the piezoelectric alloy system $\mathrm{PbTiO_3 - BiScO_3}$. Phys. Rev. B., 93(10):104103, 2016.

[140] M. Hinterstein, M. Hoelzel, J. Rouquette, J. Haines, J. Glaum, H. Kungl, and M. Hoffman. Interplay of strain mechanisms in morphotropic piezoceramics. Acta Mater., 94:319–327, 2015.

[141] H.D. Megaw and C.N.W. Darlington. Geometrical and structural relations in the rhombohedral perovskites. Acta Crystallogr. A, 31(2):161–173, 1975.

[142] K.F. Hane and T.W. Shield. Microstructure in the cubic to trigonal transition. Mater. Sci. Eng. A, 291(1-2):147–159, 2000.

[143] Y.H. Seo, D.J. Franzbach, J. Koruza, A. Benčan, B. Malič, M. Kosec, J.L. Jones, and K.G. Webber. Nonlinear stress-strain behavior and stress-induced phase transitions in soft $\mathrm{Pb(Zr_{1-x}Ti_x)O_3}$ at the morphotropic phase boundary. Phys. Rev. B., 87(9), 2013.

[144] J.F. Nye. Physical Properties of Crystals: Their Representation by Tensors and Matrices. Clarendon Press, 1957.

[145] D. Damjanovic. Contributions to the piezoelectric effect in ferroelectric single crystals and ceramics. J. Am. Ceram. Soc., 88(10):2663–2676, 2005.

[146] D.J. Franzbach, Y.H. Seo, A.J. Studer, Y.C. Zhang, J. Glaum, J.E. Daniels, J. Koruza, A. Benčan, B. Malič, and K.G. Webber. Electric-field-induced phase transitions in co-doped $Pb(Zr_{1-x}Ti_x)O_3$ at the morphotropic phase boundary. Sci. Technol. Adv. Mater., 15, 2014.

[147] F. Gehrig, H. Jelitto, and G.A. Schneider. Fracture criterion for a conducting crack in poled PZT-PIC 151 investigated by stable crack growth. Acta Mater., 56(2):222–229, 2008.

[148] J. Hötzer, A. Reiter, H. Hierl, P. Steinmetz, M. Selzer, and B. Nestler. The parallel multi-physics phase-field framework Pace3D. J. Comput. Sci., 26:1–12, 2018.

[149] P. Lv and C.S. Lynch. Phase-field simulation of domain walls in rhombohedral ferroelectric single crystals. Acta Mater., 155:245–252, 2018.

[150] M. Hinterstein, K.Y. Lee, S. Esslinger, J. Glaum, A.J. Studer, M. Hoffman, and M.J. Hoffmann. Determining fundamental properties from diffraction: Electric field induced strain and piezoelectric coefficient. Phys. Rev. B, 99(17):174107, 2019.

[151] J. Zhao, S.D. Funni, E.R. Molina, E.C. Dickey, and J.L. Jones. Orientation-dependent, field-induced phase transitions in soft lead zirconate titanate piezoceramics. J. Eur. Ceram. Soc., 41(6):3357–3362, 2021.

[152] O.A. Torres-Matheus, R.E. García, and C.M. Bishop. Phase coexistence near the polymorphic phase boundary. Acta Mater., 164:577–585, 2019.

[153] O.A. Torres Matheus. Multiphase field modelling of ferroelectric materials near the polymorphic phase boundary. PhD thesis, University of Canterbury, 2020.

[154] O.A Torres-Matheus, R.E. García, and C.M. Bishop. Microstructural phase coexistence kinetics near the polymorphic phase boundary. Acta Mater., 206:116579, 2021.

[155] O.A. Torres-Matheus, R.E. García, and C.M. Bishop. Physics-based optimization of landau parameters for ferroelectrics: application to BZT–50BCT. Model. Simul. Mater. Sci. Eng., 29(7):075001, 2021.

[156] J. Zhu, Y. Gao, D. Wang, T.Y. Zhang, and Y. Wang. Taming martensitic transformation via concentration modulation at nanoscale. Acta Mater., 130:196–207, 2017.

[157] J.Y. Li, C.H. Lei, L.J. Li, Y.C. Shu, and Y.Y. Liu. Unconventional phase field simulations of transforming materials with evolving microstructures. Acta Mech. Sin., 28(4):915–927, 2012.

[158] Q. Chen, Y. Zhang, W. Liu, J. Jiang, Q. Yang, and L. Jiang. Ferroelectric switching behavior of nanoscale $Hf_{0.5}Zr_{0.5}O_2$ grains. Int. J. Mech. Sci., 212:106828, 2021.

[159] B. Lai, Y. Wang, Y. Shao, Y. Deng, W. Yang, L. Jiang, and Y. Zhang. Study on the phase transition dynamics of HfO_2-based ferroelectric films under ultrafast electric pulse. J. Phys. Condens., 33(40):405402, 2021.

[160] D. Schneider, F. Schwab, E. Schoof, A. Reiter, C. Herrmann, M. Selzer, T. Böhlke, and B. Nestler. On the stress calculation within phase-field approaches: a model for finite deformations. Comput. Mech., 60(2):203–217, 2017.

[161] D. Schneider, M. Selzer, J. Bette, I. Rementeria, A. Vondrous, M.J. Hoffmann, and B. Nestler. Phase-field modeling of diffusion coupled crack propagation processes. Adv. Eng. Mater., 16(2):142–146, 2014.

[162] D. Schneider, E. Schoof, Y. Huang, M. Selzer, and B. Nestler. Phase-field modeling of crack propagation in multiphase systems. Comput. Methods. Appl. Mech. Eng., 312:186–195, 2016.

[163] S.H. Wemple, Didomenico J.M., and I. Camlibel. Dielectric and optical properties of melt-grown $BaTiO_3$. J. Phys. Chem. Solids, 29(10):1797–1803, 1968.

[164] L. Li, L. Xie, and X. Pan. Real-time studies of ferroelectric domain switching: a review. Rep. Prog. Phys., 82(12):126502, 2019.

[165] J.Y. Li, R.C. Rogan, E. Üstündag, and K. Bhattacharya. Domain switching in polycrystalline ferroelectric ceramics. Nat. Mater., 4(10):776–781, 2005.

[166] P. Muralt. Ferroelectric thin films for micro-sensors and actuators: a review. J. Micromech. Microeng., 10(2):136, 2000.

[167] N. Setter, D. Damjanovic, L. Eng, G. Fox, S. Gevorgian, S. Hong, A. Kingon, H. Kohlstedt, N.Y. Park, G.B. Stephenson, et al. Ferroelectric thin films: Review of materials, properties, and applications. J. Appl. Phys., 100(5), 2006.

[168] L. You, F. Zheng, L. Fang, Y. Zhou, L.Z. Tan, Z. Zhang, G. Ma, D. Schmidt, A. Rusydi, L. Wang, et al. Enhancing ferroelectric photovoltaic effect by polar order engineering. Sci. Adv., 4(7):eaat3438, 2018.

[169] A. Fernandez, M. Acharya, H.G. Lee, J. Schimpf, Y. Jiang, D. Lou, Z. Tian, and L.W. Martin. Thin-film ferroelectrics. Adv. Mater., 34(30):2108841, 2022.

[170] Y.L. Li and L.Q. Chen. Temperature-strain phase diagram for $BaTiO_3$ thin films. Appl. Phys. Lett., 88(7), 2006.

[171] D.G. Schlom, L.Q. Chen, C.B. Eom, K.M. Rabe, S.K. Streiffer, and J.M. Triscone. Strain tuning of ferroelectric thin films. Annu. Rev. Mater. Res., 37:589–626, 2007.

[172] G. Sheng, J.M. Hu, J.X. Zhang, Y.L. Li, Z.K. Liu, and L.Q. Chen. Phase-field simulations of thickness-dependent domain stability in $PbTiO_3$ thin films. Acta Mater., 60(8):3296–3301, 2012.

[173] D. Liu, J. Wang, H.M. Jafri, X. Wang, X. Shi, D. Liang, C. Yang, X. Cheng, and H. Huang. Phase-field simulations of vortex chirality manipulation in ferroelectric thin films. npj QM., 7(1):34, 2022.

[174] D. Liu, X. Shi, J. Wang, X. Cheng, and H. Huang. Phase-field simulations of surface charge-induced ferroelectric vortex. J. Phys. D: Appl. Phys., 54(40):405302, 2021.

[175] Y.Q. Xu, S.Y. Wu, L.J. Zhang, L.N. Wu, and C.C. Ding. First-principles study of structural, electronic, elastic, and optical properties of cubic $KNbO_3$ and $KTaO_3$ crystals. Phys. Status Solidi. B, 254(5):1600620, 2017.

[176] K.S. Lee, J.H. Choi, J.Y. Lee, and S. Baik. Domain formation in epitaxial $Pb(Zr_{1-x}Ti_x)O_3$ thin films. J. Appl. Phys., 90(8):4095–4102, 2001.

[177] R. People and J.C. Bean. Calculation of critical layer thickness versus lattice mismatch for Ge_xSi_{1-x}/Si strained-layer heterostructures. Appl. Phys. Lett., 47(3):322–324, 1985.

[178] R. People and J.C. Bean. Erratum: Calculation of critical layer thickness versus lattice mismatch for Ge_xSi_{1-x}/Si strained-layer heterostructures [appl. phys. lett. 4 7, 322 (1985)]. Appl. Phys. Lett., 49(4):229–229, 1986.

[179] B.S. Kwak, A. Erbil, J.D. Budai, M.F. Chisholm, L.A. Boatner, and B.J. Wilkens. Domain formation and strain relaxation in epitaxial ferroelectric heterostructures. Phys. Rev. B, 49(21):14865, 1994.

[180] S.D Stranks, G.E Eperon, G. Grancini, C. Menelaou, M.JP Alcocer, T. Leijtens, L.M Herz, A. Petrozza, and H.J Snaith. Electron-hole diffusion lengths exceeding 1 micrometer in an organometal trihalide perovskite absorber. Science, 342(6156):341–344, 2013.

[181] K. Tvingstedt, O. Malinkiewicz, A. Baumann, C. Deibel, H.J Snaith, V. Dyakonov, and H.J Bolink. Radiative efficiency of lead iodide based perovskite solar cells. Sci. Rep., 4(1):6071, 2014.

[182] Q. Lin, A. Armin, R. C. R. Nagiri, P.L Burn, and P. Meredith. Electro-optics of perovskite solar cells. Nat. Photonics., 9(2):106–112, 2015.

[183] J. Sun, J. Wu, X. Tong, F. Lin, Y. Wang, and Z.M Wang. Organic/inorganic metal halide perovskite optoelectronic devices beyond solar cells. Adv. Sci., 5(5):1700780, 2018.

[184] J.M Frost, K.T Butler, and A. Walsh. Molecular ferroelectric contributions to anomalous hysteresis in hybrid perovskite solar cells. APL Mater., 2(8), 2014.

[185] A.MA Leguy, J.M. Frost, A.P McMahon, V.G. Sakai, W. Kockelmann, C. Law, X. Li, F. Foglia, A. Walsh, B.C O'regan, et al. The dynamics of methylammonium ions in hybrid organic–inorganic perovskite solar cells. Nat. Commun., 6(1):7124, 2015.

[186] A. Stroppa, C. Quarti, F. De Angelis, and S. Picozzi. Ferroelectric polarization of ch3nh3pbi3: a detailed study based on density functional theory and symmetry mode analysis. J. Phys. Chem. Lett., 6(12):2223–2231, 2015.

[187] A. Poglitsch and D. Weber. Dynamic disorder in methylammoniumtrihalogenoplumbates (ii) observed by millimeter-wave spectroscopy. The Journal of chemical physics, 87(11):6373–6378, 1987.

[188] Y. Dang, Y. Liu, Y. Sun, D. Yuan, X. Liu, W. Lu, G. Liu, H. Xia, and X. Tao. Bulk crystal growth of hybrid perovskite material ch 3 nh 3 pbi 3. CrystEngComm, 17(3):665–670, 2015.

[189] T. Leonhard, H. Röhm, F.J. Altermann, M.J. Hoffmann, and A. Colsmann. Evolution of ferroelectric domains in methylammonium lead iodide and correlation with the performance of perovskite solar cells. J. Mater. Chem. A, 9(38):21845–21858, 2021.

[190] H. Röhm, T. Leonhard, M.J. Hoffmann, and A. Colsmann. Ferroelectric poling of methylammonium lead iodide thin films. Adv. Funct. Mater., 30(5):1908657, 2020.

[191] M. Hinterstein. Unpublished data provided by Manuel Hinterstein, Fraunhofer Institute for Mechanics of Materials IWM, 2023.

[192] A.C. Ferreira, A. Létoublon, S. Paofai, S. Raymond, C. Ecolivet, B. Rufflé, S. Cordier, C. Katan, M.I Saidaminov, A.A. Zhumekenov, et al. Elastic softness of hybrid lead halide perovskites. Phys. Rev. Lett., 121(8):085502, 2018.

[193] T. Leonhard, A.D. Schulz, H. Röhm, S. Wagner, F.J. Altermann, W. Rheinheimer, M.J. Hoffmann, and A. Colsmann. Probing the microstructure of methylammonium lead iodide perovskite solar cells. Energy Technol., 7(3):1800989, 2019.

Publications and Honors

Articles in scholarly journals

Thesis Components:

- **L. Fan**, M. Reder, D. Schneider, M. Hinterstein, and B. Nestler. Multiphase-field modeling of domain structure evolution in ferroelectric thin film. J. Eur. Ceram. Soc., page 116875, 2025.
- **L. Fan**, M. Reder, D. Schneider, M. Hinterstein, and B. Nestler. A phase-field model for ferroelectric materials—based on the multiphase-field method. Comput. Mater. Sci., 230:112510, 2023.
- **L. Fan**, W. Werner, S. Subotić, D. Schneider, M. Hinterstein, and B. Nestler. Multigrain phase-field simulation in ferroelectrics with phase coexistences: An improved phase-field model. Comput. Mater. Sci., 203:111056, 2022.

Other collaborations (not included in this dissertation):

- **L. Fan**, C. Shen, K. Hu, H. Liu, and H. Zhang. DFT calculations and thermodynamic re-assessment of the Fe-Y binary system, J. Ph. Equilibria. Diffus., 42(3):348–362, 2021
- C. Shen, K. Hu, **L. Fan**, and H. Zhang. Thermodynamic reassessment of the Au-In binary system supported with first principles calculations, J. Ph. Equilibria Diffus.,2(4):479–488, 2021.
- C. Shen, N. Hadaeghi, H.K. Singh, L. Teng, **L. Fan**, G.Z, Qin, and H.B. Zhang. Two-dimensional buckling structure induces the ultra-low thermal conductivity: A comparative study of the group GaX (X= N, P, As), J. Mater. Chem. C, 10(4):1436–1444, 2022.

Conference contributions

- **L. Fan**, M. Reder, D. Schneider, M. Hinterstein, and B. Nestler. A phase-field model for ferroelectric materials—based on the multiphase-field method. The 5th

International Symposium on Phase-Field Modelling in Materials Science; 05/2024; oral presentation.

- **L. Fan**, M. Reder, D. Schneider, M. Hinterstein, and B. Nestler. A phase-field model for ferroelectric materials—based on the multiphase-field method. 9th GAMM (German Association of Applied Mathmatics and Mechanics) Workshop on Phase-field modeling; 02/2024; oral presentation.
- **L. Fan**, W. Werner, S. Subotić, D. Schneider, M. Hinterstein, M. Reder, and B. Nestler. A phase-field model for polycrystalline ferroelectricity with phase-coexistence. 8th GAMM (German Association of Applied Mathmatics and Mechanics) Workshop on Phase-field modeling; 07/2023; oral presentation.
- **L. Fan**, W. Werner, S. Subotić, D. Schneider, M. Hinterstein, M. Reder, and B. Nestler. A new phase-field model for polycrystalline ferroelectricity with phase-coexistence. ISAF (International Symposium on Application of Ferroelectrics); 06/2022; oral presentation.
- **L. Fan**, M. Reder, D. Schneider, M. Hinterstein, and B. Nestler. A phase-field model for ferroelectric materials—based on the multiphase-field method. Materials/Microstructure modelling: Analytics & Benchmarks; 10/2023; poster presentation.
- **L. Fan**, W. Werner, S. Subotić, D. Schneider, M. Hinterstein, M. Reder, and B. Nestler. A phase-field model for polycrystalline ferroelectricity with phase-coexistence. Phase-field models for the evolution of complex structures; 09/2022; poster presentation.

Honors

- Young Scientists in 73th Lindau Nobel Laureate Meeting, 2024